Late Transition Metal Bimetallics for Photocatalytic Hydrogen Production, M–X and C–H Bond Activation

By

Arthur J. Esswein

B.A., The Johns Hopkins University (2002)

Submitted to the Department of Chemistry
In Partial Fulfillment of the Requirements
For the Degree of

DOCTOR OF PHILOSOPHY IN INORGANIC CHEMISTRY

at the

MASSACHUSETTS INSTITUTE OF TECHNOLOGY

September 2007

Signature of Author: _____

Department of Chemistry
July 5, 2007

Certified By: _____

Daniel G. Nocera
Henry Dreyfus Professor of Energy and Professor of Chemistry
Thesis Supervisor

Accepted By: _____

Robert W. Field
Haslam and Dewey Professor of Chemistry
Chairman, Departmental Committee on Graduate Studies

This Doctoral Thesis has been examined by a committee of the Department of Chemistry as follows:

Christopher C. Cummins
Professor of Chemistry
Committee Chairman

Daniel G. Nocera
Henry Dreyfus Professor of Energy and Professor of Chemistry
Thesis Supervisor

Richard R. Schrock
Frederick G. Keyes Professor of Chemistry

To my family, especially my mom and sisters for all your love and support during my time at MIT.

Late Transition Metal Bimetallics for Photocatalytic Hydrogen Production, M–X and C–H Bond Activation

By

Arthur J. Esswein

Submitted to the Department of Chemistry on July 5, 2007, in partial fulfillment of the requirements for the degree of Doctor of Philosophy.

Abstract

Broadly defined this thesis has focused on the design and study of molecular catalysts that engender multi-electron reactions and photoreactions on small molecule substrates relevant to solar energy conversion. Specifically the molecular design elements employed have focused on bimetallic complexes of late transition metals that exhibit an unusual two-electron mixed valence ground state. Initial studies focused on the mechanistic elucidation of the reported photocatalytic production of hydrogen from homogeneous hydrohalic acid solution using a two-electron mixed valence dirhodium complex. Studies aimed at understanding and improving the photochemical quantum efficiency for challenging M–X ($X = Cl^-$, Br^-) bond photoactivations were undertaken by incorporating gold into a heterobimetallic rhodium-gold construct. Additionally the organometallic reactivity of two-electron mixed valence diiridium cores was explored with a specific emphasis on C–H bond activations in order to extend the cooperative bimetallic reactivity observed in the dirhodium systems beyond HX and H_2 substrates to alkanes and arenes.

Thesis Supervisor: Daniel G. Nocera

Title: Henry Dreyfus Professor of Energy and Professor of Chemistry

Table of Contents

List of Figures

Chapter 1

Chapter 2

Chapter 3

Chapter 4

List of Tables

Chapter 1

Chapter 2

Chapter 3

Chapter 4

List of Schemes

Chapter 1:

Introduction

Portions of this work will appear:

Esswein, A. J.; Nocera, D. G. *Accepted for Publication in Chem. Rev.*

1.1 *Solar Photocatalysis*

A great technological challenge facing our global future is the development of a secure, clean, and renewable energy source.[1] Rising standards of living in a growing world population will cause global energy consumption to increase dramatically over the next half century. Energy consumption is predicted to increase at least two-fold, from our current burn rate of 12.8 TW to 28 - 35 TW by 2050.[2,3] Proven reserves of coal, oil, and gas suggest that this energy need can be met with conventional sources.[4] However unless supplemented, increases in energy intensity derived from economic and population growth will be inextricably linked to increased carbon emissions. While the precise climatological response to continued runaway CO_2 emissions is not known, it is abundantly clear that the current atmospheric CO_2 levels of 380 ppm are significantly higher than anything seen in the last 650,000 years.[5,6] A "wait and see" policy towards human impact on global climate change amounts to nothing more than a grand experiment on global scale.

Hydrogen presents itself as one potential alternative to carboniferous fossil fuels, but many "grand challenges" remain before hydrogen can replace fossil fuels as a widespread energy source.[7] A short-term response to this challenge is the use of methane and other petroleum-based fuels as hydrogen sources.[8] However, external factors of economy, environment, and security dictate that this energy need be met eventually by renewable and sustainable sources,[9,10] with water emerging prominently as the primary carbon-neutral hydrogen source and light as an energy input.

The benefits of solar energy conversion for energy production, dubbed the "photochemistry of the future", were recognized nearly a century ago.[11] The goal of such photochemistry is to use the energy of solar photons to drive catalytic cycles composed of thermodynamically uphill chemical transformations. In this way solar energy can be stored in the form of chemical bonds, or simply, solar fuels. The photogeneration of molecular hydrogen is appealing in this regard as H_2 represents perhaps one of the simplest targets for such reactivity studies. Although significant technological challenges remain before hydrogen can be used directly as a fuel source, such as storage and fuel cell design, mature chemistries are already in hand for the use of hydrogen as an energy carrier to drive downhill transformations to generate liquid fuels, especially in the area of CO_2 hydrogenations,[12] and thus as the phosphate bond of

ATP is the basic energy currency of biology, so should the H–H bond of hydrogen become the basic energy unit for our carbon neutral society.

1.2 *Molecular Photocatalytic Hydrogen Production*

As an introduction to the thesis work presented herein an outline of the literature precedent for molecular photocatalytic hydrogen production schemes would be instructive. The discussion is broken into four classes loosely differentiated by the substrates from which the proton and electron equivalents that compose the hydrogen product originate.

(a) Direct RH Substrates. Hydrogen production from RH substrates derives electron and proton equivalents from either the homo- or heterolysis of C–H or O–H bonds, and typically involves inner sphere mechanisms that invoke intermediates with substrate directly bound to the catalyst. Common substrates include alkanes and primary or secondary alcohols. The products of this photocatalysis are hydrogen and the respective dehydrogenation product, alkenes, aldehydes or ketones.

(b) Indirect RH Substrates. The most prevalent approach to hydrogen-producing photocatalysis is the construction of three-component systems comprising a sensitizer to absorb light, a proton reduction catalyst and an electron relay to shuttle reducing equivalents from the sensitizer to the catalyst. In these systems, the electron equivalents are derived from sacrificial reducing agents that involve either the homo- or heterolytic cleavage of C–H or O–H bonds of RH substrates and acids. Unlike direct RH dehydrogenations, substrate activation is coupled indirectly to hydrogen production via the relay catalysts and cleavage of the substrate typically proceeds by an outer sphere mechanism.

(c) Carbon Monoxide. The water-gas shift (WGS) reaction couples the oxidation of CO to CO_2 with the reduction of water to hydrogen.

(d) Acids. Acids can be the direct substrate for hydrogen production. The challenge to turnover is catalyst regeneration by oxidation of the conjugate base.

In the interests of brevity this introduction will not cover research approaches to produce hydrogen photoelectrochemically, by biomass conversion, or in biological systems, and will be confined to homogenous systems; hydrogen production at solid or semiconductor surfaces from direct bandgap or sensitized photoexcitation will not be considered.

1.2.1.1 Direct RH Dehydrogenations

1.2.1.2 Alkane Dehydrogenations

Alkane dehydrogenations are among the most well defined schemes for photocatalytic hydrogen production. The reaction type is characterized by the following:

$$C_nH_m \rightleftharpoons C_nH_{m-2} + H_2 \quad (1)$$

Hydrogen production occurs generally by classical organometallic mechanisms involving alkane C–H bond activation followed by β-hydride elimination. As a consequence many of these reactions are catalyzed by Group 9 transition metal complexes. The discovery and mechanistic understanding of photochemical alkane dehydrogenation reactions has been derived largely from cycles constructed for the thermal, as opposed to photochemical, dehydrogenation of alkanes. Accordingly, a presentation of thermal alkane dehydrogenation will precede that promoted along photochemical pathways.

The discovery of the hydrogenation of alkenes using Wilkinson's complex, and the intensive study of Group 9 complexes with alkenes and hydrogen provided a backdrop for elucidating the reverse process: alkane dehydrogenation. Generally the reaction of hydrogen with a coordinatively unsaturated metal complex is thermodynamically favorable,

$$M^{n+} + H_2 \rightleftharpoons M^{n+2}(H)_2 \qquad \Delta G < 0 \quad (2)$$

and thus the dehydrogenation of alkanes typically requires an external thermodynamic driving force. Many thermal systems derive a thermodynamic advantage by coupling a hydrogen donor such as cyclooctane to the high heat of hydrogenation of a sacrificial hydrogen acceptor such as *tert*-butylethylene (TBE), eq 3-5:

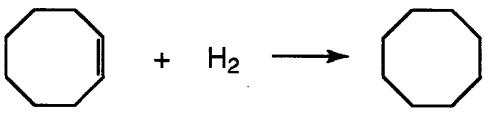

(3)

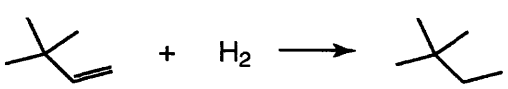

(4)

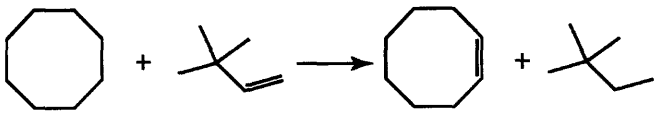

(5)

Early studies used iridium complexes to model and isolate intermediates in alkane hydrogenation cycles.[13] Following up on previous work involving dihydride olefin complexes of iridium,[14] Crabtree and coworkers noted that the *trans*-$Ir^{I}(COE)_2L_2^+$ complex (COE = cyclooctene, L = PPh_3) converted to the cyclooctadiene (COD) complex $Ir^{I}(COD)L_2^+$ and free cyclooctane when heated to 40 °C in CH_2Cl_2. The product distribution indicated that a transfer hydrogenation had occurred and suggested that iridium complexes could serve as alkane dehydrogenation catalysts under appropriate conditions. Several reports followed where the substrate scope was expanded to cyclohexene and cyclopentene to generate arenes and cyclopentadienyls, respectively.[15-17] A rhenium polyhydride, ReL_2H_7 (L= PPh_3, PEt_2Ph) was observed to engage in similar reactivity.[18-22] In both cases the reactions were stoichiometric owing to the strength of the metal arene and cyclopentadienyl interactions that resulted from dehydrogenation chemistry.

A host of Ir^{III} dihydrides were developed as alkane dehydrogenation catalysts, and are believed to operate in general by the mechanism shown in Figure 1.1 (left) for the specific case of cyclooctane dehydrogenation by $Ir^{III}H_2(CF_3CO_2)(PR_3)_2$.[23,24] For PR_3 = P(*p*-F-$C_6H_4)_3$, dehydrogenation proceeds from the dihydride $Ir^{III}H_2(CF_3CO_2)(PR_3)_2$ via a proposed initial conversion of the κ^2-CF_3CO_2 to an κ^1 binding mode to open a coordination site, followed by coordination of TBE. Presumably the ability of $CF_3CO_2^-$ to interchange binding modes is important, as the use of $CH_3CO_2^-$ in place of $CF_3CO_2^-$ gave a catalytically inactive complex. The TBE is then hydrogenated to give 2,2-dimethylbutane which binds weakly to the Ir^{I} center and upon dissociation generates a reactive three-coordinate, 14 electron Ir^{I} complex as a proposed intermediate. Alkane binding and C–H activation proceed to give a hydrido alkyl complex, which then β-hydride eliminates to give a dihydrido olefin species. Subsequent dissociation of alkene and conversion of the κ^1-CF_3CO_2 to a κ^2-binding mode regenerates the starting $Ir^{III}H_2(CF_3CO_2)(PR_3)_2$ complex and closes the catalytic cycle. The overall determinant to the effectiveness of this catalysis appears to involve removal of the dihydride ligands from the coordination sphere of the metal center. With the P(*p*-F-$C_6H_4)_3$ ligand, this is accomplished by the transfer hydrogenation of TBE, which has an unusually high heat of hydrogenation and

therefore provides the thermodynamic driving force for the overall reaction. Under these conditions using the R = *p*-F-C_6H_4 ligand, a maximum of 16 turnovers for cyclooctane dehydrogenation in the presence of excess TBE at 150 °C was observed.

In principle, the driving force for alkane dehydrogenation can be supplied by a photon instead of hydrogenation of a sacrificial alkene such as TBE.[25-27] This reactivity mode was first reported by Crabtree for $Ir^{III}H_2(CF_3CO_2)(PR_3)_2$ for R = Cy.[23,24] The cyclohexyl derivative gave only 2 equivalents of COE under thermal conditions, analogous to those used for R = *p*-F-C_6H_4

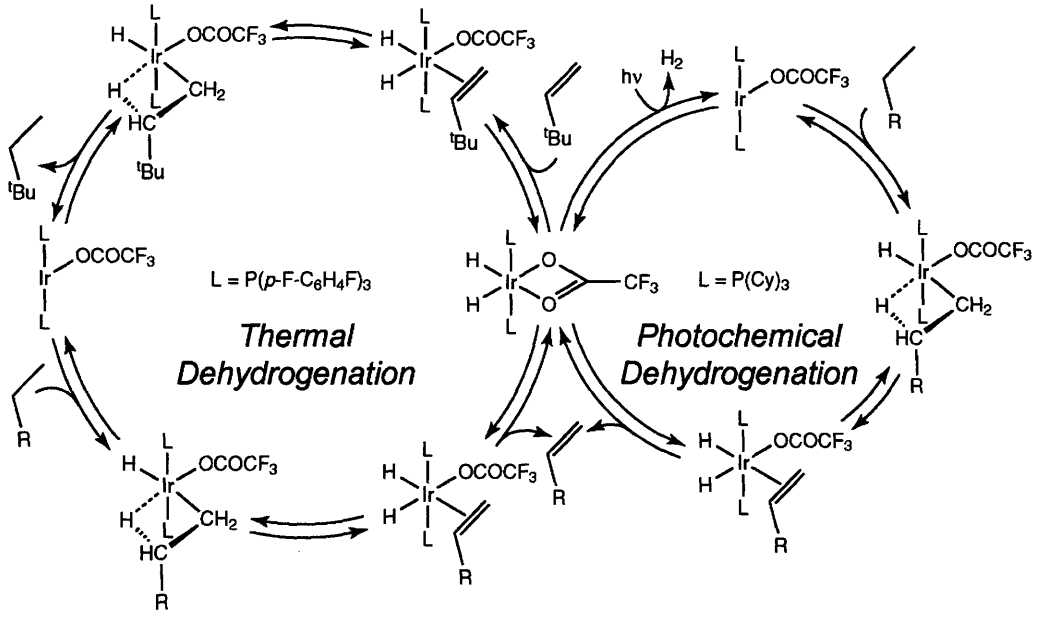

Figure 1.1. Proposed mechanism for alkane dehydrogenation catalyzed by $Ir^{III}H_2(CF_3CO_2)(PR_3)_2$ (R = *p*-F-C_6H_4, Cy) by photochemical (right) and thermal transfer hydrogenation (left) pathways.

(150 °C, neat cyclooctane, 2 days). The activity of the system increases when room temperature solutions are subject to photolysis conditions. In the presence of TBE, 28 turnovers of COE were observed after prolonged photolysis with 254 nm light (25 °C, 7 days). Activity was maintained upon removal of TBE from the system, though at decreased turnover numbers. In the absence of the H_2 acceptor, 7 turnovers were obtained after 7 days, indicating that the dehydrogenation reaction can be driven by the energy derived from photon absorption. The photocatalysis was proposed to proceed by a similar C–H activation/*β*-hydride elimination mechanism to that of the thermal dehydrogenation where photons were thought to generate the active $Ir^{I}(CF_3CO_2)(PCy_3)_2$ intermediate by expulsion of H_2 from $Ir^{III}H_2(CF_3CO_2)(PCy_3)_2$ (Figure 1.1, right).

Photocatalytic alkane dehydrogenations were also reported using monomeric rhodium complexes of the Vaska type, $Rh^{I}(PR_3)_2(CO)Cl$. Saito and coworkers were the first to report catalysis using $Rh^{I}(PR_3)_2(CO)Cl$ (R = Me, Et, Ph) complexes in neat *n*-alkane solvent (heptane or octane) at elevated temperatures (60 - 92 °C) under constant irradiation.[28] The activity of these catalysts is high compared to the dehydrogenation catalysts based on iridium or rhenium, with a maximum turnover frequency observed of 795 h^{-1} for $PR_3 = PMe_3$ at 92 °C. No appreciable rate differences were observed for the dehydrogenation of *n*-heptane vs. *n*-octane, suggesting that the rate determining step is not particularly sensitive to minor substrate modifications. Catalyst activity increased with increasing temperature and also increased with the donating ability of the phosphine along the series $PMe_3 > PEt_3 > PPh_3$. Catalyst initiation proceeded by CO photodissociation from $Rh^{I}(PR_3)_2(CO)Cl$ ($\lambda_{max} > 340$ nm), suggesting that the active intermediate is the 14 electron, 3-coordinate fragment $Rh^{I}(PR_3)_2Cl$.[29-31] The substrate scope was subsequently expanded to include cyclic alkanes such as cyclohexane and cyclooctane.[32-38] Thorough mechanistic studies were not undertaken, but the evidence suggesting initiation from the 14 electron Rh^{I} fragment led to the generally accepted proposition of an oxidative addition/*β*-hydride elimination pathway, similar to that for the iridium complexes reported by Crabtree.

Detailed mechanistic studies for the $Rh^{I}(PMe_3)_2(CO)Cl$ catalyzed photodehydrogenation of alkanes were carried out by Goldman and coworkers.[39-41] In the proposed mechanism shown in Figure 1.2, photoinitiated dissociation of CO generates a reactive $Rh^{I}(PMe_3)_2Cl$, fragment as initially deduced by Saito. This fragment then oxidatively adds alkane C–H bonds (cyclooctane in Figure 1.2) to generate an alkyl hydride species, which *β*-hydride eliminates to generate the dihydrido alkene complex. Alkene dissociation followed by H_2 loss, induced by CO coordination, regenerates the starting complex and closes the catalytic cycle. Notably the initial photodissociation of CO is the only photochemical step in the cycle, contrasting the mechanism proposed by Crabtree for $Ir^{III}H_2(CF_3CO_2)(PCy_3)_2$ where H_2 is eliminated from the dihydride in a photochemical step. Additionally, in neat cyclooctane and cyclohexane, dehydrogenation to give cyclooctene and cyclohexene proceeds with identical quantum yields, consistent with a rate determining step that does not involve alkane. CO inhibition of the reaction was not attributed to its reaction with the photogenerated $Rh^{I}(PMe_3)_2Cl$ fragment, but rather to CO coordination to the alkyl hydride intermediate, thereby preventing *β*-hydride elimination. This suggests that even

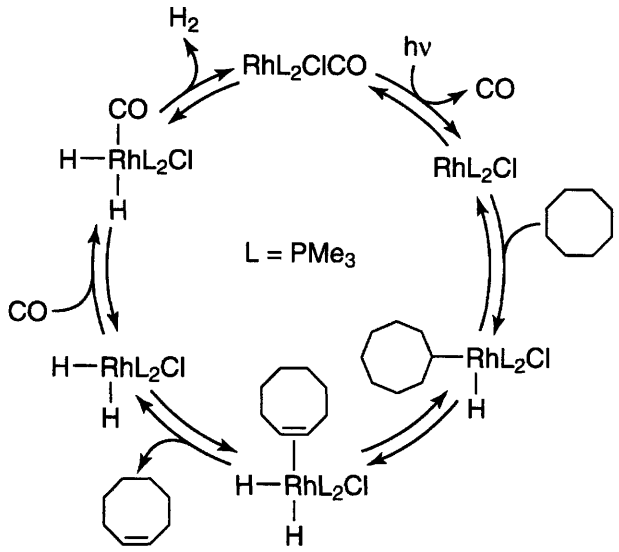

Figure 1.2. Proposed mechanism for the photocatalytic cyclooctane dehydrogenation by $Rh^{I}(PMe_3)_2(CO)Cl$ as determined by Goldman and coworkers.

under high CO pressures, CO coordination to $Rh^{I}(PMe_3)_2Cl$ cannot compete kinetically with alkane C–H bond activation, which was found to be reversible.

1.2.1.3 Alcohol Dehydrogenations

The dehydrogenation of alcohols to either ketones or aldehydes is another avenue for photocatalytic hydrogen production schemes. In some cases, the same catalysts may catalyze the dehydrogenation of both alkanes and alcohol substrate classes. In addition to the typical oxidative addition/β-hydride elimination pathways for alkane dehydrogenation, alcohol dehydrogenations can involve H atom transfers, fast stepwise electron transfer followed by proton transfer, or other radical pathways. As a result, unlike alkane dehydrogenation, these reactivity modes are not limited to late transition metal centers. Any catalyst that can open a coordination site and/or support two electron redox couples can potentially generate hydrogen by alcohol dehydrogenation. Some examples include: rhodium complexes of the Wilkinson and Vaska types, late metal $d^8\cdots d^8$ dimers, rhodium porphyrins, and polyoxometalates (POMs).

1.2.1.3.1 Late Metal Derived Catalysts

Several Rh^{I} phosphine complexes of the Wilkinson type have been used as photocatalysts for alcohol dehydrogenations. For the case of Wilkinson's complex, $Rh^{I}(PPh_3)_3Cl$, Sugi and coworkers observed the photocatalytic production of hydrogen from isopropanol solution with a

maximum turnover of 670 h^{-1}.[42] Interestingly, the catalysis was more efficient when exposed to air, although the role of oxygen in the reaction remains unclear. Irradiation with UV light (λ_{exc} < 300 nm) is required for catalysis, which nevertheless exhibits a significant induction period (1 to 1.5 hours) before hydrogen evolution is observed. Subsequent work by Smith and coworkers using $Rh^{I}(PPh_3)_3Cl$, $Rh^{I}(P(OPh)_3)_3Cl$, and mixtures of $[Rh^{I}(COD)Cl]_2$ or $[Rh^{I}(CO)_2Cl]_2$ with PPh_3 or $OPPh_3$ reported increased turnover numbers for isopropanol dehydrogenation.[43] The most active catalyst was found to be $Rh^{I}(P(OPh)_3)_3Cl$, which exhibited a turnover number of ~6400 when irradiated with UV light (λ_{ex} < 300 nm) at 21 °C. While a complete mechanistic scheme remains undefined, it was suggested that the rate enhancement was attendant to oxygen exposure and the induction period is due to a slow oxidation of dissociated PR_3 to OPR_3. As opposed to PR_3, OPR_3 more weakly coordinates the metal; the inability of the oxidized phosphine to fill a coordination site could allow for more facile binding of substrate to a putative 14 electron 3 coordinate fragment for activation. The role of the photon in this case remains undefined, but is likely involved in the photoextrusion of hydrogen from an octahedral $Rh^{III}(PPh_3)_2X(H)_2Cl$ intermediate (X = PPh_3, $OPPh_3$, or substrate) by analogy to the observations made by Ford *et al.* for $Rh^{III}(PPh_3)_3(H)_2Cl$.[44]

Rhodium phosphine complexes of the Vaska type, $Rh^{I}(PR_3)_2(CO)X$ (where PR_3 = PPh_3, $P^{i}Pr_3$, $PEtPh_2$, PEt_2Ph, PEt_3, and PMe_3; and X = Cl, Br, and I), have also been employed as isopropanol dehydrogenation photocatalysts.[45,46] The catalytic activity was found to increase with increasing donating ability of the phosphine and halide substituents. The role of the photon in the dehydrogenation cycle is revealed by the action spectrum, i.e., wavelength dependence, of the photocatalysis. Significant hydrogen photogeneration was observed when irradiation wavelengths were coincident with that required for photoexpulsion of CO from the $Rh^{I}(PR_3)_2(CO)X$ coordination sphere (340 nm < λ_{ex} < 420 nm). Additionally the turnover frequencies were observed to drop when conducted under a CO atmosphere. Based on these results, the active species is surmised to be a three coordinate 14 electron $Rh^{I}(PR_3)_2X$ fragment, consistent with that postulated for alkane dehydrogenations from similar Vaska type complexes.

1.2.1.3.2 Bimetallic Photocatalysts

Alcohol dehydrogenation accompanied by hydrogen evolution may also be accomplished by bimetallic late transition metal complexes. Methanol and isopropanol can be

photocatalytically dehydrogenated upon irradiation of solutions of *cis*-$Rh_2^{I,I}(dppm)_2Cl_2(CO)_2$ and $Pd_2^{I,I}(dppm)_2Cl_2$.[47-49] For methanol dehydrogenation, photoreactions were performed in refluxing 9:1 methanol:acetone solutions. Turnovers of 130 and 156 h^{-1} were obtained for the rhodium and palladium catalysts, respectively. Interestingly, the addition of acetone appears to be a requisite for catalytic activity. The photolysis was performed under full spectrum irradiation conditions, prompting the suggestion that direct excitation into the acetone n $\rightarrow$ π^* transition (λ_{ex} < ~312 nm) photoinitiates the reaction. The $n\pi^*$ excited state was proposed to abstract a methyl H atom from methanol to generate the methoxy radical. The observed product distributions reflect this radical reactivity as ethylene glycol and formaldehyde dimethyl acetal are observed, in addition to formaldehyde, which is the product expected from simple dehydrogenation. Control experiments using only acetone and no transition metal catalyst showed low catalytic activity and a markedly different product ratio. The major products in the liquid phase were ethylene glycol and isopropanol; formaldehyde was obtained in only small quantities. The gaseous products were composed primarily of methane and only small quantities of hydrogen (methane:hydrogen = ~70:1). These results establish that the bimetallic complex is needed to support high turnovers. Accordingly, it was proposed that the initial methanol activation occurs by H atom abstraction from a C–H bond of methanol by the directly excited acetone to generate a ketyl radical and $HOCH_2$•. Hydrogen generation is then achieved in subsequent steps by reaction of the bimetallic transition metal catalysts with the organic radicals to give formaldehyde and acetone. This strategy was later applied to isopropanol dehydrogenation using *cis*-$Rh_2^{I,I}(dppm)_2Cl_2(CO)_2$.[49] An induction period was ascribed to an initial slow dehydrogenation of isopropanol to generate acetone. As in the methanol dehydrogenation case, the acetone was proposed to act as a sensitizer once an appreciable concentration accumulated. Consistent with this contention, the induction period was eliminated when acetone was added to the solution.

Arguably, the most extensively examined system for the photocatalytic dehydrogenation of alcohols by a dinuclear complex is that of $Pt_2^{II,II}(P_2O_5H_2)_4^{4-}$, better known as PtPOP.[50] First crystallized in 1990,[51] PtPOP is a face-to-face dimer of two square planar d^8 Pt^{II} metal centers. Penetrating spectroscopic studies[52-55] reveal that the frontier metal centered molecular orbitals (MO) arises from the overlap of the d_{z^2} orbitals in $d\sigma$ and $d\sigma^*$ linear combinations.[50] In the four-fold symmetry of the D_{4h} ligand environment, an allowed $d\sigma^* \rightarrow p\sigma$ electronic transition is

assigned to an intense absorption feature at 367 nm ($\varepsilon \sim 3 \times 10^4$ M^{-1} cm^{-1}).[56] Excitation into this band generates a long lived phosphorescent $^3(d\sigma^*p\sigma)$ excited state that exhibits diradical character,[50] from which the photoreactivity of PtPOP is derived. Roundhill irradiated the $d\sigma^* \rightarrow p\sigma$ absorption manifold in the presence of isopropanol to form hydrogen with a turnover of >400 after 3 hours of irradiation at ambient temperature.[57] The photoreaction mechanism shown in Figure 1.3 was deciphered by Gray and co-workers by undertaking a series of comprehensive studies. Initial photon absorption generates the $Pt_2^{II,II}$ $^3(d\sigma^*p\sigma)$ excited state, which abstracts a hydrogen atom from isopropanol and forms the mixed valent hydride complex, $Pt_2^{II,III}H$. The

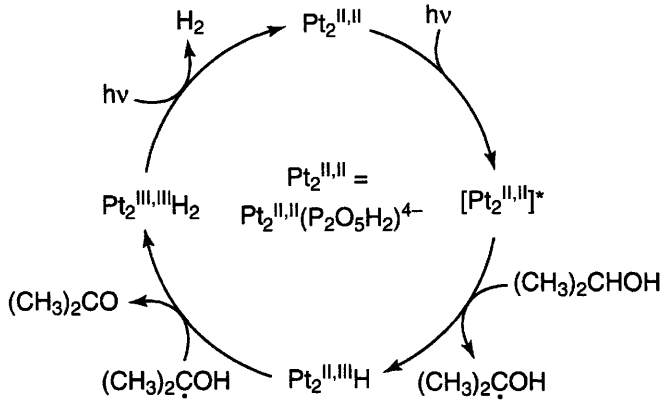

Figure 1.3. Proposed mechanism for the photocatalytic isopropanol dehydrogenation at PtPOP (POP = $P_2O_5H_2^{2-}$).

existence of this mixed valence complex was verified directly in pulse radiolysis spectra.[58] This intermediate abstracts a second H atom to form the valence symmetric dihydride, $Pt_2^{III,III}(H)_2$ by analogy with previous work concerning the thermal oxidation chemistry of $Pt_2^{II,II}$ cores.[59] An independent synthesis of the $Pt_2^{III,III}(H)_2$ provided and independent confirmation of binuclear axial dihydride formulation.[60] Hydrogen release from the dihydride requires a photon, though the precise mechanism for this effective reductive elimination has eluded identification.[60] The photocycle of Figure 1.3 has been extended to numerous secondary alcohols and also to $d^8 \cdots d^8$ complexes of iridium.[61-63]

1.2.1.3.3 Rhodium porphyrins

Rhodium porphyrin complexes are active for the photochemical dehydrogenation of alcohols. A chloro rhodium tetraphenyl porphyrin complex [Rh(TPP)Cl] was found to dehydrogenate isopropanol[64-66] and cyclohexanol[64,67] to the corresponding ketones in neat

alcohol at reflux temperatures under visible light irradiation (λ_{exc}> 360 nm). Extended photolysis (520 h) gave 3430 turnovers with exclusive formation of hydrogen and ketone products as determined by GC analysis.[66] The reaction was proposed to proceed through the intermediacy of a $Rh^{III}(TPP)H$ complex by the following reaction cascade (for the example of isopropanol):

$$[Rh^{III}(TPP)Cl] + HOCH(CH_3)_2 \longrightarrow [Rh^{III}(TPP)(OCH[CH_3]_2)] + HCl \quad (6)$$

$$[Rh^{III}(TPP)(OCH[CH_3]_2)] \longrightarrow [Rh^{I}(TPP)]^- + (CH_3)_2CO + H^+ \quad (7)$$

$$[Rh^{I}(TPP)]^- + H^+ \rightleftharpoons [Rh^{III}(TPP)H] \quad (8)$$

$$[Rh^{III}(TPP)H] \xrightarrow{h\nu} [Rh^{III}(TPP)H]^* \quad (9)$$

$$[Rh^{III}(TPP)H]^* + [Rh^{III}(TPP)H] \longrightarrow [Rh^{III}(TPP)]^+ + [Rh^{I}(TPP)]^- + H_2 \quad (10)$$

$$[Rh^{III}(TPP)]^+ + HOCH(CH_3)_2 \longrightarrow [Rh^{I}(TPP)]^- + (CH_3)_2CO + 2\,H^+ \quad (11)$$

No intermediates are observed along the pathway, but precedent for a bimolecular reactivity mode was found in the stoichiometric thermal generation of hydrogen observed by Ogoshi *et al.* from a reaction of a related $Rh^{III}(OEP)H$ complex (OEP = octaethylporphyrin) with concomitant formation of $[Rh^{II}(OEP)]_2$.[68] Wayland *et al.* later reported that the reaction is significantly enhanced under photolysis conditions indicating the involvement of $Rh^{III}(OEP)H$ excited states along the reaction pathway.[69] The authors suggest that the increased steric demands of TPP vs. OEP prevent the formation of the metal-metal bonded d^7–d^7 $Rh^{II}(TPP)$ dimer, and thus dimerization of a photoexcited $[Rh^{III}(TPP)H]^*$ and a ground state $Rh^{III}(TPP)H$ are proposed to give hydrogen and the valence disproportionated products $[Rh^{III}(TPP)]^+$ and $[Rh^{I}(TPP)]^-$. The $[Rh^{III}(TPP)]^+$ is then suggested to oxidize isopropanol by two electrons to generate $[Rh^{I}(TPP)]^-$, acetone, and two proton equivalents. The authors at this point chose to invoke successive proton and electron transfers at this stage, but the possibility of hydrogen atom transfers along the pathway, as seen for PtPOP for example, cannot be ignored.

1.2.1.3.4 Early Metal Photocatalysts

Polyoxometalates (POMs) are typically composed of molybdates and tungstates of the Keggin $[XW_{12}O_{40}]^{n-}$ (X = P, Si, Fe, H_2) or Dawson $[P_2W_{18}O_6]^{6-}$ type. POMs have been widely

studied and the rich electrochemical and photochemical properties of these compounds have been reviewed.[70,71] POMs are excellent oxidation catalysts and have been reported to photooxidize alcohols in acidic solutions.[72-74] Upon one electron reduction, the initially colorless or pale yellow solutions of POMs acquire the bright blue hue (λ_{max} = 500 - 800 nm) of the heteropolyblues (HPB). The low energy electronic transitions are attributed to intervalence charge transfer (IVCT) bands within the lattice. The HPBs are ESR active, and at low temperatures, give signals with hyperfine couplings indicative of localization of the unpaired spin on a single metal center. The observed signal broadens upon warming of the sample, suggesting extensive electron delocalization over the POM. The two electron reduction products are ESR silent, indicating strong antiferromagnetic coupling of the unpaired spins within the lattice, as is characteristic for oxo-bridged metal centers.[75]

In anaerobic solution, photoexcitation of POMs in the presence of oxidizable substrates such as alcohols gives the blue solution of HPB accompanied by hydrogen production.[76-85] The rate of hydrogen production is enhanced in the presence of a colloidal Pt catalyst. In the presence of oxygen, hydrogen production is circumvented in favor of the reduction of oxygen to water instead.[86] Wavelength selection of the excitation light shows the irradiation into the HPB blue absorption bands gives no hydrogen. Catalysis is induced when the excitation light is coincident with the higher energy oxo $\rightarrow$ metal, ligand to metal charge transfer transition (LMCT). Transient spectroscopic studies indicate that the active oxidant of a related POM, $[W_{10}O_{32}]^{4-}$, forms within 30 ps of excitation into the O $\rightarrow$ W LMCT absorption band. This excited state has a relatively long lifetime for a LMCT excited state of >15 ns, and it was found to possess significant radical character on oxygen.[87] In the presence of an oxidizable substrate, the oxygen radical abstracts an H atom, which then gives the one electron reduced HPB after the loss of a proton (Figure 1.4). The observation of H atom abstractions with rates above the diffusion limit suggest that the initial event proceeds through a pre-associated complex,[88] and the preassociation of substrate with the POM in ground state has been supported by X-ray structural evidence and shifted substrate NMR signals.[89-91] In the absence of water, H atom abstraction from the alcohol occurs directly,[92,93] but in aqueous solutions, water preferentially binds to the surface of the POM over alcohol, disposing the initial H atom abstraction process to proceed from water to yield hydroxyl radicals.[94] The hydroxyl radicals react with alcoholic substrates at a diffusion

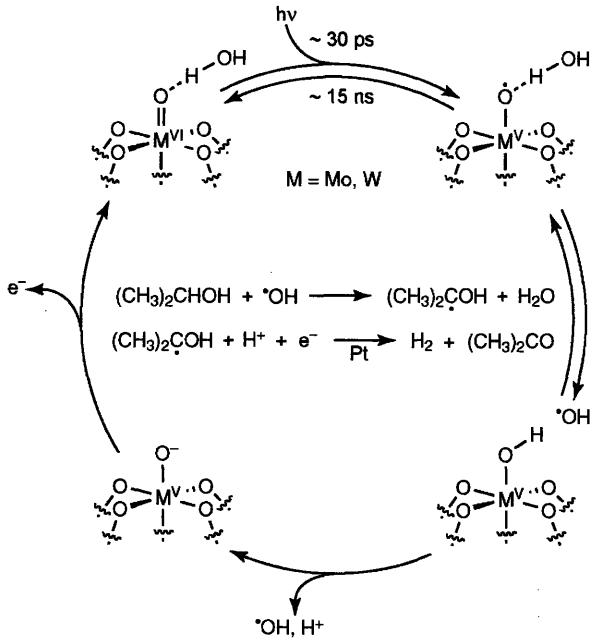

Figure 1.4. Proposed mechanism for the polyoxometalate catalyzed anaerobic photocatalytic dehydrogenation of isopropanol. Hydrogen production is accelerated in the presence of colloidal Pt, but the Pt catalyst is not required.

controlled rate, eventually giving hydrogen and acetone for the case of isopropanol dehydrogenations as shown in Figure 1.4.[95]

The selectivity for acetone is under kinetic rather than thermodynamic control as POMs are known to fully degrade alcohols to H_2O and CO_2.[96-99] The complete oxidation pathway is circumvented by much slower reaction kinetics (100 times slower) as compared to the kinetics for the oxidation of isopropanol to acetone. The generation of hydroxyl radicals is further supported by the observation of identical kinetics and product distributions for the dehydrogenation of isopropanol by •OH generated using ^{60}Co-γ-radiation.[100]

1.2.2 Indirect RH Substrates

Oxidation-reduction reactions of electronically excited transition metal complexes customarily proceed by single electron mechanisms. The molecule in its excited state is simultaneously a more potent oxidant and reductant than in its ground state. By itself, single electron transfer is confining inasmuch as the reduction of protons to evolve molecular hydrogen is a two electron process. It follows that in order to employ a traditional one electron excited state, the primary photoredox event must be coupled to hydrogen reduction, remote to the excited state. In the absence of such novel excited states, the one-electron excited state must be conveyed

to a homogeneous or heterogeneous site capable of storing multiple redox equivalents. Such constructs are achieved with the so called "three component system".

The most prevalent design of three component schemes is shown in Figure 1.5. The scheme comprises a one-electron photosensitizer (S), a redox mediator (M), and the redox-storing catalyst (Cat). The sensitizer, S, functions as both a light harvesting complex for photon absorption and the primary photoreductant, and may be a metal complex or organic compound. Most metal based sensitizers are metal polypyridyl complexes or porphyrins. Organic

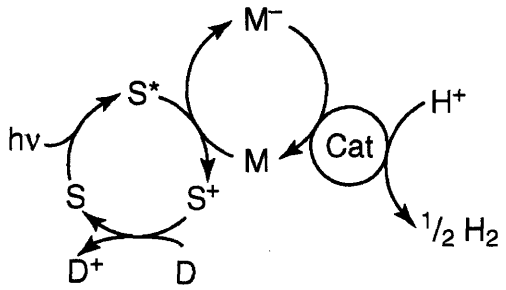

Figure 1.5. A generalized three component photocatalytic system for hydrogen production where S = photosensitizer, D = sacrificial electron donor, M = electron shuttle or relay, Cat = proton reduction catalyst.

photosensitizers are typically conjugated organic molecules with accessible π^* excited states. The mediator is any molecule that can be reversibly reduced by one- or two- electrons. In most cases, the mediator serves as a bimolecular quencher of the photosensitizer by outer sphere electron transfer. Diffusion of the reduced mediator from the oxidized sensitizer aids in the prevention of energy wasting back electron transfer. The catalyst is any species that carries out the reduction of protons to hydrogen. These are typically chosen for low proton reduction overpotentials and most commonly are colloidal noble metals such as platinum, biological constructs such as hydrogenase or small molecule catalysts. The photooxidized sensitizer, S^+, must be re-reduced to effect catalysis. The reducing equivalents for this process are typically derived from sacrificial donors such as triethylamine (TEA),[101] triethanolamine (TEOA),[102] ascorbic acid (H_2A), NADH, EDTA[103] or cysteine, which decomposes upon oxidation. The decomposition pathways for some of the more common sacrificial electron donors are outlined in Figure 1.6. Alternative three component systems are designed to reduce the system complexity by eliminating or combining the roles of one or more components. Wherein, reduction chemistry beyond simple proton reduction has been investigated including the simultaneous photocatalytic reduction of CO_2 to CO and H^+ to H_2. These schemes employ photosensitizers for light

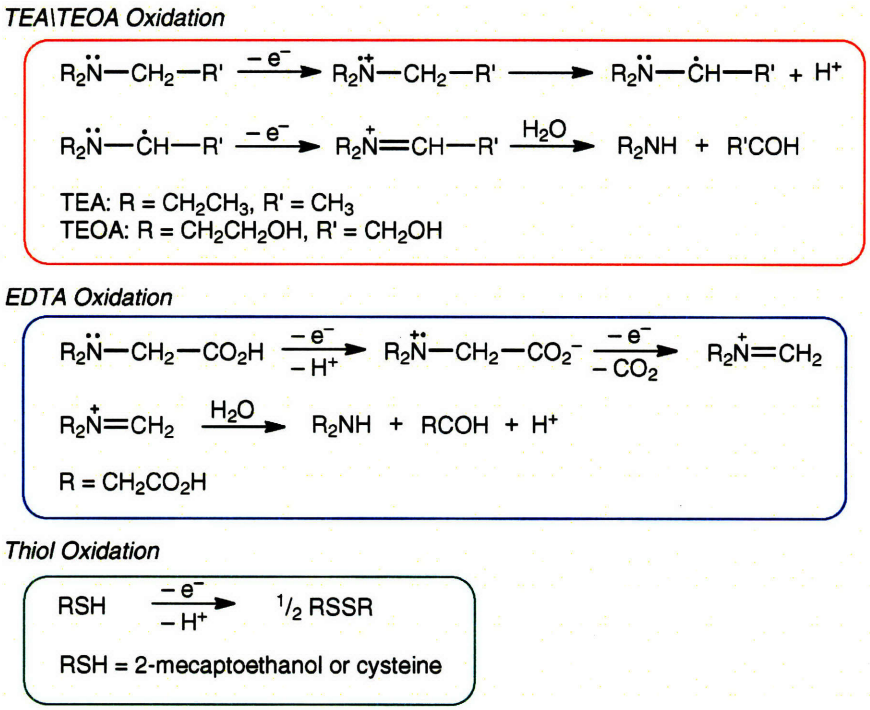

Figure 1.6. Decomposition pathways for TEA, TEOA, EDTA, and thiol derived sacrificial electron donors.

harvesting and sacrificial electron donors for reducing equivalents but differ from the three component system of Figure 1.5 inasmuch as no redox mediator or colloidal catalyst is employed. Table 1.1 compiles the sensitizers, redox shuttles and catalysts discussed below.

1.2.2.1 Inorganic Sensitizers

Classical three component systems commonly employ $Ru^{II}(bpy)_3^{2+}$ as a light harvesting complex. $Ru^{II}(bpy)_3^{2+}$ and derivatives thereof have a rich and long history in inorganic chemistry and photochemistry. The parent compound, first prepared in 1936,[104] was later obtained by a more practical synthesis,[105] thus opening the way for Adamson's first use of the $Ru^{II}(bpy)_3^{2+*}$ excited state as a photochemical reductant in 1972.[106] The potential of this excited state for water splitting was quickly noted by other authors[107,108] and the numerous attempts to realize this reactivity directly grew into the field of three component catalysis. The first reports using $Ru^{II}(bpy)_3^{2+}$ for "water splitting" focused on the hydrogen half reaction, using a modified photosensitizer that can be cast into films.[109-112] Though the hydrogen generating properties of the systems were ill-defined, this work was the predecessor of three component systems composed of a $Ru^{II}(bpy)_3^{2+}$ sensitizer, colloidal platinum as a hydrogen production catalyst, and methylviologen (MV^{2+}) as a electron shuttle.[113]

Table 1.1. Compilation of Photosensitizers, Redox Shuttles, Sacrificial Donors, and Catalysts used in three component photocatalytic hydrogen production schemes.

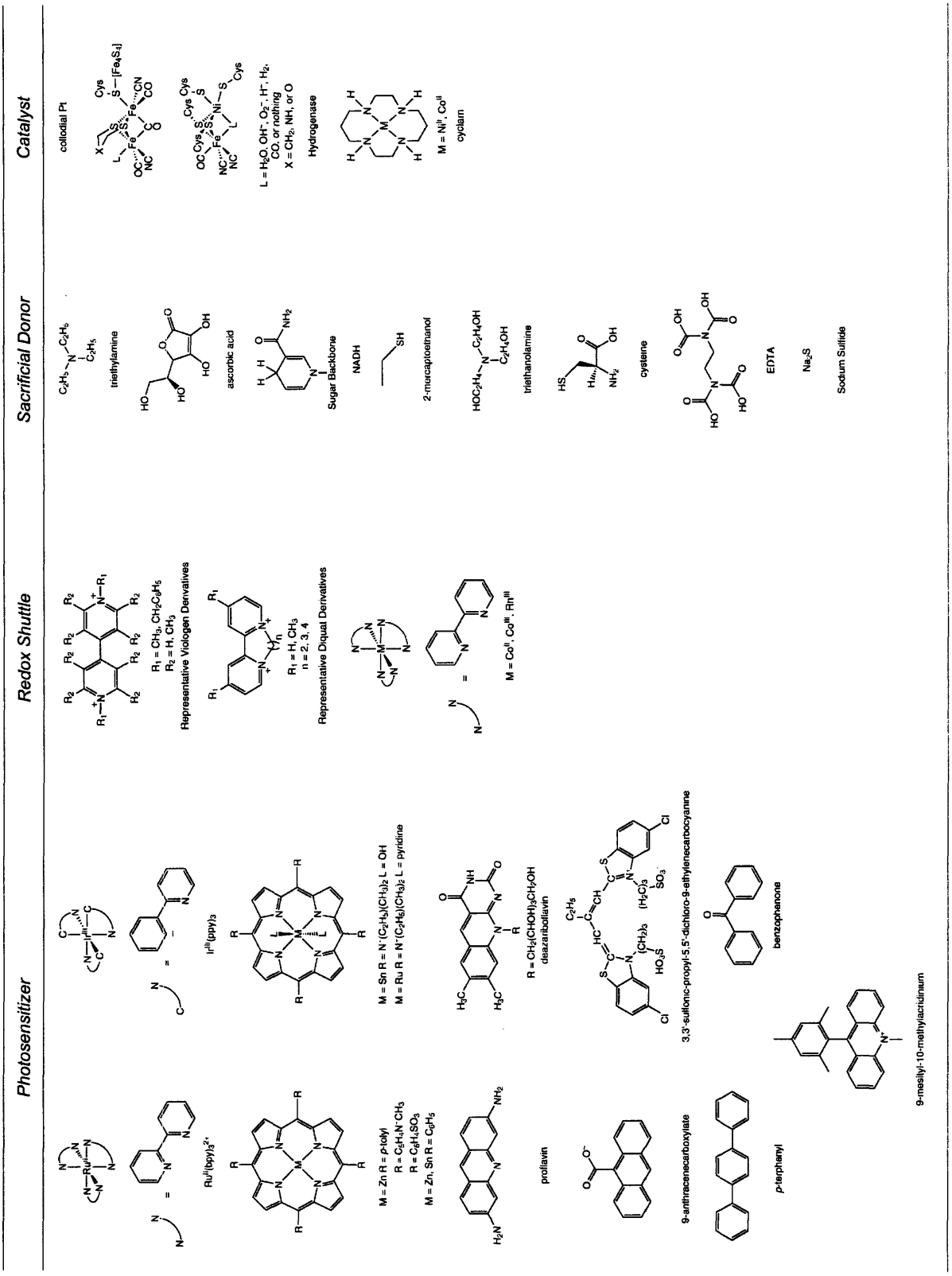

The primary photoprocess occurs by fast oxidative quenching of the $Ru^{II}(bpy)_3^{2+}$* excited state by electron transfer to MV^{2+} to generate $Ru^{III}(bpy)_3^{3+}$ and the cation radical $MV^{\bullet+}$. Hydrogen production is catalyzed at the surface of colloidal Pt, which efficiently couples the one-electron $MV^{\bullet+}$ oxidation to two-electron proton reduction.[101,102,113-115] The photoreactant is returned to its resting state by reduction of $Ru^{III}(bpy)_3^{3+}$ with a sacrificial donor. Although MV^{2+} serves as a paradigm, other alkylated bipyridine derivatives have been employed as redox shuttles including tetramethyl- or hexamethyl-viologen and diquats of various substitution patterns (Table 3). Functionally these derivatives are largely the same and in all cases the efficiency of the MV^{2+} or diquat based systems are gradually attenuated by the irreversible hydrogenation of the redox shuttle catalyzed by the Pt surface.[116,117] The efficiency of the MV^{2+} based system is attenuated by the irreversible hydrogenation of MV^{2+}, which is thought to be initiated by protonation of the $MV^{\bullet+}$. The protonated cation radical is proposed to be an active intermediate for the direct production of hydrogen at low pH. At higher pH, hydrogen production is believed to be dominated by electron transfer from reduced $MV^{\bullet+}$ to the Pt surface.[103,118,119] The efficiency of the system is observed to increase with more reducing viologen or diquat derivatives and is typically attributed to the increased driving force for electron transfer from the cation radicals of more reducing shuttles to the Pt surface.[120–122]

Sauvage and coworkers,[123,124] modified the three component approach by using a Rh polypyridyl complex as the redox mediator. The advantage of this approach is that the mediator is both a proton carrier and two-electron shuttle. Initial mechanistic proposals invoked a dihydride of the formula $Rh^{III}(bpy)_2(H)_2^{+}$ as the critical shuttle.[123,124] This proposal was subsequently modified by Cruetz and Sutin[125,126] and using $Ru^{II}(bpy)_3^{2+}$, $Rh^{III}(bpy)_3^{3+}$, TEOA system at neutral pH (7-8) in the absence of platinum. The one electron reduction product $Rh^{II}(bpy)_3^{2+}$ was found to be unstable with respect to a disproportionation driven by the loss of bpy to yield $Rh^{III}(bpy)_3^{3+}$ and $Rh^{I}(bpy)_2^{+}$, which reacts with a proton to yield the hydride $Rh^{III}(bpy)_2(H_2O)H^{2+}$ at low pH. $Rh^{II}(bpy)_3^{2+}$ may serve as a one-electron reductant to generate $Rh^{II}(bpy)_2(H_2O)H^{+}$, which was thought to produce hydrogen either by protonation of the hydride or by the bimolecular reaction of two hydride species. The same mechanism is believed to be operative if $Rh^{III}(bpy)_3^{3+}$ is replaced by $Co^{III}(bpy)_3^{3+}$.[127-131] The foregoing mechanism does not require Pt as a catalyst for H_2 generation. Indeed, the systems are operative in the absence of the noble metal. If present, the Rh bpy complex functions simply as a redox reservoir, similar to

MV^{2+}, as the electron transfer from $Rh^{II}(bpy)_3^{2+}$ to the Pt surface is faster than disproportionation and bpy loss that gives $Rh^{I}(bpy)_2^{+}$.[126]

Iridium coordination complexes have also been employed as sensitizers for hydrogen production in three component systems.[132,133] Anionic donors derived from 2-phenylpyridine (ppy) replace the ubiquitous bpy ligands of Ru-based photosensitizers. The electronic properties of the Ir excited state may be modulated by the functionalization of ppy, as has routinely been performed for the development of OLED devices.[134] Using high throughput techniques to screen a library of ppy-modified complexes, it was found that the heteroleptic $[Ir^{III}(dF[DF_3]ppy)_2(dtbbpy)]PF_6$ (where $dF[DF_3]ppy$ = 2-(2,4-difluoromethyl)-5-trifluoromethyl-pyridine and dtbbpy = 4,4′-di-*tert*-butyl-2,2′-bipyridine) was the most active photocatalyst ($Co^{II}(bpy)_3Cl_2$ = electron relay and TEOA = sacrificial electron donor), achieving 430 equivalents of H_2 with quantum yields of ~37 times greater than that of $Ru^{II}(bpy)_3^{2+}$ sensitized systems. The authors suggest that the enhanced efficiencies are a result of the long lifetime and increased reducing strength of the Ir^{III} excited state.

Recent efforts have sought to eliminate the electron relay and colloidal Pt catalyst by appending $Pt^{II}(bpy)Cl_2$ to $Ru^{II}(bpy)_2(phen)$ (phen = 1,10-phenanthroline), Figure 1.7 (left).[135] This complex was active for photocatalytic hydrogen production in the presence of EDTA, however at low turnover and quantum yield (~5 and 0.01). At about the same time Rau and coworkers presented a similar construct linking a Ru^{II} polypyridyl complex to a Pd^{II} center via a tetrapyridophenazine unit as a conjugated and reducible bridge, Figure 1.7 (right).[136] Hydrogen

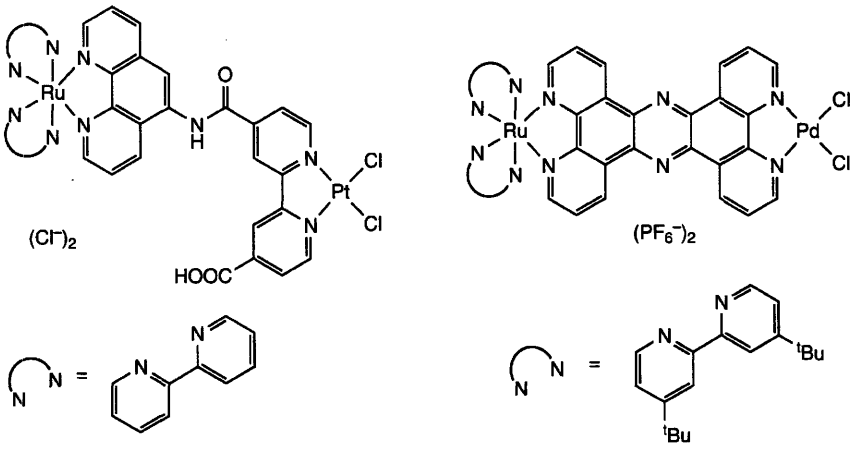

Figure 1.7. Heterobimetallic constructs of Sakai (left) and Rau (left) for photocatalytic hydrogen production.

production proceeded with TEA as a sacrificial electron donor giving 56 turnovers after ~30 hours of irradiation. This assembly was also active for the hydrogenation of tolane to *cis*-stilbene without added hydrogen, leading the authors to suggest that hydrogen production proceeds through a palladium hydride species.

Zinc porphyrins (PZn) may be used in place of Ru polypyridyl complexes as light harvesters in a three component system. In a parallel function to $Ru^{II}(bpy)_3^{2+}$, photon absorption the initially formed PZn singlet excited state relaxes to the long lived triplet from which electron transfer to MV^{2+} occurs. As is generally the case for a three component system, a sacrificial electron donor reduces the oxidized porphyrin macrocycle and $MV^{\bullet+}$ oxidation is attendant to hydrogen generation at a Pt surface. McClendon *et al.* were the first to report such a strategy using both Zn(II) tetra(*N*-methylpyridyl)porphyrin ($Zn^{II}TMPP$) and Zn(II) tetra(sulphonato-phenyl)porphyrin ($Zn^{II}TPPS_4$) with EDTA and a Pt catalyst in aqueous solutions.[137] Using $Zn^{II}TMPP$, a maximum rate of 175 equivalents of hydrogen per hour was attained. The hydrogen was derived from the protons of water as evidenced by the production of >95% D_2 when the photolysis was conducted in D_2O. Similar results are obtained for other PZn sensitizers.[138-142]

$Zn^{II}TMPP$ can also function as a photosensitizer when adsorbed onto the exterior of a zeolite.[143] Photocatalytic hydrogen was produced from acidic aqueous solutions (pH = 4) when the zeolite channel was platinized and the sodium cations were replaced with MV^{2+}. Interestingly electron transfer from the $Zn^{II}TMPP$ sensitizer originates from the singlet excited state as the normally facile intersystem crossing to the triplet is circumvented by an adsorption-induced 200 mV shift of the $Zn^{II}TMPP$ redox potential.

1.2.2.2 Organic Sensitizers

Photosensitization is not an exclusive perquisite of metal polypyridyls and porphyrins – organic excited states may function as sensitizers of hydrogen production as well. Benzophenone has seen some use for photocatalytic hydrogen production in a role that is similar to the metal complexes alcohol dehydrogenation cycles. UV excitation of the $n \rightarrow \pi^*$ transition of benzophenone generates the reactive diradical, which has long been known to rapidly abstract H atoms to form a stable ketyl radical.[144,145] The reaction can be diverted towards photocatalytic hydrogen production under certain conditions. For instance, irradiation of isopropanol solutions of benzophenone in the presence of colloidal platinum under anaerobic conditions favors

photocatalytic hydrogen production over radical dimerization to form pinacols.[146,147] The mechanism is proposed to proceed by direct n → π* excitation of benzophenone to generate a ketyl radical after H atom abstraction from isopropanol. A second H atom abstraction from the isopropanol derived organic radical intermediate by another benzophenone excited state generates acetone. Colloidal platinum re-oxidizes the ketyl radicals to regenerate benzophenone and hydrogen is evolved by the coupling of two hydrogen atoms at the heterogeneous surface. The isopropanol dehydrogenation is similar to those reported using late metal phosphine complexes, excepting the requirement of the heterogeneous noble metal catalyst. The benzophenone excited state is sufficiently reactive to carry out the dehydrogenation of cyclohexane to cyclohexene,[148] in this case however the dehydrogenation was performed aerobically generating H_2O as the terminal reduction product as opposed to hydrogen.

Hydrogen generation may be promoted by a host of other organic photosensitizers. 9-anthracenecarboxylate, in the presence of MV^{2+} and Pt, produces hydrogen according to the scheme shown in Figure 15. The triplet form of 9-anthracenecarboxylate can either be formed by direct excitation[149] or by energy transfer from photoexcited $Ru^{II}(bpy)_3^{2+}$* or $Cu^{I}(dpp)_2^{+}$* (dpp = 2,9-diphenylphenanthroline).[150,151] Krasna first reported the use of proflavin to photocatalytically generate hydrogen from a variety of sacrificial electron donors, using MV^{2+} and either platinum or isolated hydrogenase (*vide infra*) as a catalyst.[152] The triplet excited state of proflavin is reduced by EDTA (for example), and in turn, the reduced proflavin reduces MV^{2+} followed by electron transfer from $MV^{\bullet+}$ to the colloidal platinum or hydrogenase that effects hydrogen production.[153] The efficiencies for MV^{2+} reduction using proflavin sensitizers were approximately twice as high as those using $Ru^{II}(bpy)_3^{2+}$. The maximum quantum yields for $MV^{\bullet+}$ generation were observed at pH 6-8. Although the reductive quenching reaction is more efficient at higher pH, the hydrogen production reactions were slow, presumably due to the low concentrations of protons. The rate of MV^{2+} reduction may be accelerated if the proflavin sensitizer is substituted with deazariboflavin; a fivefold increase in the rate of $MV^{\bullet+}$ formation was observed in some cases.[154] In these systems, the scope of the sacrificial reagent was expanded to include amino acids and also simple sugars such as glucose and fructose. In an interesting application, flavin-sensitized hydrogen production has been elaborated in a photogalvanic cell. Excitation of the flavin followed by one electron reduction by EDTA furnishes the reduced flavin, which is rapidly oxidized at a Pt disk anode. The circuit may be

completed by proton reduction at the cathode in a separate compartment linked via a salt bridge.[155]

1.2.2.3 CO_2 Reduction Systems

Sacrificial electron donors may be employed to simultaneously reduce protons to H_2 and CO_2 to CO. Photocatalytic hydrogen production linked to carbon dioxide reduction has been observed using Co(II) and Ni(II) complexes of macrocyclic tetradentate nitrogen donors ligands for which cyclam (L) is the prototype.[156-159] The $[LM^{II}]^{2+}$ (M = Co, Ni) complex serves as both the redox shuttle and catalyst in the presence of a $Ru^{II}(bpy)_3^{2+}$ photosensitizer and an ascorbate sacrificial electron donor. Figure 1.8 shows the reaction sequence that leads to H_2 and CO production.

The reaction cascade is initiated by reductive quenching of the $Ru^{II}(bpy)_3^{2+}$* excited state by ascorbate to generate $Ru^{I}(bpy)_3^{+}$,which goes on to reduce the $[LM^{II}]^{2+}$ to $[LM^{I}]^{+}$. The reduced macrocyclic complex is proposed to either react either with CO_2 or H^+ to generate $[LM(CO_2)]^+$ or $[LM^{III}H]^{2+}$. Hydrogen may then evolve from the hydride directly by net H atom transfer to regenerate the $[LM^{II}]^{2+}$, or $[LM^{III}H]^{2+}$ can insert CO_2 to generate a metal formate complex (a

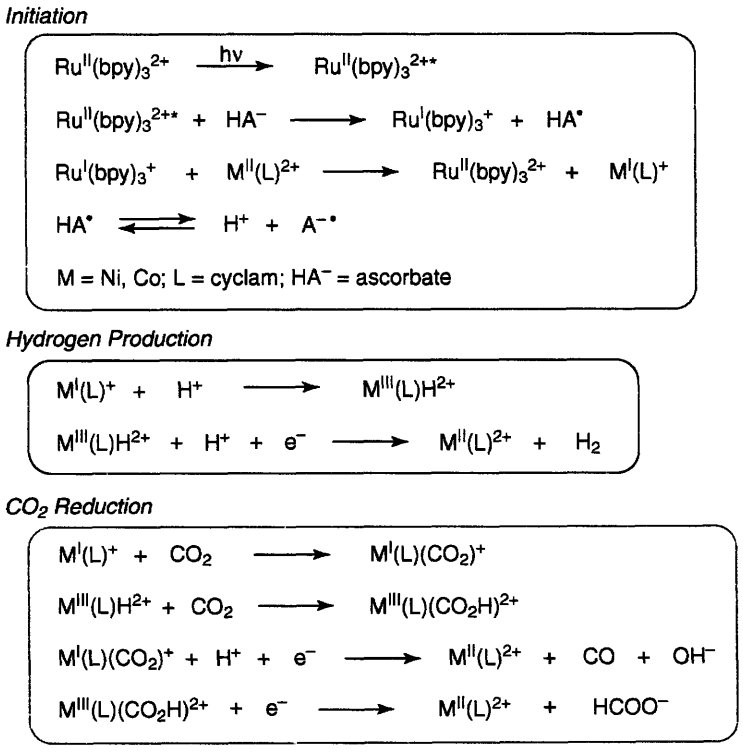

Figure 1.8. Reactions of nickel or cobalt cyclams (or cyclam derivatives) leading to the simultaneous photocatalytic reduction of protons to hydrogen and CO_2 to CO.

metal carboxylato complex however cannot be ruled out as the precise nature of the CO_2 insertion product is not known). The formate species can either react by H atom transfer to generate the $[LM^{II}]^{2+}$ complex along with hydroxide and carbon monoxide or by a one electron reduction to generate $[LM^{II}]^{2+}$ and free formate ion. A critical feature of this catalytic scheme is that the $[LM^{I}]^{+}$ intermediate is reactive towards both protons and CO_2. As a result of the catalyst's promiscuity, the CO and H_2 yields are not stoichiometrically defined. Additionally, the CO/H_2 ratios appear to be very sensitive to the experimental conditions as differing ratios are reported by different investigators, even when the same catalyst (e.g., Ni^{II}cyclam) is employed. For the case where the reducing equivalents are provided electrochemically rather than in homogeneous solution, H_2 production is completely shut down.[160,161] Strategies for enhancing selectivity for H_2 over CO include the use of *p*-terphenyl as a sensitizer and TEA as a sacrificial electron donor, although the reasons for this selectivity enhancement is not clear.[162,163] Attempts to increase the efficiency of the process has led to the development of constructs wherein the nickel macrocycle is covalently tethered to the ruthenium polypyridyl sensitizer.[164,165] Nonetheless, no significant gains in efficiency or selectivity were observed over bimolecular constructs.

1.2.3 Carbon Monoxide

The water gas shift reaction (WGS),

$$CO + H_2O \rightleftharpoons CO_2 + H_2 \qquad (12)$$

is widely employed in industry to enrich the hydrogen content in water gas (synthesis gas) after the steam reforming of methane. The WGS reaction is typically performed at high temperatures over heterogeneous iron oxide or copper oxide catalysts. Interest in the WGS shift reaction under mild, homogenous conditions has been longstanding.[166,167] Many soluble transition metal carbonyl complexes show activity for thermal WGS catalysis,[168] usually in basic media and rarely in acidic media.[169] In some cases, WGS activity is promoted photocatalytically, where the photons are typically used to open coordination sites by the expulsion of CO or photoextrusion of H_2 from the transition metal center.

1.2.3.1 Homoleptic Metal Carbonyls

King and Ford employed $M(CO)_6$ complexes (M = Cr, Mo, W) for homogenous WGS catalysis initially under thermal conditions[170,171] according to the cycle shown in Figure 1.9. Thermal expulsion of a CO ligand from $M(CO)_6$ generates an open coordination site at the metal center, which is rapidly coordinated by a formate ion that is produced *in situ* by the reaction of OH^- and CO. Dissociation of an additional CO opens a coordination site for β-hydride elimination from the formate[172] accompanied by CO_2 elimination. Uptake of an equivalent of CO generates the $M(CO)_5H^-$ complex, which is proposed to abstract a proton from H_2O to regenerate OH^- and the $M(CO)_5(H_2)$ dihydrogen complex. Thermal dissociation of H_2 regenerates the active $M(CO)_5$ species for catalytic turnover.[173,174] This catalytic cycle involving homogeneous reagents operates at significantly reduced temperatures (100 - 170 °C) as compared to the heterogeneous systems using Fe or Cu oxide catalysts (200 and 300+ °C). The highest turnover frequencies were observed for $W(CO)_6$, with 900 molecules of hydrogen produced per day.

The initiation step of the WGS cycle in Figure 1.9 is the thermal dissociation of CO from $M(CO)_6$ to generate the active $M(CO)_5$ for reaction with formate ion (M = Cr, Mo, W). In principle the active WGS catalyst may be accessed by the photochemical elimination of CO at even milder temperatures. Indeed, the benefit of the photon for WGS was recognized shortly after reports of $M(CO)_6$ catalyzed WGS appeared. Using $W(CO)_6$, King reported sluggish thermal WGS chemistry at 75 °C with a turnover frequency for hydrogen of ~5 day^{-1}; exposure to sunlight enhanced this turnover frequency to 83 day^{-1}.[175] The mechanism was proposed to

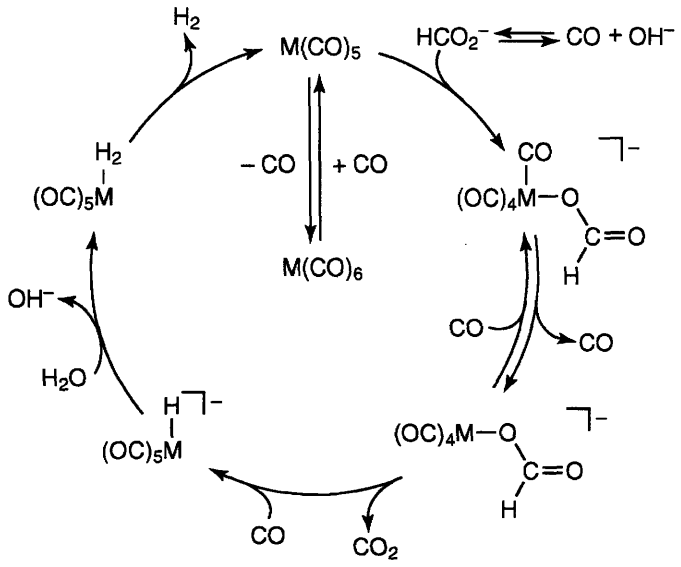

Figure 1.9. Proposed mechanism for the thermal WGS reaction catalyzed by homoleptic group 6 carbonyls.

largely follow that outlined in Figure 1.9 with the notable distinction of the introduction of the photon to remove CO from the hexacarbonyl starting complex. King reports that irradiated solutions retain catalytic activity for hours after the cessation of illumination, indicating that the catalysis was catalytic in photons. This observation is entirely consistent with the mechanism of Figure 1.9 since the photon is needed only once to extrude CO.

Detailed kinetic analysis of the photochemical WGS reaction using H_2O/methanol solvent mixtures under pseudo first order conditions with respect to substrate allowed for an analysis of the post formate binding steps.[176,177] Dissociation of an additional CO and replacement by solvent gives active intermediates of the general formula $M(CO)_{4-x}(S)_xOCOH^-$ (S = H_2O or methanol). Additionally, in the absence of a rate determining CO dissociation from $M(CO)_6$ to activate the catalyst, a second rate-determining step was reported to result from decarboxylation of $M(CO)_{4-x}(S)_xOCOH^-$ to give $M(CO)_{4-x}(S)_xH^-$ and CO_2. This was determined on the basis of the observed normal kinetic isotope effect of 3.4 ± 0.9 for Cr and 4.4 ± 0.2 for W upon deuterium substitution. An enhanced rate of this secondary reaction with photolysis was attributed to photoinduced dissociation of another CO ligand to open a coordination site for the β-hydride elimination. Hydrogen production was postulated to proceed by subsequent protonation of the $M(CO)_{4-x}(S)_xH^-$ by H_2O in a thermal step.[178]

Iron pentacarbonyl can also support WGS upon the in situ treatment of the complex with three equivalents of NaOH to furnish $Fe(CO)_4H^-$.[179] Photolysis of 9:1 THF:H_2O solutions of $Fe(CO)_4H^-$ furnishes a 1:1 ratio of H_2:CO_2 at ~6 turnovers after ~60 hours of irradiation. Interestingly, the hydrogen production step was not proposed to stem from deprotonation of water by the hydride as is the case for $M(CO)_5H^-$ (M = Cr, Mo, or W), but rather from reaction of $Fe(CO)_4H^-$ with photochemically generated $Fe(CO)_3H^-$ via the dinuclear elimination mechanism.[180–182] In this mechanism, hydrogen evolution proceeds from a bridging hydride intermediate formed by the association of $Fe(CO)_4H^-$ and $Fe(CO)_3H^-$.

1.2.3.2 Heteroleptic Metal Carbonyls

The $M(CO)_6$ pre-catalysts (M = Cr, Mo, or W) perform WGS by acting on HCO_2^- that results from the reaction of free CO with hydroxide in solution as opposed to a direct reaction with a coordinated carbonyl. In the case of *cis*-$Ru^{II}(bpy)_2Cl_2$ (bpy = 2,2′-bipyridine), CO is proposed to trap the metal center upon dissociation of Cl^- and a metallocarboxylic acid is formed

by attack of OH^- on the coordinated CO. The WGS with these systems operates at 100 - 140 °C in water under 1 - 3 atm of CO and under white light irradiation.[183] Decarboxylation of the metallocarboxylic acid complex generates $Ru^{II}(bpy)_2HCl$ followed by its protonation to yield $Ru^{II}(bpy)_2(H_2)\ Cl^+$. Hydrogen elimination is rate-determining and proposed to be photoinduced. The product of this photoreaction is $Ru^{II}(bpy)_2Cl^+$, which is available to re-enter the catalytic cycle. Turnovers frequencies as high as 20 h^{-1} were reported and the catalysis was observed to proceed at relatively low pressures of CO and in moderately acidic solutions. These experimental conditions disfavor production of formate from free CO. As expected for reactivity derived from both H^+ and OH^- induced transformations, a complicated dependence of the hydrogen production rate on pH was observed, with significant rate enhancement observed at both slightly basic (pH 8.9) and slightly acidic (pH 6.88) conditions. The role of photons in the catalysis is unclear, however, as subsequent reports indicated that the catalysis proceeds at nearly the same efficiency without irradiation.[184,185]

Ziessel reported that $Ir^{III}(\eta^5\text{-}C_5Me_5)(bpy)Cl^+$ catalyzes WGS at room temperature, 1 atm CO, neutral pH and with a high quantum yield using visible light irradiation.[186-188] The bpy = 4,4′-COOH-2,2′-bipyridine catalyst, was especially active, proceeding with a 12.7% photoreaction quantum yield (37 turnovers after 2 hours) at 410 nm. The proposed photoinduced mechanism for WGS catalysis is outlined in Figure 1.10. The chloride ligand of the starting complex is liberated by CO coordination to give a dicationic $Ir^{III}(\eta^5\text{-}C_5Me_5)(bpy)CO^{2+}$ species. Attack of CO by water generates the $Ir^{III}(\eta^5\text{-}C_5Me_5)(bpy)(COOH)^+$ cation, which is proposed to undergo a rate-determining decarboxylation accompanied by proton loss. The overall transformation $Ir^{III}(\eta^5\text{-}C_5Me_5)(bpy)(COOH)^+ \rightarrow Ir^{I}(\eta^5\text{-}C_5Me_5)(bpy)$ amounts to a two-electron reduction of the iridium center. Subsequent protonation to generate the hydride, $Ir^{III}(\eta^5\text{-}C_5Me_5)(bpy)H^+$, offers the intermediate needed for hydrogen production. The electronic excited state of the hydride, $[Ir^{III}(\eta^5\text{-}C_5Me_5)(bpy)H^+]^*$, is proposed to be protonated by HCl to give hydrogen and return the starting complex, $Ir^{III}(\eta^5\text{-}C_5Me_5)(bpy)Cl^+$.

It is interesting to note that Ziessel chooses a stepwise path for the decarboxylation and protonation steps as opposed to the concerted β-hydride elimination as proposed in other WGS systems. This appears to be based on the fact that $Ir^{I}(\eta^5\text{-}C_5Me_5)(bpy)$ is an isolable compound and not a high energy intermediate. Hydride protonation of the excited state is also unusual. This reactivity mode is supported by ^1H NMR studies where the $Ir^{III}(\eta^5\text{-}C_5Me_5)(bpy)H^+$ hydride signal

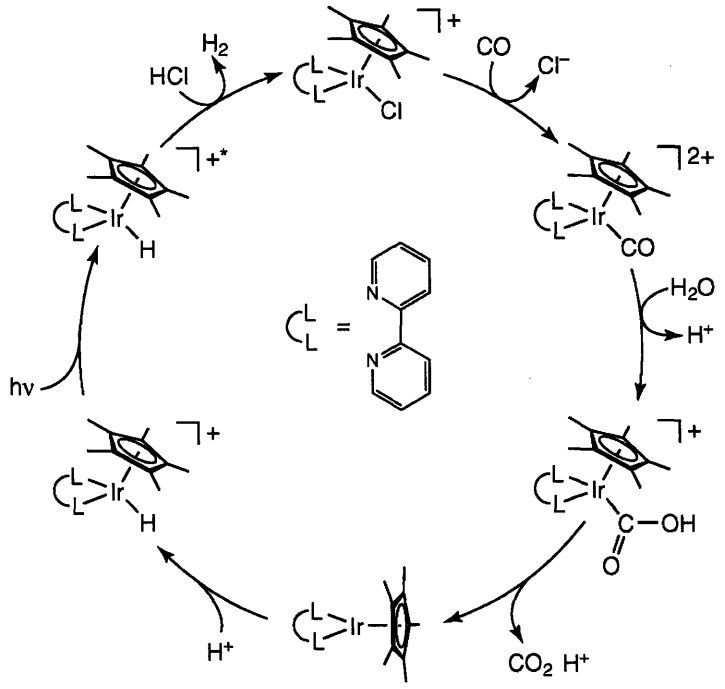

Figure 1.10. Proposed mechanism for photocatalytic WGS chemistry by an $Ir^{III}(\eta^5\text{-}C^5Me^5)(bpy)Cl^+$ complex.

at –11.45 ppm is stable in the dark but rapidly vanishes upon exposure of the solution to visible light. This suggests that visible light irradiation of $Ir^{III}(\eta^5\text{-}C_5Me_5)(bpy)H^+$ complex pumps a transition that engenders significant hydridic character to coordinated hydride.

1.2.4 Acids

In contrast to the numerous photocatalytic hydrogen generation schemes employing substrates such as alkanes, alcohols or sacrificial electron donors outlined in the previous sections, photodriven hydrogen generation processes directly from acidic solutions are rare. In the former examples (*vide supra*) the electron and proton equivalents that constitute the hydrogen product are derived from organic molecules, which upon oxidation by H atom abstraction or ET/PT reaction pathways, generate organic fragments that do not form strong covalent interactions with catalytic center (Figure 1.6 for example) and often have a strong thermodynamic bias for further reactivity. Simple mineral acids like HCl and HBr on the other hand, have conjugate bases that form very strong M–X bonds (X = Cl, Br) with many transition metals. Therefore a potential catalyst must be able to activate stable M–X bonds in order to achieve turnover. Equivalently, the catalyst must not only simultaneously be sufficiently reducing to generate H_2 from H^+, but must also be capable of driving a thermodynamically

challenging oxidation of X^- to X_2 to close the HX redox cycle. Correspondingly, few systems have been able to achieve this type of reactivity to date.

1.2.4.1 Mononuclear Catalysts

Some of the earliest reports of hydrogen photogeneration involve acidic solutions of simple metal salts. Whereas most reduced metal ions produce H_2 promptly upon their addition to mineral acids, some are thermally stable towards acid. In these cases, photoexcitation leads to the generation of hydrogen stoichiometrically: Eu^{2+},[189] Cr^{2+},[190] Fe^{2+},[191] Ce^{3+},[192] Cu^{+}[193] are all active under photolysis conditions.

A photocatalytic system for hydrogen production using a simple metal salt from aqueous HCl solutions was reported by Gray and coworkers using $Ir^{III}Cl_6^{3-}$ and was proposed to proceed by the series of reactions shown in Figure 1.11.[194,195] Irradiation into the Cl → Ir^{III} LMCT bands with 254 nm light evidenced the disappearance of $Ir^{III}Cl_6^{3-}$ and produced the one electron oxidized species $Ir^{IV}Cl_6^{2-}$ with the concomitant production of half an equivalent of molecular hydrogen. The steps leading to this reactivity are proposed to involve a proton coordination pre-equilibrium between $Ir^{III}Cl_6^{3-}$ and $HIr^{III}Cl_6^{2-}$ followed by photoexcitation of $HIr^{III}Cl_6^{2-}$ to generate the excited state $[HIr^{III}Cl_6^{2-}]^*$ (possessing significant Ir^{II}–$Cl^\bullet$ character), which is then

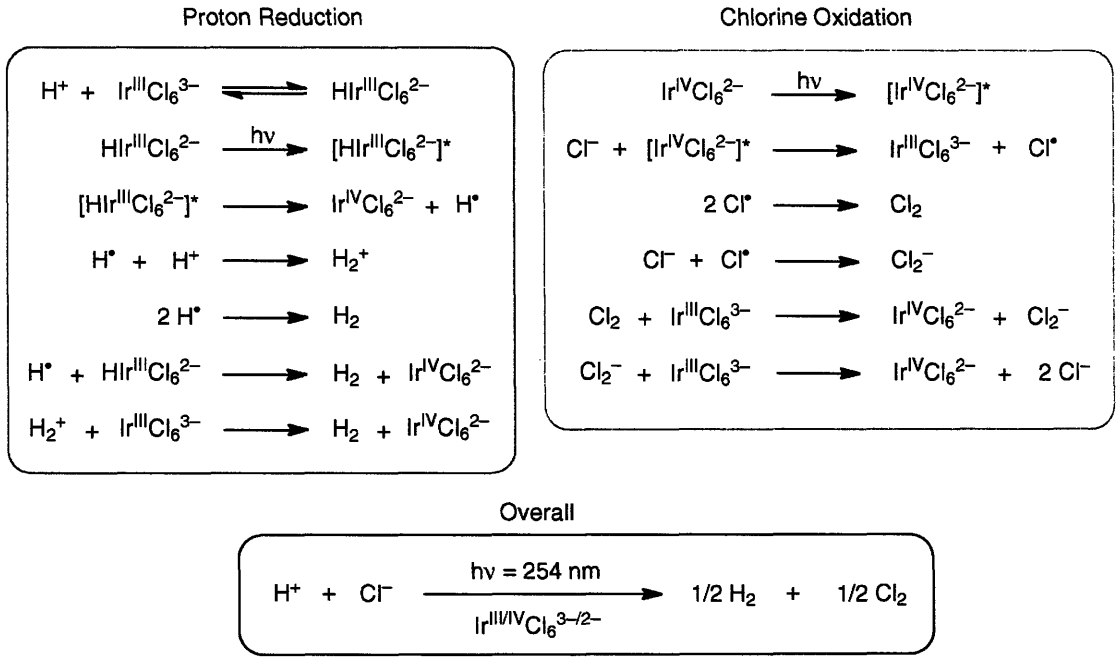

Figure 1.11. Proposed reactions involved in the photocatalytic production of hydrogen from aqueous HCl solutions using an $Ir^{III}Cl_6^{3-}$ catalyst.

proposed to decompose to a hydrogen atom and $Ir^{IV}Cl_6^{2-}$. Possible reaction pathways for the resulting hydrogen atoms include dimerization to generate H_2, reaction with a proton to generate H_2^+ which is subsequently reduced to H_2 by another equivalent of $Ir^{III}Cl_6^{3-}$. Catalysis is accomplished by secondary photolysis of the $Ir^{IV}Cl_6^{2-}$ generated during the course of hydrogen production. In a similar fashion to proton reduction, $Cl \rightarrow Ir^{IV}$ LMCT excitation generates a charge transfer complex with Ir^{III}–$Cl^{\bullet}$ character, which is capable of oxidizing a free Cl^- ion from the aqueous mineral acid solution to furnish unbound chlorine radicals and $Ir^{III}Cl_6^{3-}$. The chlorine radicals are then proposed to undergo radical-based reactivity similar to that of the hydrogen atoms to eventually generate chlorine and the starting $Ir^{IV}Cl_6^{2-}$ photoreactant. The catalytic cycle is closed with the recovery of $Ir^{III}Cl_6^{3-}$ by the secondary photolysis reaction of $Ir^{IV}Cl_6^{2-}$ and provides the net conversion of HCl to ½ H_2 and ½ Cl_2. The quantum efficiency of the overall conversion is 0.28 in 12 M HCl using 254 nm irradiation. This quantum efficiency is observed to drop off sharply with decreasing photon energy and turns off completely when using wavelengths longer than 366 nm, consistent with photoreactivity derived from high energy $Cl \rightarrow$ Ir charge transfer excited states. Although the system carries out the photocatalytic splitting of HCl to ½ H_2 and ½ Cl_2 while under constant irradiation, the Cl_2 produced is observed to reoxidize the $Ir^{III}Cl_6^{3-}$ to $Ir^{IV}Cl_6^{2-}$ when the photolysis is ceased.

1.2.4.2 Binuclear Catalysts

Some of the first reports of binuclear photocatalysts for hydrogen production from acidic solution are simply a direct extension of the stoichiometric photochemical oxidations of dissolved mononuclear metal ions (*vide supra*). The quadruply bonded $Mo_2^{II,II}(SO_4)_4^{4-}$ dimer was reported by Gray to react photochemically in aqueous H_2SO_4 solutions upon UV excitation (λ_{exc} = 254 nm) to give the single electron oxidation product, $Mo_2^{II,III}(SO_4)_4^{3-}$, and half an equivalent of hydrogen. In this case the redox chemistry is restricted to single electron pathways due to the stability of the $Mo_2^{II,III}$ dimer.[196,197] Substituting the SO_4^{2-} bridging ligands with simple halo or aquo ligands allowed for multiple electron photooxidations of the bimetallic core. In these reports the photoreactions of $Mo_2^{II,II}X_8^{4-}$ (X = Cl^-, Br^-) and $Mo_2^{II,II}(H_2O)_8^{4+}$ dimeric complexes in aqueous strong acid were not arrested at the $Mo_2^{II,III}$ mixed valence state and gave hydroxide bridged $Mo_2^{III,III}$ dimers and molecular hydrogen as final photoproducts.[197]

Two-electron photochemistry could also be achieved from a bimetallic Rh^{I} bridged by 1,3-diisocyanopropane (bridge) ligands. Similarly, under irradiation with photons coincident with the $d\sigma^* \rightarrow p\sigma$ absorption manifold (λ_{exc} = 546 nm) the $d^8\cdots d^8$ $Rh_2^{I,I}(bridge)_4^{2+}$ starting material was observed to generate one equivalent of hydrogen and the metal metal bonded d^7–d^7 $Rh_2^{II,II}(bridge)_4X_2^{2+}$ complex.[198-200] A stepwise mechanism was proposed invoking a $Rh_4^{II,I,I,II}(bridge)_8Cl_2^{4+}$ dimer of dimers resulting from a thermal reaction of the $Rh_2^{I,I}$ core with HCl, eq 13 and 14.

$$2\ Rh_2^{I,I}(bridge)_4^{2+} \xrightarrow[12\ M\ HCl]{} Rh_4^{II,I,I,II}(bridge)_8Cl_2^{4+} + H_2 \qquad (13)$$

$$Rh_4^{II,I,I,II}(bridge)_8Cl_2^{4+} \xrightarrow{546\ nm} 2\ Rh_2^{II,II}(bridge)_4Cl_2^{2+} + H_2 \qquad (14)$$

The photochemical step was reasoned to involve the photoinduced scission of the putative Rh^{I}–Rh^{I} bond in the $Rh_2^{II,I,I,II}(bridge)_8Cl_2^{4+}$ tetranuclear complex followed by reaction of the two resulting $Rh_2^{II,I}(bridge)_4Cl^{2+}$ fragments with HCl to generate two equivalents of $Rh_2^{II,II}(bridge)_4Cl_2^{2+}$ and hydrogen via an undefined mechanism, eq 14.[201,202] Proton reduction is limited to stoichiometric conversion in this case as the oxidized $Rh_2^{II,II}(bridge)_4Cl_2^{2+}$ is unable to activate the strong Rh^{II}–Cl bonds to regenerate the active $Rh_2^{I,I}(bridge)_4^{2+}$ for reentry into a catalytic cycle.

Stoichiometric two-electron proton reduction photochemistry was observed for a quadruply bonded d^4d^4 molybdenum dimmer, $Mo_2^{II,II}(HPO_4)_4^{4-}$, bridged by HPO_4^{2-} ligands. Attempts to facilitate proton reduction chemistry out of a zwitterionic (M^+–M^-) excited state, pumped by photochemical excitation into a $\delta \rightarrow \delta^*$ transition,[203] showed that although the M^+–M^- δ^* excited state was efficiently quenched by protons, hydrogen production was not observed.[204] Instead careful mechanistic work has shown that hydrogen production from the starting $Mo_2^{II,II}(HPO_4)_4^{4-}$ complex proceeds via a $d\pi \rightarrow d\pi^*$ photoexcitation (254 nm < λ_{exc} < 400 nm) whereupon two stepwise one electron oxidations by H^+ give the triply bonded $Mo_2^{III,III}(HPO_4)_4^{2-}$ and two hydrogen atoms.[205] Coupling of two hydrogen atoms eventually gives hydrogen, and although the mechanism was not expressly determined, the intermediacy of Mo–H species was not postulated. The reaction in this case is limited to stoichiometric conversion due to the inability of the $Mo_2^{III,III}(HPO_4)_4^{2-}$ complex to close the catalytic cycle by reforming the reduced $Mo_2^{II,II}(HPO_4)_4^{4-}$ complex.

1.2.5 Summary of Literature Precedent

Molecular photocatalytic hydrogen production schemes elucidated to date are generally inefficient and do not achieve appreciable conversion of solar energy. Inefficiencies generally arise from poor matching of the chromophore absorption manifold to the solar spectrum and also from low photochemical quantum yields for either excited state population or the following reactions from the primary excited state. In the specific case of three component systems, shuttles are needed for coupling one-electron redox events to a hydrogen generating catalyst, usually colloidal Pt. The relay catalyst, upon its reduction by the photosensitizer, often participates in energy wasting recombination reactions that regenerate ground state materials. Additionally photocatalytic hydrogen production schemes generally rely on the use of high energy substrates such as alkanes, alcohols, or sacrificial electron donors and thus do not store the energy of absorbed solar photons. Moreover many of these schemes are require the use of noble metals, rendering large scale application economically unfeasible. Strategies for the use of low energy substrates for hydrogen production, such as inorganic acids or water, suffer from extreme difficulty in achieving turnover as either the catalysts form strong bonds with substrate or the oxidized catalysts cannot regenerate complexes active for reduction so that the redox cycles may be closed.

1.3 *Multielectron Chemistry and Photochemistry*

Current research has focused on the development of new excited states that lead to the efficient production of hydrogen via photochemical mechanisms that confront minimal energetic barriers. For instance, hydrogen may be produced along one-electron pathways to produce H•. However, this production of H• requires 1.8 V, which is recovered upon the second one-electron reduction. Thus, though $2H^+ + 2e^- \rightarrow H_2$ is thermoneutral, its production along the one-electron pathway minimally confronts a 1.8 V barrier. This barrier may be obviated if efficient two-electron redox pathways are developed. Moreover concerted two-electron redox proton reduction pathways would avoid inefficiencies derived from energy wasting back reactions that plague single electron redox mechanisms.

Although standard oxidative addition/reductive elimination cycles represent common multielectron transformations for monometallic sites, these reactivity modes are typically restricted to the $16/18e^-$ cycles of the noble metals. One promising approach for metal catalyzed

multielectron redox chemistry is to store redox equivalents in an organic ligand as has been observed for metal porphyrinogens[206–208] and *o*-catecholate,[209] *o*-iminocatecholate,[210,211] or *o*-phenylenediamide[212] derived ligands. Another common approach for multielectron redox chemistry is to employ a bimetallic complex, wherein an overall multiple electron redox transformation can be achieved by the cooperation of two metal centers.[213–216] Not surprisingly inspiration for this strategy can be found in natural systems where dinuclear or higher nuclearity metal sites are commonly encountered: in the diiron enzymes[217] soluble methane monooxygenase[218,219] and class I ribonucleotide reductase,[220,221] in the dicopper and iron-copper sites of cytochrome *c* oxidase,[222,223] in the dinickel center of urease,[224] in the O_2-transport proteins hemerythrin[217,225] and hemocyanin,[226] in the photosystem II oxygen-evolving complex,[227] in the nitrogenase enzymes,[228-230] and in nickel-carbon monoxide dehydrogenase/acetyl coenzyme A synthase[231-234] in at least a dozen zinc enzymes,[235,236] and in certain iron-sulfur clusters,[237,238] *inter alia,*[239,240] and of course the iron only and Ni-Fe active sites of hydrogenase.[241–246] Most of these enzymes activate small molecules by multielectron transformations. Though the precise mechanistic details of substrate activation in many such systems await elucidation, reactivity and spectroscopic studies indicate that the metals of the bioactive site may work cooperatively to activate substrates one electron at a time.[247]

Synthetic bimetallic catalysts are attractive for small molecule activations of pertinence to energy catalysis as the two and four electron redox events of pertinence to HX dismutation (X = Cl, Br, OH) can potentially be shared over multiple metal sites, Figure 1.12. In this way energetically costly redox intermediates such as H• or redox cycles involving extreme formal

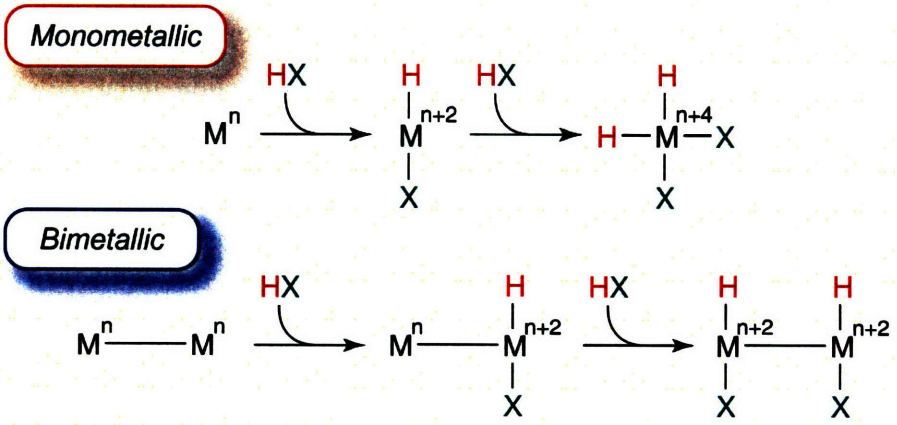

Figure 1.12. Demonstrative schemes involving two sequential activations of HX at monometallic and bimetallic metal complexes, in the bimetallic case the redox and coordination site equivalents are distributed over the entire bimetallic core.

oxidation state swings can be avoided, leading to attenuated energetic barriers for the overall transformation.

Binuclear complexes of noble metals are perhaps the most well studied and have been shown to largely maintain the chemistries of their mononuclear analogs, both at single metal sites of the binuclear core and also distributed over both metals. For example, facile oxidative additions to bimetallic complexes have been the subject of numerous reports, whether it is the two-center oxidative additions typified by the biradical excited states [•M–M•]* of $d^8 \cdots d^8$ complexes outlined in Section 1.2.1, the one-center oxidative additions of A-frames[248-252] or the one- and two-center additions of pyrazolate bridged d^8 dimers.[253-258] The corresponding reductive elimination chemistry is less developed, and while direct reductive eliminations across a bimetallic core are symmetry forbidden,[259] the elimination can be facilitated by a so called dinuclear elimination mechanism,[180–182] eq 15. This reactivity mode has primarily been observed for the elimination of H–R (R = H, Me) from mononuclear fragments that are able to open a coordination site to achieve coordinative unsaturatation. The requirement of hydride ligation in the dinuclear elimination mechanism stems from an intermediate bridging hydride complex that participates in three center two-electron bonding interaction prior to H–R bond coupling, eq 15.

(15)

In this way binuclear complexes have shown some precedence for multielectron reactivity but this reactivity is often difficult to realize in practice. In particular Bosnich has argued that unless flexible ligand sets are employed, redox chemistry at one metal center in a dinuclear construct will only serve to deactivate the second due to strong "mechanical coupling", thereby precluding bimetallic cooperation.[213,214]

1.3.1 Two-Electron Mixed Valence Bimetallics

Although challenging, bimetallic cooperation has been successfully employed for the photocatalytic production of hydrogen from homogeneous acidic solutions when using a bimetallic rhodium complex that exhibits an unusual two-electron mixed valence ground state. The use of two-electron mixed valence catalysts for multielectron redox chemistry is a logical extension of the single electron redox chemistry of classical one-electron mixed valence complexes.[260,261] Designing molecules with the valance asymmetry built into the ground state,

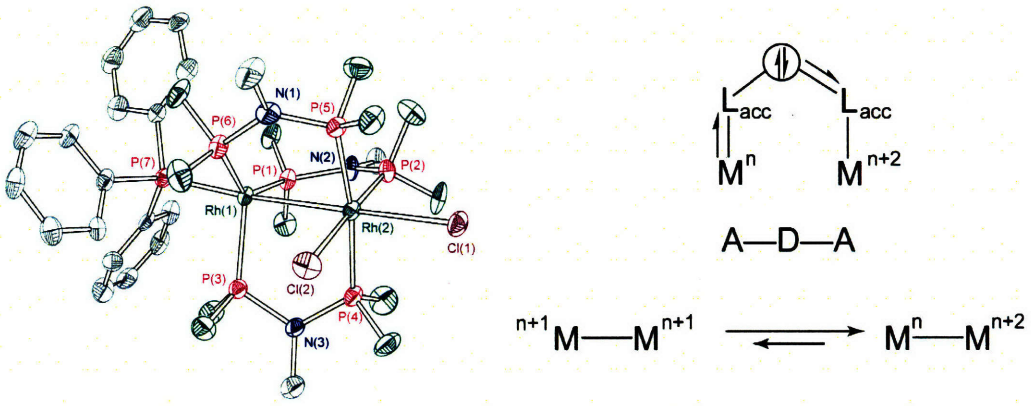

Figure 1.13. Thermal ellipsoid plot of $Rh_2^{0,II}(dfpma)_3Cl_2PPh_3$ (left), and the Acceptor-Donor-Acceptor asymmetric π-donation that is believed to stabilize the two-electron mixed valence ground state (right). Thermal ellipsoids are drawn at the 50% probability level with hydrogens omitted for clarity.

rather than an MMCT excited state grew out of the inability of the zwitterionic M^+–M^- excited states of $Mo_2^{II,II}(HPO_4)_4^{4-}$ to engender direct proton reductions in concerted multielectron steps. Following up on the synthetic work of King concerning the coordination chemistry of cobalt with a fluorinated diphosphazane ligand dfpma (dfpma = bis[difluorophosphino]methylamine, $CH_3N[PF_2]_2$),[262-267] two-electron mixed valence rhodium bimetallics of the general formula $Rh_2^{0,II}(dfpma)_3X_2L$ (X = Cl, Br; L = PR_3, CN^tBu, CO) were synthesized, Figure 1.13, left.[268,269] The parent complex is composed of a trigonal bipyramidal Rh^0 center and an octahedral Rh^{II} center with a formal Rh–Rh bond. The metal-metal single bond can be envisioned as arising from the pairing of odd electrons in the out of plane d_{z^2} orbitals on the d^9–d^7 (or $[d^8]d^1$–$d^1[d^6]$) bimetallic core.[270] In the dfpma architecture, π-accepting PF_2 groups are adjacent to the lone pair of an amine bridgehead, giving rise to an acceptor-donor-acceptor (A–D–A) electronic motif, Figure 1.13, right. Because the PF_2 groups may π-accept electrons from the metal or from the lone pair of nitrogen, asymmetric π-donation of the bridgehead amine lone pair along the ligand backbone allows the ligand to concomitantly accommodate metals both in low and moderate oxidation states. The A–D–A model is supported crystallographically as the dfpma P–N bond lengths for the PF_2 units bound to the Rh^{II} center are ~0.03 Å shorter than those bound to the Rh^0 center. Notably the Rh dfpma architecture is able to support four-electron redox chemistry in discrete two-electron steps: $Rh_2^{0,0}(dfpma)_3L_2$, $Rh_2^{0,II}(dfpma)_3X_2L$, and $Rh_2^{II,II}(dfpma)_3X_4$ with the maintenance of the Rh–Rh bond along the series, Figure 1.14.[271] When a photolabile ligand such as CO is coordinated to the Rh^0 center, proton reduction is observed upon excitation.

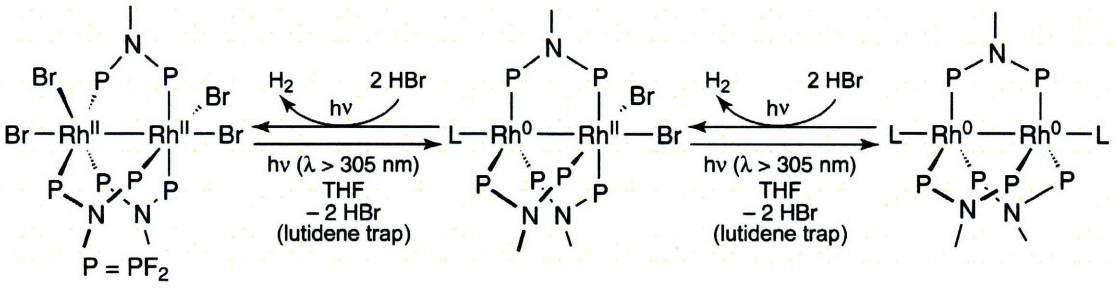

Figure 1.14. Four-electron chemistry and photochemistry supported by dirhodium cores bridged by dfpma ligands.

Notably the Rh dfpma architecture is able to support four-electron redox chemistry in discrete two-electron steps: $Rh_2^{0,0}(dfpma)_3L_2$, $Rh_2^{0,II}(dfpma)_3X_2L$, and $Rh_2^{II,II}(dfpma)_3X_4$ with the maintenance of the Rh–Rh bond along the series, Figure 1.14.[272] When a photolabile ligand such as CO is coordinated to the Rh^0 center, proton reduction is observed upon excitation.

Moreover the oxidized cores are capable of Rh^{II}–X bond photoactivations with the expulsion of halogen radicals by excitation into a Rh–Rh $d_{z^2}d_{z^2}$ $d\sigma \rightarrow d\sigma^*$ transition.[272] Population of this excited state formally nullifies the metal-metal bond and is simultaneously σ^* with respect to the axial halogen ligands. The related ligand tfepma (tfepma = $CH_3N[P(OCH_2CF_3)_2]_2$) can also achieve this Rh–X bond photoactivation chemistry.[273] Excitation into this absorption manifold leads to Rh–X bond homolysis and in the presence of a suitable halogen radical trap (such as THF or 2,3-dimethyl-1,3-butadiene) and a suitable two-electron

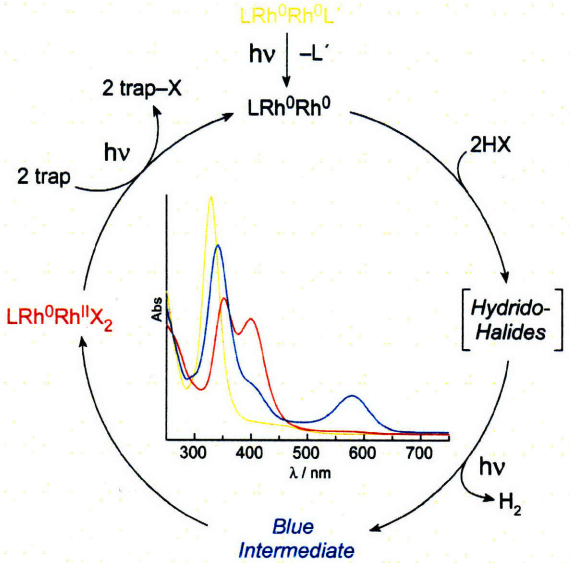

Figure 1.15. Photocycle for H_2 production by $Rh_2^{0,0}$ dfpma in HX solutions. Observed photoproducts of the cycle are indicated with their accompanying color-coded absorption spectra.

donor ligand (such as PPh_3) eventually gives the reduced complexes in discrete two-electron steps, Figure 1.14. The ambidextrous ability of these compounds to not only reduce protons but also photochemically recover reduced metal centers suggested that a photocatalytic hydrogen production cycle can be closed. In keeping with this, solutions of the reduced complex, $Rh_2^{0,0}(dfpma)_3(PPh_3)(CO)$, in THF were observed to photocatalytically reduce HCl to hydrogen upon light excitation ($\lambda_{exc} > 338$ nm), Figure 1.15.[274] In this case the Cl radicals generated in the photochemical M–X bond activation were trapped by the abstraction of hydrogen atoms from the THF solvent. At 20°C in 0.1 M HCl in THF the catalyst $Rh_2^{0,0}(dfpma)_3(PPh_3)(CO)$ was able to achieve ~ 80 turnovers of hydrogen with ($\lambda_{exc} > 338$ nm). Monitoring the solution during the course of the photocatalysis by UV-Vis spectroscopy showed a new band at 580 nm that quickly converted into the isolable two-electron mixed valence $Rh_2^{0,II}(dfpma)_3X_2L$ complex. While this study provided a landmark achievement for homogenous photocatalysis many details remained unknown, especially the nature of the putative HX addition products and the identity of the elusive blue intermediate.

1.4 *Closing Remarks*

The preceding sections cull the literature for the most relevant and well defined schemes for photocatalytic hydrogen production from molecular based catalysts and serve as an introduction to the research described herein. In summary, previous schemes typically require sacrificial high energy substrates or very high energy photons in order to engender catalysis. The C=C and C=O bond formation of alkane and alcohol photodehydrogenations, sacrificial electron donor decompositions of three component systems, CO_2 formation of water gas shift reactivity, and halogen radical trapping of HX splitting are all downhill processes that engender thermodynamic driving forces for hydrogen production. In these examples the goal of converting the energy of solar photons into chemical potential energy has been sidelined for thermochemical considerations required for catalyst turnover; where the photon, at best, can be described as simply providing the activation energy for an ensuing cascade of thermodynamically favorable reactions. In order to achieve net energy storage, low energy, and consequently very stable, starting substrates must be employed such as H_2O and HX. In order to achieve efficient redox catalysis of thermodynamically challenging substrates new systems must be elucidated that

provide platforms from which the basic science of solar energy conversion can be examined in detail.

1.5 *References*

(1) Lewis, N. S.; Nocera, D. G. *Proc. Nat. Acad. Sci.* **2006**, *103*, 15729-15735.

(2) Hoffert, M. I.; Caldeira, K.; Jain, A. K.; Haites, E. F.; Harvey, L. D. D.; Potter, S. D.; Schlesinger, M. E.; Schneider, S. H.; Watts, R. G.; Wigley T. M. L.; Wuebbles, D. J. *Nature* **1998**, *395*, 881-884.

(3) Lewis, N. S. In *Energy and Transportation*; The National Academies Press: Washington, DC, 2003; pp 33-39.

(4) *World Energy Assessment Report: Energy and the Challenge of Sustainability*; United Nations Development Program; United Nations: New York, 2003.

(5) Petit, J. R.; Jouzel, J.; Raynaud, D.; Barkov, N. I.; Barnola, J.-M; Basile, I.; Bender, M.; Chappellaz, J.; Davis, M.; Delaygue, G.; Delmotte, M.; Kotlyakov, V. M.; Legrand, M.; Lipenkov, V. Y.; Lorius, C.; Pépin, L.; Ritz, C.; Saltzman, E.; Stievenard, M. *Nature*, **1999**, *399*, 429-436.

(6) Siegenthaler, U.; Stocker, T. F.; Monnin, E.; Lüthi, D.; Schwander, J.; Stauffer, B.; Raynaud, D.; Barnola, J.-M.; Fischer, H.; Masson-Delmotte, V.; Jouzel, J. *Science*, **2005**, *310*, 1313-1317.

(7) Crabtree, G. W.; Dresselhaus, M. S.; Buchanan, M. V. *Physics Today*, **2004**, *57*, 39-45.

(8) *Basic Research Needs for the Hydrogen Economy*; A Report from the Basic Energy Sciences Workshop on Hydrogen Production, Storage, and Use; U.S. Department of Energy: Washington, DC, 2003.

(9) *Basic Research Needs to Assure a Secure Energy Future*; A Report from the Basic Energy Sciences Advisory Committee; U.S. Department of Energy: Washington, DC, 2003.

(10) *Energy and National Security*; Karas, T. H.; Sandia Report SAND2003-3287, 2003.

(11) Ciamician, G. *Science*, **1912**, *36*, 642-645.

(12) See for example: Jessop, P. G.; Ikariya, T.; Noyori, R. *Chem. Rev.* **1995**, *95*, 259-272.

(13) Crabtree, R. H.; Mihelcic, J. M.; Quirk, J. M. *J. Am. Chem. Soc.* **1979**, *101*, 7738-7740.

(14) Crabtree, R. H. *Acc. Chem. Res.* **1979**, *12*, 331-337.

(15) Crabtree, R. H.; Mellea, M. F.; Mihelcic, J. M.; Quirk, J. M. *J. Am. Chem. Soc.* **1982**, *104*, 107-113.

(16) Crabtree, R. H.; Parnell, C. P.; Uriarte, R. J. *Organometallics* **1987**, *7*, 696-699.

(17) Crabtree, R. H.; Demou, P. C.; Eden, D.; Mihelcic, J. M.; Parnell, C. A.; Quirk, J. M.; Morris, G. E. *J. Am. Chem. Soc.* **1982**, *104*, 6994-7001.

(18) Baudry, D. E.; Ephritikhine, M.; Felkin, H. *J. Chem. Soc. Chem. Commun.* **1980**, 1243-1244.

(19) Baudry, D. E.; Ephritikhine, M.; Felkin, H.; Holmes-Smith, R. *J. Chem. Soc. Chem. Commun.* **1983**, 788-789.

(20) Baudry, D. E.; Ephritikhine, M.; Felkin, H. Zakrzewski, J. *Tetrahedron Lett.* **1984**, *25*, 1283-1286.

(21) Felkin, H.; Khan-Fillebeen, T.; Gault, Y. *Tetrahedron Lett.* **1984**, *25*, 1279-1282.

(22) Felkin, H.; Khan-Fillebeen, T.; Holmes-Smith, R.; Yingrui, L. *Tetrahedron Lett.* **1985**, *26*, 1999-2000.

(23) Burk, M. J.; Crabtree, R. H.; McGrath, D. M. *J. Chem. Soc. Chem. Commun.* **1985**, 1829-1830.

(24) Burk, M. J.; Crabtree, R. H. *J. Am. Chem. Soc.* **1987**, *109*, 8025-8032.

(25) See for example: Geoffroy, G. L.; Wrighton, M. S. *Organometallic Photochemistry*; Academic Press: New York, 1979.

(26) Bitterwolf, T. E. *J. Organomet. Chem.* **2004**, *689*, 3939-3952.

(27) Vlček, A. Jr. *Coord. Chem. Rev.* **1998**, *177*, 219-256.

(28) Nomura, K.; Saito, Y. *J. Chem. Soc. Chem. Commun.* **1988**, 161-162.

(29) Brady, R.; Flynn, B. R.; Geoffroy, G. L.; Gray, H. B.; Peone, J. Jr.; Vaska, L. *Inorg. Chem.* **1976**, *15*, 1485-1488.

(30) Wink, D.; Ford, P. C. *J. Am. Chem. Soc.* **1985**, *107*, 1794-1796.

(31) Wink, D.; Ford, P. C. *J. Am. Chem. Soc.* **1987**, *109*, 436-442.

(32) Sakakura, T.; Sodeyama, T.; Tokunaga, Y.; Tanaka, M. *Chem. Lett.* **1988**, 263-264.

(33) Sakakura, T.; Ishida, K.; Tanaka, M. *Chem. Lett.* **1990**, 585-588.

(34) Nomura, K.; Saito, Y. *J. Mol. Cat.* **1989**, *54*, 57-64.

(35) Sakakura, T.; Sodeyama, T.; Tanaka, M. *New. J. Chem.* **1989**, *13*, 737-745.

(36) Tanaka, M.; Sakakura, T. *Pure and App. Chem.* **1990**, *62*, 1147-1150.

(37) Iwamoto, A.; Itagaki, H.; Saito, Y. J. *Chem. Soc. Dalton Trans.* **1991**, 1093-1097.

(38) Moriyama, H.; Sakakura, T.; Yabe, A.; Tanaka, M. *J. Mol. Cat.* **1990**, *60*, L9-L12.

(39) Maguire, J. A.; Boese, W. T.; Goldman, A. S. *J. Am. Chem. Soc.* **1989**, *111*, 7088-7093.

(40) Maguire, J. A.; Boese, W. T.; Goldman, M. E.; Goldman, A. S. *Coord. Chem. Rev.* **1990**, *97*, 179-192.

(41) Rosini, G. P.; Soubra, S.; Vixamar, M.; Wang, S.; Goldman, A. S. *J. Organomet. Chem.* **1998**, *554*, 41-47.

(42) Arakawa, H.; Sugi, Y. *Chem. Lett.* **1981**, 1323-1326.

(43) Griggs, C. G.; Smith, D. J. H. *J. Organomet. Chem.* **1984**, *173*, 105-109.

(44) Wink, D.; Ford, P. C. *J. Am. Chem. Soc.* **1986**, *108*, 4838-4842.

(45) Yamakawa, T.; Katsurao, T.; Shinoda, S.; Saito, Y. *J. Mol. Cat.* **1987**, *42*, 183-186.

(46) Nomura, K.; Saito, Y.; Shinoda, S. *J. Mol. Cat.* **1989**, *52*, 99-111.

(47) Takahashi, T.; Shinoda, S.; Saito, Y. *J. Mol. Cat.* **1985**, *31*, 301-309.

(48) Yamamoto, H.; Shinoda, S.; Saito, Y. *J. Mol. Cat.* **1985**, *30*, 259-266.

(49) Shinoda, S.; Kobayashi, A.; Aoki, T.; Saito, Y. *J. Mol. Cat.* **1986**, *38*, 279-286.

(50) Roundhill, D. M.; Gray, H. B.; Che, C.-M. *Acc. Chem. Res.* **1989**, *22*, 55-61.

(51) Filomena Dos Remedios Pinto, M. A.; Sadler, P. J.; Neidle, S.; Sanderson, M. R.; Subbiah, A.; Kuroda, R. *J. Chem. Soc. Chem. Commun.* **1980**, 13-15.

(52) Roundhill, D. M.; Gray, H. B.; Che. C. M. *Acc. Chem. Res.* **1989**, *22*, 55-61.

(53) Fordyce, W. A.; Brummer J. G.; Crosby, G. A. *J. Am. Chem. Soc.* **1981**, *103*, 7061-7064.

(54) Parker, W. L.; Crosby, G. A. *Chem. Phys. Lett.* **1984**, *105*, 544-546.

(55) Rice, S. F.; Gray, H. B. *J. Am. Chem. Soc.* **1983**, *105*, 4571-4575.

(56) Sperline, R. P.; Dickson, M. K. Roundhill D. M. *J. Chem. Soc., Chem. Commun.* **1977**, 62-63.

(57) Roundhill, D. M. *J. Am. Chem. Soc.* **1985**, *107*, 4354-4356.

(58) Roundhill, D. M.; Atherton, S. J.; Shen, Z-P. *J. Am. Chem. Soc.* **1987**, *109*, 6076-6079.

(59) Che, C.-M.; Schaefer, W. P.; Gray, H. B.; Dickson, M. K.; Stein, P.; Roundhill, D. M. *J. Am. Chem. Soc.* **1982**, *104*, 4253-4255.

(60) Harvey, E. L.; Stiegman, A. E.; Vlček, A. Jr.; Gray, H. B. *J. Am. Chem. Soc.* **1987**, *109*, 5233-5235.

(61) Che, C. M.; Lee, W. M.; Cho, K. C.; Harvey, P. D.; Gray, H. B. *J. Phys. Chem.* **1989**, *93*, 3095-3099.

(62) Smith, D. C.; Gray, H. B. *Coord. Chem. Rev.* **1990**, *100*, 169-181.

(63) Sweeney, R. J.; Harvey, E. L.; Gray, H. B. *Coord. Chem. Rev.* **1990**, *105*, 23-34.

(64) Irie, R.; Li, X.; Saito, Y. *J. Mol. Cat.* **1983**, *18*, 263-265.

(65) Irie, R.; Li, X.; Saito, Y. *J. Mol. Cat.* **1984**, *23*, 17-22.

(66) Irie, R.; Li, X.; Saito, Y. *J. Mol. Cat.* **1984**, *23*, 23-27.

(67) Shinoda, S.; Li, X.; Saito, Y. *J. Mol. Cat.* **1989**, *49*, 113-119.

(68) Ogoshi, H.; Setsune, J.; Yoshida, Z. *J. Am. Chem. Soc.* **1977**, *99*, 3869-3870.

(69) Wayland, B. B.; Newman, A. R. J. Am. Chem. Soc. **1979**, *101*, 6472-6473.

(70) Pope, M. T. Heteropoly and Isopoly Oxometallates. In *Inorganic Chemistry Concepts*, Jorgensen, C. K., Ed.; SpringerVerlag: Berlin, 1983.

(71) Papaconstantinou, E. *Chem. Soc. Rev.* **1989**, *18*, 1-31.

(72) Papaconstantinou, E. *J. Chem. Soc. Chem. Commun.* **1982**, 12-13.

(73) Papaconstantinou, E.; Ioannidis, A. *Inorg. Chim. Acta.* **1983**, *75*, 235-236.

(74) Papaconstantinou, E.; Dimotikali, D.; Politou, A. *Inorg. Chim. Acta.* **1980**, *46*, 155-158.

(75) Kahn, O. *Molecular Magnetism*; VCH Publishing: New York, NY, 1993.

(76) Darwent, J. R. *J. Chem. Soc. Chem. Commun.* **1982**, 798-799.

(77) Yamase, T. *Inorg. Chim. Acta.* **1982**, *64*, L155-L156.

(78) Savinov, E. N.; Saidkhanov, S. S.; Parman, V. N.; Zamaraev, K. I. *Dolk. Phys. Chem. SSSR* **1983**, *272*, 916-919.

(79) Yamase, T.; Takabayashi, N.; Kaji, M. *J. Chem. Soc. Dalton Trans.* **1984**, 793-799.

(80) Argitis, P.; Papaconstantinou, E. *J. Photochem.* **1985**, *30*, 445-451.

(81) Hill, C. R.; Bouchard, D. A. *J. Am. Chem. Soc.* **1985**, *107*, 5148-5157.

(82) Akid, R.; Darwent, J. R. *J. Chem. Soc. Dalton Trans.* **1985**, 395-399.

(83) Renneke, R. F.; Hill, C. L. *J. Am. Chem. Soc.* **1986**, *108*, 3528-3529

(84) Hiskia, A.; Papaconstantinou, E. *Polyhedron* **1988**, *7*, 477-481.

(85) Muradov, N.; Raissi, A. T. *J. Sol. Energy Eng.* **2006**, *128*, 326-330.

(86) Ward, M. D.; Brazdil, J. F.; Grasselli, R. K. *J. Phys. Chem.* **1984**, *88*, 4210-4213.

(87) Duncan, D. C.; Netsel, T. L.; Hill, C. L. *Inorg. Chem.* **1995**, *34*, 4640-4646.

(88) Fox, M. A.; Cardona, R.; Gailard, E. *J. Am. Chem. Soc.* **1987**, *109*, 6347-6354.

(89) Williamson, M. M.; Bouchard, D. A.; Hill, C. L. *Inorg. Chem.* **1987**, *26*, 1436-1441.

(90) Hill, C. L., Bouchard, D. A.; Kadkhodayan, M. M.; Schmidt, J. A.; Hilinski, E. F. *J. Am. Chem. Soc.* **1988**, *110*, 5471-5479.

(91) Gomez-Garcia, C. J.; Gimenez-Saiz, C.; Triki, S.; Coronado, E.; Le Magueres, P.; Quahab, L.; Ducasse, L.; Sourisseau, C.; Delhaes, P. *Inorg. Chem.* **1995**, *34*, 4139-4151.

(92) Kraut, B.; Ferraudi, G. *Inorg. Chem.* **1990**, *29*, 4834-4837.

(93) Tanielian, C.; Duffy, K.; Jones, A. *J. Phys. Chem. B* **1997**, *101*, 4276-4282.

(94) Swallow, A. J. *Prog. React. Kinet.* **1978**, *9*, 195-365 and references therein.

(95) Mylonas, A.; Hiskia, A.; Androulaki, E.; Dimotikali, D.; Papaconstantinou, E. *Phys. Chem. Chem. Phys.* **1999**, *1*, 437-440.

(96) Mylonas, A.; Papaconstantinou, E.; *J. Mol. Cat.* **1994**, *92*, 261-267.

(97) Mylonas, A.; Papaconstantinou, E. *J. Photochem. Photobiol. A.* **1996**, *94*, 77-82.

(98) Mylonas, A.; Roussis, V.; Papaconstantinou, E. *Polyhedron* **1996**, *15*, 3211-3217.

(99) Mylonas, A.; Hishkia, A.; Papaconstantinou, E.; *J. Mol. Cat.* **1996**, *114*, 191-200.

(100) Anbar, M.; Neta, P. *Int. J. Appl. Radiat. Isotopes* **1967**, *18*, 493-523.

(101) Durham, B.; Dressick, W. J.; Meyer, T. J. *J. Chem. Soc. Chem. Commun.* **1979**, 381-382.

(102) DeLaive, P. J.; Sullivan, B. P.; Meyer, T. J.; Whitten, D. G. *J. Am. Chem. Soc.* **1979**, *101*, 4007-4008.

(103) Bauer, R.; Konigstein, C. *Z. Naturforsch.* **1991**, *46b*, 1544-1548.

(104) Burstall, F. H. *J. Chem. Soc.* **1936**, 173-175.

(105) Liu, C. F.; Liu, N. C.; Bailar, J. C. Jr. *Inorg. Chem.* **1964**, *3*, 1085-1087.

(106) Gafney, H. D.; Adamson, A. W. *J. Am. Chem. Soc.* **1972**, *94*, 8238-8239.

(107) Young, R. C.; Meyer, T. J.; Whitten, D. G. *J. Am. Chem. Soc.* **1975**, *97*, 4781-4782.

(108) Meyer, T. J. *Acc. Chem. Res.* **1977**, *78*, 94-100.

(109) Valenty, S. J.; Gaines, G. L. *J. Am. Chem. Soc.* **1977**, *99*, 1285-1287.

(110) Harriman, A. *J. Chem. Soc. Chem. Commun.* **1977**, 777-778.

(111) Seefeld, K. P.; Möbius, D.; Kuhn, H. *Helv. Chim. Acta.* **1977**, *60*, 2608-2032.

(112) Yellowlees, L. J.; Dickinson, R. G.; Halliday, C. S.; Bonham, J. S.; Lyons, L. E. *Aust. J. Chem.* **1978**, *31*, 431-3.

(113) Moradpour, A.; Amouyal, E.; Keller, P.; Kagan, H. *Nouv. J. Chem.* **1979**, *2*, 547-549.

(114) Kalyanasundaram, K.; Kiwi, J.; Grätzel, M. *Helv. Chim. Acta* **1978**, *61*, 2720-2730.

(115) Miller, D.; McLendon, G. *Inorg. Chem.* **1981**, *20*, 950-953.

(116) Keller, P.; Moradpour, A. *J. Am. Chem. Soc.* **1980**, *102*, 7193.

(117) Ebbesen, T. W. *J. Phys. Chem.* **1984**, *88*, 4131.

(118) Bauer, R.; Werner, H. A. F. *J. Mol. Cat.* **1992**, *72*, 67-74.

(119) Konigstein, C. *J. Photochem. Photobiol. A.* **1995**, *90*, 141-152.

(120) Amouyal, E.; Zidler, B.; Keller, P.; Moradpour, A. *Chem. Phys. Lett.* **1980**, *74*, 314.

(121) Launikonis, A.; Loder, J. W.; Mau, A.W.-H.; Sasse, W. H. F.; Wells, D. *Israel J. Chem.* **1982**, *22*, 158.

(122) Amouyal, E.; Zidler, B. *Israel J. Chem.* **1982**, *22*, 117.

(123) Lehn, J. M.; Sauvage, J. P. *Nouv. J. Chem.* **1977**, *1*, 449-451.

(124) Kirch, M.; Lehn, J. M.; Sauvage, J. P. *Helv. Chim. Acta* **1979**, *62*, 1345-1384.

(125) Brown, G. M.; Chan, S.-F.; Creutz, C.; Schwarz, H. A.; Sutin, N. *J. Am. Chem. Soc.* **1979**, *101*, 7638-7640.

(126) Chan, S.-F.; Chou, M.; Creutz, C.; Matsubara, T.; Sutin. N. *J. Am. Chem. Soc.* **1981**, *103*, 369-379.

(127) Krishnan, C. V.; Sutin, N. *J. Am. Chem. Soc.* **1981**, *103*, 2141-2142.

(128) Krishnan, C. V.; Brunschwig, B. S.; Creutz, C.; Sutin, N. *J. Am. Chem. Soc.* **1985**, *107*, 2005-2015.

(129) Tait, A. M.; Hoffman, M. Z.; Hayon, E. *J. Am. Chem. Soc.* **1976**, *98*, 86-93.

(130) Rillema, D. P.; Endicott, J. F. *Inorg. Chem.* **1976**, *15*, 1459-1461.

(131) Krishnan, C. V.; Creutz, C.; Mahajan, D.; Schwarz, H. A.; Sutin, N. *Israel J. Chem.* **1982**, *22*, 98-106.

(132) Goldsmith, J. I.; Hudson, W. R.; Lowry, M. S.; Anderson, T. H.; Bernhard, S. *J. Am. Chem. Soc.* **2005**, *127*, 7502-7510.

(133) Lowry, M. S.; Goldsmith, J. I.; Slinker, J. D.; Rohl, R.; Pascal, R. A. Jr.; Malliaras, G. G.; Bernhard, S. *Chem. Mat.* **2005**, *17*, 5712-5719.

(134) See Chemical Reviews Thematic Issue on Organic Electronics and Optoelectronics: **2007**, *104*, 923-1386.

(135) Ozawa, H.; Haga, M.-A.; Sakai, K. *J. Am. Chem. Soc.* **2006**, *128*, 4926-4927.

(136) Rau, S.; Schäfer, B.; Gleich, D.; Anders, E.; Rudolph, M.; Friedrich, M.; Görls, H.; Henry, W.; Vos, J. G. *Angew. Chem. Int. Ed.* **2006**, *45*, 6215-6218.

(137) McLendon, G.; Miller, D. S. *J. Chem. Soc. Chem. Commun.* **1980**, 533-534.

(138) Kalyanasundaram, K.; Grätzel, M. *Helv. Chim. Acta* **1980**, *63*, 478-485.

(139) Harriman, A.; Richoux, M. C. *J. Photochem.* **1981**, *15*, 335-339.

(140) Darwent, J.; Douglas, P.; Harriman, A.; Porter, G.; Richoux, M. –C. *Coord. Chem. Rev.* **1982**, *44*, 83-126.

(141) Kalyanasundaram, K. *J. Chem. Soc. Faraday Trans. II* **1983**, *79*, 1365-1374.

(142) Okura, I.; Shin, K. *Inorg. Chim. Acta.* **1981**, *54*, L249-L250.

(143) Persaud, L.; Bard, A. J.; Campion, A.; Fox, M. A.; Mallouk, T. E.; Webber, S. E.; White, J. M. *J. Am. Chem. Soc.* **1987**, *109*, 7309-7314.

(144) Ciamician, G.; Silber, P. *Ber.* **1900**, *33*, 2911-2913.

(145) Ciamician, G.; Silber, P. *Ber.* **1901**, *34*, 2040-2046.

(146) Grätzel, C. K.; Grätzel, M. *J. Chem. Soc. Chem. Commun.* **1979**, 7741-7743.

(147) Nguyen, K.-T.; Okura, I. *J. Photochem.* **1980**, *13*, 257-259.

(148) Jones. G. H.; Edwards, D. W.; Parr, D. *J. Chem. Soc. Chem.Commun.* **1976**, 969-970.

(149) Johansen, O.; Mau, W.-H.; Sasse, W. H. F. *Chem. Phys. Lett.* **1983**, *94*, 107-112.

(150) Johansen, O.; Mau, W.-H.; Sasse, W. H. F. *Chem. Phys. Lett.* **1983**, *94*, 113-117.

(151) Edel, A.; Marnot, P. R.; Sauvage, J. P. *Nouv. J. Chem.* **1984**, *8*, 495-498.

(152) Krasna. A. I. *Photochem. Photobiol.* **1979**, *29*, 267-276.

(153) Bellin, J. S.; Alexander, R.; Mahoney, R. D. *Photochem. Photobiol.* **1973**, *17*, 17-24.

(154) Krasna, A. I. *Photochem. Photobiol.* **1979**, *31*, 75-82.

(155) Yamase, T. *Photochem. Photobiol.* **1981**, *34*, 111-114.

(156) Grant, J. L.; Goswami, K.; Spreer, L. O.; Otvos, J. W.; Calvin, M. *J. Chem. Soc. Dalton Trans.* **1987**, 2105-2109.

(157) Craig, C. A.; Spreer, L. O.; Otvos, J. W.; Calvin. M. *J. Phys. Chem.* **1990**, *94*, 7957-7960.

(158) Ziessel, R.; Hawecker, J.; Lehn, J. -M. *Helv. Chim. Acta.* **1986**, *69*, 1065-1084.

(159) Keene, R. F.; Cruetz, C.; Sutin, N. *Coord. Chem. Rev.* **1985**, *64*, 247-260.

(160) Beley, M.; Collin, J.-P.; Ruppert, R.; Sauvage, J. –P. *J. Chem. Soc. Chem. Commun.* **1984**, 1315-1316.

(161) Sutin, N.; Creutz, C.; Fujita, E. *Comments Inorg. Chem.* **1997**, *19*, 67-92.

(162) Matsuoka, S.; Yamamoto, K.; Ogata, T.; Kusaba, M.; Nakashima, N.; Fujita, E.; Yanagida, S. *J. Am. Chem. Soc.* **1993**, *115*, 601-609.

(163) Ogata, T.; Yanagida, S.; Brunschwig, B. S.; Fujita, E. *J. Am. Chem. Soc.* **1995**, *117*, 6708-6716.

(164) Kimura, E.; Bu, X.; Shionoya, M.; Wada, S.; Maruyama, S. *Inorg. Chem.* **1992**, *31*, 4542-4546.

(165) Kimura, E.; Wada, S.; Shionoya, M.; Okazaki, Y. *Inorg. Chem.* **1994**, *33*, 770-778.

(166) Ford, P. C. *Acc. Chem. Res.* **1981**, *14*, 31-37.

(167) King, R. B. *J. Organomet. Chem.* **1999**, *586*, 2-17.

(168) For a general review see: Laine, R. M.; Crawford, E. J. *J. Mol. Cat.* **1988**, *44*, 357-387.

(169) For an early example see: Cheng, C. H.; Hendriksen, D. E.; Eisenberg, R. *J. Am. Chem. Soc.* **1977**, *99*, 2791-2792.

(170) King, R. B.; Frazier, C. C.; Hanes, R. M.; King, A. D. *J. Am. Chem. Soc.* **1978**, *100*, 2925-2927.

(171) Laine, R. M.; Rinker, R. G.; Ford, P. C. *J. Am. Chem. Soc.* **1977**, *99*, 252-253.

(172) Darensbourg, D. J.; Rokicki, A. *Organometallics* **1982**, *1*, 1685-1693.

(173) Church, S. P.; Grevels, F.-W.; Hermann, H.; Schnaffner, K. *J. Chem. Soc. Chem. Commun.* **1985**, 30-32.

(174) Upmacis, R. T.; Poliakoff, M.; Turner, J. T. *J. Am. Chem. Soc.* **1986**, *108*, 3645-3651.

(175) King, A. D. Jr.; King, R. B.; Sailers, E. L. III *J. Am. Chem. Soc.* **1981**, *103*, 1867-1868.

(176) Nagorski, H.; Mirbach, M. J.; Mirbach, M. J. *J. Organomet. Chem.* **1985**, *297*, 171-176.

(177) Linn, D. E.; King, R. B.; King, A. D. Jr. *J. Mol. Cat.* **1993**, *80*, 151-163.

(178) Weiller, B. H.; Liu, J.-P.; Grant, E. R. *J. Am. Chem. Soc.* **1985**, *107*, 1595-1604.

(179) Pac, C.; Miyaka, K.; Matsuo, T.; Yanagida, S.; Sakurai, H. *J. Chem. Soc. Chem. Commun.* **1986**, 1115-1116.

(180) Norton, J. R. *Acc. Chem. Res.* **1979**, *12*, 139-145.

(181) Kristjánsdóttir, S. S.; Norton, J. A. In *Transition Metal Hydrides*; Dedieu, A., Ed.; VCH: New York, 1992, Ch. 9, pp 309-360.

(182) Broussard, M. E.; Juma, B.; Train, S. G.; Peng, W.-J.; Laneman, S. A.; Stanley, G. G. *Science* **1993**, *260*, 1784-1788.

(183) Choudary, D.; Cole-Hamilton, D. J. *J. Chem. Soc. Dalton. Trans.* **1982**, 1885-1893.

(184) Tanaka, K.; Morimoto, M.; Tanaka, T. *Chem. Lett.* **1983**, 901-904.

(185) Ishida, H.; Tanaka, K.; Morimoto, M.; Tanaka, T. *Organometallics* **1986**, *5*, 724-730.

(186) Ziessel, R. *J. Chem. Soc. Chem. Commun.* **1988**, 16-17.

(187) Ziessel, R. *Angew. Chem. Intl. Ed. Engl.* **1991**, *30*, 844-847.

(188) Ziessel, R. *J. Am. Chem. Soc.* **1993**, *115*, 118-127.

(189) Ryason, P. R. *Sol. Energy* **1977**, *19*, 445-448.

(190) Collinson, E.; Dainton, F. S.; Malati, M. A. *Trans. Faraday Soc.* **1959**, *55*, 2096-2106.

(191) Heidt, L. J.; Mullin, M. G.; Martin, W. B. Jr.; Beatty, M. J. *J. Phys. Chem.* **1962**, *66*, 336-341.

(192) Heidt, L. J.; McMillan, A. F. *J. Am. Chem. Soc.* **1954**, *76*, 2135-2139.

(193) Stevenson, K. L.; Kaehr, D. M.; Davis, D. D.; Davis, C. R. *Inorg. Chem.* **1980**, *19*, 781-783.

(194) Eidem, P. K.; Maverick, A. W.; Gray, H. B. *Inorg. Chim. Acta.* **1981**, *50*, 59-64.

(195) Gray, H. B.; Maverick, A. W. *Science* **1981**, *214*, 1201-1205.

(196) Erwin, D. K.; Geoffroy, G. L.; Gray, H. B.; Hammond, G. S.; Solomon, E. I.; Trogler, W. C.; Zagars, A. A. *J. Am. Chem. Soc.* **1977**, *99*, 3620-3621.

(197) Trogler, W. C.; Erwin, D. K.; Geoffroy, G. L.; Gray, H. B. *J. Am. Chem. Soc.* **1978**, *100*, 1160-1163.

(198) Lewis, N. S.; Mann, K. R.; Gordon, J. G. II; Gray, H. B. *J. Am. Chem. Soc.* **1976**, *98*, 7461-7643.

(199) Mann, K. R.; Lewis, N. S.; Miskowski, V. M.; Erwin, D. K.; Hammond, G. S.; Gray, H. B. *J. Am. Chem. Soc.* **1977**, *99*, 5525-5526.

(200) Mann, K. R.; Bell, R. A.; Gray, H. B. *Inorg. Chem.* **1979**, *18*, 2671-2673.

(201) Miskowski, V. M.; Sigal, I. S.; Mann, K. R.; Gray, H. B.; Milder, S. J.; Hammond, G. S.; Ryason, P. R. *J. Am. Chem. Soc.* **1979**, *101*, 4383-4385.

(202) Sigal, I. S.; Mann, K. R.; Gray, H. B. *J. Am. Chem. Soc.* **1980**, *102*, 7252-7256.

(203) Engebretson, D. S.; Zaleski, J. M.; Leroi, G. E.; Nocera D. G. *Science* **1994**, *265*, 759-762.

(204) Partigianoni, C. M.; Chang, I.-J.; Nocera, D. G. *Coord. Chem. Rev.* **1990**, *97*, 105-117.

(205) Chang, I.-J.; Nocera, D. G. *J. Am. Chem. Soc.* **1987**, *109*, 4901-4907.

(206) Floriani, C.; Floriani-Moro, R. In *The Porphyrin Handbook*; Kadish, K. M., Smith, K. M., Guilard, R., Eds.; Academic Press: San Diego, CA, 2000; Vol. 3, Chapter 25, pp 405-420.

(207) Bachmann, J.; Nocera, D. G. *J. Am. Chem. Soc.* **2004**, *126*, 2829-2837.

(208) Bachmann, J.; Nocera, D. G. *J. Am. Chem. Soc.* **2005**, *127*, 4730-4743.

(209) Pierpont, C. G.; Buchanan, R. M. *Coord. Chem. Rev.* **1981**, *38*, 45-87.

(210) Chun, H.; Verani, C. N.; Chadhuri, P.; Bothe, E.; Bill, E.; Weyermüller, T.; Wieghardt, K. *Inorg. Chem.* **2001**, *40*, 4157-4166.

(211) Blackmore, K. J.; Ziller, J. W.; Heyduk, A. F. *Inorg. Chem.* **2005**, *44*, 5559-5561.

(212) Mederos, A.; Dominguez, S.; Hernández-Molina, R.; Sanchiz, J.; Brito, F. *Coord. Chem. Rev.* **1999**, *193-195*, 913-939.

(213) Bosnich, B. *Inorg. Chem.* **1999**, *38*, 2554-2562.

(214) McCollum, D. G.; Bosnich, B. *Inorg. Chim. Acta* **1998**, *270*, 13-19.

(215) Fackler, J. P., Jr. *Inorg. Chem.* **2002**, *41*, 6959-6972.

(216) Halpern, J. *Inorg. Chim. Acta* **1982**, *62*, 31-37.

(217) Solomon, E. I.; Brunold, T. C.; Davis, M. I.; Kemsley, J. N.; Lee, S.-K.; Lehnert, N.; Neese, F.; Skulan, A. J.; Yang, Y.-S.; Zhou, J. *Chem. Rev.* **2000**, *100*, 235-349.

(218) Baikm M.-H; Newcomb, M; Friesner, R. A.; Lippard, S. J. *Chem. Rev.* **2003**, *103*, 2385-2420.

(219) Wallar, B. J.; Lipscomb, J. D. *Chem. Rev.* **1996**, *96*, 2625-2657.

(220) Stubbe, J.; van der Donk, W. *Chem. Rev.* **1998**, *98*, 705-762.

(221) Stubbe, J.; Nocera, D. G.; Yee, C. S.; Chang, M. C. Y. *Chem. Rev.* **2003**, *103*, 2167-2201.

(222) Ferguson-Miller, S.; Babcock, G. T. *Chem. Rev.* **1996**, *96*, 2889-2907.

(223) Einarsdóttir, O. *Biochim. Biophys. Acta* **1995**, *1229*, 129-147.

(224) Mobley, H. L. T.; Island, M. D.; Hausinger, R. P. *Microbiol. Rev.* **1995**, *59*, 451-480.

(225) Stenkamp, R. E. *Chem. Rev.* **1994**, *94*, 715-726.

(226) Magnus, K. A.; Ton-That, H.; Carpenter, J. E. *Chem. Rev.* **1994**, *94*, 727-736.

(227) Diner, B. A.; Rappaport, F. *Annu. Rev. Plant Biol.* **2002**, *53*, 551-580.

(228) Howard, J. B.; Rees, D. C. *Chem. Rev.* **1996**, *96*, 2965-2982.

(229) Burgess, B. K.; Lowe, D. J. *Chem. Rev.* **1996**, *96*, 2983-3011.

(230) Rees, D. C. *Annu. Rev. Biochem.* **2002**, *71*, 221-246.

(231) Dobbek, H.; Svetlitchnyi, V.; Gremer, L.; Huber, R.; Meyer, O. *Science* **2001**, *293*, 1281-1285.

(232) Drennan, C. L., Heo, J., Sintchak, M. D., Schreiter, E., Ludden, P. W. *Proc. Natl. Acad. Sci. U.S.A.* **2001**, *98*, 11973-11978.

(233) Doukov, T.; Iverson, T. M.; Seravalli, J.; Ragsdale, S. W.; Drennan, C. L. *Science* **2002**, *298*, 567-572.

(234) Darnault, C.; Volbeda, A.; Kim, E. J.; Vernède, X.; Lindahl, P. A.; Fonticella-Camps, J. C. *Nature Struct. Biol.* **2003**, *10*, 271–279.

(235) Lowther, W. T.; Matthews, B. W. *Chem. Rev.* **2002**, *102*, 4851-4608.

(236) Lipscomb, W. N.; Sträter, N. *Chem. Rev.* **1996**, *96*, 2375-2433.

(237) Beinert, H.; Holm, R. H.; Münck, E. *Science* **1997**, *277*, 653-659.

(238) Holm, R. H.; Ciurli, S.; Weigel, J. A. *Prog. Inorg. Chem.* **1990**, *39*, 1-74.

(239) Wilcox, D. E. *Chem. Rev.* **1996**, *96*, 2435-2458.

(240) Solomon, E. I.; Chen. P.; Metz, M.; Lee, S.-K.; Palmer, A. E. *Angew. Chem., Int. Ed.* **2001**, *40*, 4570-4590.

(241) Peters, J. W. *Curr. Opin. Struct. Biol.* **1999**, *9*, 670-676.

(242) Nicolet, Y.; Piras, C.; Legrand, P.; Hatchikian C. E.; Fontecilla-Camps, J. C. *Structure* **1999**, *7*, 13-23.

(243) Volbeda, A.; Fontecilla-Camps, J. C. *Coord. Chem. Rev.* **2005**, *249*, 1609-1619.

(244) For a recent review on Ni-Fe and Fe only hydrogenase see: Evans, D. J.; Pickett, C. J.; *Chem. Soc. Rev.* **2003**, *32*, 268-275.

(245) Rauchfuss, T. B. *Inorg. Chem.* **2004**, *43*, 14-26.

(246) Marr, A. C.; Spencer, D. J. E.; Schröder, M.; *Coord. Chem. Rev.* **2001**, *219*, 1055-1074.

(247) Holm, R. H.; Kennepohl, P.; Solomon, E. I. *Chem. Rev.* **1996**, *96*, 2239-2314.

(248) Kubiak, C. P.; Eisenberg, R. *J. Am. Chem. Soc.* **1977**, *99*, 6129-6131.

(249) Olmstead. M. M.; Hope, H.; Benner. L. S.; Balch. **A.** L. *J. Am. Chem. Soc.* **1971**, *99*, 5502-5503.

(250) Cowie, M.; Mague, J. T.; Sanger, A. R. *J. Am. Chem. Soc.* **1978**, *100*, 3628-3629.

(251) Brown, M. P.; Puddephatt, R. J.; Rashidi, M.; Seddon, K. R. *Inorg. Chim. Acta* **1977**, *23*, L27-L28.

(252) Brown, M. P.; Fisher, J. R.; Puddephatt, R. J.; Seddon, K. R. *Inorg. Chem.* **1979**, *18*, 2808-2813.

(253) Sola, E.; Bakhmutov, V. I.; Torres, F.; Elduque, A.; Lopez, J. A.; Lahoz, F. J.; Werner, H.; Oro, L. A. *Organometallics* **1998**,*17*, 683-696.

(254) Tejel, C.; Ciriano, M. A.; Lopez, J. A.; Lahoz, F. J.; Oro, L. A. *Organometallics* **2000**, *19*, 4977-4984.

(255) Brost, R. D.; Stobart, S. R.; *Inorg. Chem.* **1989**, *28*, 4307-4308.

(256) Brost, R. D.; Fjeldsted, D. O. K.; Stobart, S. R.; *Chem. Commun.* **1989**, 488-490.

(257) Brost, R. D.; Stobart, S. R. *Chem. Commun.* **1989**, 498-500.

(258) Jiminez, M. V.; Sola, E.; Egea, M. A.; Huet, A.; Francisco, A. C.; Lahoz, F. J.; Oro, L. A. *Inorg. Chem.* **2000**, *38*, 1108-1117.

(259) Trinquier, G.; Hoffmann, R. *Organometallics* **1984**, *3*, 370-380.

(260) Vogler, A.; Osman, A. H.; Kunkely, H. *Coord. Chem. Rev.* **1985**, *64*, 159-173.

(261) Meyer, T. J. *Prog. Inorg. Chem.* **1983**, *30*, 389-440.

(262) Newton, M. G.; King, R. B.; Chang, M.; Pantaleo, N. S.; Gimeo, J. *J. Chem. Soc., Chem. Commun.* **1977**, 531-532.

(263) King, R. B.; Gimeo, J.; Lotz, T. J. *Inorg. Chem.* **1978**, *17*, 2401-2405.

(264) Newton, M. G.; Pantaleo, N. S.; King, R. B.; Lotz, T. J. *J. Chem. Soc., Chem. Commun.* **1978**, 514-515.

(265) King, R. B. *Acc. Chem. Res.* **1980**, *13*, 243-248.

(266) Chloyard, A.; El Murr, N.; King, R. B. *J. Organomet. Chem.* **1981**, *1*, C13-C15.

(267) Babonneau, F.; Henry, M.; King, R. B.; El Murr, N. *Inorg. Chem.* **1985**, *24*, 1946-1949.

(268) Dulebohn, J. I.; Ward, D. L.; Nocera, D. G. *J. Am. Chem. Soc.* **1990**, *112*, 2969-2977.

(269) Kadis, J.; Shin, Y. K.; Dulebohn, J. I.; Ward, D. L.; Nocera, D. G. *Inorg. Chem.* **1996**, *35*, 811-817.

(270) Nocera, D. G. *Acc. Chem. Res.* **1995**, *28*, 209-217.

(271) Heyduk, A. F.; Macintosh, A. M.; Nocera, D. G. *J. Am. Chem. Soc.* **1999**, *121*, 5023-5032.

(272) Heyduk, A. F.; Macintosh, A. M.; Nocera, D. G. *J. Am. Chem. Soc.* **1999**, *121*, 5023-5032.

(273) Odom, A. L.; Heyduk, A. F.; Nocera, D. G. *Inorg. Chim. Acta* **2000**, *297*, 330-337.

(274) Heyduk, A. F.; Nocera, D. G. *Science* **2001**, *293*, 1639-1641.

Chapter 2:

Mechanistic Investigations of Photocatalytic Hydrogen Production from Two-electron Mixed Valence Dirhodium Cores

Portions of this work have appeared previously:

Esswein, A. J.; Veige, A. S.; Nocera, D. G. *J. Am. Chem. Soc.* **2005**, *127*, 16641-16651.

2.1 *Introduction*

The final section of Chapter 1 detailed the successful implementation of two-electron mixed valence dirhodium cores (Rh^0–Rh^{II}) for the photocatalytic production of hydrogen from homogenous HX (X = Cl, Br) solutions.[1] While this work established the overall photocycle, the process by which H_2 photogeneration proceeds was not precisely known, and accordingly, at the completion of that study the following questions remained unanswered: (1) What is the nature of the initial hydrogen-halide addition product? (2) What is the nature of the blue photointermediate and what is the photoreaction that leads to its production? (3) How does the blue intermediate convert to the Rh^0–$Rh^{II}X_2$ complex, thereby allowing the photocycle to be closed? and with intermediates defined, (4) What is the step in the photocycle that limits the overall H_2 production efficiency?

This chapter describes studies designed to address these outstanding issues by tuning the electronic properties of the ligands bridging the bimetallic core. Specifically, the two-electron mixed valency required for the photocycle of Figure 1.15 is enforced by the three $MeN(PF_2)_2$ (dfpma = bis(difluorophosphino)methylamine) bidentate diphosphazane ligands.[2] By tuning the electronic accepting properties of the ligand from $-PF_2$ to the slightly less π-accepting and more bulky $-P(OCH_2CF_3)_2$ of $MeN[P(OCH_2CF_3)_2]_2$ (bis[bis(trifluoroethoxy)phosphino]methylamine, tfepma)[3] and the amine donor bridgehead to the methylene group of $H_2C[P(OCH_2CF_3)_2]_2$ (bis[bis(trifluoroethoxy)phosphino]methane, tfepm) the nature of the intermediates relevant to the photocatalytic hydrogen production can be revealed. In doing so, each step of the photocycle can be examined independently and the factors controlling the photoefficiency for H_2 production can be ascertained expressly. Additionally, with the knowledge from this model chemistry in hand reaction conditions can be designed to target the catalytic intermediates in the original dfpma system for the final verification of the catalytic model.

2.2 *Rhodium Hydrido Halides*

2.2.1 Synthesis and Thermal Reactivity

Tfepma complexes of iridium are distinguished by the ability to manage both hydrogen activation and elimination across the binuclear core as well as stabilize hydrido halide species,[4-7] and therefore tfepma presented a promising ligand environment upon which to explore the corresponding rhodium chemistry. In this work the two-electron mixed valence species

$Rh^{0,II}(tfepma)_3Cl_2$ (**1**) is the keystone for the dihydride/hydrogen model chemistry of pertinence to the hydrogen production photocycle shown in Figure 1.15. The complex, whose crystal structure is shown in Figure 2.1, is distinguished by the disposition of the three A–D–A ligands about the bimetallic core. In contrast to the coordination chemistry dfpma, where the sterically less-encumbering $-PF_2$ groups engender a preference for bridging binding modes, in **1**, one tfepma ligand chelates the Rh^0 center. This affords an overall trigonal bipyramidal coordination sphere, defined by the average $\angle(P–Rh–P)_{avg} = 120°$ in the trigonal plane and a nearly linear $P_{ax}–Rh^0–Rh^{II}$ axis. Computational and synthetic studies suggest that bulky substituents on the phosphorus atoms, such as the trifluoroethoxy groups of tfepma, increases the chelating power of the ligand.[8,9] The absence of a third phosphorus ligand in the equatorial plane of Rh^{II} demands the equatorial coordination of the two halides at the Rh^{II} center, leaving its axial coordination site vacant and engendering an overall square pyramidal geometry. This precise coordination motif has been observed previously for diiridium centers.[5] Indeed, **1** and its diiridium congener are structurally homologous. The most noted deviation is a slight decrease in the metal-metal bonding distance from 2.7871(8) Å in $Ir_2^{0,II}(tfepma)_3Cl_2$ to 2.7450(12) Å in **1**.

Coordinative unsaturation trans to the metal-metal axis of the $M_2^{0,II}$ core results in an extensive reaction chemistry for the structurally congruent $Ir_2^{0,II}(tfepma)_3Cl_2$ with small molecule substrates[5,10] including hydrogen and hydrogen halides.[6,7] As exemplified by Figure 2.1, this chemistry is preserved for the structurally analogous dirhodium complex; hydrogen reacts with **1** to yield products of the formula: $Rh_2^{II,II}(tfepma)_3(H)_2Cl_2$ in three isomeric forms. The crystal structures of the three isomers are shown in Figure 2.1 and relevant bond distances and angles for the three complexes in Table 2.1. Compound **2** is the predominate product and single crystals may be isolated by repeated recrystallizations from slowly cooled CH_2Cl_2 solutions containing the mixture of isomers obtained from the hydrogenation reaction. X-ray structural determination reveals an octahedral coordination geometry about each rhodium center with the chlorides ligated trans to the metal-metal bond and the tfepma ligands strapping the bimetallic core in a triply bridging motif. The coordination of the phosphite ligands about the rhodium centers exhibits a meridonal geometry with the P–Rh–P bond angles approaching 90°.

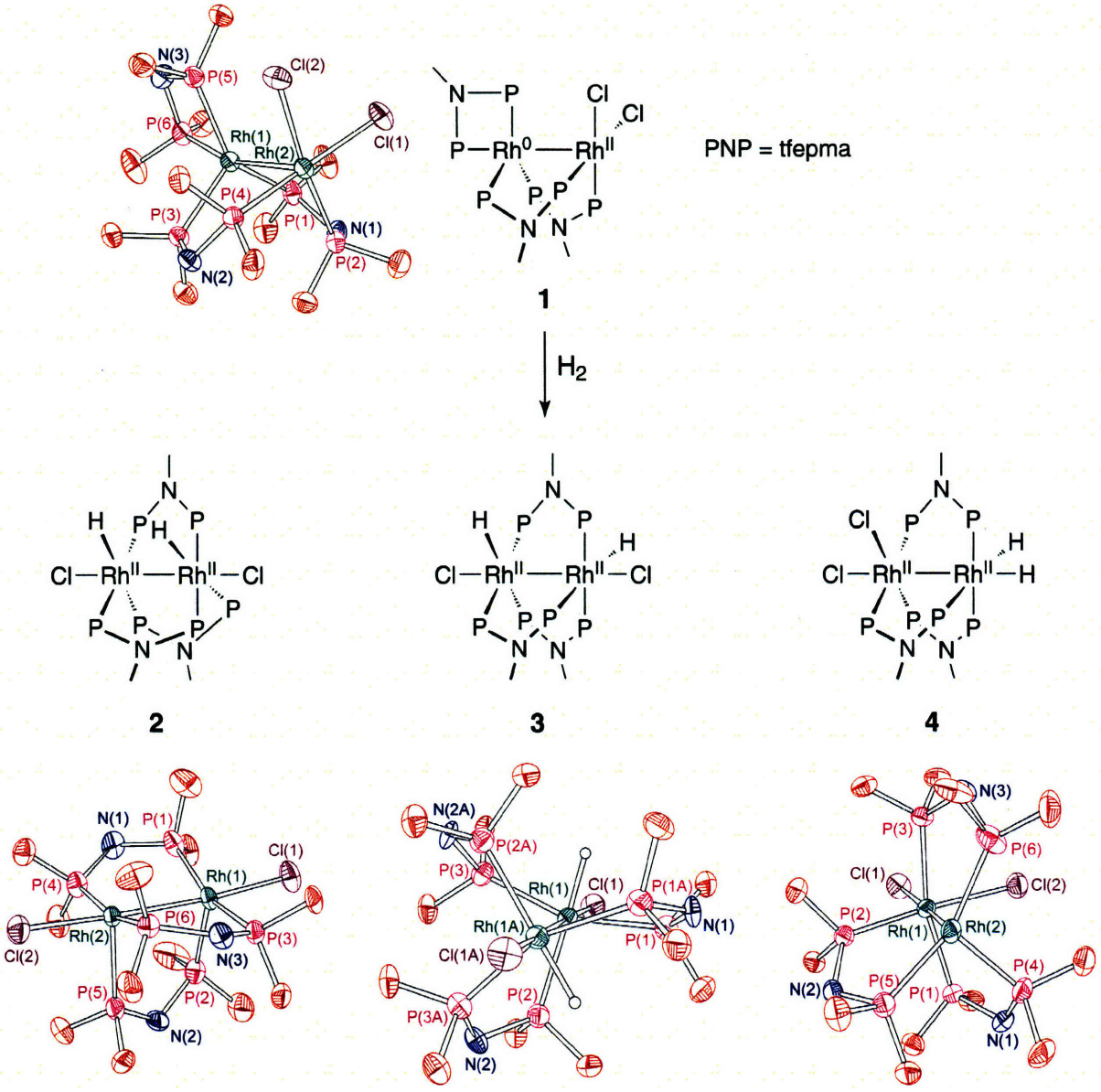

Figure 2.1. Hydrogenation of $Rh_2^{0,II}(tfepma)_3Cl_2$ (**1**) yields three dihydrido-dihalide isomers: *syn*-$Rh_2^{II,II}(tfepma)_3(H)_2Cl_2$ (**2**), *anti*-$Rh_2^{II,II}(tfepma)_3(H)_2Cl_2$ (**3**), and *cis*-$Rh_2^{II,II}(tfepma)_3(H)_2Cl_2$ (**4**) (bottom, left to right respectively). Thermal ellipsoids drawn at the 50% probability level and the –Me and $-CH_2CF_3$ groups of the tfepma ligand have been omitted for clarity. Only the crystallographically located hydrides and atom numbers of pertinence to Table 2.1 are included.

The presence of two hydrides, although not located crystallographically, is implied by two open coordination sites in equatorial planes trans to P(2) and P(5). A strong trans influence is evidenced by the increased bond length of 2.303(3) Å for the Rh–P bond diametrically opposed to the hydride as compared to Rh–P bonds that are not (d_{avg}(Rh–P) = 2.240 Å). Additionally the P(1)–Rh(1)–P(3) angle of 160.58(13)° is indicative of the reduced steric

requirements for the hydride as compared to the bulky bis(trifluoroethoxy)phosphino unit of the tfepma ligand. The P(2)–Rh(1)–Rh(2)–P(5) dihedral angle of 22.55(12)° for the trans phosphite ligand is indicative of a syn disposition of the hydrides. Coordination of a chloride and a hydride to each Rh center is consistent with the formulation of a valence symmetric $Rh_2^{II,II}$ core that results from the formal oxidative addition of hydrogen to the $Rh_2^{0,II}$ core of **1**. The Rh–Rh bond length of 2.7087(12) Å is typical of d^7–d^7 bimetallic systems.[11-13] The ^1H NMR spectrum of **2** in THF-d_8 concurs with the observed crystal structure. Two N–Me resonances are observed that integrate in a 2:1 ratio at 2.89 and 3.06 ppm, respectively, and a complicated hydride pattern, integrating as two protons, is centered at –9.77 ppm. The $^{31}P\{^1H\}$ NMR again is consistent with the observed solid state structure, with two resonances observed in a 2:1 ratio at 136.76 and 131.40 ppm respectively.

Concentrated solutions of **2** in CH_3CN left undisturbed deposit yellow blocks of *anti*-$Rh_2^{II,II}(tfepma)_3(H)_2Cl_2$ (**3**). The crystal structure of **3**, shown in Figure 2.1, reveals it to be an isomeric form of **2** with three bridging tfepma ligands spanning the core, two chlorides in axial positions trans to the metal-metal bond, and equatorially coordinated hydrides. As in **2**, the Rh–Rh bond of 2.7127(13) Å is well within the range of distances expected for a single metal-metal bond. The octahedral coordination geometry is maintained as defined by the P–Rh–P bond

Table 2.1. Selected Bond Lengths (Å) and Angles (°) for *syn*-$Rh_2^{II,II}(tfepma)_3(H)_2Cl_2$ (**2**), and *anti*-$Rh_2^{II,II}(tfepma)_3(H)_2Cl_2$ (**3**), and *cis*-$Rh_2^{II,II}(tfepma)_3(H)_2Cl_2$ (**4**).

	Bond Lengths/Å						
	2	**3**[a]	**4**[b]		**2**	**3**[a]	**4**[b]
Rh(1)–Rh(2)	2.7087(12)	2.7127(13)	2.7657(8)	Rh(1)–P(3)	2.231(3)	2.244(2)	2.1930(19)
Rh(1)–Cl(1)	2.451(3)	2.459(2)	2.5442(19)	Rh(2)–P(4)	2.243(3)	–	2.2892(19)
Rh(2)–Cl(2)	2.446(3)	–	2.4110(19)	Rh(2)–P(5)	2.305(3)	–	2.284(2)
Rh(1)–P(1)	2.249(3)	2.255(2)	2.2643(19)	Rh(2)–P(6)	2.245(3)	–	2.217(2)
Rh(1)–P(2)	2.303(3)	2.293(2)	2.7657(8)				
	Bond Angles/°						
	2	**3**[a]	**4**		**2**	**3**[a]	**4**
P(1)–Rh(1)–P(2)	96.97(12)	102.95(8)	92.96(7)	P(4)–Rh(2)–P(5)	100.02(12)	–	95.19(7)
P(1)–Rh(1)–P(3)	160.58(13)	158.62(9)	165.07(7)	P(4)–Rh(2)–P(6)	163.34(12)	–	106.44(8)
P(2)–Rh(1)–P(3)	102.38(12)	98.41(8)	100.80(7)	P(5)–Rh(2)–P(6)	96.48(12)	–	158.18(9)

[a] Distances and angles of symmetry equivalent groups, denoted by –, are reported only once. Rh(2) = Rh(1A); P(4) = P(1A); P(5) = P(3A); P(6) = P(2A).
[b] The Rh(2)–Cl(2) distance reported in the table corresponds to the Rh(1)–Cl(2) distance in the structure of **4**.

angles listed in Table 2.1. Unlike **2** however, where both arms of one tfepma ligand are coordinated trans to the hydrides, the phosphite arms trans to the hydrides originate from two different tfepma ligands resulting in an anti presentation of the hydrides. The large trans influence of the hydrides[14] is again evidenced by the increased Rh–P bond length of 2.293(3) Å as compared to d_{avg}(Rh–P) = 2.25 Å for the other Rh–P bonds.

A third isomer, *cis*-$Rh_2^{II,II}(tfepma)_3(H)_2Cl_2$ (**4**), is also obtained from CH_2Cl_2/pentane washings set aside from the isolation of **2**. As shown by the crystal structure reproduced in Figure 2.1, one Rh^{II} center is coordinated by two chlorides and the other Rh^{II} center is coordinated by two hydrides. The chlorides and void spaces for the hydrides are disposed in an anti conformation about the bimetallic core. The coordination geometry about the Rh center bonded to the hydrides is similar to that observed for both **2** and **3**, with increased lengths observed for Rh–P bonds trans to hydride (see Table 2.1). Additionally, the P(5)–Rh(2)–P(6) bond angle of 158.18(9)° agrees well with those observed in **2** and **3**, where phosphite ligands are in a trans position to hydride. Although the same octahedral geometry is obtained for **4** as in **2** and **3**, the cis coordination of two hydrides and chlorides brings about some notable metric deviations. Trans ligation of Cl to P yields a *d*(Rh–P) = 2.1930(19) Å, which is markedly shorter than the mutually trans Rh(1)–P(1) and Rh(1)–P(3) bonds on the metal center coordinated by the chlorides. This observation is consistent with the diminished trans influence of chloride vs. phosphines.[15] The Rh–Rh bond length of 2.7657(8) Å and Rh–Cl_{ax} bond length of 2.5442(19) Å are significantly increased from the analogous bond lengths observed in **2** and **3**. These bond length increases are indicative of the presence of a strong σ-donating hydride in the axial position of Rh(2).

The results of nonlocal density functional theory show that complexes **2**, **3** and **4** are nearly isoenergetic (ΔE = 470 cm^{-1}, see Table 2.2). Analytical frequency calculations were undertaken to asses the nature of the energy minima as determined by geometry optimization and allowed for zero point correction to the calculated energies of each of the ground state molecules. For computed molecules, fluorine atoms act as surrogates for trifluoroethoxy groups on phosphorus of the tfepma ligands, and hydrides, not located crystallographically, were placed at idealized positions with an M–H bond length of 1.600 Å. Agreement between calculated and observed structures suggests that these simplifications are reasonable. Consistent with the prediction that **2** is less stable than **3**/**4** (see Table 2.2), solutions of **2** left to stand in the dark

Table 2.2. Gas phase Energies of truncated derivatives of complexes **2**, **3** and **4**.[a]

	2	3	4
2	–4671.693634	–	–
3	1.168	–4671.695496	–
4	0.534	0.633	–4671.694487

[a] Diagonal entries represent the calculated gas phase molecular energies (corrected for the zero point energy) vs. neutral atoms in Hartrees, off-diagonal elements represent the energy difference (ΔE) in kcal/mol ($\Delta E = E_{column} - E_{row}$).

show the growth of new products in the ^{1}H NMR with time (~24 h). This is evidenced by the appearance of N–Me resonances that are consistent with **3** and **4**.

Because conversion of **2** to **3** and **4** is slow, hydrogen elimination from freshly prepared solutions of the **2** may be examined without the complication of the participation of the other isomers. Solutions of **2** in THF-d_8 maintained in the dark showed no reaction upon exposure to HCl. ^{1}H NMR spectra obtained periodically over one week exhibited only the growth of resonances consistent with the aforementioned isomerization of **2** to **3** and **4**. The absence of an acid-base chemistry, which is not unusual in light of the well known relative acidities of late transition metal hydrides,[16] discounts a pathway for H_2 production in which the metal bound hydride reacts directly with a proton.

NMR experiments also establish that the hydrides of complexes **2-4** once installed, do not exchange rapidly in solution with hydrogen. Although **2** isomerizes slowly to **3** and **4**, H_2 exchange may be examined by monitoring the ratio of the integrated ^{1}H NMR resonances for N–Me and hydride of all isomers. Initially solutions of **2** maintained under a D_2 atmosphere in THF-d_8 show the expected N–Me to hydride ratio of 9:2, and after 8 days in the dark, an observed ratio of 9:1.7 suggests minimal H/D exchange for the fully isomerized mixture of **2**, **3**, and **4**. The observation of minor isotopic exchange, even after long periods of exposure of **2** to D_2, indicates that the hydrides do not rapidly dissociate from the bimetallic core.

2.2.2 Photochemistry

Dihydride complexes of late metals are often thermally stable with respect to hydrogen elimination, but promptly reductively eliminate hydrogen upon photoexcitation.[17–19] A classic mononuclear example is the photoinduced extrusion of H_2 from $Rh^{III}(PPh_3)_3(H)_2Cl$ to regenerate Wilkinson's complex.[20] This reactivity mode is common in photocatalytic alkane and alcohol dehydrogenation schemes (*vide supra*). Photoinduced reductive elimination of hydrogen from

binuclear complexes has also been observed. A demonstrative example by Puddephatt describes the facile elimination of hydrogen from a binuclear Pt trihydride, $[Pt_2^{II,II}(dppm)_2(H)_2(\mu\text{-}H)]^+$, to give a solvento complex formulated as $[Pt_2^{I,I}(dppm)_2(H)(S)]^+$ (S = pyridine, CH_3CN).[21] The thermal stability of the hydrides of **2** was surprising in light of the instability of the putative hydrido halide intermediates of the dirhodium dfpma architecture, and thus photochemical experiments were undertaken to ascertain the excited state chemistry of **2**.

2.2.3 Hydrogen Photoelimination

Irradiation into the $d\sigma \rightarrow d\sigma^*$ absorption manifold (300 nm < λ_{exc} < 400 nm) of **2** in THF induces an immediate color change from yellow to blue. As indicated by Figure 2.2, the color change results from the appearance of bands centered at 450 and 600 nm and the concomitant loss of the absorbance band at 308 nm. The 600 nm band promptly disappears and the absorbance signatures of **1** are eventually recovered. ^{1}H NMR spectra of completely photolyzed solutions confirm that **1** is the final product. The conversion of the blue species to **1** is not markedly accelerated by UV or full spectrum radiation (λ_{exc} > 295 nm), as compared with solutions maintained in the dark after UV irradiation, and consequently attempts to halt the photoreaction at the stage when the blue intermediate appeared were unsuccessful. These results suggest the overall reaction proceeds in a stepwise manner, beginning with a photoinduced process to give an initial blue photoproduct, which thermally rearranges to give **1**. Toepler pump

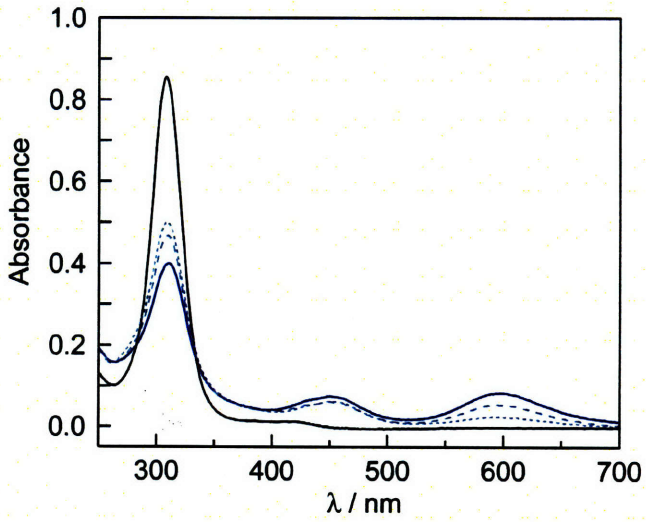

Figure 2.2. Changes in the electronic absorption spectrum during the photolysis (300 nm < λ_{exc} < 400 nm) of *syn*-$Rh_2^{II,II}(tfepma)_3(H)_2Cl_2$ (**2**) in THF. A blue photointermediate (——), produced within 30 sec of irradiation, subsequently disappears over the course of 30 sec (– – –) and 1 min (- - - -) after the excitation beam is blocked.

experiments conducted on photolyzed solutions of **2** in THF-d_8 show the production of 0.94 equivalents of a non-condensable gas, which burns over hot CuO. This result is consistent with the production of 1 equiv of H_2 per equiv of **2**, eq 1:

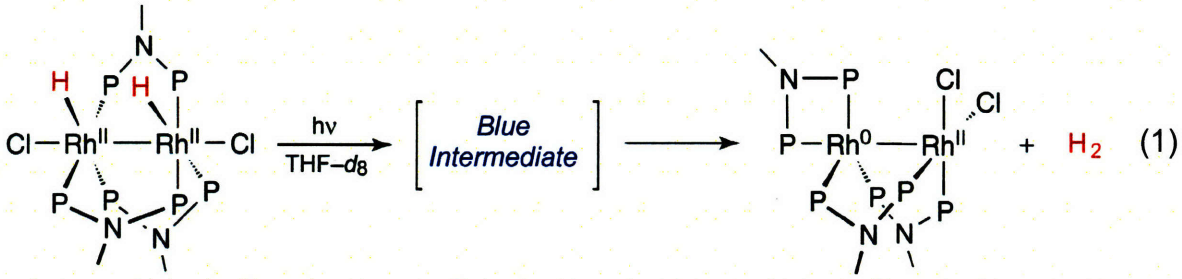

(1)

An independent ^{1}H NMR spectrum of the evolved gas shows only the sharp singlet of H_2 (4.52 ppm, CD_3CN); HD was not observed, thus ruling out the production of H_2 by an H-atom photo-abstraction involving THF-d_8. Further insight into the H_2 photoprocess comes from performing photolysis on equimolar mixtures of **2** and **2**-d_2 in THF-d_8; H_2 and D_2 are predominantly obtained with HD produced in only minor yields (4.50 ppm, $^1J_{H-D}$ = 43 Hz, CD_3CN). The absence of a statistical quantity of the isotopically scrambled HD supports a photoreaction in which hydrogen is produced by intramolecular reductive elimination. The minor occurrence of HD can be potentially attributed to one of the isomers of **2**. This contention however, has not been tested owing to the inability to obtain pure bulk samples of complexes **3** and **4**.

2.3 *Valence Symmetric Rhodium Dimers*

The observation of a transient blue species in these experiments is striking as it indicates that the intramolecular photoelimination of hydrogen from **2** shares an intermediate with a common electronic structure to the blue intermediate in the authentic dfpma system. The simple end product analyses of section 2.2.3 allowed for the postulation of a stepwise reaction sequence, namely the photochemical generation of a blue product followed by thermal rearrangement to **1**. However this fell short of a full mechanistic picture, as these observations are consistent with intramolecular hydrogen loss from the bimetallic core in either the photochemical step or the subsequent thermal rearrangement. In order to elucidate these ambiguities synthetic methodologies for the stabilization of complexes with low energy absorption features analogous to the blue intermediate of eq 1 were sought.

2.3.1 Tfepm Coordination Chemistry

The photochemistry of eq 1 corresponds to a formal reductive elimination of hydrogen from the bimetallic core of **2**, and although direct reductive eliminations across bimetallic cores are symmetry forbidden,[22] the involvement of bridging hydride along the reaction coordinate can overcome these symmetry restrictions akin to binuclear elimination mechanisms.[23–25] Bridging hydrides have been implicated in facile thermal activations of hydrogen across bimetallic group 9 complexes[26] and also diiridium cores ligated with tfepma.[5–7] Where the reversible thermal activation of hydrogen across the bimetallic core of $Ir_2^{0,II}(tfepma)_3Cl_2$ is one example eq 2:

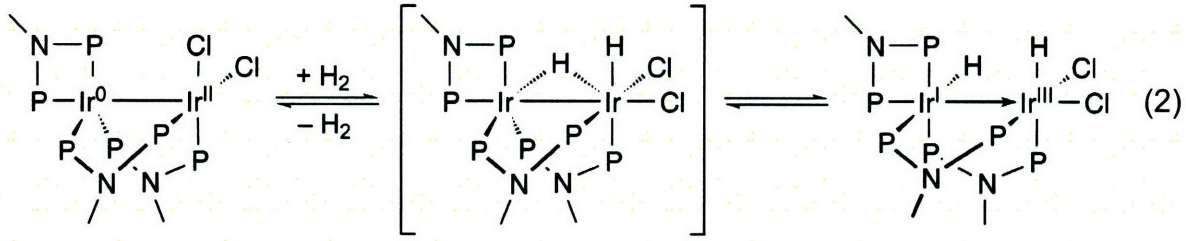

(2)

In this case the addition of hydrogen results in a two-electron mixed valence hydrido halide $Ir_2^{I,III}(tfepma)_3(H)_2Cl_2$ where the bridging hydride intermediate has been confirmed computationally.[6] On this backdrop it is reasonable to postulate that the photoinduced elimination of hydrogen from **2** might proceed via a similar bridging hydride according to the sequence of eq 3:

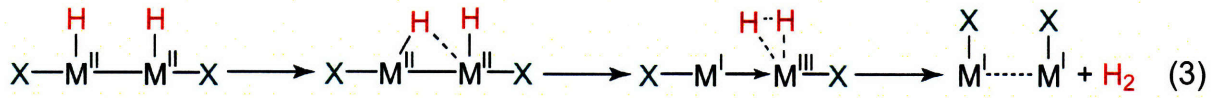

(3)

As described in Section 1.3.1 the A–D–A binding motif of diphosphazane ligands engenders two-electron mixed valence ground states, however eq 3 posits the intermediacy of valence symmetric bimetallic cores, and thus in order to test this hypothesis the stabilization of valence symmetric bimetallic products were sought. The strategy involved the relaxation of the asymmetric A–D–A π-donation of diphosphazane ligands by replacement of the N–Me bridgehead of tfepma with a methylene unit of tfepm: $H_2C[P(OCH_2CF_3)_2]_2$. Treatment of saturated CH_2Cl_2 solutions of $[Rh^I(COD)Cl]_2$ with three equivalents of tfepm provides the blue-purple compound, **5**, in good yield. An X-ray crystal structure of **5** (Figure 2.3) shows it to be a $ClRh^I\cdots Rh^ICl$ complex where three phosphite ligands and a chloride assume an approximately

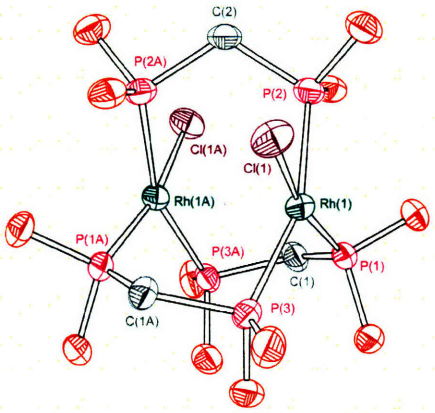

Figure 2.3. X-ray structure of $Rh_2^{I,I}(tfepm)_3Cl_2$ (**5**). Thermal ellipsoids are drawn at the 50% probability level with hydrogens and $-CH_2CF_3$ groups of the tfepm ligand omitted for clarity.

Table 2.3. Selected Bond Lengths (Å) and Angles (°) for $Rh_2^{I,I}(tfepm)_3Cl_2$ (**5**).

	Bond Lengths/Å		
Rh(1)···Rh(1A)	3.2780(4)	Rh(1)–P(2)	2.2538(6)
Rh(1)–Cl(1)	2.3801(8)	Rh(1)–P(3)	2.2641(7)
Rh(1)–P(1)	2.1608(7)		
	Bond Angles/°		
P(1)–Rh(1)–P(2)	94.46(3)	P(2)–Rh(1)–P(3)	158.80(3)
P(1)–Rh(1)–P(3)	100.44(3)		

square planar geometry about both rhodium centers. Deviation from a perfect square plane is slight as indicated by the nearly orthogonal Cl–Rh–P and a P–Rh–P bond angles listed in Table 2.3. The Rh–P bond, trans to chloride, is slightly shorter (~0.1 Å) than those trans to another Rh–P bond; the Rh–Cl bond distances are similar to those observed in **2** - **4**. The Rh···Rh distance of 3.2780(4) Å is significantly elongated from that expected for a single metal-metal bond, but shorter than that for non-interacting metal centers. These observations are consistent with a stabilized metal-metal interaction engendered by configurational mixing of the out of plane d_{z^2} and p_z orbitals that gives rise to filled dσ-dσ* and empty pσ-pσ* orbital manifolds; the metal-metal interaction resulting from this configuration interaction has been estimated to be on the order of 10 - 20 kcal/mol.[27]

The presence of an intense, low energy band centered at 507 nm in the absorption spectrum of **5** (Figure 2.4, left) is a hallmark of the electronic structure of face-to-face $d^8\cdots d^8$ dimers. Simple electronic structure considerations lead to an assignment of a dσ* → pσ transition for the absorption profile of **5** (Figure 2.4. right),[28-32] which exhibits both the low

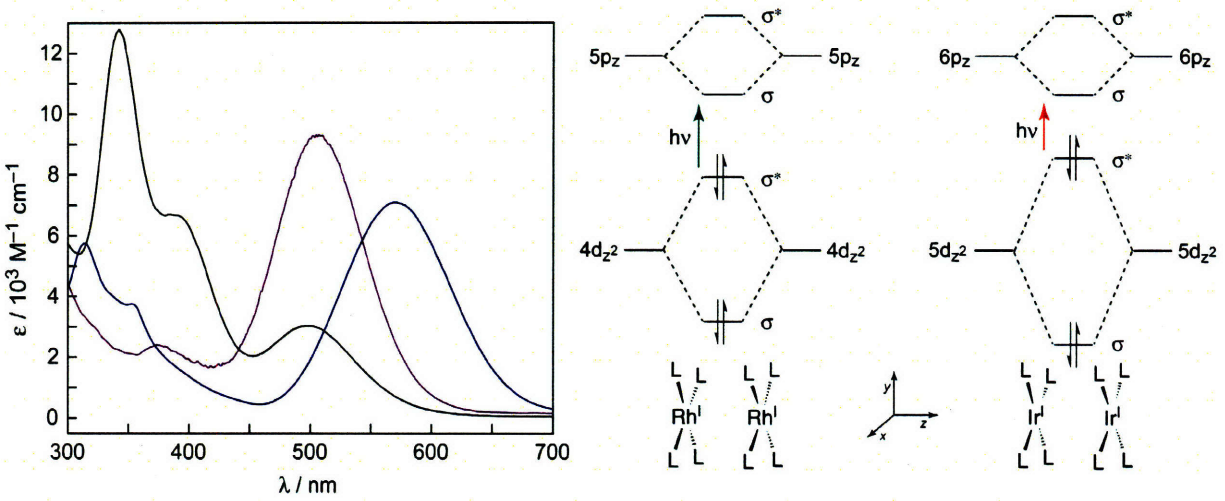

Figure 2.4. Left, electronic absorption spectra for complexes **5** (——) and **6** (——) in toluene and **8** (——) in Et_2O. Right, qualitative MO description for the $d^8\cdots d^8$ interaction that gives rise to the low energy absorption features observed for complexes **6** and **7**.

energy and intensity characteristic of such transitions. The similarity in electronic structure between the $d^8\cdots d^8$ core of **5** and the transient blue intermediate observed upon photolysis of **2**, suggests that the blue intermediate in eq 1 is the valence symmetric, face-to-face $d^8\cdots d^8$ dimer, $Rh_2^{I,I}(tfepma)_3Cl_2$, which is the compound expected to be produced in the reductive elimination of H_2 from **2** by the mechanism of eq 3.

The face-to-face $d^8\cdots d^8$ iridium congener of **5** is also afforded by a similar reaction of $[Ir^I(COD)Cl]_2$ and tfepm. In this case however, crystallized samples show two chemically distinct molecules, **6** and **7**, in the asymmetric unit. Complex **6** is structurally similar to **5** and is entirely consistent with the assignment of a valence symmetric $Ir_2^{I,I}$ core (see Figure 2.5 and Table 2.4). The metal-metal distance in **6** of 3.2641(4) Å is slightly shorter (by ~ 0.01 Å) than that observed for **5** but still outside that expected for a formal single bond. The shorter metal-metal distance is consistent with a larger configuration interaction arising from greater overlap of 5d orbitals. Where the increased orbital overlap leads to larger dσ-dσ* and pσ-pσ* splittings, which in turn are manifested in an attenuated energy gap for the dσ* → pσ electronic transition as compared to **5**; accounting for the red-shift shown in the left side of Figure 2.4 for the low energy absorption of **6**. The other molecule in the asymmetric unit, **7**, is a fascinating complex with a chloride ion folded over into a bridging position between the diiridium centers. The crystal structure of the compound shown in Figure 2.5 is a snapshot of the intermetal chloride migration that takes the symmetric $ClM^I\cdots M^ICl$ core to an internally disproportionated M^0–

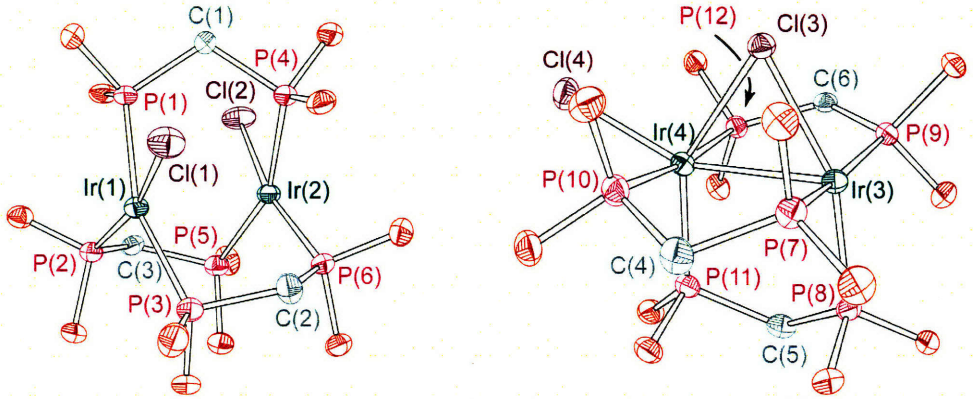

Figure 2.5. X-ray structures of the co-crystallized $Ir_2^{I,I}(tfepm)_3Cl_2$ (**6**, left) and $Ir_2^{I,I}(tfepm)_3(\mu\text{-}Cl)Cl$ (**7**, right). Thermal ellipsoids are drawn at the 50% probability level with hydrogens and $-CH_2CF_3$ groups of the tfepm ligand omitted for clarity.

Table 2.4. Selected Bond Lengths (Å) and Angles (°) for $Ir_2^{I,I}(tfepm)_3Cl_2$ (**6**) and $Ir_2^{I,I}(tfepm)_3(\mu\text{-}Cl)Cl$ (**7**).

	Bond Lengths/Å				
	6	**7**[a]		**6**	**7**[a]
Ir(1)–Ir(2)	3.2641(4)	2.7412(4)	Ir(1)–P(2)	2.1635(16)	2.1688(15)
Ir(1)–Cl(1)	2.4010(17)	2.4659(14)	Ir(1)–P(3)	2.2592(16)	2.3112(15)
Ir(2)–Cl(2)	2.3976(17)	2.4814(15)	Ir(2)–P(4)	2.2495(16)	2.3113(16)
Ir(1)–Cl(2)	–	2.5449(15)	Ir(2)–P(5)	2.2604(14)	2.1565(16)
Ir(1)–P(1)	2.2423(16)	2.255(2)	Ir(2)–P(6)	2.1670(16)	2.3179(15)
	Bond Angles/°				
	6	**7**[a]		**6**	**7**[a]
P(1)–Ir(1)–P(2)	96.97(12)	102.95(8)	Cl(1)–Ir(1)–Ir(2)	100.02(12)	58.23(3)
P(1)–Ir(1)–P(3)	160.58(13)	158.62(9)	Cl(2)–Ir(2)–Ir(1)	163.34(12)	156.49(4)
P(2)–Ir(1)–P(3)	102.38(12)	98.41(8)			

[a] The atom enumerations on the left correspond to a naming scheme of M(n) = M(n+2), Cl(n) = Cl(n+2), P(n) = P(n+6) in the thermal ellipsoid plot.

$M^{II}Cl_2$ core. An asymmetry in the Ir–Cl(bridge) bond lengths, d(Ir(3)–Cl(3)) = 2.4659(14) Å and d(Ir(4)–Cl(3)) = 2.5449(15) Å, suggests that a chloride lone pair participates in a dative Cl → Ir bonding interaction. A significant metal-metal interaction is also indicated by an Ir–Ir distance of 2.7412(4) Å, which is well within the range expected for a single metal-metal bond. The bridging tfepm ligands are nearly eclipsed, with an average P–Ir–Ir–P dihedral angle of 2°.

The terminal chloride cants significantly from the plane defined by the phosphorus atoms of the tfepm ligands as signified by a Cl–Ir–P bond angle of 114.61(6)°, engendering an overall trigonal bipyramidal geometry about Ir(4). The void space on Ir(3) in **7** is suspicious, especially in light of the coordination chemistry of **2-4**, as coordination of an additional ligand would

engender the common A-frame geometry to the bimetallic core. No evidence was found for hydride ligation by ^{1}H NMR however, confirming the unusual coordination geometry about Ir(3).

The coordination geometry observed for compound **7** indicates that bimetallic cores ligated by tfepm are on the razor's edge of mixed valency, and the reaction chemistry of **5** with σ-donor ligands confirms this contention. While the exposure of **5** to PPh_3 and CO gave no reaction, treatment of **5** with one equivalent of *tert*-butylisonitrile leads to rapid and quantitative conversion to **8**, eq 4:

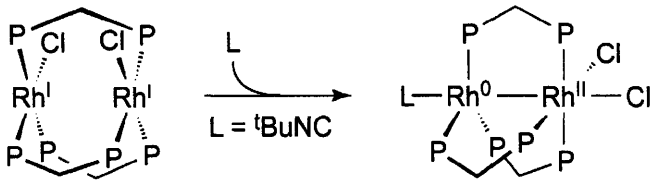

(4)

In the course of the reaction, the low energy absorption band of **5** is lost and an electronic absorption spectrum of a complex containing a $Rh_2^{0,II}$ core is obtained (Figure 2.4, left).[33] An X-ray crystal structure of **8** (Figure 2.6, right) reveals the familiar ligand environment observed previously for metal-metal bonded $Rh_2^{0,II}$ cores spanned by three diphosphazane ligands (*vide supra*). The Rh^{II} center assumes an octahedral coordination geometry with the phosphite arms of the tfepm ligands assuming a meridonal configuration. Bonding interactions with the neighboring Rh^0 center and chlorides complete the primary coordination sphere. The equatorial plane of the trigonal bipyramidal Rh^0 center is occupied by the three phosphorus donors of the tfepm with the isonitrile and Rh^{II} center occupying the axial coordination sites. The crystal structure of **8**, however, is notable from typical $Rh_2^{0,II}$ diphosphazane complexes in one regard: an alteration in bond lengths of the ligand backbone is absent. The average P–C bond lengths proximal to the Rh^0 and Rh^{II} centers are identical within error, and are ~0.15 Å longer than the P–N bonds observed in the crystal structure of congener **9** (Figure 2.6, left), $Rh_2^{0,II}(dfpma)_3Cl_2(CN^tBu)$, in which tfepm is replaced with the A–D–A stereoelectronic motif of dfpma. For the latter, the average P–N bond length proximal to Rh^{II} is ~0.03 Å shorter than that of the P–N bonds proximal to Rh^0. This bond alteration is believed to play a pivotal role in enforcing two-electron mixed valency (*vide infra*). The series is completed by the isolation and crystallization of two-electron mixed valence complex $Rh_2^{0,II}(tfepma)_3Cl_2(CN^tBu)$ **10** (Figure 2.6, middle). Although the average P–N bonds lengths are lengthened slightly from the dfpma

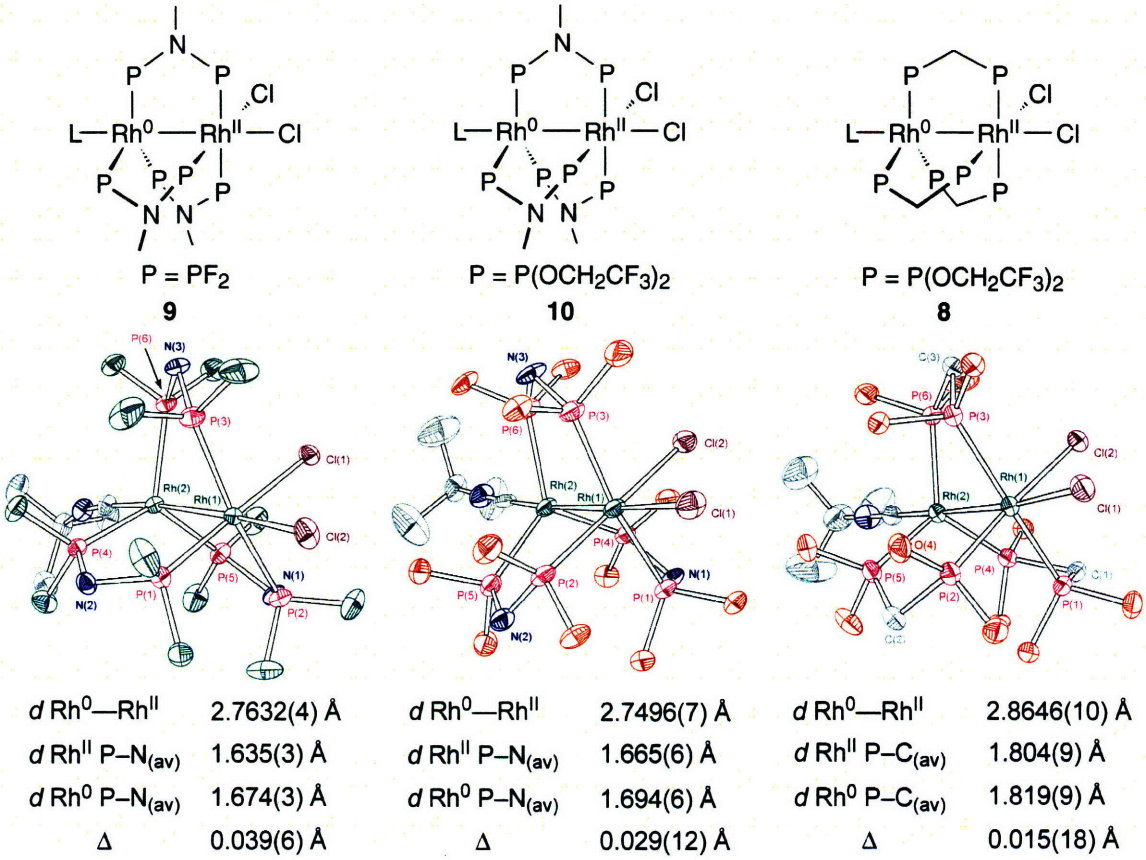

Figure 2.6. Top, line drawings of two-electron mixed valence dirhodium cores ligated by dfpma, tfepma, and tfepm ligands respectively. Middle (left to right), X-ray structures of $Rh_2^{0,II}(dfpma)_3Cl_2(CN^tBu)$ (**9**), $Rh_2^{0,II}(tfepma)_3Cl_2(CN^tBu)$ (**10**), and $Rh_2^{0,II}(tfepm)_3Cl_2(CN^tBu)$ (**8**). Thermal ellipsoids are drawn at the 50% probability level with hydrogens, bridgehead –Me, and $-CH_2CF_3$ groups of the bridging ligands omitted for clarity. Bottom, selected metrics for complexes **8**, **9**, and **10** highlighting the variances in Rh–Rh bond lengths and the average ligand P–N bond distances associated with asymmetric π-donation of the bridgehead amine lone pair in the A–D–A model.

case, the structure maintains the characteristic bond length alternations of the ligand backbone. Indeed, in no case has a $Rh_2^{I,I}$ center been isolated when coordinated by three A–D–A ligands. Only when the stereoelectronic asymmetry is absent in the ligand backbone, as in the case of tfepm, are the valence symmetric bimetallic cores isolable.

2.4 *Photocycle for Hydrogen Production*

Taken together the foregoing chemistry of tfepma and tfepm dirhodium models allow for the proposition of a photoprocess by which the Rh_2 dfpma complexes produce H_2 from HX, Figure 2.7. In brief, the addition of two equivalents of HX to a $Rh_2^{0,0}$ core produces the $Rh_2^{II,II}$ dihydride-dihalide, similar to complex **2**, which eliminates one equivalent of H_2 upon $d\sigma \rightarrow d\sigma^*$ photoexcitation. The elimination likely proceeds through a bridging hydride intermediate in

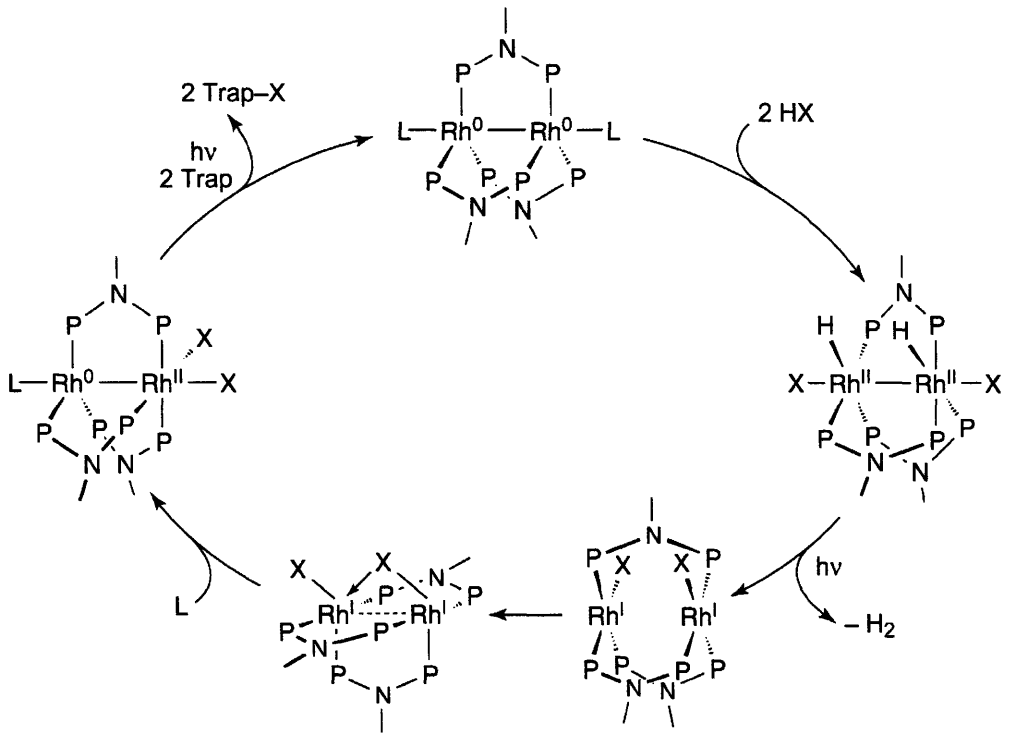

Figure 2.7. The photocycle for H_2 generation by a dirhodium dfpma photocatalyst. The proposed intermediates of the cycle are based on the chemistry of dirhodium and diiridium tfepma and tfepm synthetic analogs.

accordance with the mechanism of other dinuclear eliminations, the chemistry of dirhodium tetraphosphine complexes, and also computational results on diiridium tfepma systems. The photoelimination generates a blue, valence symmetric, face-to-face $d^8\cdots d^8$ dimer $XRh^I\cdots Rh^IX$ (X = Cl, Br) complex based on the tfepm coordination chemistry of complexes **5** and **6**. This valence symmetric, primary photoproduct when bridged by three A–D–A ligands, is unstable with respect to internal disproportionation to the Rh^0–$Rh^{II}X_2$ core. The valence disproportionation likely proceeds by folding a terminal halide into the bridging position of the dirhodium core, as evidenced by the X-ray structure of **7**. Photoexcitation of the two-electron mixed valence Rh^0–$Rh^{II}X_2$ core leads to halogen atom elimination and regeneration of the coordinatively unsaturated Rh^0–Rh^0 complex for re-entry into the photocycle.[34,35]

The proposition above is distinguished from that of Figure 1.15 by invoking redox chemistry at both Rh centers in the bimetallic core. In the initial report of H_2 photocatalysis,[1] the addition of HX to give $Rh_2^{0,II}HX$ cores was tentatively proposed to precede a dimerization reaction wherein hydrogen is eliminated, resulting in a tetranuclear Rh species. This contention was largely based on the observations of dirhodium isonitrile chemistry,[36–40] wherein oxidation of $Rh_2^{I,I}$ cores bridged by bidentate isonitriles yields blue $[Rh^IRh^{II}Rh^{II}Rh^I]^{6+}$ tetramers.[40] The

tfepma and tfepm chemistry reported here clearly shows this not to be the case. Instead in the scheme of Figure 2.7 the two-electron reduction of HX to H_2 is managed by the cooperation of both Rh centers of the bimetallic core. In this way the unusual ability of the A–D–A bridged dirhodium core to support four-electron redox chemistry is critical for the formation of $Rh_2^{II,II}(H)_2X_2$ cores from which H–H bond coupling is facile.

The blue color of **5/6** is characteristic of a transition resulting from a $d\sigma^* \rightarrow p\sigma$ transition of a face-to-face $d^8\cdots d^8$ dimer. It must be noted however, that the dfpma bridged blue compounds observed in the photocycle of Figure 1.15 and the H_2 photoelimination chemistry of tfepma bridged complex **2** possess low energy maxima (580 and 600 nm respectively in THF) that are red-shifted from that of the tfepm bridged **5** (507 nm in toluene). The sensitivity of the $d\sigma^* \rightarrow p\sigma$ transition energy to metal-metal distance most likely explains this variation in absorption maxima. Inspection of the MO diagram of Figure 2.5 suggests that a decreased metal-metal separation would serve to increase the $d\sigma$-$d\sigma^*$ splitting, effectively decreasing the HOMO-LUMO gap and redshifting the $d\sigma^* \rightarrow p\sigma$ absorption manifold. The increased P–CH_2–P bond length of tfepm in **8** as compared to P–N(Me)–P of dfpma in **9** (by ~0.15 Å) manifests itself in an increased M–M bond distance. A similar increase in M···M distance in **5** would serve to increase the $d\sigma^* \rightarrow p\sigma$ transition energy of this complex as compared to a $ClRh^I\cdots Rh^ICl$ cores bridged by diphosphazane ligands. In light of the structural sensitivity of the absorption maximum to metal-metal distance, the blue species observed in HX photocatalysis can be attributed to a valence symmetric $Rh_2^{I,I}(dfpma)_3Cl_2$ complex.

2.5 *Rhodium Hydrido Halides of Dfpma*

Previous attempts to prepare hydrido halide complexes of dfpma have met with failure, perhaps in part because the synthetic target was the two-electron mixed valence hydrides, $Rh_2^{0,II}HCl$, and not the $Rh_2^{II,II}(H)_2X_2$ cores implicated in Figure 2.7. While dirhodium dfpma cores structurally congruent to **1** are not synthetically accessible, attempts were made to access $Rh_2^{II,II}(dfpma)_3(H)_2X_2$ derivatives by halogen replacement on the readily available *anti*-$Rh_2^{II,II}(dfpma)_3Cl_4$.[41] Previous attempts to prepare hydrido halides of dirhodium cores ligated by dfpma employed hydride sources such as $NaBH_4$ or superhydride and failed to give isolable products. Notwithstanding, experiments targeting hydrido halides were initiated from the *anti*-$Rh_2^{II,II}(dfpma)_3Cl_4$ platform using the hydride transfer reagent bis(cyclopentadienyl)

zirconiumhydridochloride ($Zr(\eta^5\text{-}C_5H_5)_2HCl$) made popular by Jones for the rapid installation of hydrides on trispyrazolyl alkyl halides of rhodium.[42,43] Upon the addition of two equivalents of $Zr(\eta^5\text{-}C_5H_5)_2HCl$, green/brown solutions of *anti*-$Rh_2^{II,II}(dfpma)_3Cl_4$ in CH_2Cl_2, THF or benzene immediately turn bright purple; and although ^1H NMR analysis of the final solution shows multiple dfpma N–Me resonances, the spectrum shows complete consumption of $Zr(\eta^5\text{-}C_5H_5)_2HCl$ with the corresponding formation of $Zr(\eta^5\text{-}C_5H_5)_2Cl_2$.

The reaction rate can be attenuated by replacing the $Zr(\eta^5\text{-}C_5H_5)_2HCl$ hydride transfer reagent with Et_3SiH. In this case treatment of *anti*-$Rh_2^{II,II}(dfpma)_3Cl_4$ with 2 equivalents of Et_3SiH in THF evidenced a slow solution color change from green/brown to purple. Notably, the absorption features of *anti*-$Rh_2^{II,II}(dfpma)_3Cl_4$ are lost concomitantly with the increase of a low energy absorption feature centered at 580 nm consistent with the blue intermediate observed in HX catalysis, Figure 2.8. These data suggest that two hydrides are transferred to the bimetallic

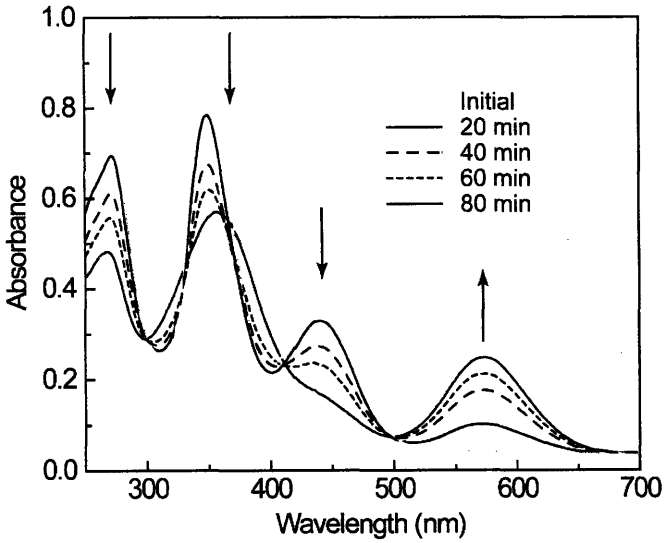

Figure 2.8. Changes in the electronic absorption spectrum during the reaction of *anti*-$Rh_2^{II,II}(dfpma)_3Cl_4$ and two equivalents of Et_3SiH in THF at 22 °C. The appearance of a band at 580 nm exactly coincides with the blue intermediate observed in the dfpma photocatalysis.

core of *anti*-$Rh_2^{II,II}(dfpma)_3Cl_4$ to generate either *cis*-$Rh_2^{II,II}(dfpma)_3(H)_2Cl_2$ or *anti*-$Rh_2^{II,II}(dfpma)_3(H)_2Cl_2$, from which hydrogen is eliminated (although rapid isomerization to *syn*-$Rh_2^{II,II}(dfpma)_3(H)_2Cl_2$ from either the cis or anti isomers cannot be ruled out), to give the valence symmetric $Rh_2^{I,I}(dfpma)_3Cl_2$ product as evidenced by the absorption band at 580 nm. These results are not conclusive however as the purple $Rh_2^{I,I}(dfpma)_3Cl_2$ complex is unstable and quickly decomposes to a complicated product mixture ($t_{1/2}$ ~ 1 hour at 22 °C), frustrating

repeated attempts at isolation or unambiguous NMR characterizations even when conducted at low temperatures.

2.6 *Concluding Remarks*

2.6.1 Ligand Bridgehead Electronics

The tfepma and tfepm coordination chemistry of this chapter shows that the formal oxidation states for binuclear cores comprised of Group 9 metals may be controlled by modifying the stereoelectronic properties of a bidentate phosphine ligand as outlined in Figure 2.9. Ligands possessing an A–D–A motif stabilize M^n–M^{n+2} cores (Figure 2.9, left). Conversely, a wealth of dirhodium chemistry shows that a valence symmetric $M^{n+1}\cdots M^{n+1}$ core is obtained for "electronically neutral" ligands such as bridging phosphines (Figure 2.9, right).[44–49] Complexes at these formal oxidation state limits may be obtained by tuning the electron donating properties of the bridgehead and the electron withdrawing properties of the phosphine (Figure 2.9, middle), thus allowing the relevant intermediates of the H_2 photocycle shown to be unveiled.

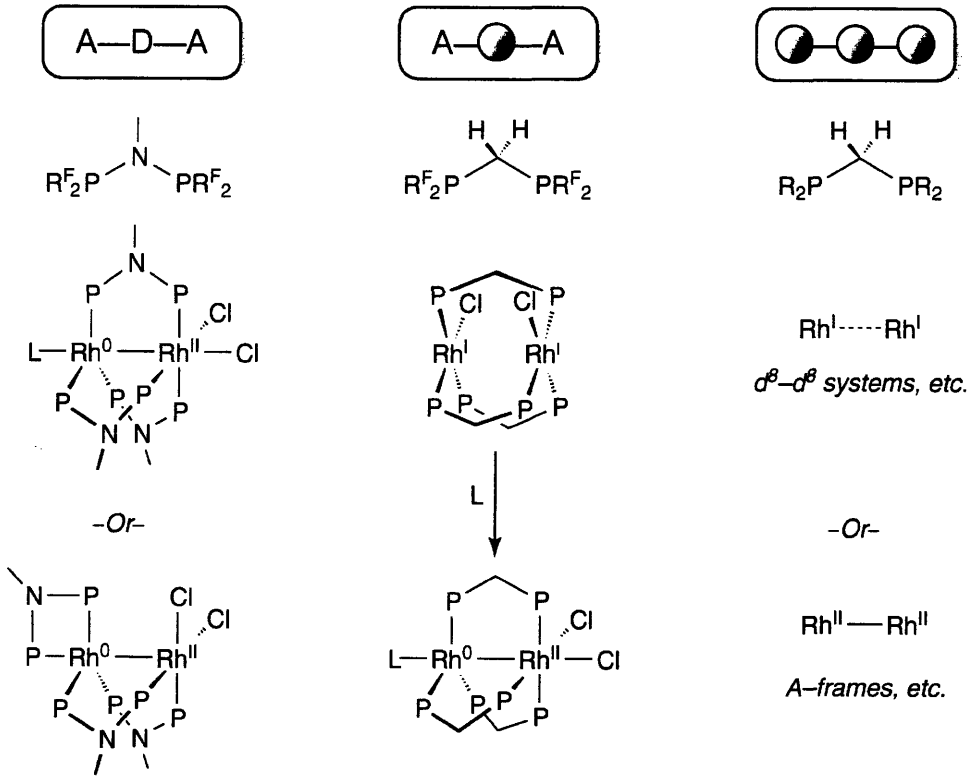

Figure 2.9. Schematic that summarizes the relation between the electronic structure of a bridging bidentate ligand and the formal oxidation state of a dirhodium binuclear core.

2.6.2 HX Photocatalysis

The overall photoefficiency for H_2 production by the photocycle in Figure 1.15 is less than 1%, commensurate with that observed for Rh–X bond photoactivation.[1] Whereas H_2 photoelimination from the $Rh_2^{II,II}(H)_2Cl_2$ is efficient, as deduced from the photochemistry of **2**, the photoconversion of $Rh_2^{0,II}(dfpma)_3X_2L$ to $Rh_2^{0,0}(dfpma)_3L_2$ has been independently measured to proceed with a quantum efficiency of ca 0.005 (ϕ_p = 0.006(2) for X = Cl, and ϕ_p = 0.0035(3) for X = Br),[34,35] indicating that the activation of the Rh–X bond is the critical determinant to overall photocatalytic activity. Accordingly, the work described herein establishes that the issue of H_2 photoefficiency is not directly related to the primary photoprocess of H_2 photoelimination from the dihydride, but rather is equated to halogen atom elimination from the bimetallic core. Moreover the hydrogen photocatalysis described here falls short of true energy storing catalysis, as a halogen radical trap (THF) is necessary to permit turnover of the oxidized catalyst. Toward this end, current studies aimed at achieving higher H_2 yields target strategies to promote the efficient photoactivation of M–X bonds.

2.7 *Experimental Section*

2.7.1 General Considerations

All manipulations were carried out in an N_2-filled glovebox or under an inert atmosphere provided by a Schlenk line unless otherwise noted. All solvents were reagent grade (Aldrich) or better and were dried and degassed by standard methods.[50] $MeN(P[OCH_2CF_3]_2)_2$ (tfepma),[51,52] $CH_2(P[OCH_2CF_3]_2)_2$ (tfepm),[53,54] $MeN(PF_2)_2$ (dfpma),[55] *anti*-$Rh_2^{II,II}(dfpma)_3Cl_4$,[41] and $Rh_2^{II,II}(tfepma)_3Cl_4$[56] were prepared by literature methods. H_2 (BOC gases, grade 5.0) and D_2 (Cambridge Isotope Labs) were passed through a U-tube immersed in liquid nitrogen prior to admission into the reaction vessels. $[Rh^{I}(COD)Cl]_2$ and $[Ir^{I}(COD)Cl]_2$ (COD = 1,5-cyclooctadiene) (Strem), HCl and *tert*-butylisonitrile (Aldrich) were purchased from the suppliers indicated and used without further purification.

2.7.2 Physical Methods

NMR data were collected at the MIT Department of Chemistry Instrument Facility (DCIF) on a Varian Inova Unity 500 spectrometer. NMR solvents (CD_3CN,CD_2Cl_2, toluene-d_8 and THF-d_8) were purchased from Cambridge Isotope labs and purified by standard procedures prior to use.[50] ^1H NMR spectra (500 MHz) were referenced to the residual protean impurities of the given solvent. $^{31}P\{^1H\}$ NMR (202.5 MHz) spectra were referenced to an external 85% H_3PO_4 standard. ^2H NMR spectra (76.8 MHz) were collected in protio solvent and reference to the natural abundance deuterium signal of the given solvent. All chemical shifts are reported in the standard δ notation in parts per million; positive chemical shifts are to higher frequency from the given reference. Elemental analyses were performed by Robertson Microlit Laboratories, Madison NJ. Photolysis experiments were conducted using a 1000 W Xe/Hg lamp in an Oriel model 66021 lamp housing. Wavelength selection of the excitation light was accomplished by employing appropriate glass filters. Photolysis experiments were conducted in 1-cm quartz cells isolated from the ambient atmosphere by two Teflon valves. NMR photolysis experiments were conducted in quartz J. Young NMR tubes. Solutions were freeze-pump-thaw degassed for three cycles (1×10^{-5} Torr) prior to photolysis. UV-vis spectra were recorded on a Spectral Instruments 400 series diode array spectrometer and referenced against the appropriate solvent.

The Toepler pump was calibrated by introducing a known pressure of hydrogen into a gas bulb of known volume and burning over hot CuO.

2.7.3 Crystallographic Procedures

Single crystals were immersed in a drop of Paratone N oil on a clean microscope slide, affixed to either a glass fiber or a human hair coated in epoxy resin and then cooled to either –75(2) or –173(2) °C. The crystals were then mounted on a Bruker K8 three circle goniometer platform equipped with an APEX CCD detector. A graphite monochromator was employed for wavelength selection of the Mo K_α radiation (λ = 0.71073 Å). The data were processed and refined using the program SAINT supplied by Siemens Industrial Automation Inc. Structures were solved by a Patterson heavy atom map and refined by standard difference Fourier techniques in the SHELXTL program suite (6.10 v., Sheldrick G. M., and Siemens Industrial Automation Inc., 2000). Disordered atoms in the $-CH_2CF_3$ groups were fixed at idealized bond lengths where necessary, site occupancies refined, and refined anisotropically for those groups that were split evenly. Otherwise the minor components of unevenly split $-CH_2CF_3$ groups were refined isotropically. Hydrogen atoms were placed in calculated positions using the standard riding model and refined isotropically; all other atoms were refined anisotropically. Unit cell parameters, morphology, and solution statistics for complexes **1** - **10** are summarized in Tables 2.5 - 2.8. All thermal ellipsoid plots are drawn at the 50% probability level, with $-CH_2CF_3$ groups, –N–Me groups, and solvents of crystallization omitted for clarity.

2.7.4 Computational Details

The Gaussian 98 program suite was employed for computational studies.[57] Geometry optimizations were initiated using atomic coordinates obtained from X-ray diffraction data. Trifluoroethoxy groups on the tfepma and tfepm ligands were replaced with fluorines. Hydrides not located crystallographically were placed at idealized positions with an M–H bond length of 1.600 Å. DFT calculations were carried out using the exchange functional of Becke[58] in conjunction with the P86 correlation functional of Perdew.[59] Relativistic core potentials were used for rhodium along with the standard Hay-Wadt double zeta basis set,[60] augmented by the optimized Rh 5p function of Couty and Hall.[61] The 6-31G(d,p) basis of Pople and co-workers[62,63] was applied to all other atoms. Optimized geometries were confirmed as energy minima by analytical frequency calculations. Reported energies are the sum of electronic and thermal free

energies and are corrected for zero point energies. The calculations reported here are for molecules in the gas phase and no attempt has been made to correct for the effects of solvation.

2.7.5 Preparation of $Rh_2^{0,II}(tfepma)_3Cl_2$ (1)

To a saturated CH_2Cl_2 solution of $[Rh^I(COD)Cl]_2$ (778 mg, 1.58 mmol), tfepma (2.305 g, 4.73 mmol, 3 equiv) was added dropwise to effect an immediate color change from dark orange to green. The solution was allowed to stir overnight, the green precipitate allowed to settle, and the supernatant removed. The solid was collected on a frit, washed with CH_2Cl_2 (5 mL), pentane (4 × 5 mL), and dried under vacuum to yield 2.279 g (83%) of **1** as a green powder. Broadened NMR resonances are symptomatic of the dynamic solution behavior of **1** in polar solvents.[5] ^1H NMR (THF-d_8): 2.74 ppm (bs, 3H), 2.96 ppm (bs, 6H), 4.54 ppm (m, 8H), 4.68 - 5.07 ppm (m, 16H). $^{31}P\{^1H\}$ NMR (THF-d_8): 101 ppm (b, 1P), 126 - 135 ppm (m, 5P). Anal. Calc. for $C_{27}H_{33}N_3Cl_2F_{36}O_{12}P_6Rh_2$: C, 18.69; H, 1.91; N, 2.42. Found: C, 18.69; H, 1.68; N, 2.34. Crystals suitable for X-ray diffraction were grown from CH_2Cl_2/pentane solution as green shards.

2.7.6 Preparation of $Rh_2^{II,II}(tfepma)_3(H)_2Cl_2$ (2 - 4)

In a thick walled 200-mL glass bomb, 1.995 g (1.15 mmol) of **1** was dissolved in 15 mL THF. The bomb was attached to a high vacuum line, the solution was freeze pump thawed (three cycles), and 1 atm of H_2 was added. The solution was thawed and allowed to stir in the dark for one week during which time the solution had turned from green/brown to dark red. The solvent was removed in vacuo, and the resulting sticky solid was washed with pentane (5 × 5 mL) and finally CH_2Cl_2 (5 mL) to give a yellow solid. The solid was recrystallized twice from a minimum of hot CH_2Cl_2 to give 0.574 g (29%) of **2** as a yellow crystalline solid. NMR spectra of the crystalline material dissolved in THF-d_8 reveals multiple products with **2** as the ~ 95% constituent. ^1H NMR (THF-d_8) δ / ppm: –9.77 (m, 2H), 2.89 (t, 3.4 Hz, 6H), 3.06 (t, 6.1 Hz, 3H), 4.48 - 4.82 (m, 24 H). $^{31}P\{^1H\}$ NMR (THF-d_8) δ / ppm: 131.40 (bs, 2P), 136.77 (bd, 131.0 Hz, 4P). Anal. Calc. for $C_{27}H_{35}N_3Cl_2F_{36}O_{12}P_6Rh_2$: C, 18.64; H, 2.03; N, 2.41. Found: C, 18.63; H, 1.95; N, 2.56. Yellow block crystals suitable for X-ray diffraction were obtained from repeated recrystallizations of solid from hot CH_2Cl_2 solutions. Deuterated material (**2**-d_2) was synthesized by the addition of deuterium to 2.030 g of **1** in an analogous procedure and workup to give 0.732 g (35%) of **2**-d_2 after two recrystallizations from CH_2Cl_2. ^1H NMR (THF-d_8) δ / ppm: 2.89 (t, 3.4 Hz, 6H), 3.06 (t, 6.1 Hz, 3H), 4.48 - 4.82 (m, 24 H). ^2H NMR (THF) δ / ppm: –10.3 (m). $^{31}P\{^1H\}$

NMR (THF-d_8) δ / ppm: 134.20 (bs, 2P), 139.55 (bd, 134.3 Hz, 4P). Anal. Calc. for $C_{27}H_{33}D_2N_3Cl_2F_{36}O_{12}P_6Rh_2$: C, 18.61; H, 2.14; N, 2.41. Found: C, 18.60; H, 2.04; N, 2.36.

Undisturbed CH_3CN solutions of **2** promote the deposition of **3** as crystalline yellow blocks suitable for X-ray diffraction. The asymmetric unit contained half the molecule with the remaining portion generated by a crystallographic C_2 axis. Dissolution of these crystals in THF-d_8 revealed multiple products by ^{1}H NMR, the major product of which has N–Me resonances at 3.03 and 2.78 ppm integrating in a 2:1 ratio. Multiple overlapping hydride resonances precluded assignment. After standing for long periods (> 1 week), CH_2Cl_2/pentane solutions collected from the isolation of **2** afforded yellow/green blocks of **4** suitable for X-ray diffraction. Dissolution of the yellow green single crystals of **4** in THF-d_8 initially gives a light green solution that rapidly changes to yellow. Multiple components are observed in the ^{1}H NMR, with N–Me resonances at 2.78, 2.86, and 2.97 (a shoulder at 3.03 ppm accords with a resonance of **3**). Consistent with the dynamic behavior of **2**, solutions of the compound maintained in the dark show the growth of the N–Me resonances diagnostic of **3** and **4** at the expense of N–Me resonances of **2** at 2.89 and 3.06 ppm.

2.7.7 Preparation of $Rh_2^{I,I}(tfepm)_3Cl_2$ (5)

To a minimum amount of CH_2Cl_2, 731 mg (1.48 mmol) of $[Rh^I(COD)Cl]_2$ was added to afford an orange solution. 2.1 g (4.45 mmol, 3 equiv) of tfepm was then added dropwise, immediately effecting a color change to dark purple. The solution was stirred for 12 h after which a microcrystalline precipitate was allowed to settle. The purple supernatant was removed and the solid was washed repeatedly with pentane until the washings showed no discernable color. Residual solvent was removed in vacuo, giving 2.07 g (82%) of **5** as a purple solid. ^{1}H NMR (CD_2Cl_2) δ / ppm: 3.04 (q, 13.4 Hz, 2H), 3.32 (t, 12.2Hz, 2H), 3.51 (dt, 12.5 Hz, 9.8 Hz, 2H), 3.97 (q, 9.2 Hz, 2H), 4.2 - 4.7 (m, 22H). $^{31}P\{^1H\}$ NMR (CD_2Cl_2) δ / ppm: 158.03 (dm, 625.8 Hz, 2P), 165.64 (m, 2P), 171.28 (dm, 625.8 Hz, 2P). Anal. Calc. for $C_{27}H_{30}Cl_2F_{36}O_{12}P_6Rh_2$: C, 19.15; H, 1.79. Found: C, 19.10; H, 1.35. λ_{max}/nm (ε/$M^{-1}cm^{-1}$) in toluene: 293 (4800); 376 (2400); 507 (9300). Crystals suitable for X-ray diffraction were grown from CH_2Cl_2/pentane solution as dark pink blocks.

2.7.8 Preparation of $Ir_2^{I,I}(tfepm)_3Cl_2$ (6)

To a stirred suspension of $[Ir^{I}(COD)Cl]_2$ (141 mg, 0.210 mmol) in 10 mL of toluene 297 mg (3.0 equiv), tfepm was added dropwise immediately causing a color change from light orange to dark brown/red. The solution was allowed to stir for 3 days during which the solution color turned to dark purple. The solution was placed in the freezer (–40 °C) overnight, filtered, concentrated to a volume of 5 mL, and then recrystallized with pentane. The resulting solid was then washed with pentane (3 × 5 mL) giving 114 mg (29%) of **6** as a purple solid. ^{1}H NMR (toluene-d_8) δ / ppm: 2.77 (q, 14.5 Hz, 2H), 2.84 (t, 13.1 Hz, 2H), 3.09 (dt, 12.5 Hz, 11.9 Hz, 2H), 3.63 (quint, 9.2 Hz, 2H), 3.83 (m, 4H), 4.1- 4.7 (m, 18H). $^{31}P\{^{1}H\}$ NMR (toluene-d_8) δ / ppm: 116.61 (m, 2P), 142.29 (dm, 623.8 Hz, 2P), 155.15 (dm, 623.8 Hz, 2P). Anal. Calc. for $C_{27}H_{30}Cl_2F_{36}O_{12}P_6Ir_2$: C, 17.33; H, 1.61. Found: C, 17.61; H, 1.69. λ_{max}/nm (ε/$M^{-1}cm^{-1}$) in toluene: 313 (5800); 352 (3800); 571 (7100). Crystals suitable for X-ray diffraction were grown from slowly evaporated toluene solutions as purple blocks. The asymmetric unit contained two crystallographically and chemically distinct molecules (**6** and **7**) and five and a half toluene molecules. Two toluenes were disordered over two positions, and the half toluene was disordered over a crystallographic inversion center. Crystals of **6** and **7** isolated from each other could be obtained from slowly evaporating benzene solutions. **6** grew as purple blocks; the asymmetric unit contained half the molecule and two benzene molecules as solvents of crystallization **7** grew as yellow shards from the purple benzene solutions of **6**. The asymmetric unit contained two molecules of benzene as solvents of crystallization. Attempts to synthesize **7** directly have so far proven unsuccessful, obviating a full NMR characterization.

2.7.9 Preparation of $Rh_2^{0,II}(tfepm)_3Cl_2CN^tBu$ (8)

To a stirred solution of $Rh_2^{I,I}(tfepm)_3Cl_2$ (**5**) (500 mg, 0.295 mmol) in CH_2Cl_2, 25 mg (0.301 mmol, 1 equiv) of *tert*-butylisonitrile was added causing an immediate color change from purple to dark red. The reaction was allowed to stir for 3 h and then solvent was removed. The resulting orange solid was washed with pentane to yield 520 mg (99%) of **7**. ^{1}H NMR (CD_3CN) δ / ppm: 1.40 (s, 9H), 3.63 (bd, 11.6 Hz, 2H), 3.79 (dd, 7.6 Hz, 6.7 Hz, 2H), 4.27 - 4.67 (m, 20H), 4.88 (d, 14.0 Hz, 2H), 5.02 (m, 4H). $^{31}P\{^{1}H\}$ NMR (CD_3CN) δ / ppm: 157.68 (m, 1P), 159.55 (m, 2P), 168.82 (ov m, 3P). Anal. Calc. for $C_{32}H_{39}Cl_2F_{36}NO_{12}P_6Rh_2$: C, 21.64; H, 2.21; N, 0.79. Found: C, 21.62; H, 2.19; N, 0.73. λ_{max}/nm (ε/$M^{-1}cm^{-1}$) in Et_2O: 342 (11600); 389

(7000); 498 (2500). Crystals suitable for X-ray diffraction were grown from CH_2Cl_2/pentane solution as red blocks. The asymmetric unit contained two crystallographically distinct but chemically equivalent molecules and a molecule each of pentane and CH_2Cl_2 as solvents of crystallization.

2.7.10 Preparation of $Rh_2^{0,II}(dfpma)_3Cl_2CN^tBu$ (9)

To a stirred solution of $[Rh^I(COD)Cl]_2$ (272 mg, 0.551 mmol) in 10 mL of CH_2Cl_2, 46 mg (0.551 mmol, 1 equiv) of *tert*-butylisonitrile was added. Dropwise addition of 276 mg (1.655 mmol, 3 equiv) of dfpma dissolved in 2 mL of CH_2Cl_2 affected an immediate color change to dark red. The solution was allowed to stir for 3 h and the solvent stripped. The resulting solid was then suspended in Et_2O, filtered, washed with Et_2O (4 × 5 mL), and then washed off the filter with CH_2Cl_2. The solvent was stripped to give 167 mg (35 %) of **9** as an orange solid. ^1H NMR (CD_3CN) δ / ppm: 1.52 (s, 9H), 2.99 (bt, 3H), 3.06 (bs, 6H). Anal. Calc. for $C_8H_{18}Cl_2F_{12}N_4P_6Rh_2$: C, 11.16; H, 2.11; N, 6.51 Found: C, 11.40; H, 1.88; N, 6.35. Crystals suitable for X-ray diffraction were grown from CH_2Cl_2/pentane solution as orange blocks.

2.7.11 Preparation of $Rh_2^{0,II}(tfepma)_3Cl_2CN^tBu$ (10)

In a scintillation vial 265 mg of $Rh_2^{II,II}(tfepma)_3Cl_4$ (0.147 mmol, 1 equiv) was dissolved in 10 mL of THF and 13 mg of *tert*-butylisonitrile (0.161 mmol, 1.1 equiv) was added, and then the solution was frozen in a Coldwell. In a separate vial 56 mg of cobaltocene (Cp_2Co^{II}, Cp = $C_5H_5^-$) (0.296 mmol, 2 equiv) was dissolved in 5 mL of THF and frozen in a Coldwell. Upon thawing the cobaltocene solution was added to the $Rh_2^{II,II}(tfepma)_3Cl_4$ solution dropwise with stirring. A large amount of yellow precipitate immediately formed, and the solution was allowed to stir overnight. The THF was then stripped, the resulting sticky solid triturated once with Et_2O, and then dissolved in 10 mL of Et_2O and filtered. The Et_2O was stripped, and the resulting solid was washed with pentane (2 × 4 mL) before being redissolved in Et_2O and then placed in a freezer at –20 °C overnight to give 127 mg of $Rh_2^{0,II}(tfepma)_3Cl_2CN^tBu$ (**10**) as an red/orange solid (48%). ^1H NMR (CD_3CN) δ / ppm: 1.43 (s, 9H), 2.78 (dm, 8.1 Hz, 3H), 2.93 (bs, 6H), 4.46-4.58 (ovm, 24H). $^{31}P\{^1H\}$ NMR (CD_3CN) δ / ppm: 122.46 (m), 138.7 (m). Crystals suitable for X-ray diffraction were grown from Et_2O/pentane solutions as orange blocks.

2.8 Crystallographic Tables

Table 2.5. Crystallographic data and structural refinement parameters for $Rh_2^{0,II}(tfepma)_3Cl_2$ (**1**), *syn*-$Rh_2^{II,II}(tfepma)_3(H)_2Cl_2$ (**2**), and *anti*-$Rh_2^{II,II}(tfepma)_3(H)_2Cl_2$ (**3**).

	1•0.25 (CH_2Cl_2)	**2**	**3**•CH_3CN
Empirical formula	$C_{27}H_{33}N_3Cl_2F_{36}O_{12}P_6Rh_2$	$C_{27}H_{35}Cl_2F_{36}N_3O_{12}P_6Rh_2$	$C_{29}H_{38}Cl_2F_{36}N_4O_{12}P_6Rh_2$
Formula weight	1760.84	1740.12	1781.17
Temperature	–123(2)°C	–80(2)°C	–80(2)°C
Wavelength	0.71073 Å	0.71073 Å	0.71073 Å
Crystal system	Monoclinic	Monoclinic	Monoclinic
Space group	*C*2/*c*	$P2_1/n$	*C*2/*c*
Unit cell dimensions	a = 22.716(9) Å	a = 13.0479(11) Å	a = 22.496(4) Å
	b = 12.743(9) Å	b = 17.4813(14) Å	b = 13.547(2) Å
	c = 39.700(15) Å	c = 25.268(2) Å	c = 21.382(4) Å
	α = 90°	α = 90°	α = 90°
	β = 92.475(14)°	β = 100.247(2)°	β = 91.910(4)°
	γ = 90°	γ = 90°	γ = 90°
Volume	11482(10) Å^3	5671.6(8) Å^3	6513(2) Å^3
Z	8	4	4
Density (calc)	2.037 Mg/m^3	2.038 Mg/m^3	1.817 Mg/m^3
Absorption coefficient	1.029 mm^{-1}	1.018 mm^{-1}	0.889 mm^{-1}
F(000)	6890	3408	3496
Crystal size (mm)	0.11 × 0.10 × 0.08	0.19 × 0.18 × 0.15	0.27 × 0.18 × 0.15
Θ range for data collection	1.79 to 28.34°	1.64 to 20.92°	1.81 to 23.26°
Index Ranges	$-30 \le h \le 27$	$-13 \le h \le 12$	$-23 \le h \le 17$
	$-16 \le k \le 16$	$-17 \le k \le 13$	$-15 \le k \le 14$
	$-47 \le \ell \le 47$	$-25 \le \ell \le 20$	$-10 \le \ell \le 23$
Reflections collected	27530	20436	6690
Ind. reflections	12541	5994	4407
Absorption correction	Empirical SADABS	Empirical SADABS	Empirical SADABS
Refinement method	Full–matrix ls on F^2	Full–matrix ls on F^2	Full–matrix ls on F^2
Data	12542	5994	4407
Restraints	34	0	0
Parameters	786	792	432
Goodness-of-fit on F^2 [a]	1.042	1.139	1.033
Final *R* indices [I>2σ(*I*)][b]	R_1 = 0.0644	R_1 = 0.0712	R_1 = 0.0613
	wR_2 = 0.1620	wR_2 = 0.1718	wR_2 = 0.1397
R indices (all data)[b]	R_1 = 0.0780	R_1 = 0.0906	R_1 = 0.0896
	wR_2 = 0.1686	wR_2 = 0.1823	wR_2 =0.1589
largest diff. peak	1.769 e/Å^3	1.213 e/Å^3	0.643 e/Å^3
largest diff. hole	–0.948 e/Å^3	–0.807 e/Å^3	–0.718 e/Å^3

[a] GOF = $[\Sigma w(F_o^2 - F_c^2)^2/(n-p)]^{1/2}$ (n = number of data, p = number of parameters varied.
[b] $R_1 = \Sigma||F_o| - |F_c||/\Sigma|F_o|$; $wR_2 = [\Sigma w(F_o^2 - F_c^2)^2/\Sigma wF_o^4]^{1/2}$.

Table 2.6. Crystallographic data and structural refinement parameters for *cis*-$Rh_2^{II,II}(tfepma)_3(H)_2Cl_2$ (**4**), $Rh_2^{I,I}(tfepm)_3Cl_2$ (**5**), and the cocrystal of $Ir_2^{I,I}(tfepm)_3Cl_2$ (**6**) and $Ir_2^{I,I}(tfepm)_3(\mu\text{-Cl})Cl$ (**7**).

	4	**5**	**6 • 7**
Empirical formula	$C_{27}H_{35}Cl_2F_{36}N_3O_{12}P_6Rh_2$	$C_{27}H_{30}Cl_2F_{36}O_{12}P_6Rh_2$	$C_{46.25}H_{52}Cl_2F_{36}Ir_2O_{12}P_6$
Formula weight	1740.12	1693.05	2125.00
Temperature	−123(2)°C	−150(2)°C	−173(2)°C
Wavelength	0.71073 Å	0.71073 Å	0.71073 Å
Crystal system	Triclinic	Tetragonal	Triclinic
Space group	$P\bar{1}$	$I\bar{4}2d$	$P\bar{1}$
Unit cell dimensions	a = 11.5832(10) Å	a = 23.8123(8) Å	a = 12.2242(12) Å
	b = 12.5020(11) Å	b = 23.8123(8) Å	b = 21.880(2) Å
	c = 21.6206(19) Å	c = 20.0571(13) Å	c = 27.148(3) Å
	α = 98.106(2)°	α = 90°	α = 91.330(2)°
	β = 93.609(2)°	β = 90°	β = 102.312(2)°
	γ = 109.725(2)°	γ = 90°	γ = 90.810(2)°
Volume	2897.2(4) Å^3	11372.9(9) Å^3	7090.9(12) Å^3
Z	2	8	2
Density (calc)	1.995 Mg/m^3	1.978 Mg/m^3	1.991 Mg/m^3
Absorption coefficient	0.996 mm^{-1}	1.011 mm^{-1}	4.108 mm^{-1}
F(000)	1704	6608	4110
Crystal size (mm)	0.21 × 0.18 × 0.14	0.30 × 0.25 × 0.19	0.28 × 0.20 × 0.07
Θ range for data collection	0.96 to 23.29°	1.33 to 28.27°	0.77 to 24.77°
Index Ranges	$-12 \le h \le 12$	$-31 \le h \le 31$	$-14 \le h \le 14$
	$-12 \le k \le 13$	$-31 \le k \le 23$	$-25 \le k \le 25$
	$-22 \le \ell \le 24$	$-21 \le \ell \le 26$	$-31 \le \ell \le 23$
Reflections collected	13479	40549	39109
Ind. reflections	8314	7053	24076
Absorption correction	Empirical SADABS	Empirical SADABS	Empirical SADABS
Refinement method	Full–matrix ls on F^2	Full–matrix ls on F^2	Full–matrix ls on F^2
Data	8314	7053	24076
Restraints	17	0	24
Parameters	814	385	1820
Goodness-of-fit on F^2 [a]	1.068	1.058	1.048
Final R indices	R_1 = 0.0585	R_1 = 0.0274	R_1 = 0.0392
$[I>2\sigma(I)]$[b]	wR_2 = 0.1239	wR_2 = 0.0715	wR_2 = 0.0953
R indices (all data)[b]	R_1 = 0.0753	R_1 = 0.0288	R_1 = 0.0474
	wR_2 = 0.1313	wR_2 = 0.0726	wR_2 =0.1026
largest diff. peak	0.972 e/Å^3	0.548 e/Å^3	2.292 e/Å^3
largest diff. hole	−0.866 e/Å^3	−0.333 e/Å^3	−1.634 e/Å^3

[a] GOF = $[\Sigma w(F_o^2 - F_c^2)^2/(n-p)]^{1/2}$ (n = number of data, p = number of parameters varied.
[b] $R_1 = \Sigma||F_o| - |F_c||/\Sigma|F_o|$; $wR_2 = [\Sigma w(F_o^2 - F_c^2)^2/\Sigma wF_o^4]^{1/2}$.

Table 2.7. Crystallographic data and structural refinement parameters for $Ir_2^{I,I}(tfepm)_3Cl_2$ (**6**), $Ir_2^{I,I}(tfepm)_3(\mu\text{-}Cl)Cl$ (**7**) , and $Rh_2^{0,II}(tfepm)_3Cl_2CN^tBu$ (**8**).

	6	**7 • 2 (C_6H_6)**	**8**
Empirical formula	$C_{96}H_{102}Cl_4F_{72}Ir_4O_{24}P_{12}$	$C_{27}H_{30}Cl_2F_{36}O_{12}P_6Ir_2$	$C_{32}H_{39}Cl_3F_{36}NO_{12}P_6Rh_2$
Formula weight	4290.02	2027.85	1854.72
Temperature	−173(2)°C	−173(2)°C	−123(2)°C
Wavelength	0.71073 Å	0.71073 Å	0.71073 Å
Crystal system	Orthorhombic	Monoclinic	Triclinic
Space group	F*ddd*	*Cc*	Pī
Unit cell dimensions	a = 26.8372(18) Å	a = 24.408(2) Å	a = 16.226(2) Å
	b = 27.313(3) Å	b = 17.8402(16) Å	b = 19.218(3) Å
	c = 38.801(3) Å	c = 15.7183(14) Å	c = 24.2373(3) Å
	α = 90°	α = 90°	α = 110.279(3)°
	β = 90°	β = 110.416(2)°	β = 94.226°
	γ = 90°	γ = 90°	γ = 104.932°
Volume	28441(4) Å^3	6414.5(10) Å^3	6738.3(16) Å^3
Z	8	4	4
Density (calc)	2.004 Mg/m^3	2.100 Mg/m^3	1.828 Mg/m^3
Absorption coefficient	4.098 mm^{-1}	4.536 mm^{-1}	0.900 mm^{-1}
F(000)	16592	3896	3656
Crystal size (mm)	0.13 × 0.12 × 0.06	0.18 × 0.15 × 0.11	0.13 × 0.10 × 0.07
Θ range for data collection	1.19 to 28.33°	1.77 to 28.29°	0.91 to 23.26°
Index Ranges	$-34 \le h \le 35$	$-32 \le h \le 32$	$-17 \le h \le 16$
	$-36 \le k \le 35$	$-23 \le k \le 23$	$-18 \le k \le 21$
	$-51 \le \ell \le 27$	$-20 \le \ell \le 15$	$-25 \le \ell \le 26$
Reflections collected	50766	22862	37447
Ind. reflections	8866	11020	19061
Absorption correction	Empirical SADABS	Empirical SADABS	Empirical SADABS
Refinement method	Full–matrix ls on F^2	Full–matrix ls on F^2	Full–matrix ls on F^2
Data	8866	11020	19061
Restraints	0	18	32
Parameters	479	911	1693
Goodness-of-fit on F^2 [a]	1.057	1.045	1.041
Final R indices [I>2σ(I)][b]	R_1 = 0.0255	R_1 = 0.0277	R_1 = 0.0734
	wR_2 = 0.0523	wR_2 = 0.0634	wR_2 = 0.1954
R indices (all data)[b]	R_1 = 0.0314	R_1 = 0.0296	R_1 = 0.0931
	wR_2 = 0.0552	wR_2 = 0.0640	wR_2 =0.2118
largest diff. peak	1.215 e/Å^3	1.675 e/Å^3	2.060 e/Å^3
largest diff. hole	−0.759 e/Å^3	−1.041 e/Å^3	−1.363 e/Å^3

[a] GOF = $[\Sigma w(F_o^2 - F_c^2)^2/(n-p)]^{1/2}$ (n = number of data, p = number of parameters varied.
[b] $R_1 = \Sigma||F_o| - |F_c||/\Sigma|F_o|$; $wR_2 = [\Sigma w(F_o^2 - F_c^2)^2/\Sigma wF_o^4]^{1/2}$.

Table 2.8. Crystallographic data and structural refinement parameters for $Rh_2^{0,II}(dfpma)_3Cl_2CN^tBu$ (**9**) and $Rh_2^{0,II}(tfepma)_3Cl_2CN^tBu$ (**10**).

	9	**10**
Empirical formula	$C_8H_{18}Cl_2F_{12}N_4P_6Rh_2$	$C_{32}H_{42}F_{36}N_4O_{12}P_6Cl_2Rh_2$
Formula weight	860.80	1821.24
Temperature	−173(2)°C	−173(2)°C
Wavelength	0.71073 Å	0.71073 Å
Crystal system	Monoclinic	Monoclinic
Space group	$P2_1/n$	$P2_1/n$
Unit cell dimensions	a = 22.716(9) Å	a = 13.981(2) Å
	b = 12.743(9) Å	b = 19.509(3) Å
	c = 39.700(15) Å	c = 22.853(4) Å
	α = 90°	α = 90°
	β = 92.084(2)°	β = 91.919(4)°
	γ = 90°	γ = 90°
Volume	2581.6(6) Å^3	6229.5(19) Å^3
Z	4	4
Density (calc)	2.215 Mg/m^3	1.942 Mg/m^3
Absorption coefficient	1.952 mm^{-1}	0.932 mm^{-1}
F(000)	1664	3584
Crystal size (mm)	0.14 × 0.12 × 0.09	0.10 × 0.09 × 0.08
Θ range for data collection	5.02 to 28.33°	1.37 to 23.32°
Index Ranges	$-12 \le h \le 12$	$-14 \le h \le 15$
	$-12 \le k \le 12$	$-21 \le k \le 21$
	$-39 \le \ell \le 39$	$-23 \le \ell \le 25$
Reflections collected	24082	28797
Ind. reflections	6376	8932
Absorption correction	Empirical SADABS	Empirical SADABS
Refinement method	Full–matrix ls on F^2	Full–matrix ls on F^2
Data	6376	8932
Restraints	0	2
Parameters	313	837
Goodness-of-fit on F^2 [a]	1.148	1.039
Final R indices [I>2σ(I)][b]	R_1 = 0.0363	R_1 = 0.0542
	wR_2 = 0.0932	wR_2 = 0.1331
R indices (all data)[b]	R_1 = 0.0371	R_1 = 0.0768
	wR_2 = 0.0939	wR_2 = 0.1524
largest diff. peak	1.560 e/Å^3	1.028 e/Å^3
largest diff. hole	−1.640 e/Å^3	−0.969 e/Å^3

[a] GOF = $[\Sigma w(F_o^2 - F_c^2)^2/(n-p)]^{1/2}$ (n = number of data, p = number of parameters varied.
[b] $R_1 = \Sigma||F_o| - |F_c||/\Sigma|F_o|$; $wR_2 = [\Sigma w(F_o^2 - F_c^2)^2/\Sigma wF_o^4]^{1/2}$.

2.9 References

(1) Heyduk, A. F.; Nocera, D. G. *Science* **2001**, *293*, 1639-1641.

(2) Gray, T. G.; Nocera, D. G. *Chem. Commun.* **2005**, 1540-1542.

(3) Tolman, C. A. *Chem. Rev.* **1977**, *77*, 313-348.

(4) Heyduk, A. F.; Nocera, D. G. *Chem. Commun.* **1999**, 1519-1520.

(5) Heyduk A. F.; Nocera, D. G. *J. Am. Chem. Soc.* **2000**, *122*, 9415-9426.

(6) Gray, T. G.; Veige, A. S.; Nocera, D. G. *J. Am. Chem. Soc.* **2004**, *126*, 9760-9678.

(7) Veige, A. S.; Gray, T. G.; Nocera, D. G. *Inorg. Chem.* **2005**, *44*, 17-26.

(8) McKee, M. L.; Hill, W. E. *J. Chem. Phys. A* **2002**, *106*, 6201-6205.

(9) Barklay, J. V.; Ellis, M.; Higgins, S. J.; McCart, M. K. *Organometallics* **1998**, *17*, 1725-1731.

(10) Veige, A. S.; Nocera, D. G. *Chem. Commun.* **2004**, *17*, 1958-1959.

(11) Jenkins, J. A.; Ennett, J. P.; Cowie, M. *Organometallics* **1988**, *7*, 1845-1853.

(12) Cotton, F. A.; Eagle, C. T.; Price, A. C. *Inorg. Chem.* **1988**, *27*, 4362-4368.

(13) Cotton, F. A.; Dunbar, K. R.; Verbruggen, M. G. *J. Am. Chem. Soc.* **1987**, *109*, 5498-5506.

(14) Crabtree, R. H. *The Organometallic Chemistry of the Transition Metals*; Wiley: New York, 1994.

(15) Collman, J. P.; Hegedus, L. S.; Norton, J. R.; Finke, R. G. *Principles and Applications of Organotransition Metal Chemistry*; University Science Books, Sausalito CA, 1987.

(16) Labinger, J. A. Nucleophilic Reactivity of Transition Metal Hydrides. In *Transition* Metal Hydrides, Dedieu, A., Ed.;VCH publishers: New York, New York, 1992; pp 361-379.

(17) Geoffroy, G. L.; Wrighton, M. S. *Organometallic Photochemistry*; Academic Press: New York, 1979.

(18) Bitterwolf, T. E. *J. Organomet. Chem.* **2004**, *689*, 3939-3952.

(19) Vlček, A. Jr. *Coord. Chem. Rev.* **1998**, *177*, 219-256.

(20) See for example: Wink, D.; Ford, P. C. *J. Am. Chem. Soc.* **1986**, *108*, 4838-4842.

(21) Hill, R. H.; De Mayo, P.; Puddephatt, R. J. *Inorg. Chem.* **1982**, *21*, 3642-3646.

(22) Trinquier, G.; Hoffmann, R. *Organometallics* **1984**, *3*, 370-380.

(23) Norton, J. R. *Acc. Chem. Res.* **1979**, *12*, 139-145.

(24) Broussard, M. E.; Juma, B.; Train, S. G.; Peng, W.-J.; Laneman, S. A.; Stanley, G. G. *Science* **1993**, *260*, 1784-1788.

(25) Kristjánsdóttir, S. S.; Norton, J. A. In *Transition Metal Hydrides*; Dedieu, A., Ed.; VCH: New York, 1992, Ch. 9, pp 309-360.

(26) Broussard, M. E.; Juma, B.; Train, S. G.; Peng, W.-J.; Laneman, S. A.; Stanley, G. G. *Science* **1993**, *260*, 1784-1788.

(27) Rice, S. F.; Miskowski, V. M.; Gray, H. B. *Inorg. Chem.* **1988**, *27*, 4704-4708.

(28) Mann, K. R.; Gordon, J. G. II, Gray, H. B. *J. Am. Chem. Soc.* **1975**, *97*, 3553-3555.

(29) Rice, S. F.; Gray, H. B. *J. Am. Chem. Soc.* **1981**, *103*, 1593-1595.

(30) Fordyce, W. A.; Brummer, J. G.; Crosby, G. A. *J. Am. Chem. Soc.* **1981**, *103*, 7061-7064.

(31) Balch, A. L. *J. Am. Chem. Soc.* **1976**, *98*, 8049-8054.

(32) Balch A. L.; Tulyathan, B. *Inorg. Chem.* **1977**, *16*, 2840-2845.

(33) Kadis, J.; Shin, Y. G.; Dulebohn, J. I.; Ward, D. L.; Nocera, D. G. *Inorg. Chem.* **1996**, *35*, 811-817.

(34) Heyduk, A. F.; Macintosh, A. M.; Nocera, D. G. *J. Am. Chem. Soc.* **1999**, *121*, 5023-5032.

(35) Odom, A. L.; Heyduk, A. F.; Nocera, D. G. *Inorg. Chim. Acta* **2000**, *297*, 330-337.

(36) Lewis, N. S.; Mann, K. R.; Gordon, J. G. II; Gray, H. B. *J. Am. Chem. Soc.* **1976**, *98*, 7461-7643.

(37) Mann, K. R.; Lewis, N. S.; Miskowski, V. M.; Erwin, D. K.; Hammond, G. S.; Gray, H. B. *J. Am. Chem. Soc.* **1977**, *99*, 5525-5526.

(38) Mann, K. R.; Bell, R. A.; Gray, H. B. *Inorg. Chem.* **1979**, *18*, 2671-2673.

(39) Miskowski, V. M.; Sigal, I. S.; Mann, K. R.; Gray, H. B.; Milder, S. J.; Hammond, G. S.; Ryason, P. R. *J. Am. Chem. Soc.* **1979**, *101*, 4383-4385.

(40) Sigal, I. S.; Mann, K. R.; Gray, H. B. *J. Am. Chem. Soc.* **1980**, *102*, 7252-7256.

(41) Dulebohn, J. I.; Ward, D. L.; Nocera, D. G. *J. Am. Chem. Soc.* **1990**, *112*, 2969-2977.

(42) Wick, D. D.; Reynolds, K. A.; Jones, W. D. *J. Am. Chem. Soc.* **1999**, *121*, 3974-3983.

(43) Jones, W. D. *Acc. Chem. Res.* **2003**, *36*, 140-146.

(44) Balch A. L.; Tulyathan, B. *Inorg. Chem.* **1977**, *16*, 2840-2845

(45) Mague, J. T.; Mitchener, J. P. *Inorg. Chem.* **1969**, *8*, 119-125.

(46) Sanger, A. R. *J. Chem. Soc., Chem. Commun.* **1975**, 893-894.

(47) Kubiak, C. P.; Eisenberg, R. *J. Am. Chem. Soc.* **1977**, *99*, 6129-6131.

(48) Cowie, M.; Mague, J. T.; Sanger, R. A. *J. Am. Chem. Soc.* **1978**, *100*, 3628-3629.

(49) Puddephatt, R. *J. Chem. Soc. Rev.* **1983**, *12*, 99-127.

(50) Armarego, W. L. F.; Perrin, D. D. *Purification of Laboratory Chemicals*, 4th ed.; Butterworth-Heinmann: Oxford, 1996.

(51) Ganesan, M; Krishnamurthy, S. S.; Nethaji, M. *J. Organomet. Chem.* **1998**, *570*, 247-254.

(52) Balakrishna, M. S.; Prakasha, T. K.; Krishnamurthy, S. S.; Siriwardane, U; Hosmane, N. S. *J. Organomet. Chem.* **1990**, *390*, 203-216.

(53) Hietkamp, S.; Sommer, H.; Stelzer, O. *Inorg. Synth.* **1989**, *27*, 120-121.

(54) Bitterwolf, T. E.; Raaghuveer, K. S. *Inorg. Chim. Acta.* **1990**, *172*, 59-64.

(55) Nixon, J. F. *J. Chem. Soc. A* **1968**, 2689-2692.

(56) Heyduk, A. F. Ph. D. Thesis. Massachusetts Institute of Technology, 2001.

(57) Frisch, M. J.; Trucks, G. W.; Schlegel, H. B.; Scuseria, G. E.; Robb, M. A.; Cheeseman, J. R.; Zakrzewski, V. G.; Montgomery, J. A., Jr.; Stratmann, R. E.; Burant, J. C.; Dapprich, S.; Millam, J. M.; Daniels, A. D.; Kudin, K. N.; Strain, M. C.; Farkas, O.; Tomasi, J.; Barone, V.; Cossi, M.; Cammi, R.; Mennucci, B.; Pomelli, C.; Adamo, C.; Clifford, S.; Ochterski, J.; Petersson, G. A.; Ayala, P. Y.; Cui, Q.; Morokuma, K.; Malick, D. K.; Rabuck, A. D.; Raghavachari, K.; Foresman, J. B.; Cioslowski, J.; Ortiz, J. V.; Stefanov, B. B.; Liu, G.; Liashenko, A.; Piskorz, P.; Komaromi, I.; Gomperts, R.; Martin, R. L.; Fox, D. J.; Keith, T.; Al-Laham, M. A.; Peng, C. Y.; Nanayakkara, A.; Gonzalez, C.; Challacombe, M.; Gill, P. M. W.; Johnson, B. G.; Chen, W.; Wong, M. W.; Andres, J. L.; Head-Gordon, M.; Replogle, E. S.; Pople, J. A.; Gaussian 98, Revision A.9: Gaussian, Inc.: Pittsburg, PA, 1998.

(58) Becke, A. D. *Phys. Rev. A* **1988**, *38*, 3098- 3100.

(59) Perdew, J. P. *Phys. Rev. B* **1986**, *33*, 8822-8824.

(60) Hay, P. J.; Wadt, W. R. *J. Chem. Phys.* **1985**, *82*, 270-283; 284-298; 299-310.

(61) Couty, M.; Hall, M. B. *J. Comput. Chem.* **1996**, *11*, 1359-1370.

(62) Hariharan, P. C.; Pople, J. A. *Theor. Chim. Acta* **1973**, *28*, 213-222.

(63) Francl, M. M.; Pietro, W. J.; Hehre, W. J.; Binkley, J. S.; Gordon, M. S.; DeFrees, D. J.; Pople, J. A. *J. Chem. Phys.* **1982**, *77*, 3654-3655.

Chapter 3:

Rhodium Gold Heterobimetallics

Portions of this work have appeared previously:

Rosenthal, J.; Bachman, J.; Dempsey, J. L.; Esswein, A. J.; Gray, T. G.; Hodgkiss, J. M.; Manke, D. R.; Luckett, T. D.; Pistorio, B. J.; Veige, A. S.; Nocera, D. G. *Coord. Chem. Rev.* **2005**, *249*, 1316-1326.

Dempsey, J. L.; Esswein, A. J.; Manke, D. R.; Rosenthal, J.; Soper, J. D.; Nocera, D. G. *Inorg. Chem.* **2005**, *44*, 6879-6892.

Esswein, A. J.; Dempsey J. L.; Nocera, D. G. *Inorg. Chem.* **2007**, *46*, 2362-2364.

3.1 *Introduction*

The photocatalytic HX reduction by dirhodium dfpma complexes described in the Chapters 1 and 2 represents an exceptionally rare example of catalytic hydrogen generation from a thermodynamically challenging substrate. Mineral acid reduction schemes are generally limited to stoichiometric conversions as catalysts for proton reduction typically cannot regenerate their reduced forms to close the catalytic cycle (*vide supra*). Or, equivalently stated for the specific case of HX (X = Cl^-, Br^-) substrates, the metal complexes cannot carry out the oxidation of the X^- conjugate base to X_2 and generally are deactivated by the formation of strong metal halogen bonds in their oxidized forms. Despite these challenges some progress in this field has been made, and in the dirhodium dfpma example discussed previously metal halogen bonds could be activated and cleaved by populating a $d\sigma^*$ excited state coupled with the assistance of a halogen radical trap. While the incorporation of trapping reagents introduces thermodynamic driving forces that likely preclude net solar energy storage, the complexes are remarkable for their ability to photoactivate strong Rh^{II}–X bonds to regenerate the reducing $Rh_2^{0,0}$ species for reentry into the catalytic cycle. The M–X bond photoactivation reaction however is hampered by low photochemical quantum yields, where for example the conversion of $Rh_2^{0,II}(dfpma)_3Cl_2PPh_3$ to $Rh_2^{0,0}(dfpma)_3(\eta^1\text{-dfpma})_2$ proceeds with a measured quantum yield of 0.6%. This conversion is reasoned to be the rate determining factor for the proton reduction photocycle, evidenced by nearly identical quantum yields for the isolated $Rh_2^{0,II}X_2$ to $Rh_2^{0,0}$ step (0.6%) to the overall cycle (~1%). It follows that any yield improvements for the Rh^{II}–X bond photoactivation step could potentially translate directly into improvements in the overall HX reduction efficiency.

Intuitive reactivity trends dictate that reducing metal centers react by oxidative addition whereas electron poor metal complexes favor reductive elimination.[1,2] While well established for mononuclear centers, the same arguments should hold for bimetallic constructs, wherein the oxidative addition and reductive elimination reactions need not occur at a single metal center, Scheme 3.1. Following this logic, electron poor bimetallic complexes were targeted, with the goal of facilitating the recovery of reduced catalysts by halogen elimination. An initial foray employed dianionic amido-borane Donor-Acceptor-Donor (D–A–D) ligands as bridging ligands for early transition metals in a strategy diametrically opposed to the A–D–A approach that supported two-electron mixed valance dimers of group 9 metals. In this way two-electron mixed valence complexes in high oxidation states might be stabilized and engender the multielectron

Scheme 3.1.

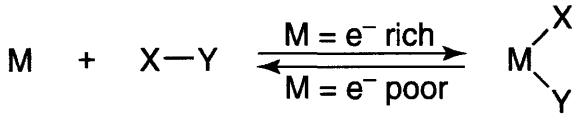

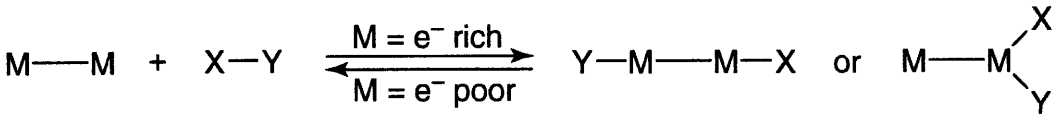

oxidative chemistry required for facile M–X bond activations. Although dimers of Mo^{III} and W^{III} were synthetically accessible,[3] the stability of the M≡M interaction effectively buried the metal centered orbitals, directing the redox chemistry of the bimetallic core to simple oxidations of the anionic D–A–D ligands. Alternatively, electronegative late transition metals, such as gold, can be incorporated into a bimetallic construct to achieve a similar effect. The high d electron counts of late metals precludes multiple bonding interactions between the constituent metals, potentially avoiding the pitfalls of the D–A–D systems, while also yielding electronic structures that allow for the photochemical population of dσ* excited states that proved critical to the success of the dirhodium dfpma systems.

Gold is an attractive target for such studies as homobimetallic gold complexes have a shown the ability to manage the coordination chemistry of halogens. In particular, when bridged by anionic ylide[4–19] or methylenethiophosphinate[20,21] ligands, Au_2 cores display a remarkably coordinative malleability and can be synthesized in $Au_2^{I,I}$, $Au_2^{I,III}$, $Au_2^{II,II}$, and $Au_2^{III,III}$ oxidation states. The accessibility of metal-metal bonded $Au_2^{II,II}$ d^9–d^9 cores with a vacant dσ* LUMO, suggested that this excited state could be exploited for facile photochemical M–X bond activations. But while the coordination chemistry and spectroscopy of Au_2 cores has been reasonably well studied, the photochemistry has largely been ignored,[22] excepting anecdotal notes of decomposition upon exposure to light.[18] While gold has unique characteristics for halogen coordination chemistry, rhodium centers are well suited for managing the coordination chemistry of hydrides and hydrogen. Thus a heterobimetallic construct of rhodium and gold might achieve facile HX photoreduction catalysis by initiating proton reduction to hydrogen at the comparatively reducing rhodium center, and halogen oxidation at the oxidizing gold center. These considerations led to the examination of heterobimetallic $Rh^I\cdots Au^I$ $d^8\cdots d^{10}$ systems for the purposes of enhancing the photochemical quantum yields for HX photoreduction. This

chapter outlines studies aimed at elucidating the suitability of heterobimetallic RhAu dimers for HX splitting photocatalysis, beginning with an assessment of the consequences of internuclear $Rh^{I}\cdots Au^{I}$ separation on the electronic structure of the bimetallic core, followed by a description of the synthesis of a d^7–d^9 Rh^{II}–Au^{II} binuclear core by two-electron oxidation of the parent $d^8\cdots d^{10}$ complex, and finishes with an exploration of the coordination chemistry of ambidentate PS ligands in order to develop synthetic methodologies for the targeted formation of RhAu heterodimers.

3.2 *Rhodium Gold Bisphosphine Complexes*

Numerous $d^8\cdots d^{10}$ heterobimetallics have been prepared containing d^8 metals Rh^{I}, Ir^{I}, Pd^{II}, Pt^{II} and the d^{10} coinage metals Cu^{I}, Ag^{I}, and Au^{I}.[23–37] These highly colored and intensely emissive complexes are stabilized by bidentate phosphine ligands such as dppm (bis[diphenylphosphino]methane, $CH_2[P(C_6H_5)_2]_2$) and neutral or anionic π-acceptor ligands, commonly ^{t}BuNC or CN^{-}. The complexes typically attain pseudo C_{2v} geometries with square planar d^8 and linear d^{10} metal centers, Figure 3.1, left, giving a simplified electronic structure shown in Figure 3.1, right.

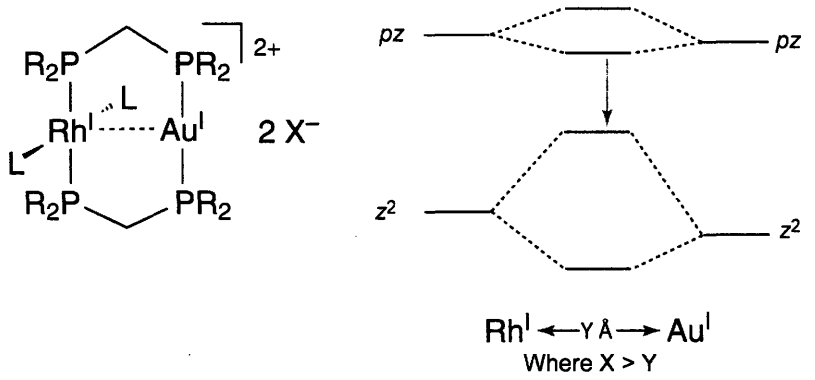

Figure 3.1. General molecular (left) and simplified frontier electronic (right) structures for $d^8\cdots d^{10}$ $Rh^{I}Au^{I}$ heterobimetallic complexes.

An orbitally allowed ndσ*→(n+1)pσ electronic transition leads to a visible absorption band that dominates the UV-vis absorption spectrum. Efficient intersystem crossing of the initially formed ^{1}(dσ*pσ) excited state to the ^{3}(dσ*pσ) emitting state leads to bright phosphorescence akin to the related and more extensively studied $d^8\cdots d^8$ and $d^{10}\cdots d^{10}$ homobimetallic systems.[38,39] The factors that govern the energetics of the absorption and

emissive properties of these heterobimetallics systems are of interest for their use as potential photocatalysts.

Initial studies were undertaken to probe the effects of the ground state structure on the absorptive and emissive properties of the RhAu heterobimetallic core. The frontier molecular orbital picture of Figure 3.1 and the corresponding studies of homobimetallic rhodium and iridium tfepm complexes of the previous chapter suggest that the $d\sigma^* \rightarrow p\sigma$ absorption energy should strongly depend on the $Rh^I \cdots Au^I$ internuclear distance. In particular, a short RhAu distance should result in increased overlap between the d_{z^2} orbitals and therefore an increased energetic separation between the d_{z^2} bonding and antibonding combinations. A similar effect is predicted for the p_z manifold, resulting in a decreased HOMO-LUMO gap. To experimentally probe this contention, the synthesis and crystallographic characterization of a series of Rh^IAu^I heterobimetallic dimers was conducted and the HOMO-LUMO energies probed by emission spectroscopy.

3.2.1 Synthesis and X-ray Crystallography

Heterobimetallic $d^8 \cdots d^{10}$ Rh^IAu^I cores have mostly been studied using the bidentate phosphine dppm, with the first synthesis of $Rh^IAu^I(dppm)_2(CN^tBu)_2Cl_2$ (**1**) by Shaw in 1983.[23] The synthetic procedure involves the sequential addition of dppm, ^{t}BuNC and finally an Au^I source (Au^ICIL, where L = tetrahydrothiophene (tht), dimethylsulfide (DMS), PEt_3, or PPh_3) to a stirred solution of $[Rh^I(COD)Cl]_2$ in CH_2Cl_2, Scheme 3.2.

Scheme 3.2.

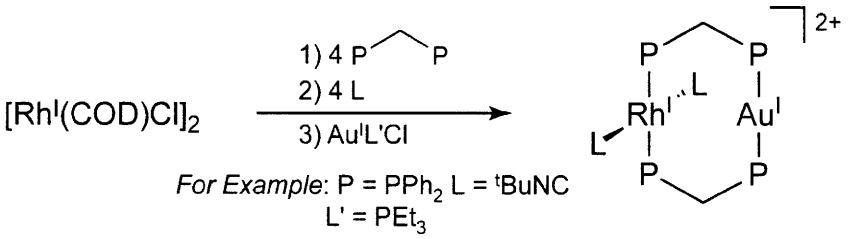

Despite considerable physical scrutiny of the excited state dynamics,[40,41] the dppm bridged dimer, **1**, was not crystallographically characterized until recently.[42] Crystals suitable for X-ray diffraction can readily be grown from CH_2Cl_2/Et_2O vapor diffusions and give the structure shown in Figure 3.2. The observed square planar rhodium and linear gold geometries are consistent with those expected for metals with d^8 and d^{10} electron counts. The metal phosphine

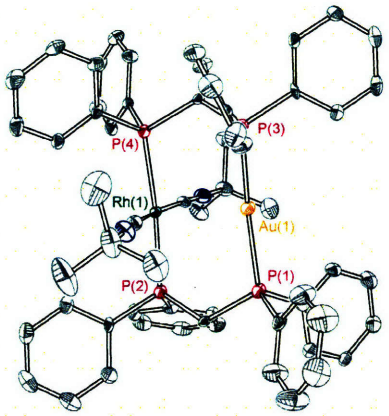

Figure 3.2 X-ray structure of $Rh^{I}Au^{I}(dppm)_2(CN^{t}Bu)_2Cl_2$ (**1**) with hydrogen atoms, non-coordinating counterions and solvents of crystallization omitted for clarity. Thermal ellipsoids are drawn at the 50% probability level.

and isonitrile distances are normal and the Cl^- counterions show no interaction with either the Rh^I or Au^I metal centers. In keeping with the electronic structure shown in Figure 3.1, a long internuclear distance of 2.9214(9) Å is observed in the solid sate, indicative of a formal bond order of zero between the d^8 and d^{10} metal centers. Two multiplets at 16.80 and 27.83 ppm are observed in the $^{31}P\{^1H\}$ NMR spectrum. A $^2J_{Rh-P}$ coupling of 118.6 Hz pins the assignment of the multiplet at 16.80 ppm as the phosphorus bound to rhodium. In the ^1H NMR the equivalent ^{t}BuNC proton resonances appear as a singlet at 0.693 ppm, the bridgehead methylene proton resonances appear at 4.38 ppm, and the phenyl resonances as a complex series of overlapping multiplets in the typical aryl region.

Although the dppm ligated compound **1** is readily prepared by the methods of Scheme 3.2, the only derivatives reported in the literature are the ClO_4^- [29] and PF_6^- [40,41] anion exchange products neither of which have been crystallographically characterized. Attempts to extend the stepwise synthetic route to other bisphosphine and diphosphazane ligands such as dfpma (bis(difluorophosphino)methylamine), dppma (bis[diphenylphosphino]methylamine, dmpm (bis[dimethylphosphino]methane), and dfppm (bis[bis(pentafluorophenyl)phosphino]methane) all fail, giving intractable product mixtures instead of smooth conversion to the desired RhAu heterobimetallic products. The reason for this is thought to stem from the inability of the aforementioned ligands to stabilize a square planar Rh^I bischelate complex. As shown in Scheme 3.2, the synthesis of **1** proceeds in a stepwise fashion, initiated by the addition of four equivalents of dppm to a solution of $[Rh^I(COD)Cl]_2$. Halting the reaction progress at this point evidences complete dissociation of COD and only one set of dppm methylene resonances at 4.58 ppm in

the ^{1}H NMR, while a sharp doublet at –16.30 ppm ($^{1}J_{Rh-P}$ = 115.9 Hz) ppm is the only observable resonance in the $^{31}P\{^{1}H\}$ NMR. X-ray structural analysis unambiguously establishes the product as $Rh^{I}(dppm)_2Cl$ (**2**). Interestingly the complex crystallizes in both four and five coordinate forms, Figure 3.4 right and left respectively. In the five coordinate formulation, the long 2.6453(12) Å Rh(1)···Cl(1) contact engenders a slight pyramidalization of the Rh coordination sphere with the Rh(1) center puckered ~0.258 Å out of the plane defined by the phosphorus atoms. All other bond lengths and angles are unremarkable. The sharp $^{31}P\{^{1}H\}$ NMR resonances observed in room temperature solution studies suggest that the four and five coordinate isomerization is purely a crystal packing phenomenon.

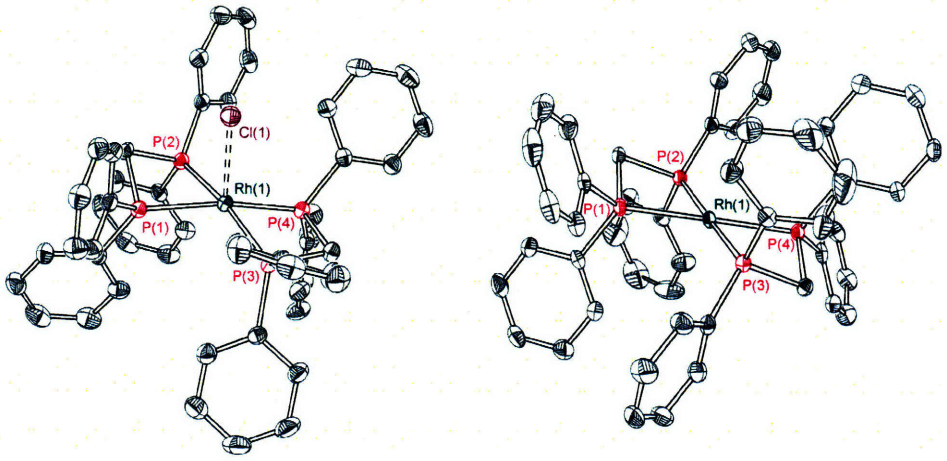

Figure 3.3. X-ray structures of $Rh^{I}(dppm)_2Cl$ in both four (**2**, right) and five (**2′**, left) coordinate forms. Hydrogen atoms, non-coordinating counterions, and solvents of crystallization are omitted for clarity. Thermal ellipsoids are drawn at the 50% probability level.

Addition of ^{t}BuNC to CH_2Cl_2 solutions of **2** immediately followed by $Au^{I}ClL$ (L = tht, DMS, PEt_3) in CH_2Cl_2 affords complex **1**, suggesting the necessity of bischelate intermediates for the directed synthesis of RhAu heterodimers. In keeping with this hypothesis, phosphines that fail to give RhAu heterodimers by the synthetic route in Scheme 3.2 such as dfpma, dppma, dmpm, or dfppm also fail to give access to bischelate Rh^{I} monomers analogous to complex **2**. Synthetic and computational studies using PNP derived bisphosphines have shown an increased propensity for chelation when the phosphorus donors are substituted with sterically demanding groups.[43,44] While this argument aids in the explanation of failed syntheses using dfpma and dmpm, the reasons why dppma and dfppm ligands do not afford monomeric bischelate materials are unclear. Nevertheless, treatment of $[Rh^{I}(COD)Cl]_2$ with four equivalents of dcpm

(bis[dicyclohexylphosphino]methane, $CH_2[P(C_6H_{11})_2]_2$) or tfepma readily affords bischelate Rh^I monomers. The $Rh^I(dcpm)_2Cl$ (**3**) complex was identified by a single pseudoquintet methylene resonance at 2.87 ppm in the ^1H NMR and a single sharp doublet at –11.93 ppm ($^1J_{Rh-P}$ = 111.1 Hz) in the $^{31}P\{^1H\}$ NMR. The electron withdrawing tfepma ligand gives $Rh^I(tfepma)_2Cl$ (**4**) with an N–Me resonance at 2.57 ppm in the ^1H NMR, and a doublet ^{31}P resonance at 109.8 ppm ($^1J_{Rh-P}$ = 181.6 Hz) that is shifted downfield significantly, compared to the dppm and dcpm congeners.

In accordance with Scheme 3.2 a series of PCP bridged Rh^IAu^I dimers can be synthesized from the bischelate complexes **2** and **3** by the sequential addition of donor ligands such as *tert*-butylisonitrile or 2,6-dimethylphenylisonitrile (CNdmp), followed by an appropriate Au^I source such as Au^IPEt_3Cl or $Au^I(tht)Cl$. Anion exchange from the native chloride salts can be achieved by metathesis with $LiClO_4$ or $LiPF_6$, thus providing a method for the synthesis of: $Rh^IAu^I(dppm)_2(CN^tBu)_2(ClO_4)_2$ (**5**), $Rh^IAu^I(dppm)_2(CN^tBu)_2(PF_6)_2$ (**6**), $Rh^IAu^I(dppm)_2(CNdmp)_2Cl_2$ (**7**), $Rh^IAu^I(dppm)_2(CNdmp)_2(ClO_4)_2$ (**8**), $Rh^IAu^I(dcpm)_2(CN^tBu)_2Cl_2$ (**9**), and $Rh^IAu^I(dcpm)_2(CN^tBu)_2(ClO_4)_2$ (**10**). The ^1H and $^{31}P\{^1H\}$ NMR characteristics of complexes **5** - **10** are similar to those of **1**. Crystals suitable for X-ray diffraction could be grown for complexes **5**, **7**, **8**, and **10** by the diffusion of Et_2O or pentane into CH_2Cl_2 or CH_3CN solutions of the RhAu complex. The results of this crystallographic survey are displayed in the top portion of Figure 3.4, wherein the general Rh^I and Au^I ligand topologies are conserved across the series. Relevant bond lengths and angles for complexes **1**, **5**, **7**, **8**, and **10** are summarized in Table 3.1. Expanded views of the RhAu core highlighting the $Rh^I\cdots Au^I$ separation are shown in the bottom section of Figure 3.4.

Table 3.1. Selected Bond Lengths (Å) and Angles (°) for **1**, **5**, **7**, **8**, and **10**.

	Bond Lengths (Å)				
	1	**5**	**7**[a]	**8**	**10**
Au(1)–Rh(1)	2.9214(9)	2.8930(4)	2.8761(5)	2.8807(7)	2.8985(4)
Au(1)–P(1)	2.314(3)	2.3010(8)	2.3211(10)	2.306(2)	2.3077(14)
Au(1)–P(2)	2.316(3)	2.3051(9)	–	2.313(2)	2.3114(13)
Rh(1)–P(3)	2.314(3)	2.3253(8)	2.3020(11)	2.311(2)	2.3337(14)
Rh(1)–P(4)	2.323(3)	2.3189(9)	–	2.322(2)	2.3263(14)
	Bond Angles (°)				
	1	**5**	**7**[a]	**8**	**10**
P(1)–Au(1)–P(2)	173.01(10)	170.54(3)	175.36(5)	171.49(7)	172.41(5)
P(3)–Rh(1)–P(4)	174.99(10)	178.25(3)	172.61(5)	177.82(7)	176.86(5)
P(3)–Rh(1)–C_{cis}	90.7(3)	93.70(10)	88.54(12)	89.1(2)	87.46(14)
	Dihedral Angles (°)				
	1	**5**	**7**[a]	**8**	**10**
P(1)–Au(1)–Rh(1)–P(3)	–1.0	4.92(3)	26.4	10.13(7)	–0.69(5)
P(2)–Au(1)–Rh(1)–P(4)	2.2	4.61(3)	26.5	12.27(7)	–1.46(5)

[a] Symmetry equivalent metrics only reported once; P(2) = P(1A), P(3) = P(2), P(4) = P(2A).

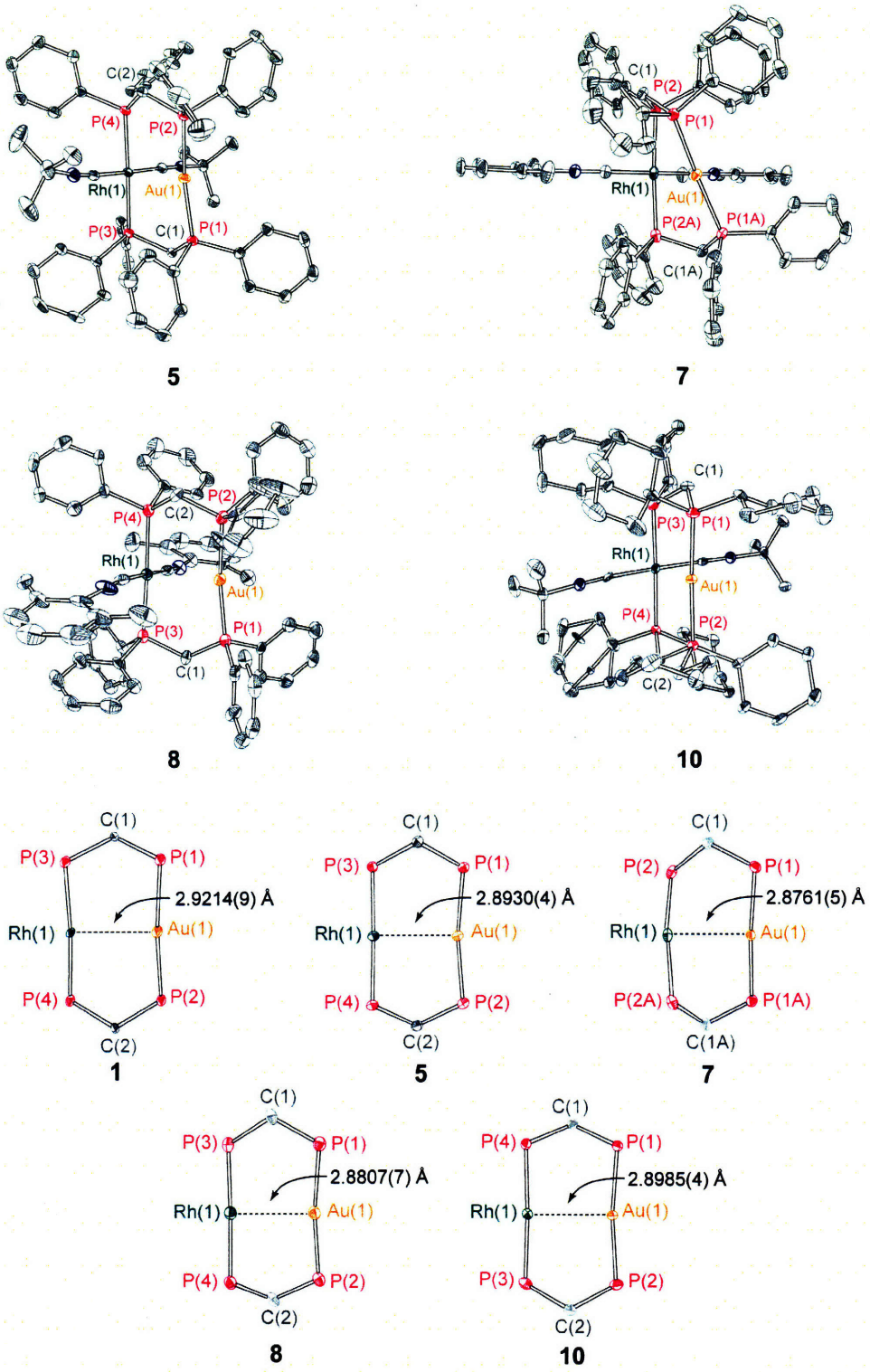

Figure 3.4. Top: X-ray structures of $Rh^{I}Au^{I}(dppm)_2(CN^{t}Bu)_2(ClO_4)_2$ (**5**), $Rh^{I}Au^{I}(dppm)_2(CNdmp)_2Cl_2$ (**7**), $Rh^{I}Au^{I}(dppm)_2(CNdmp)_2(ClO_4)_2$ (**8**), and $Rh^{I}Au^{I}(dcpm)_2(CN^{t}Bu)_2(ClO_4)_2$ (**10**) with hydrogen atoms, solvents of crystallization and non-coordinating counterions omitted for clarity. Bottom: Expanded views of the binuclear core of **1**, **5**, **7**, **8**, and **10** highlighting the Rh···Au internuclear distance. All thermal ellipsoids are drawn at the 50% probability level.

The $Rh^{I}Au^{I}$ contact distances for the crystallographically characterized complexes range over ~ 0.045 Å, with the shortest contact of 2.8761(5) Å observed for **7** and the longest of 2.9214(9) Å for **1**. Interestingly the long RhAu distance of **1** is accompanied by a nearly eclipsed disposition of the PCP bridging ligands as measured by the small P(1)–Au(1)–Rh(1)–P(3) dihedral angle of –1.0°, correspondingly the shortest RhAu contact in **7** evidences the largest dihedral angle of 26.4°. The RhAu distance also seems to be dependent on the crystal packing forces as RhAu distance decreases by 0.0284 Å upon substitution of the outer sphere chloride anions of **1** with perchlorates of complex **5**. This correlation does not hold for the CNdmp derivatives, **7** and **8**, as the chloride complex has a slightly shorter RhAu contact, Table 3.1. On the basis of the crystallographic survey no predictive trend emerges for the determination of internuclear distance. Also the large deviation upon substitution of the outer sphere Cl^- counterions of **1** with the non-interacting ClO_4^- of **5** suggest that these metrics might be unique to the crystalline lattice, and cast doubt on their retention in the solid state or solution.

3.2.2 Calculations and Emission Spectroscopy

For the purposes of orbital visualization non-local density functional theory calculations were carried out using the coordinates obtained from the crystal structure of complex **1**. To facilitate convergence the phenyl and *tert*-butyl groups of the dppm and *tert*-butylisonitrile ligands were replaced with protons. Significant progress has been made for the elucidation of the effects of relativity on the electronic structure of gold complexes.[4546474849] However, these effects are beyond the scope of the considerations presented herein. Population analysis gives a HOMO that is calculated to be a Rh···Au σ* interaction involving primarily metal d orbitals (94.4%), with 73.5% of the orbital amplitude on rhodium and 12.6% on gold Figure 3.5. The rhodium

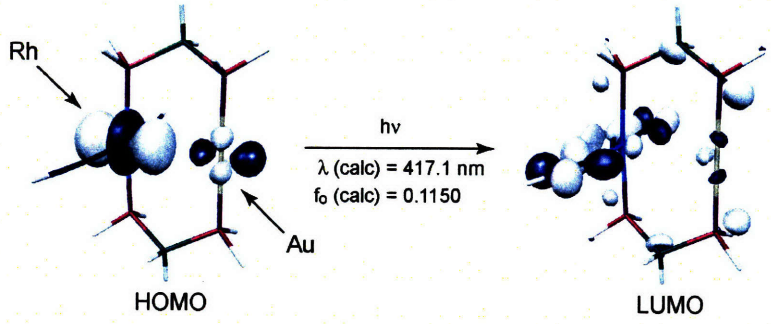

Figure 3.5. Calculated HOMO (left) and LUMO (left) for the model complex $Rh^{I}Au^{I}[CH_2(PH_2)_2]_2(CNH)_2^{2+}$ at the B3LYP level. Transition energies and oscillator strengths were calculated by TDDFT.

contribution is mostly d_{z^2} (79.1%) in nature, while the gold portion is calculated to be of mixed parentage containing 15.6% p_z character in addition to 78.4% d character (79.1% of which stems from d_{z^2} orbital contributions) with the balance composed of s orbital character. The calculated LUMO is more convoluted as significant ligand participation is observed, including CN π^* interactions of the CNH groups and phosphine Au σ^* interactions. Nevertheless 17.8 % and 12.7% of the total LUMO orbital amplitude is localized on the rhodium and gold centers respectively. Critically the LUMO contains an in phase σ bonding combination between the metal centers which is 95.7% p_z on rhodium and a mixture of ~50% s, ~36% p and ~14% d on gold. These calculations confirm that the simplified MO approach represented in Figure 3.1 sufficiently models the HOMO as a $d\sigma^*$ interaction of primarily $d_{z^2}d_{z^2}$ parentage. The LUMO, simplistically predicted to be a p_zp_z σ bonding interaction, is complicated by orbital amplitude from ligand derived orbitals but contains a significant RhAu σ bonding participation with the gold portion partially derived from a p_z atomic orbital as has been observed with other $d^8\cdots d^{10}$ complexes.[28] Time dependent calculations initiated on the converged geometry and implicate an allowed singlet electronic transition between the HOMO and LUMO at 417.1 nm (2.9725 eV) with an oscillator strength of 0.1150. Simple symmetry considerations in the C_{2v} symmetry of the molecular core corroborate this contention, as a transition between the a_1 $d_{z^2}d_{z^2}$ $d\sigma^*$ HOMO and the a_1 p_zp_z $p\sigma$ LUMO is predicted to be allowed. This transition corresponds to the strong visible absorption feature observed for the $d^8\cdots d^{10}$ cores in solution (see experimental section).

The luminescence spectroscopy of RhAu complexes has been the subject of numerous examinations in the literature,[28,40,41] in brief, photon absorption into the RhAu $d\sigma^* \rightarrow$ CNR π^*/RhAu $p\sigma$ (abbreviated $d\sigma^*p\sigma$) manifold generates a $^1(d\sigma^*p\sigma)$ excited state that is efficiently drained by intersystem crossing to the $^3(d\sigma^*p\sigma)$ electronic state. At low temperatures weak fluorescence is observed from the $^1(d\sigma^*p\sigma)$ excited state but is dominated by intense phosphorescence originating from the $^3(d\sigma^*p\sigma)$ state. The large contribution of CNR π^* orbital character to the LUMO suggests that C≡N bond vibrations might participate in the efficiency of $^3(d\sigma^*p\sigma)$ non-radiative excited state deactivation at room temperature. In keeping with the molecular orbital description of Scheme 3.1 and by analogy with the observations of $d^8\cdots d^8$ $Rh_2^{I,I}$ and $Ir_2^{I,I}$ cores bridged by tfepm ligands in Chapter 2, the phosphorescence energy of the $^3(d\sigma^*p\sigma)$ excited state of the $d^8\cdots d^{10}$ core should be sensitive to variations in the RhAu distance.

The spectroscopic response to nuanced structural variation would most faithfully be represented by single crystal measurements, however the solvated lattices of the RhAu salts in question do not maintain crystallinity under the requisite experimental conditions. Therefore luminescence measurements were performed in the solid state in an effort to maintain, as closely as possible, the structural metrics obtained for each complex from X-ray crystallographic studies. Corrected, normalized, solid state emission spectra collected at 77K for complexes **1**, **5-10** are presented in Figure 3.6, left. The spectra show the intense phosphorescence bands centered between ~615-660 nm characteristic of $d^8\cdots d^{10}$ $^3(d\sigma^*p\sigma)$ excited states, Table 3.2.[40,41] Emission from the $^1(d\sigma^*p\sigma)$ is negligible in the solid state, but is enhanced relative to the phosphorescence in butyronitrile glasses at 77K, Figure 3.6, right. The reasons for this are unclear, but some precedent for fluorescence has been observed upon intermolecular associations of Au centers.[50] However the expected concentration dependence on the ratio of $^1(d\sigma^*p\sigma)$ to $^3(d\sigma^*p\sigma)$ emission is not observed in this case (not shown).

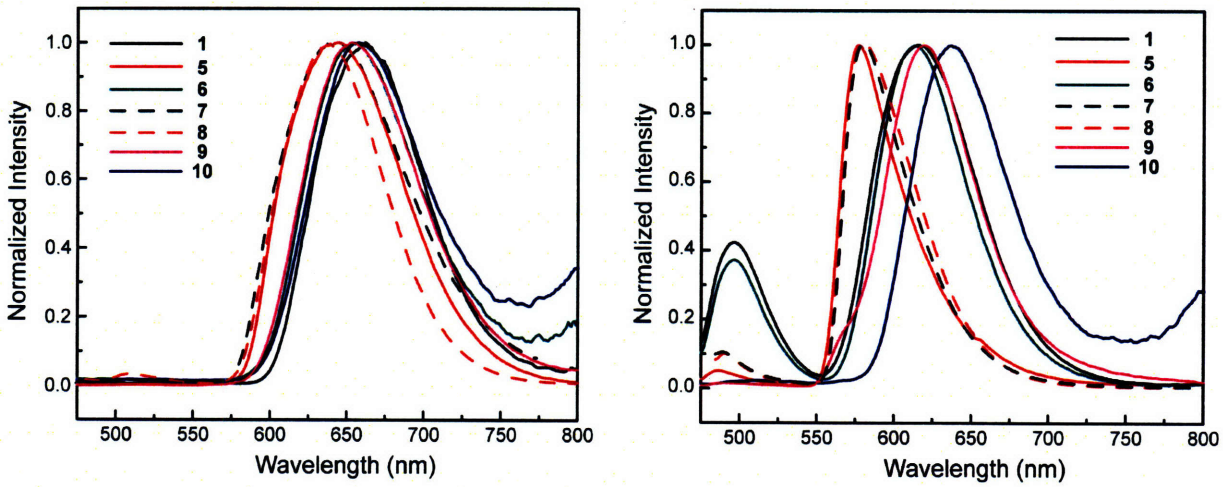

Figure 3.6. Normalized luminescence spectra for complexes **1**, **5-10** in the solid state (left) and in butyronitrile glass (right). All spectra collected at 77K with 450 nm excitation.

Table 3.2. Emission maxima for complexes **1**, **5-10** in the solid state and butyronitrile glasses at 77K.

	Emission Maximum (nm)						
	1	**5**	**6**	**7**	**8**	**9**	**10**
Solid	662	643	654	658	640	657	653
Butyronitrile	616	577	614	577	577	619	637

Examination of the solid state emission data reveals that the phosphorescence energy is not significantly perturbed across the series. A blue shift of 19 nm observed for complex **5** relative to the parent complex **1**, is the largest shift observed between directly comparable

species. Curiously this hypsochromic shift accompanies a decrease in the $Rh^{I}\cdots Au^{I}$ distance from **1** to **5** of 0.0284 Å and is opposed to the predicted trend. The effect, however, is small, compared to the ~ 70 nm bathochromic shift observed between $Rh_2^{I,I}(tfepm)_3Cl_2$ and $Ir_2^{I,I}(tfepm)_3Cl_2$ observed in Chapter 2 by absorption spectroscopy. The data collected in a butyronitrile glass show a bit more variability, with phosphorescence maxima ranging from 577 nm for **5** to 637 nm for **10**. In light of the sensitivity of the metal-metal internuclear distance to crystal packing forces (e.g. between **1** and **5**) and the opposing trend in the solid state data, these shifts are difficult to rationalize. The extensive participation of CNR π* orbitals in the calculated LUMO, Figure 3.5, suggested that the introduction of an R group with an accessible π system might have a more pronounced effect on the HOMO-LUMO gap than the RhAu distance. This reasoning led to the use of CNdmp in place of $CN^{t}Bu$, however this substitution appears to have a negligible effect as the observed emission maxima of complexes **5** and **8** at 643 nm and 641 nm, respectively, are nearly identical.

The small effects on the solid state emission spectra can be rationalized by a closer examination of the molecular orbital diagram for a $Rh^{I}\cdots Au^{I}$ $d^8\cdots d^{10}$ interaction, Figure 3.7. Although a fragmentary molecular orbital analysis for the approach of a square planar d^8 and a linear d^{10} metal center might suggest the presence of metal-metal σ, π and δ orbital interactions similar to a homobimetallic $d^{8}\cdots d^{8}$ complex,[38a-e,51] a full population analysis by DFT reveals significant perturbations. The frontier occupied orbitals of the model complex $Rh^{I}Au^{I}(CH_2(PH_2))_2(CNH)_2^{2+}$ are primarily composed of rhodium atomic orbitals, with the HOMO–1 of exclusively rhodium d_{yz} character. Additionally the HOMO–2 and HOMO–3 contain essentially no gold contributions and are simply rhodium d_{xz} and rhodium d_{xy} π* interactions with the isonitrile ligands. The unfilled $d_{x^2-y^2}$ orbital of the d^8 Rh^{I} center forms the σ* interactions with the phosphine and isonitrile ligands (not shown). The gold atomic d orbitals are buried further in the metal-metal bonding molecular orbital with the HOMO–6 to HOMO–10 composed exclusively of nearly pure gold d orbital character. Simple extended Hükel arguments from the electronic structure theories of Wolfsberg and Hemholtz[52] suggest that a large energetic disparity between the constituent atomic orbitals leads to poor overlap of the resulting molecular orbital, and therefore a smaller energetic splitting between bonding and antibonding combinations. With this simple relationship and DFT results of Figure 3.7 the minimal effect of internuclear distance on the observed $Rh^{I}Au^{I}$ HOMO-LUMO gap can be explained.

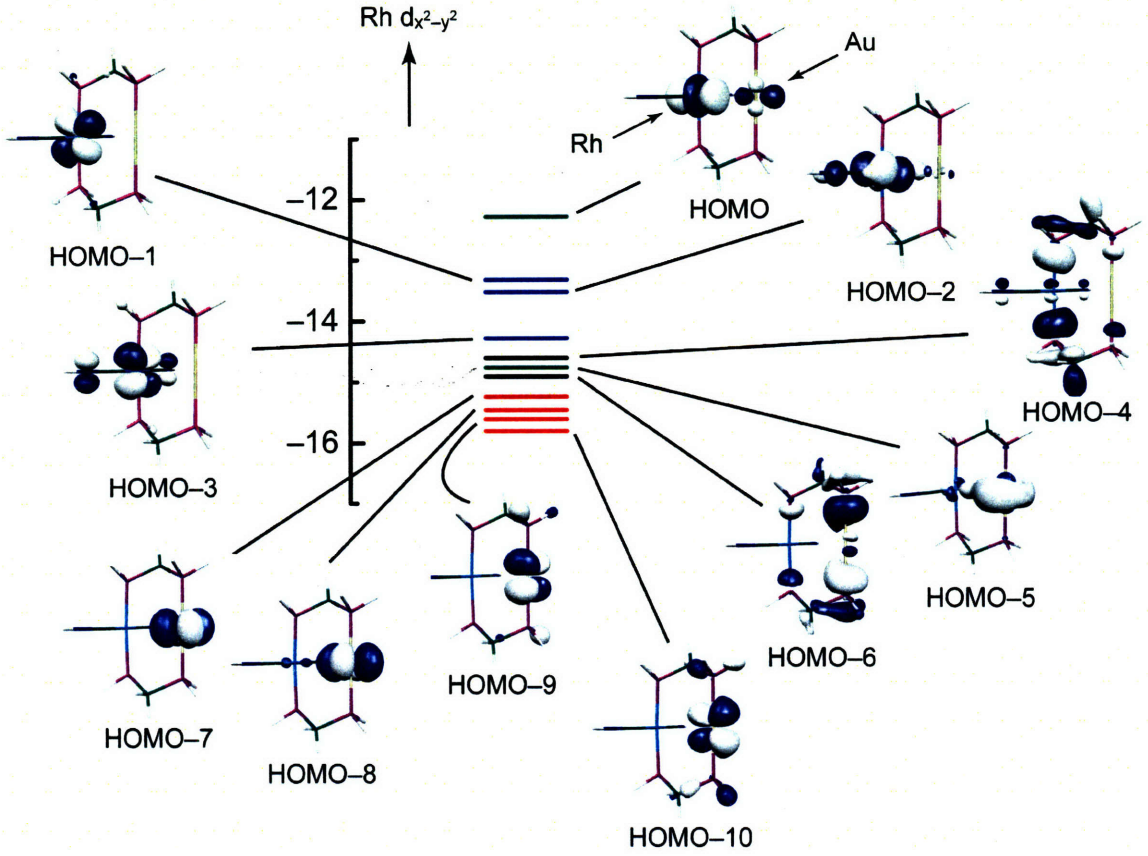

Figure 3.7. Calculated HOMO to HOMO–10 for the model complex $Rh^{I}Au^{I}[CH_2(PH_2)_2]_2(CNH)_2^{2+}$ at the B3LYP level, the ordinate axis is in units of electron volts. The coloring scheme differentiates molecular orbitals composed primarily of Au d character (—), Rh d character (—), and the dσ/dσ* interactions of the $Rh^{I}\cdots Au^{I}$ core (—).

In the homobimetallic valence-symmetric example the constituent metal fragments are energetically congruent and therefore the d orbitals exhibit extensive overlap, forming, dπ, dδ and a strong dσ interaction leading to significant splitting between the dσ and dσ* combinations, Figure 3.8, left.[51] In contrast the heterobimetallic $d^{8}\cdots d^{10}$ interaction between Rh^{I} and Au^{I} metal fragments involves d orbitals of vastly differing energies, resulting in effectively non-bonding metal-metal dπ and dδ interactions and poor overlap between the σ orbitals, Figure 3.8 right, and Figure 3.7. Due to the poor overlap in the σ manifold, small perturbations in the RhAu distance do not have a large effect on the energy of the dσ* HOMO, and thus do not effect the HOMO-LUMO gap as significantly as in homobimetallic complexes.

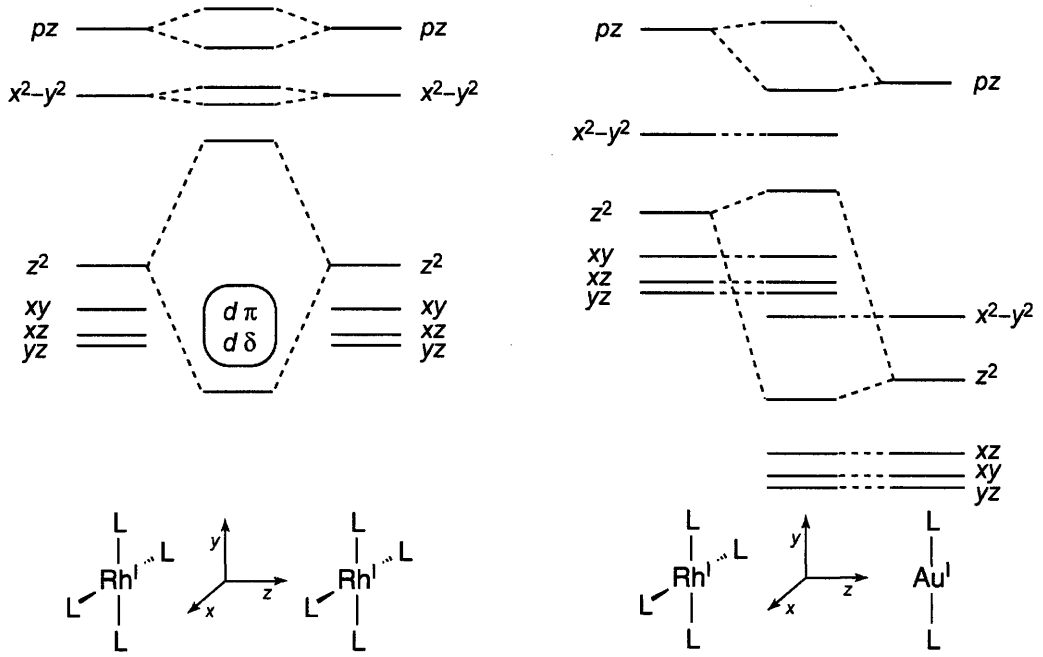

Figure 3.8. Comparison of the frontier metal-metal molecular orbitals for a homobimetallic $d^8\cdots d^8$ interaction typified by face-to-face $Rh_2^{I,I}$ dimers, right, and a RhAu heterobimetallic $d^8\cdots d^{10}$ interaction, left.

3.3 *Rh^IAu^I Redox Chemistry*

Although pσ excited states of $d^8\cdots d^8$ homodimers have considerable precedent for photochemical reactivity, these excited state are more suited for atom abstraction reactions as typified by the alcohol dehydrogenation chemistry of the $d^8\cdots d^8$ biradical excited state of PtPOP outlined in Chapter 1. Photoinduced bond scission reactivity however, is more suited to the dσ*

Scheme 3.3.

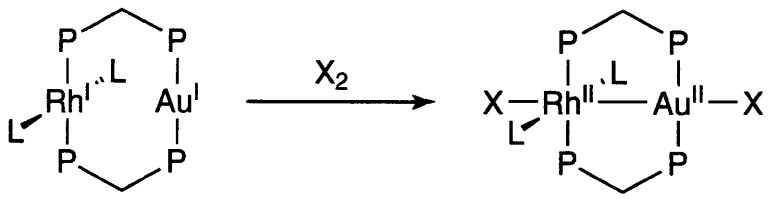

excited states of the singly bonded diphosphazane bridged dirhodium complexes. It follows that this photoreactivity necessarily requires a vacant and photochemically accessible dσ* combination in the metal-metal bonding molecular orbital. The electronic structure calculations of Rh^IAu^I $d^8\cdots d^{10}$ heterodimers suggest that a two electron oxidation by X_2 with concomitant

Rh–X and Au–X bond formation should generate a stable d^7–d^9 Rh^{II}–Au^{II} bimetallic core, Scheme 3.3.

Despite this straightforward motivation, investigations of $d^8 \cdots d^{10}$ cores have been largely spectroscopic, leaving the reaction chemistry underdeveloped. Initial attempts to access this redox chemistry were conducted using the readily accessible RhAu core of **1**, wherein cold solutions of **1** in CH_2Cl_2 were treated with $PhICl_2$ (as a chlorine delivery agent) giving a rapid color change from orange to red. The red color immediately bleached, even when the solution was refrozen, to eventually give a pale yellow solution. NMR analysis showed multiple products that eluded isolation, and suggested that the oxidized material is unstable in the ligand environment afforded by dppm. Indeed, from CH_2Cl_2/pentane layers of the yellow reaction mixture, yellow crystals suitable for X-ray diffraction could be obtained and reveals the structure shown in Figure 3.9. In this structure, the discrete bimetallic core of **1** is cleaved upon oxidation, resulting in the formation of an octahedral Rh^{III} center bridged to two linear Au^{I} centers via dppm ligands. The 2:1 Rh:Au stoichiometry in the product indicates that other decomposition pathways also occur to give the final product. The group trans to the CN^tBu ligand on the Rh^{III} is site disordered on the crystalline lattice between Cl^- and CN^- groups. The formation of CN^- from CN^tBu can be rationalized by invoking homolytic cleavage of an N–CMe_3 bond, giving a highly reducing ^tBu radical. The organic radical could then undergo one electron reduction of either the metal complex or the putatively formed CN• to generate $^tBu^+$, followed by rapid trapping of the

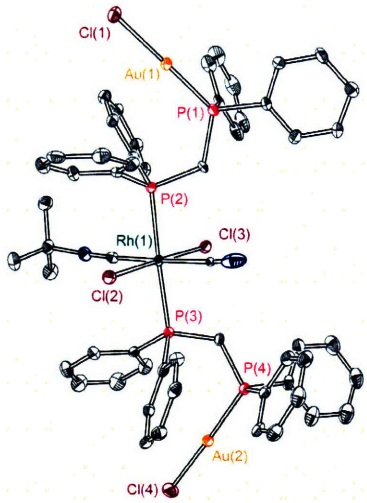

Figure 3.9. X-ray structure of a site disordered mixture of $Rh^{III}Au_2^{I,I}(dppm)_2Cl_4(CN)(CN^tBu)$ (**11**, shown) and $Rh^{III}Au_2^{I,I}(dppm)_2Cl_5(CN^tBu)$ as two components of a complex product mixture that results from the oxidation of $Rh^{I}Au^{I}(dppm)_2(CN^tBu)_2Cl_2$ (**1**) with $PhICl_2$ in CH_2Cl_2. Thermal ellipsoids are drawn at the 50% probability level with hydrogen atoms omitted for clarity.

carbocation by Cl^- to give 2-chloro-2-methylpropane. Attempts to oxidize complex **1** with $KAu^{III}Cl_4$ and outer sphere one electron oxidants, such as NO^+ or $NR_3^{\bullet+}$, evidenced the same transient red solution but did not result in stable product formation. The dcpm derivative, $Rh^IAu^I(dcpm)_2(CN^tBu)_2Cl_2$ (**9**), gave similar results under the oxidative conditions applied to **1**.

Heterobimetallic oxidation products with enhanced stability can be accessed when bridged by tfepma ligands. The parent compound, $Rh^IAu^I(tfepma)_2(CN^tBu)_2Cl_2$ (**12**), can be synthesized by the sequential addition of tfepma, *tert*-butylisonitrile and $Au^I(tht)Cl$ to a concentrated solution of $[Rh^I(COD)Cl]_2$ in CH_2Cl_2. The assembly of the dinuclear construct proceeds through the intermediacy of $Rh^I(tfepma)_2Cl$ (**4**) in accordance with Scheme 3.2. The NMR spectrum of **12** in CD_3CN shows a sharp singlet at 1.45 ppm for the *tert*-butyl protons of the terminal isonitriles and a pseudotriplet at 2.98 ppm ($^3J_{P-H}$ = 3.0 Hz) for the bridgehead N-methyl protons. Correspondingly the $^{31}P\{^1H\}$ NMR shows two multiplets at 136.9 and 151.3 ppm, assigned as equivalent phosphorus ligation to rhodium and gold respectively. Single crystals of **12** may be obtained from CH_2Cl_2 solutions of the complex layered with Et_2O, providing the structure shown in Figure 3.10.

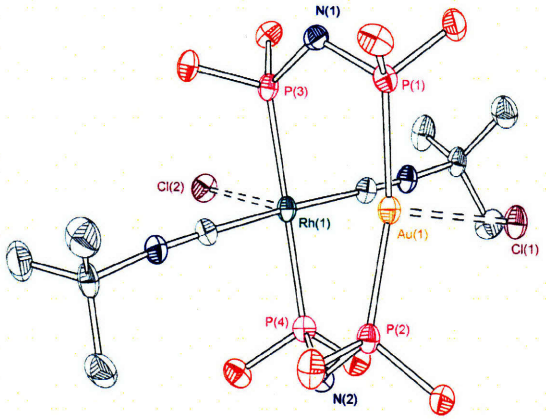

Figure 3.10. X-ray structure of $Rh^IAu^I(tfepma)_2(CN^tBu)_2Cl_2$ (**12**). Thermal ellipsoids drawn at the 50% probability level with hydrogen atoms omitted for clarity.

The ligand geometries about the rhodium and gold centers are in accordance with that expected for their respective d-electron counts: the Rh^I center is approximately square planar and the Au^I center is a trigonally distorted as defined by P(1)–Au(1)–P(2) and P(1)–Au(1)–Cl(1) angles of 151.41(3)° and 101.39(3)°, respectively (Table 3.3). The chloride counterions show close metal contacts of d(Au(1)···Cl(1)) = 2.6632(9) Å and d(Rh(1)···Cl(2)) = 2.6027(9) Å. The long Rh(1)···Au(1) distance of 2.8181(3) Å is typical of dinuclear complexes with no net metal-

Table 3.3. Selected Bond Lengths (Å) and Angles (°) for $Rh^{I}Au^{I}(tfepma)_2(CN^{t}Bu)_2Cl_2$ (**12**).

Bond Lengths (Å)					
Au(1)···Rh(1)	2.8181(3)	Au(1)–Cl(1)	2.6632(9)	Rh(1)–Cl(2)	2.6027(9)
Au(1)–P(1)	2.2713(10)	Rh(1)–P(3)	2.3147(10)	Rh(1)–C(3)	1.988(4)
Au(1)–P(2)	2.2741(10)	Rh(1)–P(4)	2.2603(10)	Rh(1)–C(8)	1.975(4)
Bond Angles (°)					
	P(1)–Au(1)–P(2)	151.41(3)	P(3)–Rh(1)–P(4)	166.48(3)	
	P(2)–Au(1)–Cl(1)	101.10(3)	C(3)–Rh(1)–C(8)	175.39(14)	

metal bond (*vide supra*). The structural motif of **12** is similar to that of other $d^8\cdots d^{10}$ $M\cdots Au^{I}$ dimers (M = Rh^{I},[42] Ir^{I},[30,31] Ni^{II},[28] Pt^{II} [32–37]) when dppm and dcpm bridging ligands are used, excepting that the closely associated chlorides dispose the Au^{I} center towards a trigonal geometry in lieu of the nearly linear geometry observed in other systems.

Scheme 3.4.

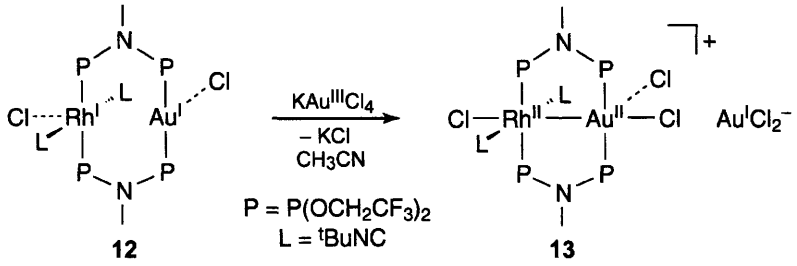

The close chloride contacts in the solid state structure of **12** suggested that formation of the two-electron oxidation product might be facilitated, as the terminal halogen ligands expected for a d^7–d^9 Rh^{II}–Au^{II} core are already present. Notwithstanding, oxidation of **12** with outer sphere one-electron oxidants such as NO^+ and $R_3N^{\bullet+}$ gives intractable product mixtures, and results similar to those observed in the oxidation of **1** are obtained when using $PhICl_2$. Conversely, upon addition of $KAu^{III}Cl_4$ to CH_3CN solutions of **12** at low temperature, a prompt and sustained color change from orange to red is observed, Scheme 3.4. A UV-vis absorption spectrum of the reaction mixture confirms that the conversion proceeds smoothly. The diagnostic absorption bands of **12** at 380 and 421 nm, which are in line with those reported for a RhAu $d\sigma^*$ → CNR π^*/RhAu $p\sigma$ transition,[29] are replaced by two new absorption bands at 329 and 460 nm (Figure 3.11).

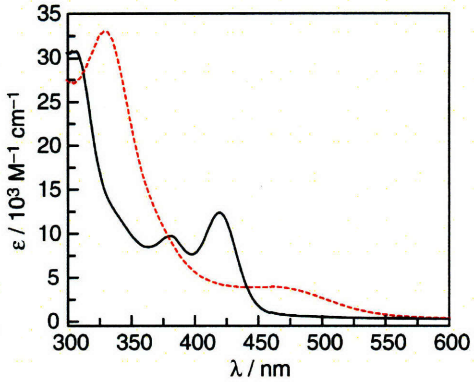

Figure 3.11. UV-vis absorption spectra from 300 to 600 nm (25 °C, CH_3CN) for **12** (—) and immediately after the addition of 1.05 equivalents of $KAu^{III}Cl_4$ to generate **13** (- - -).

The oxidation product, **13**, may be isolated as a strawberry solid in 44% yield after removal of KCl and subsequent recrystallization from CH_2Cl_2 layered with pentane at –40 °C. The NMR signals of **13** are significantly shifted from those of **12**. A ^1H singlet for the equivalent *tert*-butyl protons is observed at 1.61 ppm and a pseudotriplet ($^3J_{P-H}$ = 4.4 Hz) is observed for the bridgehead N–Me groups at 3.05 ppm. The $-OCH_2CF_3$ protons appear as a series of complex multiplets at ~4.65, 4.99 and 5.79 ppm. The $^{31}P\{^1H\}$ NMR spectrum of **13** also indicates a large structural deviation from **12**, as the two distinct ^{31}P resonances of **12** at 136.9 and 151.3 ppm are lost and replaced by a complex set of overlapping multiplets centered at ~98 ppm. Single crystal X-ray diffraction studies of **13** unequivocally establish its identity as $[Rh^{II}Au^{II}(tfepma)_2(CN^tBu)_2Cl_3]^+[Au^ICl_2]^-$ (Figure 3.12).

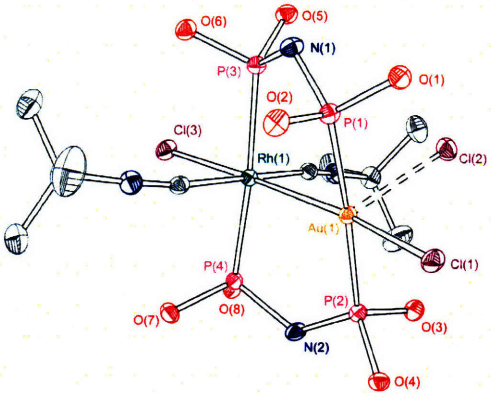

Figure 3.12. X-ray structure of $[Rh^{II}Au^{II}(tfepma)_2(CN^tBu)_2Cl_3]^+[Au^ICl_2]^-$ (**13**). Thermal ellipsoids drawn at the 50% probability level with hydrogens atoms, non-coordinating counterions, –Me groups and $-CH_2CF_3$ groups omitted for clarity.

Table 3.4. Selected bond distances (Å) and angles (°) for $[Rh^{II}Au^{II}(tfepma)_2(CN^tBu)_2Cl_3]^+[Au^ICl_2]^-$ (**13**).

Bond Lengths (Å)					
Au(1)–Rh(1)	2.6549(4)	Au(1)–Cl(2)	2.8492(9)	Rh(1)–Cl(3)	2.3764(9)
Au(1)–P(1)	2.3035(10)	Rh(1)–P(3)	2.3136(9)	Rh(1)–C(3)	1.994(3)
Au(1)–P(2)	2.2969(10)	Rh(1)–P(4)	2.2958(9)	Rh(1)–C(8)	1.991(3)
Au(1)–Cl(1)	2.4267(8)				

Bond Angles (°)			
P(1)–Au(1)–P(2)	174.64(3)	P(3)–Rh(1)–P(4)	174.62(3)
P(2)–Au(1)–Cl(1)	91.04(3)	C(3)–Rh(1)–C(8)	175.73(13)

The Rh^{II} center is pseudo-octahedral and the Au^{II} center is roughly square planar. Metal-halide bonding interactions are reflected by Rh(1)–Cl(3) and Au(1)–Cl(1) distances of 2.3764(9) Å and 2.4267(8) Å, respectively (Table 3.4). Additionally, the short Rh(1)–Au(1) distance of 2.6549(4) Å in **13** is indicative of a formal metal-metal bond, thus affording the first structural characterization of a Rh^{II}–Au^{II} interaction.[53] A chloride ion is loosely associated at an apical position of the Au^{II} square plane at a contact distance of 2.8492(9) Å. The cationic complex is charge balanced by an outer sphere $Au^ICl_2^-$ counterion.

DFT calculations were initiated using the coordinates obtained from the crystal structure of **13**. Hydrogen atom surrogates were used in place of –Me, $-^tBu$ and $-OCH_2CF_3$ groups. Agreement between calculated and observed structures suggests that these simplifications are reasonable. Details of the computation are provided in the experimental methods section. Time dependent calculations identify an allowed singlet dσ → dσ* transition between the HOMO–2 and LUMO, Figure 3.13. This result is consistent with a d^7–d^9 electron count, which can also be described as $(d^6)d^1$–$(d^8)d^1$ where the odd electron on each of the individual metal centers resides in a d_{z^2} orbital.[51]

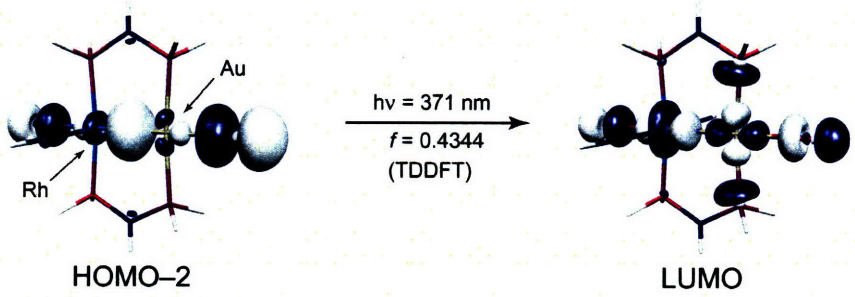

Figure 3.13. DFT calculation of the orbitals involved in the dσ → dσ* transition of $Rh^{II}Au^{II}(HN[PH_2]_2)_2(CNH)_2Cl_2^{2+}$. Oscillator strengths and transition energies calculated by TDDFT.

Luminescence spectroscopic measurements on butyronitrile glasses of **12** maintained at 77 K display a weak emission band at 565 nm and a strong band at 707 nm (λ_{exc} = 420 nm) with lifetimes of <10 ns and 20 μs indicating an excited state parentage that is singlet and triplet respectively,[40,41] or indicative of intermolecular association (for the short lifetime component) of a bimetallic containing Au.[50] Complex **13** is also emissive at 77 K and displays two bands at 529 and 733 nm. As in **12**, the red band is assigned as phosphorescence based on the observed lifetime of 30 μs. The low energy phosphorescence is consistent with emission from dσ* excited states, as is observed for bimetallic Rh cores.[54] The lifetime of the emissive state centered at 529 nm was <10 ns.

At ambient temperatures complex **13** is unstable in solution and thermally reacts in CH_3CN or CH_2Cl_2 over the course of several hours. The complex multiplet centered at ~98 ppm in the $^{31}P\{^1H\}$ NMR spectrum of **13** disappears with the concomitant appearance of a singlet resonance at 134.4 ppm and a sharp doublet at 75.5 ppm with a $^1J_{Rh-P}$ coupling constant of 141.9 Hz. Although the ^1H NMR spectrum contains multiple overlapping N–Me resonances, a ^{t}BuNC resonance appears at 1.56 ppm, consistent with the formation of $Au^I(CN^tBu)Cl$.[55]

Direct evidence for cleavage of the heterobimetallic Rh^{II}–Au^{II} bond is provided by X-ray structural analysis of single crystals obtained from CH_2Cl_2/pentane layers of reacted solutions. Wherein the asymmetric unit was found to contain *fac*-Rh^{III}(tfepma)$(CN^tBu)Cl_3$ and $Au_2^{I,I}(tfepma)_2Cl_2$ (Figure 3.14), tentatively assigned as the resonances at 75.5 and 134.4 ppm in the $^{31}P\{^1H\}$ NMR respectively. The structure of *fac*-Rh^{III}(tfepma)$(CN^tBu)Cl_3$ comprises a

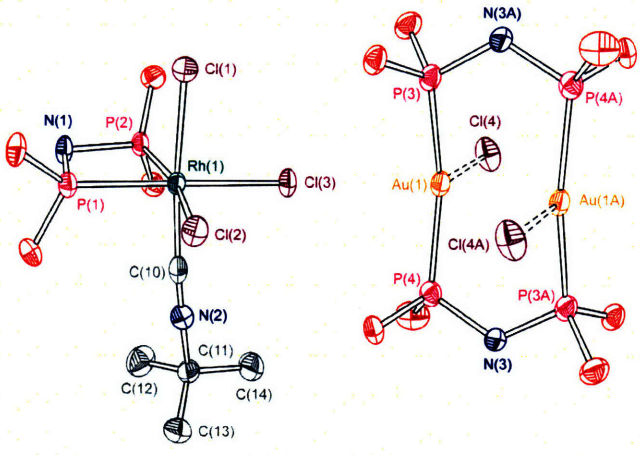

Figure 3.14. X-ray structure of the co-crystallized products *fac*-Rh^{III}(tfepma)$(CN^tBu)Cl_3$ (**14**, left) and $Au_2^{I,I}(tfepma)_2Cl_2$ (**15**, right) when solutions of **13** are left to stand at room temperature in CH_3CN. Hydrogen atoms, –Me and $–CH_2CF_3$ groups are omitted for clarity. Thermal ellipsoids are drawn at the 50% probability level.

Table 3.5. Selected Bond Lengths (Å) and Angles (°) for *fac*-Rh^{III}(tfepma)(CN^tBu)Cl_3 (**14**) and $Au_2^{I,I}$(tfepma)$_2Cl_2$ (**15**).

Bond Lengths (Å)					
Au(1)–Au(1A)	2.8390(5)	Rh(1)–C(10)	1.931(7)	Rh(1)–Cl(2)	2.4128(16)
Au(1)–P(3)	2.2973(18)	Rh(1)–P(1)	2.2144(16)	Rh(1)–Cl(3)	2.4047(15)
Au(1)–P(4)	2.2878(17)	Rh(1)–P(2)	2.2083(16)	P(1)–N(1)	1.659(5)
Au(1)–Cl(4)	2.6364(16)	Rh(1)–Cl(1)	2.3707(15)	P(2)–N(1)	1.676(5)
Bond Angles (°)					
P(3)–Au(1)–P(4)	159.40(6)	P(3)–Au(1)–Cl(4)	98.00(6)	Cl(1)–Rh(1)–Cl(2)	91.87(6)
P(4)–Au(1)–Cl(4)	102.46(6)	Cl(1)–Rh(1)–C(10)	174.00(18)	P(1)–Rh(1)–P(2)	70.94(6)

pseudooctahedral Rh^{III} center ligated by three chloride ligands in a facial geometry with ~90° cis angles and typical Rh–Cl bond lengths of 2.37 - 2.41 Å. A single CN^tBu ligand is coordinated trans to Cl(1) with a linear Cl(1)–Rh(1)–C(10) angle of 174.00(18)°. The largest deviation from an ideal octahedral geometry is the tight P(1)–Rh(1)–P(2) bite angle of 70.94(6)° that is imposed by the chelating tfepma ligand. The overall structural motif is analogous to that observed in *fac*-Rh^{III}(dppm)(CH_3CN)Cl_3.[56] $Au_2^{I,I}$(tfepma)$_2Cl_2$ sits on a special position in the crystal lattice and the bimetallic core is bisected by a crystallographic inversion center. The coordination geometry about the gold center in $Au_2^{I,I}$(tfepma)$_2Cl_2$ is analogous to that of **12** with similar Au–P distances of 2.2973(18) and 2.2878(17) Å; the Au(1)···Cl(4) contact is long at 2.6364(16) Å. The distorted trigonal geometry is defined by P(3)–Au(1)–P(4) and P(3)–Au(1)–Cl(4) angles of 159.40(6)° and 98.00(6)° respectively. The tfepma ligand engenders an observed Au(1)···Au(1A) distance of 2.8390(5) Å. This intermetal distance is shorter by about ~0.1 Å with respect to gold dimers of similar formulations with bridging dppm or dcpm ligands.[6,39]

The thermal decomposition reaction of **13** indicates that the formal Rh^{II}–Au^{II} metal-metal bonded core is eradicated by intermetal charge transfer and disproportionation by the overall stoichiometry: $[Rh^{II}Au^{II}(tfepma)_2(CN^tBu)_2Cl_3]^+[Au^ICl_2]^- \rightarrow$ *fac*-Rh^{III}(tfepma)(CN^tBu)Cl_3 + ½ $Au_2^{I,I}$(tfepma)$_2Cl_2$ + $Au^I(^tBuNC)Cl$. It is not unreasonable, on the basis of electronegativity differences, and the electronic structure calculations of Section 3.2.2 for the related $Rh^IAu^I(CH_2[PH_2]_2)_2(CNH)_2^{2+}$ complex, to invoke a bonding interaction between the d^7 Rh^{II} center and d^9 Au^{II} center that is highly polarized towards gold; in this instance, a d^6←d^{10} electron count for a Rh^{III}←Au^I interaction is the limiting oxidation state formalism. If this electronic contribution were significant, then the high valent Rh^{III} center would be expected to expel neutral

π acceptor ligands in lieu of anionic π donor ligands such as Cl^-. The rapid thermal consumption of **13** precludes unambiguous investigations into the photochemical M–X bond activation chemistry from this platform. In attempts to address this issue, heterobimetallic cores are currently being explored where the constituent metals have more congruent d orbital energies, such as Pt^{II} and Au^{I}. This could allow for increased thermal stability of d^7–d^9 Pt^{III}–Au^{II} core with respect to disproportionation due to greater covalency of the metal-metal bonding interaction in the oxidized complex.

3.4 *Ambidentate PS Ligands*

In attempts to circumvent the strict ligand requirements for controlled $d^8\cdots d^{10}$ heterodimer formation when using the bisphosphine ligands of the previous sections, the coordination chemistry of ambidentate ligands containing both phosphorus and sulfur donors was explored. In this construct the phosphine arm would preferentially bind to the rhodium center and the sulfur donor to gold. The stepwise assembly of Scheme 3.2 could still be employed for the construction of the heterobimetallic core, but in this case the use of ambidendate donor ligands could provide for precise control over the synthetic outcome. In particular, an unfurling mechanism is envisioned, Scheme 3.5, wherein the ambidentate ligand initially chelates the Rh^{I} center in an analogous fashion to compounds **2** - **4**, and then preferentially dissociates the sulfur donor upon the addition of a suitable donor ligand such as ^{t}BuNC. The heterobimetallic could then be selectively completed upon treatment with a suitable Au^{I} source.

Scheme 3.5.

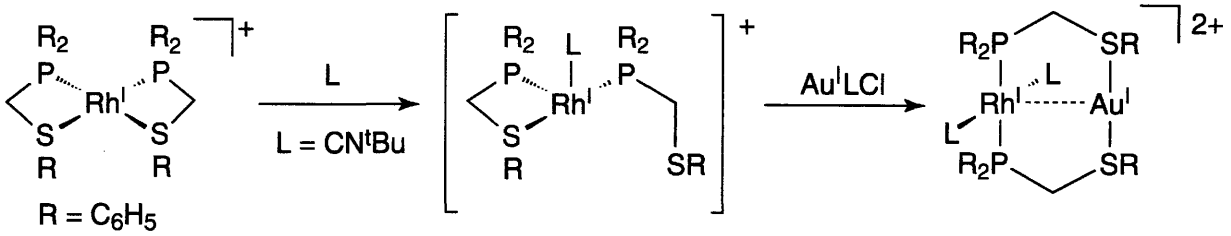

As an initial foray into this area the first ligand targeted was $(C_6H_5)_2PCH_2S(C_6H_5)$ (PS(1)), which is readily synthesized by published procedures.[57] Sanger explored some coordination chemistry of PS(1) with late transition metals, including Rh^{I}, but only characterized the products by combustion analysis and infrared spectroscopy. In keeping with Sanger's results,

the addition of PS(1) to solutions of $[Rh^{I}(COD)Cl]_2$ gives complex **16** in good yields. ^{1}H NMR analysis of the resulting light orange powder gives a spectrum with a sharp doublet at 4.13 ppm ($^{2}J_{P-H}$ = 5.1 Hz) for the bridgehead methylene protons and also diagnostic COD peaks at 1.91, 2.04, 2.38, and 5.51 ppm. The $^{31}P\{^{1}H\}$ NMR shows only a single doublet resonance at 27.74 ppm ($^{1}J_{Rh-P}$ = 149.5 Hz). The solution data is confirmed by X-ray structural analysis and shows a roughly square planar Rh^{I} center composed of a chelating COD ligand a terminal chloride and the PS(1) ligand bound through the $P(C_6H_5)_2$ unit, Figure 3.15, left.

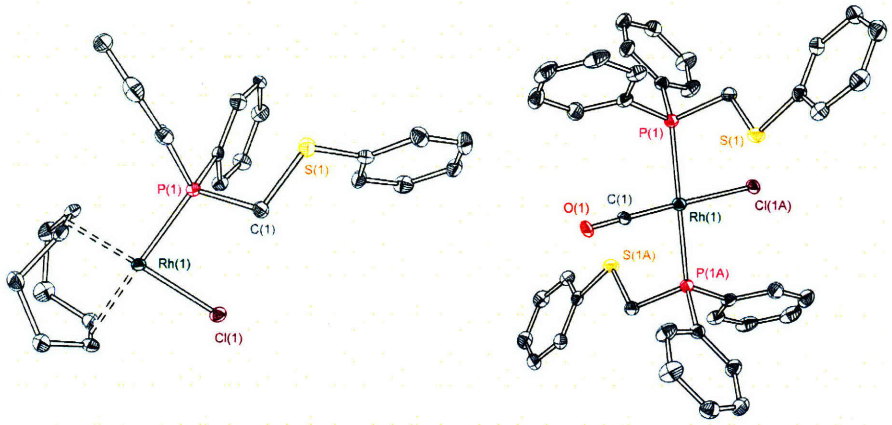

Figure 3.15. X-ray structures of $Rh^{I}(PS[1])(COD)Cl$ (**16**), left, and $Rh^{I}(PS[1])_2ClCO$ (**17**), right. Thermal ellipsoids drawn at the 50% probability level with hydrogen atoms and solvents of crystallization omitted for clarity.

The structure shows that the sulfur donor has a low affinity for the Rh^{I} center and that the $P(C_6H_5)_2$ donor cannot displace the chelating COD ligand of the $[Rh^{I}(COD)Cl]_2$ starting material. Treatment of $[Rh^{I}(COD)Cl]_2$ with four equivalents of PS(1) does not induce COD displacement and the only observable products are **16** and free PS(1) by ^{1}H and $^{31}P\{^{1}H\}$ NMR spectroscopy. Double substitution of Rh^{I} can be afforded by the treatment of $[Rh^{I}(CO)_2Cl]_2$ with four equivalents of PS(1) where a solution color change from orange to yellow is accompanied by vigorous gas evolution. ^{1}H NMR analysis of the final product shows a single doublet resonance at 4.23 ppm for the methylene bridgehead protons; the $^{31}P\{^{1}H\}$ NMR correspondingly shows a single resonance at 25.64 ppm with rhodium coupling of 125.1 Hz, indicative of a single PS(1) ligand environment. Infrared analysis in CD_2Cl_2 shows a strong CO stretching vibration at 1978 cm^{-1} indicating at least one CO ligand is maintained within the Rh^{I} coordination sphere. X-ray quality crystals are readily obtained from CH_2Cl_2/pentane layers and give the structure of $Rh^{I}[PS(1)]_2ClCO$ (**17**) shown in Figure 3.15, right. Compound **17** shows the expected square planar coordination environment for a d^8 Rh^{I} center, notably however both PS(1) ligands

coordinate the Rh^{I} center through the $P(C_6H_5)_2$ groups exclusively, leaving the sulfur donors available to bind a d^{10} Au^{I} center, and suggested that heterobimetallic RhAu cores could be accessed by the addition of an appropriate Au^{I} according to Scheme 3.5. Multiple products are observed by $^{31}P\{^{1}H\}$ NMR, however, upon addition of $Au^{I}(tht)Cl$ or $Au^{I}(tht)_2(CF_3SO_3)$ as Au^{I} sources to solutions of **17**. Some resonances lost the diagnostic $^{1}J_{Rh-P}$ coupling suggesting that the $P(C_6H_5)_2$ groups do not remain coordinated to the Rh^{I} center. Attempts to isolate pure materials from the product mixtures proved fruitless. Undaunted, colorless rods could be picked from CH_2Cl_2/pentane layers of the product mixture where analysis by X-ray crystallography gave the structure of the previously reported homobimetallic gold dimer: $Au_2^{I,I}(PS[1])_2(CF_3SO_3)_2$ shown in Figure 3.16.[58]

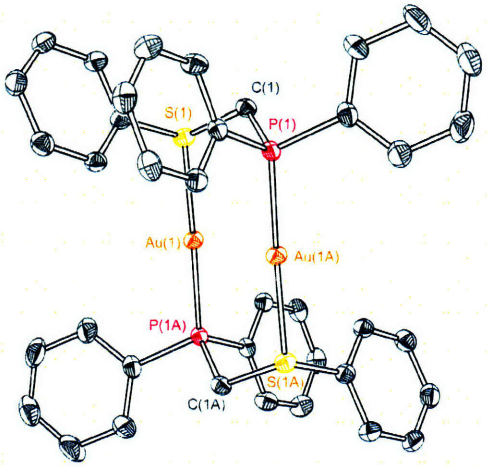

Figure 3.16. X-ray structure of $Au_2^{I,I}(PS[1])_2(CF_3SO_3)_2$ (**18**) crystallized as a colorless rod pulled from CH_2Cl_2/pentane layers of product mixtures. Thermal ellipsoids drawn at the 50% probability level with hydrogen atoms, non-coordinating anions, and solvents of crystallization omitted for clarity.

The head to tail ligand binding motif suggests that the thioether donors of PS(1) cannot stabilize the linear S–Au^{I}–S geometry required for RhAu heterodimer formation. Taken along with the inability of PS(1) to form a bischelate monomer by displacement of the COD, CO, or Cl ligands of **16** and **17** suggest that the thioether bonding interactions are simply too weak to ligate either the Rh^{I} or Au^{I} centers in an effective manner. Additionally the ligand transfer from the monomeric rhodium core of **17** to the gold center of **18** suggested that the $P(C_6H_5)_2$ group is too labile when coordinated to the d^{8} Rh^{I} center, and should be substituted with less sterically demanding and more electron withdrawing groups to prevent ligand dissociation. To address both of these concerns new ambidentate ligands for directed heterodimer synthesis might employ

anionic sulfur donors derived from thiol functionalities for Au^{I} ligation, and electron poor phosphite groups such as $P(OCH_2CF_3)_2$ for tighter binding to the Rh^{I} center. As a suitable starting point, modifications to the reported synthesis of $(C_6H_5)_2PCH_2SH$[59] that allow for the installation of electron withdrawing functionalities on the phosphorus donor have been pursued, but as of yet a viable synthetic strategy has not been elucidated.

3.5 *Concluding Remarks*

The studies outlined in this chapter have focused on efforts to increase the quantum yields for M–X bond photoactivations by the incorporation of gold as an electronegative late transition metal into a heterodinuclear complex. Although this hypothesis could not be directly probed by the complexes described herein, these synthetic forays revealed nuances of photocatalyst design unique to heterobimetallic cores. This work has shown that the $d\sigma^* \rightarrow p\sigma$ electronic transition energy is not appreciably affected by the internuclear $Rh^{I}\cdots Au^{I}$ separation because of the extreme energetic disparity between the Rh^{I} and Au^{I} d-orbital energies that constitute the metal-metal interaction. Two-electron oxidation to the d^7–d^9 Rh^{II}–Au^{II} core reveals the consequences of this energetic mismatch as the metal-metal bonded dinuclear core is unstable towards redox disproportionation, and reacts to form d^6 Rh^{III} and d^{10} Au^{I} products. In attempts to circumvent the synthetic limitations of bisphosphine bridging ligands a first generation ambidentate ligand was investigated for targeted $Rh^{I}\cdots Au^{I}$ heterodimer formation. However, these studies failed to achieve the desired results due to unfavorable binding characteristics of the ligand employed, but they have provided valuable insight for the design of new ambidentate ligands.

3.6 *Experimental Section*

3.6.1 General Synthetic Considerations

All manipulations were carried out in an N_2-filled glovebox or under an inert atmosphere provided by a Schlenk line unless otherwise noted. All solvents were reagent grade (Aldrich) or better and were dried and degassed by standard methods.[60] $Rh^{I}Au^{I}(dppm)_2(CN^{t}Bu)_2Cl_2$ (**1**),23 $Ag^{I}(tht)(CF_3SO_3)$,[61] $Au^{I}(tht)Cl$,[62] $Au^{I}(tht)_2(CF_3SO_3)$,[63] $(C_6H_5)_2PCH_2S(C_6H_5)$,[57] dfpma,[64] tfepma,[65,66] dppma[67] were prepared by literature methods. $[Rh^{I}(CO)_2Cl]_2$, $[Rh^{I}(COD)Cl]_2$, dppm, dmpm, $HAu^{III}Cl_4$, $KAu^{III}Cl_4$, and $Au^{I}(PPh_3)Cl$ (Strem), *tert*-butylisonitrile, dcpm (bis[dicyclohexylphosphino]methane), $Au^{I}(DMS)Cl$, and $Au^{I}(PEt_3)Cl$, (Aldrich), 2,6-dimethylphenylisonitrile (Fluka) were purchased from the commercial sources indicated and used as received.

3.6.2 Physical Methods

NMR data were collected at the MIT Department of Chemistry Instrument Facility (DCIF) on a Varian Mercury 300 spectrometer. NMR solvents (CD_3CN) were purchased from Cambridge Isotope labs and purified by standard procedures prior to use.[60] ^1H NMR spectra (300 MHz) were referenced to the residual protio impurities of the given solvent. $^{31}P\{^1H\}$ NMR (121.4 MHz) spectra were referenced to an external 85% H_3PO_4 standard. All chemical shifts are reported in the standard δ notation in parts per million; positive chemical shifts are to higher frequency from the given reference. Elemental analyses were performed by Robertson Microlit Laboratories, Madison NJ. UV-vis spectra were recorded on a Spectral Instruments 400 series diode array spectrometer and referenced against the appropriate solvent. IR spectra were recorded on a Bio–Rad XPS 150 FT–IR spectrometer in a Perkin–Elmer liquid cell equipped with KBr windows.

3.6.3 Crystallographic Procedures

Single crystals were immersed in a drop of Paratone N oil on a clean microscope slide, affixed to either a glass fiber or a human hair coated in epoxy resin and then cooled to –173 °C. The crystals were then mounted on a Bruker K8 three circle goniometer platform equipped with an APEX CCD detector. A graphite monochromator was employed for wavelength selection of the Mo K_α radiation (λ = 0.71073 Å). The data were processed and refined using the program

SAINT supplied by Siemens Industrial Automation Inc. Structures were solved by a Patterson heavy atom map and refined by standard difference Fourier techniques in the SHELXTL program suite (6.10 v., Sheldrick G. M., and Siemens Industrial Automation Inc., 2000). Hydrogen atoms were placed in calculated positions using the standard riding model and refined isotropically; all other atoms were refined anisotropically. Unit cell parameters, morphology, and solution statistics for complexes **1**, **2**, **2′**, **5-8**, and **10-18** are summarized in Tables 3.6-3.10. All thermal ellipsoid plots are drawn at the 50% probability level, with solvents of crystallization, non-coordinating counterions, and hydrogen atoms omitted for clarity.

3.6.4 Luminescence Measurements

Samples were prepared in custom quartz EPR tubes equipped with a ground glass joint isolated from the atmosphere by a Teflon valve. Samples were prepared in a glovebox and then attached to a high vacuum line to and evacuated to 1×10^{-5} Torr. Steady state emission spectra were recorded on an automated Photon Technology International (PTI) QM 4 fluorimeter equipped with a 150-W Xe arc lamp and a Hamamatsu R928 or photomultiplier tube. Reported emission spectra are corrected for detector response using the instrument specific correction file supplied by PTI. Time resolved phosphorescence lifetimes were recorded on a nanosecond laser system described previously.[68] Time resolved emission measurements on the < 20 ns timescale were made with the frequency doubled (400 nm) pump light provided by a Ti:sapphire laser system (~100 fs pulsewidth) and collected on a Hamamatsu C4334 Streak Scope streak camera as previously described.[69]

3.6.5 Computational Details

The Gaussian 98 program suites were employed for all computational studies.[70] For Section 3.2, the geometry optimizations were initiated using atomic coordinates obtained from X-ray diffraction data for complex **1**. Phenyl groups on the dppm ligands and *tert*-butyl groups of the *tert*-butylisonitriles were replaced with protons. For Section 3.3, the geometry optimizations were initiated using the atomic coordinates obtained from X-ray diffraction data for complex **13**. The –Me and $-CH_2CF_3$ groups on the tfepma ligands and *tert*-butyl groups of the *tert*-butylisonitriles were replaced with protons. DFT calculations were carried out using the three parameter hybrid exchange functional of Becke[71] in conjunction with the correlation functional of Lee, Yang, and Parr, which includes both local and non-local terms (B3LYP).[72,73] Relativistic

core potentials were used for rhodium and gold along with the standard Hay-Wadt double zeta basis set,[74] and augmented for rhodium by the optimized Rh 5p function of Couty and Hall.[75] The 6-31G(d,p) basis of Pople and co-workers[76,77] was applied to all other atoms. Optimized geometries were confirmed as energy minima by analytical frequency calculations. Time dependent calculations were initiated from the optimized geometry using the B3LYP exchange and correlation functionals. The calculations reported here are for molecules in the gas phase and no attempt has been made to correct for the effects of solvation. Canonical Kohn-Sham orbitals were imaged using the program Molekel, with the default isodensity values applied.[78,79]

3.6.6 Preparation of $Rh^{I}(dppm)_2Cl$ (2)

In a scintillation vial equipped with a stirbar, 68 mg $[Rh^{I}(COD)Cl]_2$ (0.138 mmol, 2 equiv) was dissolved in 2 mL of CH_2Cl_2 with stirring giving a light orange solution. 212 mg of dppm (0.551 mmol, 4 equiv) was then added as a solid affecting a color change to dark orange. The solution was allowed to stir for 1 hour and then 5 mL of Et_2O was added to give 214 mg of $Rh^{I}(dppm)_2Cl$ (86%) as an orange solid. ^{1}H NMR (CD_3CN) δ / ppm: 4.58 (bs, 4H), 7.27 (m, 16H), 7.40 (m, 8H), 7.48 (m, 16H). $^{31}P\{^{1}H\}$ NMR (CD_3CN) δ / ppm: –16.30 (d, $^{1}J_{Rh-P}$ = 115.9 Hz). Anal. Calc. for $C_{50}H_{44}ClP_4Rh$: C, 66.20; H, 4.89; N, 0. Found: C, 66.38; H, 5.11; N, 0.

3.6.7 Preparation of $Rh^{I}(dcpm)_2Cl$ (3)

In a scintillation vial equipped with a stirbar, 50 mg $[Rh^{I}(COD)Cl]_2$ (0.101 mmol, 2 equiv) was dissolved in 2 mL of CH_2Cl_2 with stirring giving a light orange solution. 166 mg of dcpm (0.406 mmol, 4 equiv) was then added as a solid affecting a color change to dark orange. The solution was allowed to stir for 1 hour and then 5 mL of Et_2O was added to give 123 mg of $Rh^{I}(dcpm)_2Cl$ (64%) as an orange solid. ^{1}H NMR ($CDCl_3$) δ / ppm: 1.12 (ovm, 40H), 1.55-1.75 (ovm, 40H), 1.93 (bs, 8H), 2.87 (pseudoquintet, 3.3 Hz, 4H). $^{31}P\{^{1}H\}$ NMR ($CDCl_3$) δ / ppm: –11.93 (d, $^{1}J_{Rh-P}$ = 111.1 Hz). Anal. Calc. for $C_{50}H_{92}P_4ClRh$: C, 62.85; H, 9.70; N, 0. Found: C, 63.23; H, 10.01; N, 0.

3.6.8 Preparation of $Rh^{I}(tfepma)_2Cl$ (4)

In a scintillation vial equipped with a stirbar, 58 mg $[Rh^{I}(COD)Cl]_2$ (0.118 mmol, 2 equiv) was dissolved in 2 mL of CH_2Cl_2 with stirring giving a light orange solution. 229 mg of tfepma (0.470 mmol, 4 equiv) was then added as a solid affecting a color change to light yellow.

The solution was allowed to stir for 1 hour and then 5 mL of pentane was added to give 168 mg of $Rh^{I}(tfepma)_2Cl$ (64%) as a light yellow powder. ^1H NMR ($CDCl_3$) δ / ppm: 2.57 (pseudoquintet, 5.5 Hz, 6H), 4.50-4.60 (bm, 8H), 4.65-4.75 (bm, 8H). $^{31}P\{^1H\}$ NMR ($CDCl_3$) δ / ppm: 109.8 (d, $^1J_{Rh-P}$ = 181.6 Hz). Anal. Calc. for $C_{18}H_{22}N_2O_8F_{24}P_4ClRh$: C, 19.43; H, 1.99; N, 2.52. Found: C, 19.56; H, 2.12; N, 2.44.

3.6.9 Preparation of $Rh^{I}Au^{I}(dppm)_2(CN^{t}Bu)_2(ClO_4)_2$ (5)

$Rh^{I}Au^{I}(dppm)_2(CN^{t}Bu)_2(ClO4)_2$ (**5**) was prepared by salt metathesis of **1** with a methanolic solution of $LiClO_4$ in an analogous fashion to anion exchange reactions of similar heterobimetallic complexes.[80] 198 mg of **1** (0.141 mmol, 1 equiv) was dissolved in 2 mL of MeOH under ambient atmosphere with stirring. 45 mg $LiClO_4$ (0.423 mmol, 3 equiv) was dissolved in 1 mL MeOH and added dropwise to the stirred solution of **1** immediately forming an orange precipitate. The reaction was allowed to stir for 10 minutes, filtered, washed with 1 mL MeOH, and then washed off the filter with CH_2Cl_2. Removal of the solvent in vacuo gave 156 mg (72%) of $Rh^{I}Au^{I}(dppm)_2(CN^{t}Bu)_2(ClO4)_2$ (**5**) as an orange solid. ^1H NMR (CD_3CN) δ / ppm: 0.645 (2, 18 H), 4.08 (pseudoquintet, 3.3 Hz, 4H), 7.37 – 7.49 (ovm, 24 H), 7.74 (q, 6.0 Hz, 8H), 7.95(q, 6.4 Hz, 8H). $^{31}P\{^1H\}$ NMR (CD_3CN) δ / ppm: 26.90 (dm, $^1J_{Rh-P}$ = 120.0 Hz), 37.69 (m). Anal. Calc. for $C_{60}H_{62}N_2O_8Cl_2P_4RhAu$: C, 50.26; H, 4.36; N, 1.95. Found: C, 50.77; H, 4.12; N, 1.66. IR(CH_2Cl_2) $\nu_{C\equiv N}$ /cm^{-1}: 2148. λ_{max} /nm (ε/$M^{-1}cm^{-1}$) in CH_2Cl_2: 347 (14400); 467 (18700). Crystals suitable for X-ray diffraction were grown from CH_2Cl_2/Et_2O layers as orange blocks.

3.6.10 Preparation of $Rh^{I}Au^{I}(dppm)_2(CN^{t}Bu)_2(PF_6)_2$ (6)

Prepared in an analogous procedure to that which gave 5, using 107 mg of **1** (0.082 mmol, 1 equiv) and 68 mg of $LiPF_6$ (0.207 mmol, 2.5 equiv) to give 111 mg (89%) of $Rh^{I}Au^{I}(dppm)_2(CN^{t}Bu)_2(PF_6)_2$ (**6**) as an orange solid. ^1H NMR (CD_3CN) δ / ppm: 0.61 (s, 18H) 4.01 (pseudoquintet, 4.4 Hz, 4H), 7.39 (m, 12 H), 7.55 (m, 12H), 7.70 (m, 8H), 7.39 (m, 8H). $^{31}P\{^1H\}$ NMR (CD_3CN) δ / ppm: –138.66 (quint, $^1J_{P-F}$ = 706.8 Hz), 29.39 (dm, $^1J_{Rh-P}$ = 120.5 Hz), 40.35 (m). Anal. Calc. for $C_{60}H_{62}N_2F_{12}P_6RhAu$: C, 47.26; H, 4.10; N, 1.84. Found: C, 47.16; H, 4.04; N, 1.75. λ_{max}/nm (ε/$M^{-1}cm^{-1}$) in CH_2Cl_2: 343 (10500); 456 (31600).

3.6.11 Preparation of $Rh^{I}Au^{I}(dppm)_2(CNdmp)_2Cl_2$ (7)

Prepared in a similar fashion to **1** , wherein 48 mg of $[Rh^{I}(COD)Cl]_2$ (0.097 mmol, 1 equiv) in 3 mL CH_2Cl_2, 150 mg dppm (0.390 mmol, 4 equiv), 51 mg 2,6-dimethylphenylisonitrile (0.389 mmol, 4 equiv), and 68 mg $Au^{I}(PEt_3)Cl$ (0.194 mmol, 2 equiv). After stirring for 1 hour, 5 mL Et_2O was added to afford 140 mg of $Rh^{I}Au^{I}(dppm)_2(CNdmp)_2Cl_2$ (51%) as a light orange solid. ^1H NMR (CD_3CN) δ / ppm: 1.53 (s, 12H), 4.56 (bs, 4H), 6.84 (d, 8.0 Hz, 4H), 7.05 (t, 8.0 Hz, 2H), 7.18 (b, 12H), 7.45 (b, 12H), 7.90 (b, 8H), 8.16 (b, 8H). $^{31}P\{^1H\}$ NMR (CD_3CN) δ / ppm: 31.21 (dm, $^1J_{Rh-P}$ = 101 Hz), 40.42 (m). Anal. Calc. for $C_{68}H_{62}N_2Cl_2P_4RhAu$: C, 58.26; H, 4.46; N, 2.00. Found: C, 58.44; H, 4.62; N, 1.84. λ_{max}/nm ($\varepsilon/M^{-1}cm^{-1}$) in CH_2Cl_2: 332 (10200); 446 (17700). Crystals suitable for X-ray diffraction were grown from CH_2Cl_2/pentane layers as orange blocks. Refinement of the RhAu core proceeded normally but extreme solvent disorder in the crystal lattice necessitated the employment of SQUEEZE to remove the disordered electron density. In this way 84 e^- were removed from a solvent accessible void of 880 $Å^3$, which corresponds well to four pentane molecules in the unit cell (one for each asymmetric unit). An ordered CH_2Cl_2 molecule was retained in the crystallographic model.

3.6.12 Preparation of $Rh^{I}Au^{I}(dppm)_2(CNdmp)_2(ClO_4)_2$ (8)

Prepared in a similar fashion to **5** and **6** using 76 mg of 6 (0.0542 mmol, 1equiv) in 1 mL MeOH and 14 mg $LiClO_4$ (0.132 mmol, 2.5 equiv) in 1 mL MeOH. An analogous workup to **5** and **6** gave 43 mg of $Rh^{I}Au^{I}(dppm)_2(CNdmp)_2(ClO_4)_2$ as an orange powder (52%). ^1H NMR (CD_3CN) δ / ppm: 1.491 (bs, 12H), 4.359 (pseudoquintet, 4.4 Hz, 4H), 6.89 - 8.00 ppm (ovm, 46 H). $^{31}P\{^1H\}$ NMR (CD_3CN) δ / ppm: 30.41 (dm, 116 Hz, 2P), 39.03 (m, 2P). Anal. Calc. for $C_{68}H_{62}N_2O_8Cl_2P_4RhAu•(CH_2Cl_2)$: C, 51.20; H, 3.66; N, 1.73. Found: C, 51.32; H, 3.47; N, 1.73. λ_{max}/nm ($\varepsilon/M^{-1}cm^{-1}$) in CH_2Cl_2: 350 (17700); 466 (20600). Crystals suitable for X-ray diffraction were grown from CH_2Cl_2/Et_2O vapor diffusion as yellow needles.

3.6.13 Preparation of $Rh^{I}Au^{I}(dcpm)_2(CN^{t}Bu)_2Cl_2$ (9)

In a scintillation vial equipped with a stirbar, 25 mg $[Rh^{I}(COD)Cl]_2$ (0.0507 mmol, 2 equiv rhodium) was dissolved in 2 mL CH_2Cl_2 with stirring giving an orange solution. 83 mg of dcpm (0.203 mmol, 4 equiv) was then added as a solid and the solution was allowed to stir for 5 minutes. 24 μL of *tert*-butylisonitrile (0.735 g/mL, 0.213 mmol, 4.2 equiv) was then added

effecting an immediate color change to dark red. 33 mg $Au^{I}(PEt_3)Cl$ (0.103 mmol, 2 equiv) was then added as a solid affecting a color change to orange. The vial was then allowed to stir in the dark for 3 hours at which time the solution was filtered and 5 mL pentane added to afford 102 mg of $Rh^{I}Au^{I}(dcpm)_2(CN^{t}Bu)_2Cl_2$ (**3**) as an orange powder (74%). ^{1}H NMR (CD_3CN) δ / ppm: 1.577 (s), 2.512 (broadened triplet, 3.8 Hz, 4H), the cyclohexyl protons appear as overlaping broad multiplets from 0.8 ppm to 2.0 ppm. $^{31}P\{^{1}H\}$ NMR (CD_3CN) δ / ppm: 35.73 (dm, 115 Hz, 2P), 55.20 (m, 2P). Anal. Calc. for $C_{60}H_{110}N_2Cl_2P_4RhAu$: C, 53.22; H, 8.19; N, 2.07. Crystals suitable for X-ray diffraction were readily obtained from CH_2Cl_2/Et_2O liquid layering, however the bimetallic core was disordered in crystal lattice obviating a straightforward solution, crystallizations from other solvent systems yielded similar results.

3.6.14 Preparation of $Rh^{I}Au^{I}(dcpm)_2(CN^{t}Bu)_2(ClO_4)_2$ (10)

In a scintillation vial equipped with a stirbar 39 mg of $Rh^{I}Au^{I}(dcpm)_2(CN^{t}Bu)_2Cl_2$ (**9**) (0.0291 mmol, 1 equiv) was dissolved in 2 ml MeOH under ambient atmosphere to give a clear orange solution. 9 mg $LiClO_4$ (0.0845 mmol, 3 equiv) was dissolved in MeOH and added dropwise to the stirred solution of **9**. An orange precipitate began to form immediately and after 5 minutes of stirring the solution was filtered, washed with MeOH (2 × 1 mL) and dried in vacuo to give 27 mg of $Rh^{I}Au^{I}(dcpm)_2(CN^{t}Bu)_2(ClO_4)_2$ (**10**) as an orange solid (63%). ^{1}H NMR (CD_3CN) δ / ppm: 1.572 (s), 2.475 (t, 4.3 Hz, 4H), the cyclohexyl protons appear as overlaping broadened multiplets from 0.8 ppm to 2.0 ppm. $^{31}P\{^{1}H\}$ NMR (CD_3CN) δ / ppm: 40.43 (dm, 115 Hz, 2P), 60.01 (m, 2P). Anal. Calc. for $C_{60}H_{110}N_2O_8Cl_2P_4RhAu$: C, 48.62; H, 7.48; N, 1.89. Found: C, 48.42; H, 7.49; N, 1.70. λ_{max}/nm (ε/$M^{-1}cm^{-1}$) in CH_2Cl_2: 273 (7000); 333 (8500); 461 (20700). Crystals suitable for X-ray diffraction were grown from CH_2Cl_2/Et_2O vapor diffusion as yellow needles.

3.6.15 Preparation of $Rh^{I}Au^{I}(tfepma)_2(CN^{t}Bu)_2Cl_2$ (12)

In a scintillation vial equipped with a stirbar, 154 mg $[Rh^{I}(COD)Cl]_2$ (0.312 mmol, 2 equiv rhodium) was dissolved in 2 mL of CH_2Cl_2 with stirring to give an orange solution. 608 mg of tfepma (1.25 mmol, 2 equiv per rhodium) was then added dropwise to cause the solution to turn green and subsequently gradually fade to yellow. The solution was stirred for 5 min at which time 145 μL of *tert*-butylisonitrile (0.735 g/mL, 1.31 mmol, 2.1 equiv per rhodium) was added. The solution immediately turned orange. 201 mg $Au^{I}(tht)Cl$ (0.625 mmol, 1 equiv per

rhodium) was added as a solid to give an orange solution. The vial was wrapped in aluminum foil and allowed to stir for 2 hrs during which time an orange precipitate formed. The yellow supernatant was decanted and the solid washed with pentane (2 × 5 mL) to give 781 mg of $Rh^{I}Au^{I}(tfepma)_2(CN^{t}Bu)_2Cl_2$ (**11**) (83% based on rhodium) as an orange solid. ^{1}H NMR (CD_3CN) δ / ppm: 1.454 (s, 18H), 2.983 (pseudotriplet, $^{3}J_{P-H}$ = 3.0 Hz, 6 H), 4.86 (bs, 16 H). $^{31}P\{^{1}H\}$ NMR (CD_3CN) δ / ppm: 136.9 (dm, $^{1}J_{Rh-P}$ = 172.3 Hz), 151.3 (m). Anal. Calc. for $C_{28}H_{40}N_4O_8F_{24}Cl_2P_4RhAu$: C, 22.25; H, 2.67; N, 3.71. Found: C, 22.29; H, 2.67; N, 3.68. λ_{max}/nm (ε/$M^{-1}cm^{-1}$) in CH_3CN: 307 (30800); 380 (9700); 419 (12400). Crystals suitable for X-ray diffraction were grown from CH_2Cl_2/pentane liquid layers as orange blocks.

3.6.16 Preparation of $[Rh^{II}Au^{II}(tfepma)_2(CN^{t}Bu)_2Cl_3]^{+}[Au^{I}Cl_2]^{-}$ (13)

In a scintillation vial equipped with a stirbar, 57 mg of $Rh^{I}Au^{I}(tfepma)_2(CN^{t}Bu)_2Cl_2$ (**11**) (0.0377 mmol, 1 equiv) was dissolved in 2 mL of CH_3CN and frozen in a coldwell. In a separate vial, 14.3 mg of $KAu^{III}Cl_4$ (0.0377 mmol, 1 equiv) was dissolved in 2 mL of CH_3CN and the solution was frozen in a coldwell. Both vials were brought out of the coldwell and, upon thawing, the $KAu^{III}Cl_4$ solution was added dropwise to the solution of **11** with stirring; the solution color turned from orange to red. The vial was covered in tin foil and the CH_3CN was stripped away to leave a solid, which was suspended in Et_2O (5 mL), filtered, washed with Et_2O (2 x 2 mL). The solid was washed from the filter with CH_2Cl_2 (2 mL), and the solvent was removed in vacuo to give 30 mg (44%) of $[Rh^{II}Au^{II}(tfepma)_2(CN^{t}Bu)_2Cl_3]^{+}$ $[Au^{I}Cl_2]^{-}$ (**12**) as a strawberry colored solid. ^{1}H NMR (CD_3CN) δ / ppm: 1.609 (s, 18H), 3.050 (pseudotriplet, 4.4 Hz, 6H), 4.61-4.72 (m, 8H), 4.99 (m, 4H), 5.79 (m, 4H). $^{31}P\{^{1}H\}$ NMR (CD_3CN) δ / ppm: 95.6-100.5 (ovm). Anal. Calc. for $C_{28}H_{40}N_4O_8F_{24}Cl_5P_4RhAu_2$: C, 18.53; H, 2.22; N, 3.09. Found: C, 18.68; H, 2.02; N, 3.06. λ_{max}/nm (ε/$M^{-1}cm^{-1}$) in CH_3CN: 329 (33000); 460 (4000). Crystals suitable for X-ray diffraction were grown from CH_2Cl_2/pentane layers as red blocks.

3.6.17 Preparation of Rh^{I}(PS[1])(COD)Cl (16)

In a scintillation vial equipped with a stirbar, 105 mg $[Rh^{I}(COD)Cl]_2$ (0.213 mmol, 2 equiv rhodium) was dissolved in 5 mL CH_2Cl_2 with stirring giving an orange solution. 131 mg PS(1) (0.425 mmol, 2 equiv) was then added as a solid giving an immediate color change to yellow. After stirring for one hour the solution was concentrated to ~2 mL and then 5 mL of pentane was layered on top giving 196 mg of Rh^{I}(PS[1])(COD)Cl (83%) as a light orange

powder. ^{1}H NMR ($CDCl_3$) δ / ppm: 1.91 (m, 2H), 2.04 (m, 2H), 2.38 (bs, 4H), 4.13 (d, $^{2}J_{P-H}$ = 5.1 Hz, 2H), 5.51 (bs, 2H), 7.13–7.30 (m, 5H), 7.41 (m, 4H), 7.79 (m, 4H). $^{31}P\{^{1}H\}$ NMR (CD_3CN) δ / ppm: 27.74 (d, $^{1}J_{Rh-P}$ = 149.5 Hz). Anal. Calc. for $C_{27}H_{29}ClPSRh$: C, 58.44; H, 5.27; N, 0. Found: C, 58.64; H, 5.19; N, 0. Crystals suitable for X-ray diffraction were grown from CH_2Cl_2/pentane layers as yellow blocks. Treatment of $[Rh^{I}(COD)Cl]_2$ with more than two equivalents of PS(1) did not induce displacement of COD, and instead gave only **16** and free PS(1) as observable products.

3.6.18 Preparation of $Rh^{I}(PS[1])_2(CO)Cl$ (17)

In a scintillation vial equipped with a stirbar 111 mg of $[Rh^{I}(CO)_2Cl]_2$ (0.0286 mmol, 2 equiv rhodium) was dissolved in 5 mL CH_2Cl_2 with stirring to give a yellow solution. 352 mg of PS(1) (1.14 mmol, 4 equiv) was added as a solid. The vial was capped after gas evolution ceased. After stirring for 1 hour the solution was concentrated to 2 mL and ~ 5 mL of pentane was layered on top giving 420 mg of $Rh^{I}(PS[1])_2COCl$ (94%) as a yellow powder. ^{1}H NMR ($CDCl_3$) δ / ppm: 4.23 (bs, 4H), 7.17 (m, 10H), 7.39 m (12H), 7.83 (m, 8H). $^{31}P\{^{1}H\}$ NMR ($CDCl_3$) δ / ppm: 25.64 (d, $^{1}J_{Rh-P}$ = 125.1 Hz). IR(CD_2Cl_2) $\nu_{C\equiv O}$ /cm^{-1}: 1978. Anal. Calc. for $C_{39}H_{34}OClP_2S_2Rh$: C, 59.81; H, 4.38; N, 0. Found: C, 59.35; H, 4.25; N, 0. Crystals suitable for X-ray diffraction were grown from CH_2Cl_2/pentane layers as yellow blocks

3.7 Crystallographic Tables

Table 3.6. Crystallographic data and structural refinement parameters for $Rh^{I}Au^{I}(dppm)_2(CN^{t}Bu)_2Cl_2$ (**1**), $Rh^{I}(dppm)_2Cl$ (**2**), and $[Rh^{I}(dppm)2]^{+}Cl^{-}$ (**2′**).

	1 • 3(CH_2Cl_2)	**2 • 2(THF)**	**2′ • (THF)**
Empirical formula	$C_{63}H_{68}N_2P_4Cl_8RhAu$	$C_{58}H_{59}O_2ClP_4Rh$	$C_{52}H_{44}OClP_4Rh$
Formula weight	1560.55	1050.29	939.11
Temperature	−123(2)°C	100(2)°C	−80(2)°C
Wavelength	0.71073 Å	0.71073 Å	0.71073 Å
Crystal system	Monoclinic	Monoclinic	Monoclinic
Space group	$P2_1/c$	Cc	$P2_1/n$
Unit cell dimensions	a = 26.651(4)Å	a = 12.404(3) Å	a = 9.8878(10) Å
	b = 13.2594(18)Å	b = 23.572(6) Å	b = 21.298(2) Å
	c = 18.991(3)Å	c = 18.255(5) Å	c = 21.629(2) Å
	α = 90°	α = 90°	α = 90°
	β = 102.282(3)°	β = 103.248(5)°	β = 103.049(2)°
	γ = 90°	γ = 90°	γ = 90°
Volume	6557.5(16)Å^3	5195.5(18) Å^3	4437.2(8) Å^3
Z	4	4	4
Density (calc)	1.581 Mg/m^3	1.343 Mg/m^3	1.406 Mg/m^3
Absorption coefficient	2.950 mm^{-1}	0.545 mm^{-1}	0.626 mm^{-1}
F(000)	3120	2184	1928
Crystal size (mm)	0.20 × 0.13 × 0.06	0.25 × 0.15 × 0.10	0.12 × 0.10 × 0.07
Θ range for data collection	0.78 to 23.29°	1.73 to 28.27°	1.36 to 28.28°
Index Ranges	$-29 \le h \le 26$	$-8 \le h \le 16$	$-13 \le h \le 12$
	$-12 \le k \le 14$	$-31 \le k \le 29$	$-12 \le k \le 28$
	$-21 \le \ell \le 20$	$-24 \le \ell \le 23$	$-28 \le \ell \le 28$
Reflections collected	30738	18691	31071
Ind. reflections	9425	8645	10944
Absorption correction	Empirical SADABS	Empirical SADABS	Empirical SADABS
Refinement method	Full–matrix ls on F^2	Full–matrix ls on F^2	Full–matrix ls on F^2
Data	9425	8645	10944
Restraints	685	2	0
Parameters	741	596	542
Goodness-of-fit on F^2 [a]	1.131	1.045	1.213
Final R indices [I>2σ(I)][b]	R_1 = 0.0683	R_1 = 0.0289	R_1 = 0.0603
	wR_2 = 0.1595	wR_2 = 0.0738	wR_2 = 0.1430
R indices (all data) [b]	R_1 = 0.0844	R_1 = 0.0301	R_1 = 0.0706
	wR_2 = 0.1661	wR_2 = 0.0747	wR_2 =0.1467
largest diff. peak	2.358 e/Å^3	0.573 e/Å^3	1.047 e/Å^3
largest diff. hole	−2.003 e/Å^3	−0.516 e/Å^3	−1.319 e/Å^3

[a] GOF = $[\Sigma w(F_o^2 - F_c^2)^2/(n-p)]^{1/2}$ (n = number of data, p = number of parameters varied.

[b] $R_1 = \Sigma||F_o| - |F_c||/\Sigma|F_o|$; $wR_2 = [\Sigma w(F_o^2 - F_c^2)^2/\Sigma wF_o^4]^{1/2}$.

Table 3.7. Crystallographic data and structural refinement parameters for $Rh^{I}Au^{I}(dppm)_2(CN^{t}Bu)_2(ClO4)_2$ (**5**), $Rh^{I}Au^{I}(dppm)_2(CNdmp)_2Cl_2$ (**7**), and $Rh^{I}Au^{I}(dppm)_2(CNdmp)_2(ClO_4)_2$ (**8**).

	5 • (CH_2Cl_2)	**7• (CH_2Cl_2)**[a]	**8**
Empirical formula	$C_{61}H_{62}N_2O_8P_4Cl_4RhAu$	$C_{72}H_{68}Cl_9N_2P4RhAu$	$C_{76}H_{74}Cl_2N_2O_8P4RhAu$
Formula weight	1524.68	1704.09	1694.07
Temperature	−173(2)°C	−173(2)°C	−173(2)°C
Wavelength	0.71073 Å	0.71073 Å	0.71073 Å
Crystal system	Monoclinic	Monoclinic	Orthorhombic
Space group	$P2_1/n$	*C2/c*	*Iba2*
Unit cell dimensions	a = 16.956(2)Å	a = 18.113(3) Å	a = 48.220(5) Å
	b = 16.375(2)Å	b = 21.133(3) Å	b = 14.2144(13) Å
	c = 23.812(3)Å	c = 21.473(3) Å	c = 22.6171(18) Å
	α = 90°	α = 90°	α = 90°
	β = 104.013(6)°	β = 92.239(7)°	β = 90°
	γ = 90°	γ = 90°	γ = 90°
Volume	6414.9(15)Å^3	8213.4(19) Å^3	15502(2) Å^3
Z	4	4	8
Density (calc)	1.579 Mg/m^3	1.378 Mg/m^3	1.452 Mg/m^3
Absorption coefficient	2.862 mm^{-1}	2.393 mm^{-1}	2.311 mm^{-1}
F(000)	3048	3404	6832
Crystal size (mm)	0.10 × 0.08 × 0.04	0.25 × 0.20 × 0.10	0.10 × 0.08 × 0.05
Θ range for data collection	1.33 to 28.35°	1.74 to 28.64°	0.84 to 23.28°
Index Ranges	$-22 \le h \le 22$	$-24 \le h \le 24$	$-53 \le h \le 53$
	$-21 \le k \le 21$	$-28 \le k \le 28$	$-15 \le k \le 15$
	$-31 \le \ell \le 31$	$-28 \le \ell \le 28$	$-25 \le \ell \le 25$
Reflections collected	155734	82181	106602
Ind. reflections	15962	10434	11142
Absorption correction	Empirical SADABS	Empirical SADABS	Empirical SADABS
Refinement method	Full–matrix ls on F^2	Full–matrix ls on F^2	Full–matrix ls on F^2
Data	15992	10434	11142
Restraints	0	0	3
Parameters	755	423	931
Goodness-of-fit on F^2 [b]	1.035	1.087	1.055
Final R indices	R_1 = 0.0329	R_1 = 0.0463	R_1 = 0.0361
[I>2σ(I)][c]	wR_2 = 0.0750	wR_2 = 0.1288	wR_2 = 0.0876
R indices (all data) [c]	R_1 = 0.0487	R_1 = 0.0494	R_1 = 0.0452
	wR_2 = 0.0820	wR_2 = 0.1313	wR_2 =0.0935
largest diff. peak	1.410 e/Å^3	3.030 e/Å^3	1.184 e/Å^3
largest diff. hole	−0.855 e/Å^3	−6.025 e/Å^3	−0.538 e/Å^3

[a] One molecule of disordered pentane removed using SQUEEZE.

[b] GOF = $[\Sigma w(F_o^2 - F_c^2)^2/(n-p)]^{1/2}$ (n = number of data, p = number of parameters varied.

[c] $R_1 = \Sigma||F_o| - |F_c||/\Sigma|F_o|$; $wR_2 = [\Sigma w(F_o^2 - F_c^2)^2/\Sigma wF_o^4]^{1/2}$.

Table 3.8. Crystallographic data and structural refinement parameters for $Rh^{I}Au^{I}(dcpm)_2(CN^tBu)_2(ClO_4)_2$ (**10**), the site disordered mixture of $Rh^{III}Au_2^{I,I}(dppm)_2Cl_4(CN)(CN^tBu)$ and $Rh^{III}Au_2^{I,I}(dppm)_2Cl_5(CN^tBu)$ (**11**), and $Rh^{I}Au^{I}(tfepma)_2(CN^tBu)_2Cl_2$ (**12**).

	10 • 3 (CH_2Cl_2)	**11**[a]	**12**
Empirical formula	$C_{63}H_{108}N_2O_8P_4Cl_8RhAu$	$C_{112}H_{106}N_4P_4Cl_8Rh_2Au_4$	$C_{28}H_{40}N_4O_8F_{24}P_4Cl_2RhAu$
Formula weight	1728.87	3033.05	1511.30
Temperature	−173(2)°C	−173(2)°C	−173(2)°C
Wavelength	0.71073 Å	0.71073 Å	0.71073 Å
Crystal system	Triclinic	Triclinic	Monoclinic
Space group	$P\bar{1}$	$P\bar{1}$	$P2_1/c$
Unit cell dimensions	a = 12.8725(9)Å	a = 10.2665(6) Å	a = 23.5341(13) Å
	b = 15.6008(11)Å	b = 13.1520(10) Å	b = 10.8576(6) Å
	c = 19.3341(14)Å	c = 44.751(2) Å	c = 22.7690(12) Å
	α = 91.615(2)°	α = 82.333(2)°	α = 90°
	β = 90.923(2)°	β = 89.922(2)°	β = 116.4540(10)°
	γ = 94.282(2)°	γ = 67.044(2)°	γ = 90°
Volume	3869.7(5)Å^3	5505.7(6) Å^3	5208.8(5) Å^3
Z	2	2	4
Density (calc)	1.484 Mg/m^3	1.830 Mg/m^3	1.927 Mg/m^3
Absorption coefficient	2.514 mm^{-1}	5.962 mm^{-1}	3.487 mm^{-1}
F(000)	1768	2936	2936
Crystal size (mm)	0.18 × 0.06 × 0.03	0.25 × 0.20 × 0.20	0.20 × 0.15 × 0.12
Θ range for data collection	1.05 to 28.34°	1.70 to 30.51°	0.97 to 28.27°
Index Ranges	$-17 \le h \le 17$	$-13 \le h \le 12$	$-29 \le h \le 31$
	$-20 \le k \le 20$	$-13 \le k \le 18$	$-12 \le k \le 14$
	$-25 \le \ell \le 25$	$-62 \le \ell \le 60$	$-29 \le \ell \le 30$
Reflections collected	68307	43732	36938
Ind. reflections	19176	29482	12896
Absorption correction	Empirical SADABS	Empirical SADABS	Empirical SADABS
Refinement method	Full–matrix ls on F^2	Full–matrix ls on F^2	Full–matrix ls on F^2
Data	19176	29482	12896
Restraints	0	0	0
Parameters	800	1244	657
Goodness-of-fit on F^2[b]	1.014	1.168	1.031
Final R indices [I>2σ(I)][c]	R_1 = 0.0519	R_1 = 0.0495	R_1 = 0.0334
	wR_2 = 0.0992	wR_2 = 0.1061	wR_2 = 0.0757
R indices (all data)[c]	R_1 = 0.0880	R_1 = 0.0606	R_1 = 0.0445
	wR_2 = 0.1150	wR_2 = 0.1126	wR_2 = 0.0827
largest diff. peak	1.775 e/Å^3	2.778 e/Å^3	1.606 e/Å^3
largest diff. hole	−1.432 e/Å^3	−2.305 e/Å^3	−1.302 e/Å^3

[a] Two chemically identical but crystallographically distinct molecules in the asymmetric unit.
[b] GOF = $[\Sigma w(F_o^2 - F_c^2)^2/(n-p)]^{1/2}$ (n = number of data, p = number of parameters varied.
[c] $R_1 = \Sigma||F_o| - |F_c||/\Sigma|F_o|$; $wR_2 = [\Sigma w(F_o^2 - F_c^2)^2/\Sigma wF_o^4]^{1/2}$.

Table 3.9. Crystallographic data and structural refinement parameters for $[Rh^{II}Au^{II}(tfepma)_2(CN^tBu)_2Cl_3]^+[Au^ICl_2]^-$ (**13**), *fac*-$Rh^{III}(tfepma)(CN^tBu)Cl_3$ (**14**) and $Au_2^{I,I}(tfepma)_2Cl_2$ (**15**), and $Rh^I(PS[1])(COD)Cl$ (**16**).

	13	**14/15**	**16**
Empirical formula	$C_{28}H_{40}N_4O_8F_{24}P_4Cl_5RhAu_2$	$C_{23}H_{31}N_3O_8F_{24}P_4Cl_4RhAu$	$C_{27}H_{29}ClPSRh_2$
Formula weight	1814.61	1499.06	554.89
Temperature	−173(2)°C	−173(2) °C	−173(2)°C
Wavelength	0.71073 Å	0.71073 Å	0.71073 Å
Crystal system	Monoclinic	Monoclinic	Monoclinic
Space group	$P2_1/n$	$P2_1/n$	Pc
Unit cell dimensions	a = 16.111(3) Å	a = 12.9108(14)Å	a = 11.615(2) Å
	b = 20.119(3) Å	b = 24.1573(3)Å	b = 9.4084(16) Å
	c = 17.299(3) Å	c = 16.0471(17)Å	c = 22.576(4) Å
	α = 90°	α = 90°	α = 90°
	β = 92.803(3)°	β = 103.708(4)°	β = 104.136(3)°
	γ = 90°	γ = 90°	γ = 90°
Volume	5600.5(16) Å^3	4862.4(9)Å^3	2392.4(7) Å^3
Z	4	4	4
Density (calc)	2.152 Mg/m^3	2.048 Mg/m^3	1.541 Mg/m^3
Absorption coefficient	5.995 mm^{-1}	3.840 mm^{-1}	0.993 mm^{-1}
F(000)	3456	2888	1136
Crystal size (mm)	0.25 × 0.20 × 0.18	0.20 × 0.10 × 0.05	0.12 × 0.10 × 0.08
Θ range for data collection	1.55 to 28.26°	1.55 to 26.44°	1.81 to 28.35°
Index Ranges	$-21 \le h \le 14$	$-16 \le h \le 13$	$-15 \le h \le 15$
	$-26 \le k \le 26$	$-30 \le k \le 26$	$-12 \le k \le 12$
	$-23 \le \ell \le 20$	$-19 \le \ell \le 20$	$-30 \le \ell \le 30$
Reflections collected	31787	29054	47735
Ind. reflections	13291	9971	11795
Absorption correction	Empirical SADABS	Empirical SADABS	Empirical SADABS
Refinement method	Full–matrix ls on F^2	Full–matrix ls on F^2	Full–matrix ls on F^2
Data	13291	9971	11795
Restraints	0	0	2
Parameters	693	628	560
Goodness-of-fit on F^2 [a]	1.010	1.094	1.060
Final R indices [I>2σ(I)] [b]	R_1 = 0.0299	R_1 = 0.0434	R_1 = 0.0402
	wR_2 = 0.0751	wR_2 = 0.1090	wR_2 = 0.0966
R indices (all data) [b]	R_1 = 0.0347	R_1 = 0.0607	R_1 = 0.0432
	wR_2 =0.0773	wR_2 = 0.1274	wR_2 = 0.1008
largest diff. peak	2.183 e/Å^3	1.727 e/Å^3	3.413 e/Å^3
largest diff. hole	−1.961 e/Å^3	−1.203 e/Å^3	−0.508 e/Å^3

[a] GOF = $[\Sigma w(F_o^2 - F_c^2)^2/(n-p)]^{1/2}$ (n = number of data, p = number of parameters varied.
[b] $R_1 = \Sigma||F_o| - |F_c||/\Sigma|F_o|$; $wR_2 = [\Sigma w(F_o^2 - F_c^2)^2/\Sigma wF_o^4]^{1/2}$.

Table 3.10. Crystallographic data and structural refinement parameters for $Rh^{I}(PS[1])_2(CO)Cl$ (**17**) and $Au_2^{I,I}(PS[1])_2(CF_3SO_3)_2$ (**18**).

	17	**18 • (CH_2Cl_2)**
Empirical formula	$C_{39}H_{34}ClOP_2S_2Rh$	$C_{42}H_{36}O_6F_6S_4P_4Cl_8Au_2$
Formula weight	783.08	1476.62
Temperature	−173(2)°C	−173(2)°C
Wavelength	0.71073 Å	0.71073 Å
Crystal system	Triclinic	Triclinic
Space group	$P\bar{1}$	$P\bar{1}$
Unit cell dimensions	a = 9.9386(6) Å	a = 10.0634(9)Å
	b = 9.9695(6) Å	b = 11.2829(9)Å
	c = 10.8622(7) Å	c = 12.2490(11)Å
	α = 82.3660(10)°	α = 70.662(2)°
	β = 63.2370(10)°	β = 71.778(2)°
	γ = 61.4040(10)°	γ = 80.026(2)°
Volume	839.04(9) $Å^3$	1242.76(19)$Å^3$
Z	1	1
Density (calc)	1.550 Mg/m^3	1.973 Mg/m^3
Absorption coefficient	0.841 mm^{-1}	6.411 mm^{-1}
$F(000)$	400	710
Crystal size (mm)	0.10 × 0.08 × 0.06	0.15 × 0.08 × 0.08
Θ range for data collection	2.11 to 28.30°	1.83 to 28.49°
Index Ranges	$-13 \le h \le 13$	$-13 \le h \le 13$
	$-11 \le k \le 13$	$-15 \le k \le 15$
	$-14 \le \ell \le 14$	$-16 \le \ell \le 16$
Reflections collected	7031	20479
Ind. reflections	3788	6222
Absorption correction	Empirical SADABS	Empirical SADABS
Refinement method	Full–matrix ls on F^2	Full–matrix ls on F^2
Data	3788	6222
Restraints	0	0
Parameters	224	364
Goodness-of-fit on F^2 [a]	1.059	1.056
Final R indices	R_1 = 0.0258	R_1 = 0.0240
$[I>2\sigma(I)]$ [b]	wR_2 = 0.0662	wR_2 = 0.0606
R indices (all data) [b]	R_1 = 0.0267	R_1 = 0.0253
	wR_2 =0.0669	wR_2 = 0.0612
largest diff. peak	1.009 e/$Å^3$	2.941 e/$Å^3$
largest diff. hole	−0.346 e/$Å^3$	−0.958 e/$Å^3$

[a] GOF = $[\Sigma w(F_o^2 - F_c^2)^2/(n - p)]^{1/2}$ (n = number of data, p = number of parameters varied.

[b] $R_1 = \Sigma||F_o| - |F_c||/\Sigma|F_o|$; $wR_2 = [\Sigma w(F_o^2 - F_c^2)^2/\Sigma wF_o^4]^{1/2}$.

3.8 References

(1) Crabtree, R. H. *The Organometallic Chemistry of the Transition Metals*; Wiley: New York, 1994.

(2) Collman, J. P.; Hegedus, L. S.; Norton, J. R.; Finke, R. G. *Principles and Applications of Organotransition Metal Chemistry*; University Science Books, Sausalito CA, 1987.

(3) Manke, D. R.; Loh, Z.-H.; Nocera, D. G. *Inorg. Chem.* **2004**, *43*, 3618-3624.

(4) Schmidbaur, H.; Franke, R. *Angew. Chem.* **1973**, *85*, 449-450.

(5) Schmidbaur, H.; Franke, R. *Inorg. Chim. Acta* **1975**, *13*, 85-89.

(6) Schmidbaur, H.; Wohlleben, A.; Schubert, U.; Frank, A.; Huttner, G. *Chem. Ber.* **1977**, *110*, 2751-2757.

(7) Jandik, P.; Schubert, U.; Schmidbaur, H. *Angew. Chem.* **1982**, *94*, 74-75.

(8) Fackler, J. P., Jr.; Basil, J. D. *Organometallics* **1982**, *1*, 871-873.

(9) Schmidbaur, H.; Jandik, P. *Inorg. Chim. Acta* **1983**, *74*, 97-99.

(10) Fackler, J. P., Jr.; Murray, H. H.; Basil, J. D. *Organometallics* **1984**, *3*, 821-823.

(11) Murray, H. H.; Fackler, J. P., Jr.; Mazany, A. M. *Organometallics* **1984**, *3*, 1310-1311.

(12) Dudis, D. S.; Fackler, J. P., Jr. *Inorg. Chem.* **1985**, *24*, 3758-3762.

(13) Basil, J. D.; Murray, H. H.; Fackler, J. P., Jr.; Tocher, J.; Mazany, A. M.; Trzcinska-Bancroft, B.; Knachel, H.; Dudis, D.; Delord, T. J.; Marler, D. *J. Am. Chem. Soc.* **1985**, *107*, 6908-6915.

(14) Murray, H. H.; Fackler, J. P., Jr.; Tocher, D. A. *J. Chem. Soc., Chem. Commun.* **1985**, 1278-1280.

(15) King, C.; Wang, J. C.; Khan, M. N. I.; Fackler, J. P., Jr. *Inorg. Chem.* **1989**, *28*, 2145-2149.

(16) Murray, H. H.; Porter, L. C.; Fackler, J. P., Jr.; Raptis, R. G. *J. Chem. Soc., Dalton Trans.* **1988**, 2669-2674.

(17) Raptis, R. G.; Fackler, J. P., Jr.; Basil, J. D.; Dudis, D. S. *Inorg. Chem.* **1991**, *30*, 3072-3075.

(18) Fackler, J. P. Jr. *Inorg. Chem.* **2002**, *41*, 6959-6972.

(19) Schmidbaur, H.; Schier, A. *Sci. Synth.* **2004**, *3*, 691-761.

(20) Mazany, A. M.; Fackler, J. P., Jr. *J. Am. Chem. Soc.* **1984**, *106*, 801-806.

(21) Murray, H. H.; Garzón, G.; Raptis, R. G.; Mazany, A. M.; Porter, L. C.; Fackler, J. P., Jr. *Inorg. Chem.* **1988**, *27*, 836-842.

(22) Manke, D. R. PhD Thesis. Massachusetts Institute of Technology, 2005.

(23) Langrick, C. R.; McEwan, D. M.; Pringle, P. G.; Shaw, B. L. *J. Chem. Soc., Dalton Trans.* **1983**, 2487-2493.

(24) Langrick, C. R.; Pringle, P. G.; Shaw, B. L. *J. Chem. Soc., Dalton Trans.* **1984**, 1233-1238.

(25) Cooper, G. R.; Hutton, A. T.; Langrick, C. R.; McEwan, D. M.; Pringle, P. G.; Shaw, B. L. *J. Chem. Soc., Dalton Trans.* **1984**, 855-862.

(26) Hassan, F. S. M.; Markham, D. P.; Pringle, P. G.; Shaw, B. L. *J. Chem. Soc., Dalton Trans.* **1985**, 279-283.

(27) Langrick, C. R.; Shaw, B. L. *J. Chem. Soc., Dalton Trans.* **1985**, 511-516.

(28) Kim, H. P.; Fanwick, P. E.; Kubiak, C. P. *J. Organomet. Chem.* **1988**, *346*, C39-C42.

(29) Yip, H.-K.; Lin, H.-M.; Wang, Y.; Che, C.-M. *Inorg. Chem.* **1993**, *32*, 3402-3407.

(30) Balch, A. L.; Catalano, V. J.; Olmstead, M. M. *Inorg. Chem.* **1990**, *29*, 585-586.

(31) Balch, A. L.; Catalano, V. J. *Inorg. Chem.* **1991**, *30*, 1302-1308.

(32) Manojlović-Muir, L.; Henderson, A. N.; Treurnicht, I.; Puddephatt, R. J. *Organometallics* **1989**, *8*, 2055-2061.

(33) Yip, H.-K.; Che, C.-M.; Peng, S.-M. *J. Chem. Soc., Chem. Commun.* **1991**, 1626-1628.

(34) Yip, H.-K.; Lin, H.-M.; Wang, Y.; Che, C.-M. *J. Chem. Soc., Dalton Trans.* **1993**, 2939-2944.

(35) Yip, H.-K.; Lin, H.-M.; Cheung, K.-K.; Che, C.-M.; Wang, Y. *Inorg. Chem.* **1994**, *33*, 1644-1651.

(36) Xu, C.; Anderson, G. K.; Brammer, L. Wilking-Braddock, J.; Rath, N. P. *Organometallics* **1996**, *15*, 3972-3979.

(37) Xia, B.-H.; Zhang, H.-X.; Che, C.-M.; Leung, K.-H.; Phillips, D. L.; Zhu, N.; Zhou, Z.-Y. *J. Am. Chem. Soc.* **2003** *125*, 10362-10374.

(38) For some examples of studies related to $d^8\cdots d^8$ interactions see: (a) Dallinger, R. F.; Miskowski, V. M.; Gray, H. B.; Woodruff, W. H. *J. Am. Chem. Soc.* **1981**, *103*, 1595-1596. (b) Rice, S. F.; Gray, H. B. *J. Am. Chem. Soc.* **1981**, *103*, 1593-1595. (c) Rice, S. F.; Milder, S. J.; Gray, H. B. *Coord. Chem. Rev.* **1982**, *43*, 349-354. (d) Stiegman, A. E.; Rice, S. F.; Gray, H. B.; Miskowski, V. M. *Inorg. Chem.* **1987**, *26*, 1112-1116. (e) Rice, S. F.; Miskowski, V. M.; Gray, H. B. *Inorg. Chem.* **1988**, *27*, 4704-4708. (f) Che, C.-M.; Yam, V. W.-W.; Wong, W.-T.; Lai, T.-F. *Inorg. Chem.* **1989**, *28*, 2908-2910. (g) Yip, H.-K.; Lai, T.-F.; Che, C.-M. *J. Chem. Soc., Dalton Trans.* **1991**, 1639-1641. (h) Bailey, J. A.; Miskowski, V. M.; Gray, H. B. *Inorg. Chem.* **1993**, *32*, 369-370. (i) Yip, H.-K.; Cheng, L.-K.; Cheung, K.-K.; Che, C.-M. *J. Chem. Soc., Dalton Trans.* **1993**, 2933-2938. (j) Navarro, J. A. R.; Romero, M. A.; Salas, J. M.; Quirós, M.; Bahraoui, J. E.; Molina, J. *Inorg. Chem.* **1996**, *35*, 7829-7835. (k) Lai, S.-W.; Chan, M. C.-W.; Cheung, T.-C.; Peng, S.-M.; Che, C.-M. *Inorg. Chem.* **1999**, *38*, 4046-4055. (l) Xia, B.-H.; Che, C.-M.; Phillips, D. L.; Leung, K.-H.; Cheung, K.-K. *Inorg. Chem.* **2002**, *41*, 3866-3875. (m) Xia, B.-H.; Che, C.-M.; Zhou, Z.-Y. *Chem. Eur. J.* **2003**, *9*, 3055-3064.

(39) For some examples of studies related to $d^{10}\cdots d^{10}$ interactions see: (a) Harvey, P. D.; Gray, H. B. *J. Am. Chem. Soc.* **1988**, *110*, 2145-2147. (b) Che, C.-M.; Kwong, H.-L.; Yam, V. W.-W.; Cho, K. C. *J. Chem. Soc., Chem. Commun.* **1989**, 885-886. (c) King, C.; Wang, J.-C.; Khan, M. N. I.; Fackler, J. P., Jr. *Inorg. Chem.* **1989**, *28*, 2145-2149. (d) Perreault, D.; Drouin, M.; Michel, A.; Miskowski, V. M.; Schaefer, W. P.; Harvey, P. D. *Inorg. Chem.* **1992**, *31*, 695-702. (e) Fu, W.-F.; Chan, K.-C.; Miskowski, V. M.; Che, C.-

M. *Angew. Chem., Int. Ed.* **1999**, *38*, 2783-2785. (f) Leung, K.-H.; Phillips, D. L.; Tse, M.-C.; Che, C.-M.; Miskowski, V. M. *J. Am. Chem. Soc.* **1999**, *121*, 4799-4803. (g) Che, C.-M.; Mao, Z.; Miskowski, V. M.; Tse, M.-C.; Chan, C.-K.; Cheung, K.-K.; Phillips, D. L.; Leung, K.-H. *Angew. Chem., Int. Ed.* **2000**, *39*, 4084-4088. (h) Che, C.-M.; Tse, M.-C.; Chan, M. C. W.; Cheung, K.-K.; Phillips, D. L.; Leung, K.-H. *J. Am. Chem. Soc.* **2000**, *122*, 2464-2468. (i) Rawashdeh-Omary, M. A.; Omary, M. A.; Patterson, H. H.; Fackler, J. P., Jr. *J. Am. Chem. Soc.* **2001**, *123*, 11237-11247. (j) Fu, W.-F.; Chan, K.-C.; Cheung, K.-K.; Che, C.-M. *Chem. Eur. J.* **2001**, *7*, 4656-4664. (k) Zhang, H.-X.; Che, C.-M. *Chem. Eur. J.* **2001**, *7*, 4887-4893.

(40) Striplin, D. R.; Crosby, G. A. *J. Phys. Chem.* **1995**, *99*, 7977-7984.

(41) Striplin, D. R.; Crosby, G. A. *J. Phys. Chem.* **1995**, *99*, 11041-11045.

(42) Dempsey, J. L.; Esswein, A. J.; Manke, D. R.; Rosenthal, J.; Soper, J. D.; Nocera, D. G. *Inorg. Chem.* **2005**, *44*, 6879-6892.

(43) McKee, M. L.; Hill, W. E. *J. Chem. Phys. A* **2002**, *106*, 6201-6205.

(44) Barklay, J. V.; Ellis, M.; Higgins, S. J.; McCart, M. K. *Organometallics* **1998**, *17*, 1725-1731.

(45) Pyykkö, P. *Chem. Rev.* **1988**, *88*, 563-94.

(46) Pyykkö, P. *Angew. Chem., Intl. Ed.* **2004**, *43*, 4412-4456.

(47) Pyykkö, P. *Inorg. Chim. Acta* **2005**, *358*, 4113-4130.

(48) Nakano, H.; Nakajima, T.; Tsuneda, T.; Hirao, K. in *Theory and Applications of Computational Chemistry: The First Forty Years*; Dykstra, C., Ed.; Elsevier B.V., Amsterdam, Netherlands; 2005; p 507-557.

(49) Gorin, David J.; Toste, F. D. *Nature* **2007**, *446*, 395-403.

(50) See for Example: van Zyl, W. E.; Lopez-de-Luzuriaga, J. M.; Mohamed, A. A.; Staples, R. J.; Fackler, J. P., Jr. *Inorg. Chem.* **2002**, *41*, 4579-4589.

(51) Nocera, D. G. *Acc. Chem. Res.* **1995**, *28*, 209-217.

(52) See for Example: Wolfsberg, M.; Helmholtz, L. *J. Phys. Chem.* **1952**, *20*, 837-843.

(53) As determined from a search of the Cambridge Structural Database; no matches were obtained for direct Rh–Au linkages in these formal oxidation states.

(54) Kadis, J.; Shin, Y.-g. K.; Ward, D. L.; Nocera, D. G. *Inorg. Chem.* **1996**, *35*, 811-817.

(55) Liau,; R.-L.; Mathieson, T.; Schier, A.; Berger, R. J. F.; Runeberg, N.; Schmidbaur, H. *Z. Naturforsch. B* **2002**, 57, 881-889.

(56) Cotton, F. A.; Dunbar, K. R.; Eagle, C. T.; Falvello, L. R.; Kang, S.-J.; Price, A. C.; Verbruggen, M. G. *Inorg. Chim. Acta.* **1991**, *184*, 35-42.

(57) Sanger, A. R. *Can. J. Chem.* **1982**, 2214-2219.

(58) Fernandez, E. J.; Lopez-de-Luzuriaga, J. M.; Monge, M.; Rodriguez, M. A.; Crespo, O.; Gimeno, Concepcion, M.; Laguna, A.; Jones, P. G. *Inorg. Chem.* **1998**, *37*, 6002-6006.

(59) Nilsson, B. L.; Kiessling, L. L.; Raines, R. T. *Org. Lett.* **2001**, *3*, 9-12.

(60) Armarego, W. L. F.; Perrin, D. D. *Purification of Laboratory Chemicals*, 4th ed.; Butterworth-Heinmann: Oxford, 1996.

(61) Mendía, A.; Cerrada, E.; Laguna, M.; Johnston, D. H.; Lettan, R. B. II *Inorg. Synth.* **2004**, *34*, 85-91.

(62) Usón, R.; Laguna, A.; Laguna, M. *Inorg. Synth.* **1989**, *26*, 85-91.

(63) Usón, R.; Laguna, A.; Navarro, A.; Parish, R. V.; Moore, L. S. *Inorg. Chim. Acta,* **1986**, *112*, 205-208.

(64) Nixon, J. F. *J. Chem. Soc. A* **1968**, 2689-2692.

(65) Ganesan, M; Krishnamurthy, S. S.; Nethaji, M. *J. Organomet. Chem.* **1998**, *570*, 247-254.

(66) Balakrishna, M. S.; Prakasha, T. K.; Krishnamurthy, S. S.; Siriwardane, U; Hosmane, N. S. *J. Organomet. Chem.* **1990**, *390*, 203-216.

(67) Sekabunga, E. J.; Smith, M. L.; Webb, T. R.; Hill, W. E. *Inorg. Chem.* **2002**, *41*, 1205-1214.

(68) Loh, Z.-H.; Miller, S. E.; Chang, C. J.; Carpenter, S. D.; Nocera, D. G. *J. Phys. Chem. A* **2002**, *106*, 11700-11708.

(69) Damrauer, N. H.; Hodgkiss, J. M.; Rosenthal, J.; Nocera, D. G. *J. Phys. Chem. B* **2004**, *108*, 6315-6321.

(70) Frisch, M. J.; Trucks, G. W.; Schlegel, H. B.; Scuseria, G. E.; Robb, M. A.; Cheeseman, J. R.; Zakrzewski, V. G.; Montgomery, J. A., Jr.; Stratmann, R. E.; Burant, J. C.; Dapprich, S.; Millam, J. M.; Daniels, A. D.; Kudin, K. N.; Strain, M. C.; Farkas, O.; Tomasi, J.; Barone, V.; Cossi, M.; Cammi, R.; Mennucci, B.; Pomelli, C.; Adamo, C.; Clifford, S.; Ochterski, J.; Petersson, G. A.; Ayala, P. Y.; Cui, Q.; Morokuma, K.; Malick, D. K.; Rabuck, A. D.; Raghavachari, K.; Foresman, J. B.; Cioslowski, J.; Ortiz, J. V.; Stefanov, B. B.; Liu, G.; Liashenko, A.; Piskorz, P.; Komaromi, I.; Gomperts, R.; Martin, R. L.; Fox, D. J.; Keith, T.; Al-Laham, M. A.; Peng, C. Y.; Nanayakkara, A.; Gonzalez, C.; Challacombe, M.; Gill, P. M. W.; Johnson, B. G.; Chen, W.; Wong, M. W.; Andres, J. L.; Head-Gordon, M.; Replogle, E. S.; Pople, J. A.; Gaussian 98, Revision A.9: Gaussian, Inc.: Pittsburg, PA, 1998.

(71) Becke, A. D. *J. Chem. Phys.* **1993**, *98*, 5648-5642.

(72) Lee, C.; Yang, W.; Parr, R. G. *Phys. Rev. B* **1988**, *37*, 785-789.

(73) Miehlich, B.; Savin, A.; Stoll, H.; Preuss, H. *Chem. Phys. Lett.* **1989**, *157*, 200-206.

(74) Hay, P. J.; Wadt, W. R. *J. Chem. Phys.* **1985**, *82*, 270-283; 284-298; 299-310.

(75) Couty, M.; Hall, M. B. *J. Comput. Chem.* **1996**, *11*, 1359-1370.

(76) Hariharan, P. C.; Pople, J. A. *Theor. Chim. Acta* **1973**, *28*, 213-222.

(77) Francl, M. M.; Pietro, W. J.; Hehre, W. J.; Binkley, J. S.; Gordon, M. S.; DeFrees, D. J.; Pople, J. A. *J. Chem. Phys.* **1982**, *77*, 3654-3655.

(78) Flükiger, P.; Lüthi, H. P.; Portmann, S.; Weber, J. *MOLEKEL 4.3*; Swiss Center for Scientific Computing: Manno, Switzerland, 2000-2002.

(79) Portmann, S.; Lüthi, H. P. MOLEKEL: An Interactive Molecular Graphics Tool. *Chimia* **2000**, *54*, 766-770.

(80) For example see: Balch, A. L.; Catalano, V. J. *Inorg. Chem.* **1992**, *31*, 3934-3942.

Chapter 4:

Organometallic Chemistry of Two-electron Mixed Valence Diiridium Cores

Portions of this work will appear:

Esswein, A. J.; Veige, A. S.; Nocera, D. G.; Piccoli, M. B. P.; Schultz, A. J. *Submitted to Organometallics.*

4.1 *Introduction*

The previous chapters have been primarily concerned with multielectron chemistry of solar energy conversion from the standpoint of the reduction of HX ($X = Cl^-$, Br^-) to molecular hydrogen. The two-electron mixed valence dirhodium diphosphazane complexes employed in that work achieve the multielectron redox chemistry attendant to hydrogen photocatalysis by building structural and electronic asymmetry into the ground state.[1–4] These complexes provided a key example of bimetallic cooperation,[5,6] wherein the affixed metal centers affect chemistry otherwise unattainable by mononuclear complexes. In an ideal implementation of M–M dimers, chemical transformations can be carried out on one half of the dimer, while the adjacent metal center holds in reserve electron equivalents and open coordination sites for substrate attack.[7,8] This reactivity mode is precisely observed with dirhodium dfpma (dfpma = bis(difluorophosphino) methylamine, $CH_3N[PF_2]_2$) complexes, wherein the HX photocatalysis was proposed to proceed via two oxidative additions of HX to a bimetallic $Rh_2^{0,0}$ core.[9] The success of this system is predicated on the intimate cooperation of both metal centers within the bimetallic core and also the unusual ability of the bimetallic core to support four electron redox chemistry in discrete two-electron steps.

The internal electronic asymmetry of two-electron mixed valence complexes enables the activation of small molecules such as H_2,[9–12] HX ($X = Cl^-$, Br^-),[13] H_2O and NH_3,[14] in multi-electron steps. Detailed mechanistic studies suggest that H–H bonds can be formed photochemically by $Rh_2^{II,II}(H)_2X_2$ cores[9] and activated reversibly over the two-electron mixed valence core of $Ir_2^{0,II}(tfepma)_3Cl_2$ (tfepma = (bis[bis(trifluoroethoxy)phosphino]methylamine, $MeN[P(OCH_2CF_3)_2]_2$).[10–12] In all cases the bimetallic cooperation attendant to hydrogen activation is mediated by a bridging hydride intermediate and is accompanied by significant reorganization of the flexible tfepma ligands.[11] With this precedent, two-electron mixed valence complexes have shown a considerable propensity for facilitating the bond formation and cleavage of H–H bonds, but as of yet the application of these unique dinuclear cores to the organometallic chemistry of C–H bond formation/cleavage has remained undeveloped. This chapter sets out to explore the bimetallic cooperation of HX (X = alkyl, aryl) activation facilitated by the two-electron mixed valence complex $Ir_2^{0,II}(tfepma)_3Cl_2$ in order to expand the scope of multielectron redox chemistry of consequence to covalent bond formation/cleavage beyond simple small molecules such as H_2 to larger organic functionalities.

4.2 *Diiridium C–H Bond Activations*

4.2.1 Phenyl sp^2 Activation

The two-electron mixed valent diiridium complex $Ir_2^{0,II}(tfepma)_3Cl_2$ (**1**)[15] was chosen as an entry point into the C–H bond activation chemistry of interest of this chapter, due to proximity of readily functionalizable halides on the Ir^{II} center adjacent to an electron rich Ir^0 center. When two equivalents of C_6H_5MgBr are added to a cold green/brown THF solution of **1**, the color immediately fades, and after warming to room temperature a pale yellow solution persists (Scheme 4.1). The solid-state structure revealed the bridging benzyne complex $Ir_2^{II,II}(tfepma)_3(\mu\text{-}C_6H_4)(C_6H_5)H$ (**2**) presented in Figure 4.1 (selected bond lengths and angles are listed in Table 4.1). The formation of complex **2** from **1** necessitates considerable rearrangement of the bimetallic core and is the direct result of intramolecular ortho C–H bond activation of one of coordinated phenyl groups at the formerly low valent Ir^0 center.

Scheme 4.1.

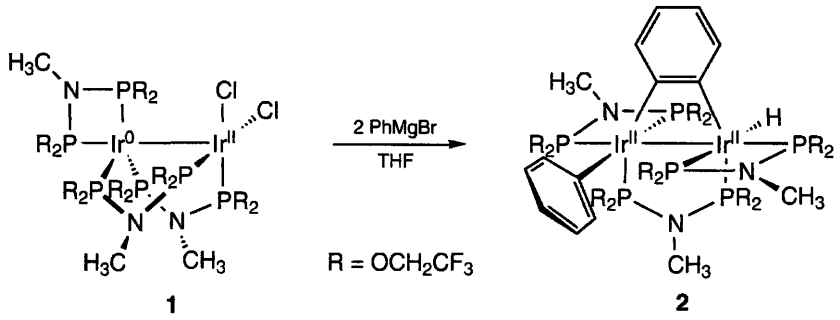

The core of the complex **2** is comprised of two octahedral Ir^{II} metal centers with an Ir–Ir bond distance of 2.7472(4) Å. The coordination spheres about each iridium center are similar, with the only exception being the terminal coordination of a phenyl group and a hydride bound to Ir(1) and Ir(2) respectively. The hydride was located crystallographically but was fixed at an idealized distance of 1.600 Å, and thus will not be the subject of metrical discussions. The coordination of a hydride trans to P(6) was also evidenced by a conspicuous open coordination site ($\angle$C(5)–Ir(2)–P(4) = 162.71(11)° and $\angle$P(5)–Ir(2)–Ir(1) = 166.95(3)°) in the early refinement cycles. The presence of one bridging and two chelating tfepma ligands represents the first occurrence of this geometric motif within this ligand system. The flexibility of the PNP backbone in the tfepma ligands is evidenced by their ability to accommodate both the tight bite angles required for chelating the iridium centers ($\angle$P(1)–N(1)–P(2) = 99.63(18)° and $\angle$P(5)–

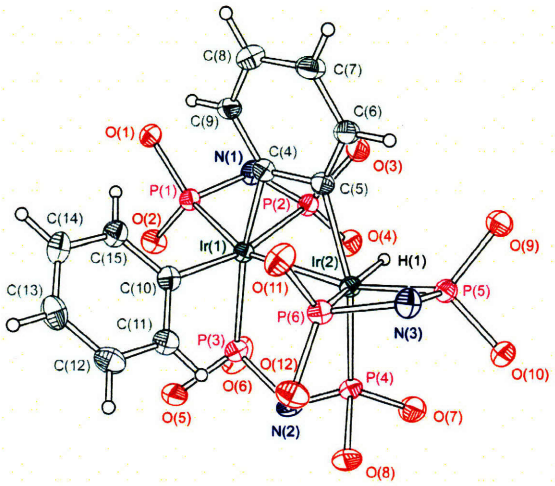

Figure 4.1. X-ray structure of $Ir_2^{II,II}(tfepma)_3(\mu\text{-}C_6H_4)(C_6H_5)H$ (**2**), thermal ellipsoids drawn at the 50% probability level. Bridgehead –Me and $-CH_2CF_3$ groups of the tfepma ligands are omitted for clarity.

Table 4.1. Bond Lengths (Å) and Angles (°) for $Ir_2^{II,II}(tfepma)_3(\mu\text{-}C_6H_4)(C_6H_5)H$ (**2**).

Bond Lengths (Å)					
Ir(1)–Ir(2)	2.7472(4)	Ir(1)–P(1)	2.2798(10)	Ir(2)–P(4)	2.2532(10)
Ir(1)–C(4)	2.092(4)	Ir(1)–P(2)	2.2770(10)	Ir(2)–P(5)	2.2228(10)
Ir(1)–C(10)	2.125(4)	Ir(1)–P(3)	2.2652(11)	Ir(2)–P(6)	2.3197(11)
Ir(2)–C(5)	2.117(4)				
Bond Angles (°)					
P(5)–Ir(2)–Ir(1)	166.95(3)	P(2)–Ir(1)–C(10)	167.87(11)	P(3)–N(2)–P(4)	120.9(12)
C(5)–Ir(2)–P(4)	162.71(11)	P(1)–N(1)–P(2)	99.63(18)	P(5)–N(3)–P(6)	99.05(18)
C(4)–Ir(1)–Ir(2)	71.34(11)	P(1)–Ir(1)–P(2)	69.09(4)	P(5)–Ir(2)–P(6)	68.74(4)
C(5)–Ir(2)–Ir(1)	71.38(11)				

N(3)–P(6) = 99.05(18)°) and the expanded angle for bridging the dinuclear core (∠P(3)–N(2)–P(4) = 120.9(2)°). The most prominent feature of this structure is the parallel, dinuclear spanning benzyne ligand. Benzyne complexes are not uncommon, but are typically encountered when bound to mono-, tri-, or higher nuclear low oxidation state metals and metal-clusters. Mononuclear benzyne complexes of both early and late metals have been the subject of recent reviews.[16,17] Bound to a single metal, the C–C bond distance is usually short, reflecting a carbon-carbon multiple bond greater than two, but the cluster bound aryne derivatives have C–C bonds closer to typical sp^2 connections.[18] Discrete bimetallics exhibiting benzyne bridges have seen some precedent.[19–23]

In **2** we find a C(4)–C(5) bond length to be 1.405(5) Å which fits the cluster bound benzyne model and can viewed as an aromatic $C_6H_4^{2-}$ moiety in which two mutually ortho protons have been substituted for iridium. To compare, the Ir(1)–C(4) and Ir(2)–C(5) bond

lengths of 2.092(4) and 2.117(4) Å, respectively, are nearly equivalent, and only marginally shorter than the sp^2 bound phenyl (Ir(1)–C(10) = 2.125(4) Å). The constrained four-atom ring created by the bridging benzyne and iridium atoms distorts the octahedral geometry of the $Ir_2^{II,II}$ core (Ir(1): ∠C(15)–Ir(1)–Ir(2) = 71.5(2)°, Ir(2): ∠C(10)–Ir(2)–Ir(1) = 71.0(3)°) and the angles around the Ir–C atom connections (C(10): (∠Ir(10)–C(10)–C(15) = 108.1(6)° and ∠C(11)–C(10)–Ir(2) = 131.6(7)°, C(15): ∠Ir(1)–C(15)–C(10) = 109.1(6)° and ∠C(14)–C(15)–Ir(1) = 131.6(7)°). Notably the Ir(2)–P(6) bond length of 2.3197(11) Å is markedly longer than the corresponding Ir(1)–P(2) bond length of 2.2770(10) Å, reflecting the significant trans influence of the hydride ligated to Ir(2). All other bond lengths and angles within the terminally bound and bridging aromatic rings are normal.

In solution, complex **2** appears to retain its solid state structure. An ^1H NMR spectrum of **2** obtained in THF-d_8 reveals an Ir–H resonance at –13.73 ppm as a doublet of doublet of triplets that exhibits coupling to its trans ($^2J_{P-H}$ = 244.8 Hz) and cis ($^2J_{P-H}$ = 20.4 Hz, 10.2 Hz) phosphorus neighbors, Figure 4.2 right. The resonances for the N–Me groups on the diphosphazane ligand appear as three triplets at 2.73 ppm ($^3J_{P-H}$ = 8.9 Hz), 2.82 ppm ($^3J_{P-H}$ = 10.2 Hz), and 2.83 ppm ($^3J_{P-H}$ = 6.4 Hz), Figure 4.2 center. The doubly chelating and one bridging binding motif observed in the solid state for **2** allows for the assignment of the resonances at 2.73 and 2.83 ppm as those that chelate the iridium centers. It is interesting to note that the observed coupling constants for the chelating tfepma ligands are larger than that of the bridging tfepma N–Me resonance by ~ 2 Hz. The trifluoroethoxy proton resonances are characteristically highly complicated and are observed as overlapping multiplets where no

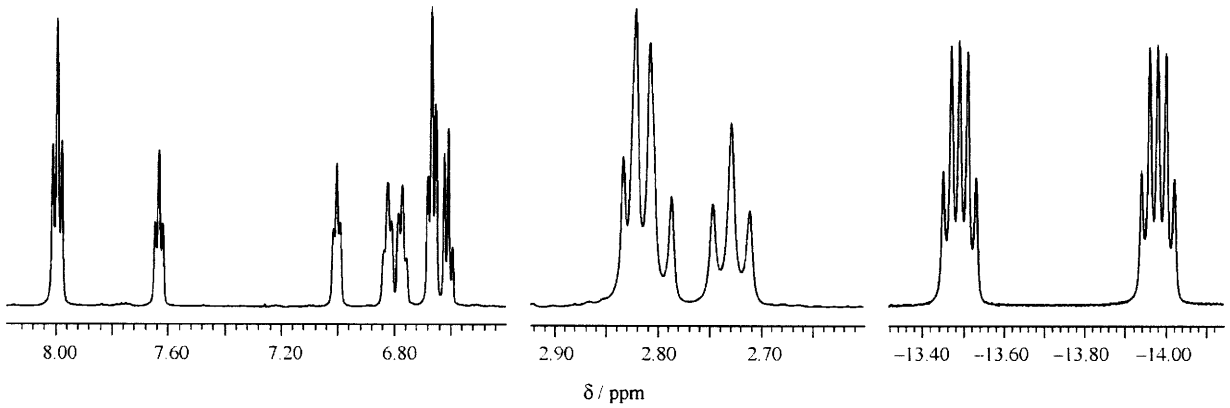

Figure 4.2. ^1H NMR spectrum of **2** in THF-d_8 depicting the aromatic, N–Me, and hydride regions from left to right respectively.

significant information can be extracted. The aryl region consists of seven well defined resonances, although sharp resonances are to be expected for the bridging benzyne, the coordinated phenyl group on Ir(1) does not display any line broadening stemming from rotation, and is most likely locked into a single configuration due to steric congestion with the $-OCH_2CF_3$ groups of the tfepma ligand, Figure 4.2 left. The solid state structure is further confirmed by the $^{31}P\{^1H\}$ NMR where six distinct resonances are observed. The spectrum is well defined but complicated, as $^2J_{P-P}$ cis phosphorus couplings between the six unique phosphorus atoms are observed both through the PNP ligand backbone and also through the iridium centers for the chelating tfepma ligands.

Although both the ^1H and $^{31}P\{H\}$ NMR of **2** exhibited sharp resonances that indicate a static structure in solution, room temperature solutions of the valence symmetric $Ir_2^{II,II}(tfepma)_3(\mu\text{-}C_6H_4)(C_6H_5)H$ core of **2**, are observed to slowly isomerize to provide the two-electron mixed valence $Ir_2^{I,III}(tfepma)_3(\mu\text{-}C_6H_4)(C_6H_5)H$ core of complex **3** (Scheme 4.2) in quantitative yield. The progress of the reaction can be monitored in solution by ^1H NMR

Scheme 4.2

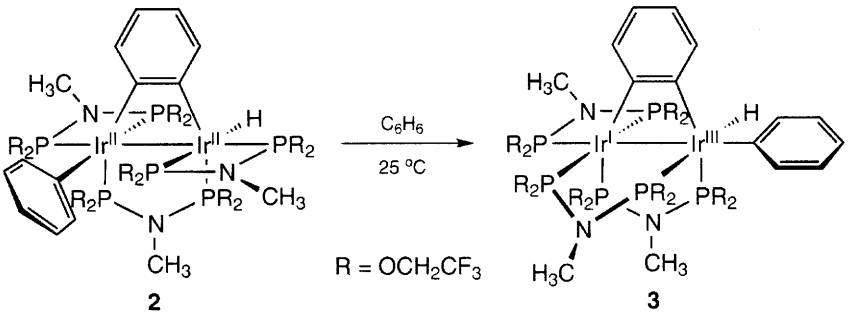

spectroscopy and is accelerated by gentle heating at 50°C in C_6H_6 for 6 hours. Analysis of the resulting colorless product by ^1H NMR in CD_3CN reveals a complex with three N–Me resonances as sharp triplets at 2.47, 2.79, and 2.87 ppm, Figure 4.3 center. The resonances integrate in a 1:1:1 ratio, and exhibit $^3J_{P-H}$ coupling constants of 7.0, 6.4, and 9.8 Hz respectively. Examination of the coupling constants indicates that the tfepma ligands have rearranged from a doubly chelating and singly bridging geometry as in **2**, to a doubly bridging and singly chelating motif. A hydride resonance, observed at –9.79 ppm is shifted downfield considerably from that in **2**, indicating a significantly altered chemical environment, Figure 4.3 right. The aryl region of **3** exhibits seven resonances as in **2**, several of which are considerably

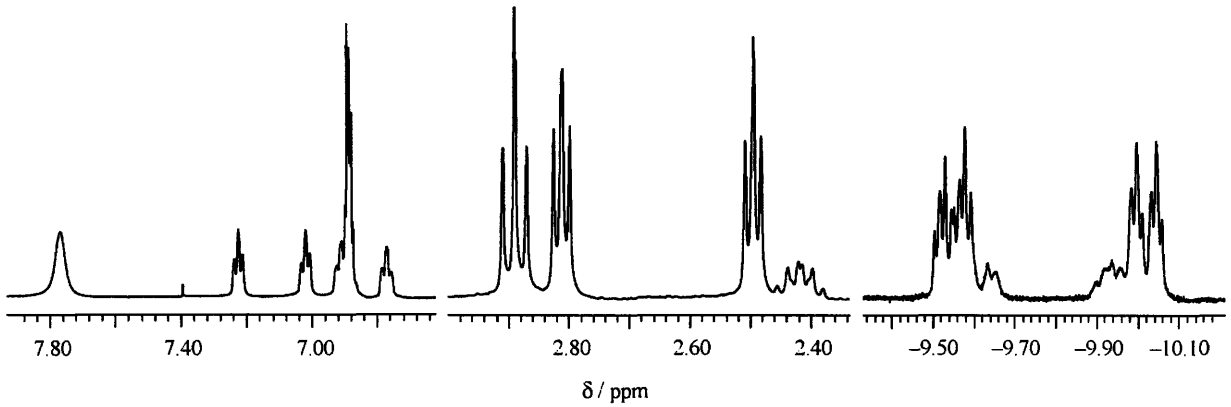

Figure 4.3. Aromatic, N–Me, and hydride regions (left to right respectively) of the ^{1}H NMR spectrum of **3** in CD_3CN.

overlapped. Interestingly the resonance at 7.74 ppm is observed as a broadened singlet at 20°C, indicating some degree of rotational freedom for these hydrogens, Figure 4.3 left. The $^{31}P\{^{1}H\}$ NMR of the resulting complex also displays six distinct resonances, and exhibits complex splitting patterns resulting from multiple $^{2}J_{P-P}$ couplings similar to those of **2**.

Suspensions of complex **2** in C_6H_6 exhibited homogenization when heated to 50°C, and after 6 hours of heating, crystals suitable for X-ray diffraction are deposited by slowly cooling the solution to room temperature. X-ray analysis reveals the molecular structure of **3** that is consistent with NMR spectroscopic data, Figure 4.4. Selected bond lengths and angles are listed in Table 4.2. The complex is comprised of two distorted octahedral iridium centers separated by 2.7791(2) Å and bridged by a $C_6H_4^{2-}$ benzyne unit. The conversion from **2** to **3** shows significant reorganization of the core. The flexible tfepma ligands have rearranged to a doubly bridging singly chelating coordination of the dinuclear core, consistent with the observed $^{3}J_{P-H}$ coupling constants in the ^{1}H NMR. The bite angle for chelating tfepma ligand is consistent with those observed for **2** with ∠P(5)–Ir(1)–P(6) = 68.46(3)°. Additionally the bridging tfepma ligands expand to strap the bimetallic core and exhibit P(1)–N(1)–P(3) and P(2)–N(2)–P(4) angles of 115.37(17)° and 121.44(17)° respectively. A hydride, inferred by the open coordination site trans to P(4) (∠C(10)–Ir(2)–Ir(1) = 160.73(10)° and ∠C(9)–Ir(2)–P(3) = 160.98(9)°), was located late in the refinement and was fixed at a bond length of 1.600 Å. In **3**, the anionic ligands have rearranged to produce a facial disposition, and strikingly, a cis coordination of a hydride and a terminal phenyl group on Ir(2). These reorganizations represent a formal disproportionation of the valence symmetric $Ir_2^{II,II}$ core observed for **2** to a two-electron mixed valent $Ir_2^{I,III}$ core of **3**. As in **2**, the tight benzyne bridge manifests itself in large distortions to the octahedral geometries

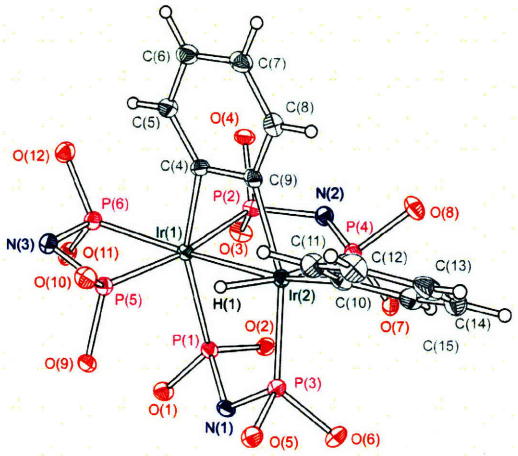

Figure 4.4 X-ray structure of $Ir_2^{I,III}(tfepma)_3(\mu\text{-}C_6H_4)(C_6H_5)H$ (**3**), with thermal ellipsoids drawn at the 50% probability level. Bridgehead –Me and $-CH_2CF_3$ groups of the tfepma ligands are omitted for clarity.

Table 4.2. Bond Lengths (Å) and Angles (°) for $Ir_2^{I,III}(tfepma)_3(\mu\text{-}C_6H_4)(C_6H_5)H$ (**3**).

Bond Lengths (Å)					
Ir(1)–Ir(2)	2.7791(9)	Ir(1)–P(1)	2.2793(10)	Ir(2)–P(4)	2.2478(9)
Ir(1)–C(4)	2.141(5)	Ir(1)–P(2)	2.2585(9)	Ir(2)–P(5)	2.2585(9)
Ir(1)–C(9)	2.096(4)	Ir(1)–P(3)	2.2225(10)	Ir(2)–P(6)	2.2878(9)
Ir(2)–C(10)	2.111(3)				
Bond Angles (°)					
C(9)–Ir(2)–P(3)	160.98(9)	P(6)–Ir(1)–Ir(2)	157.30(2)	P(3)–N(2)–P(4)	121.44(17)
C(4)–Ir(1)–P(1)	151.82(10)	P(1)–N(1)–P(3)	115.37(17)	P(5)–N(3)–P(6)	98.81(15)
C(4)–Ir(1)–Ir(2)	70.22(9)	P(1)–Ir(1)–P(2)	93.42(3)	P(3)–Ir(2)–P(4)	102.53(3)
C(9)–Ir(2)–Ir(1)	71.83(10)				

of the $Ir_2^{I,III}$ core where the internal angles within the four-atom bridge are significantly contracted (∠C(4)–Ir(1)–Ir(2) = 70.22(9)° and ∠C(9)–Ir(2)–Ir(1) = 71.83(10)°). The iridium carbon contacts with the $C_2H_4^{2-}$ unit in **3** display a slightly greater asymmetry than in **2**, the observed Ir(1)–C(4) and Ir(2)–C(9) bond lengths of 2.141(3) and 2.096(4) Å respectively (Δ(**3**) = 0.045 Å vs. Δ(**2**) = 0.025 Å), with the shortest contact for the benzyne carbon bonded to the Ir^{III} center. This is most likely due to a slight contraction of the ionic radius of Ir^{III} vs. Ir^{II}.

In **3** the terminal phenyl resides along the Ir–Ir bond axis in an axial coordination site with a C(10)–I(2)–Ir(1) angle of 160.73(10)° and an Ir(2)–C(10) bond distance of 2.111(3) Å. The two aryl groups are not mutually perpendicular. While the $C_2H_4^{2-}$ unit of the bridging benzyne maintains a nearly planar configuration with the diiridium core (C(4)–Ir(1)–Ir(2)–C(9) dihedral = 3.05(13)°), the terminal phenyl group instead is twisted by 57.85(30)° with respect to the plane comprised of diiridium benzyne unit as measured by the C(9)–Ir(2)–C(10)–C(11)

dihedral angle. Examination of the steric environments about the terminal phenyl group in the solid state reveal an expanded pocket relative to that observed for **2**, explaining the observation of slightly broadened resonances for the terminal phenyl group in the ^{1}H NMR of **3**.

4.2.2 Mechanistic Studies

The sharp ^{1}H and $^{31}P\{^{1}H\}$ NMR resonances of **2** and **3** indicate static solution structures and seem contradictory to the redox disproportionation and isomerization of **2** to **3**. The reaction is also interesting as with the significant ligand rearrangements required, it is difficult to imagine a simple mechanism for the overall conversion. Kinetic measurements by ^{1}H NMR were undertaken in order to shed some light on the isomerization mechanism. Although complexes **2** and **3** are sparingly soluble in C_6D_6, this solvent was chosen for the reaction medium because the N–Me resonances exhibit little overlap in C_6D_6. Thus mixtures of **2** and **3** display six well defined triplets in this region (Figure 4.5). The resonances at 1.97, 2.17, and 2.60 ppm are assigned to complex **2**, and the resonances at 2.02, 2.12, and 2.48 ppm to complex **3** by comparison with authentic samples. Examination of the isomerization endpoint evidences no incorporation of the deuterium labels from the C_6D_6 solvent into the coordination sphere of **3**. Integration of the hydride and N–Me resonances at 2.48 ppm gives the expected ratio of 3:1 in the final product. This result disfavors an isomerization pathway involving the complete

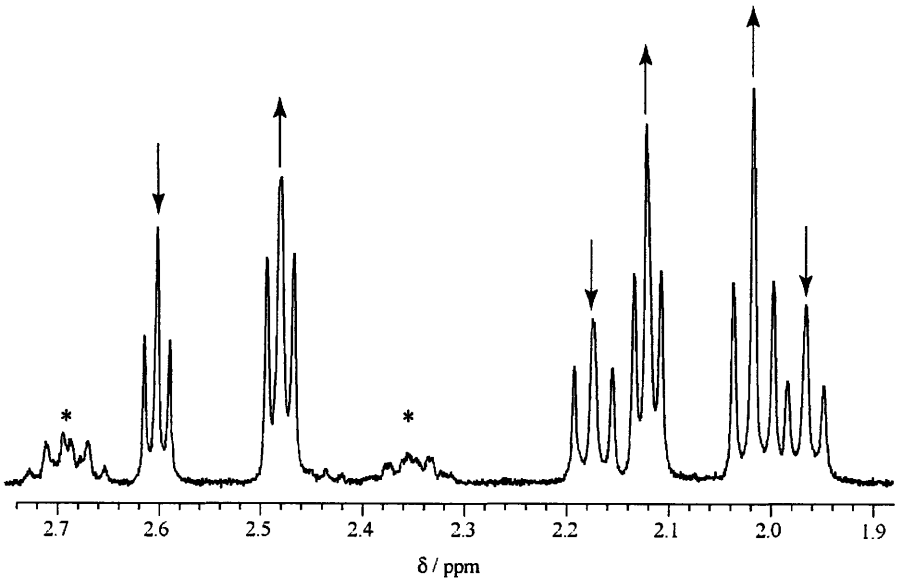

Figure 4.5. A portion of the ^{1}H NMR spectrum for a partially isomerized mixture of **2** and **3** in C_6D_6 at 20°C. The spectrum is zoomed to display the six triplet N–Me resonances with arrows indicating the course of the spectral evolution with time. For the kinetic analysis the resonances at 2.60 and 2.48 ppm were employed as markers of **2** and **3** respectively. Starred resonances are the result of methylene protons on the $-OCH_2F_3$ groups of the tfepma ligands as identified in pure samples of **2** and **3**.

dissociation of C_6H_6 along the reaction coordinate. Additionally no intermediates are observed to build up during the course of the reaction, as the only observed N–Me, aryl, or hydride resonances at any point in the reaction are readily assignable to either complex **2** or **3**.

The slow isomerization from **2** to **3** occurs on a timescale amenable to kinetic analysis by NMR and was carried out by monitoring the resonances at 2.60 and 2.48 ppm for the bridging tfepma ligands as they appear in an uncrowded portion of the spectrum. Fitting the integrated intensities for the peaks at 2.60 and 2.48 ppm to a first order exponential decay and growth respectively gives observed rate constants that agree within error. Measurements of k_{obs} for this isomerization at 20, 30 and 40°C (corrected temperatures 22.2, 31.8, and 41.5°C respectively) evidences normal Ahrrenius behavior, and allows for the calculation of the activation parameters from a linear fit of $\ln(k_{obs}/T)$ vs. 1000/T giving a $\Delta H^{\ddagger}$ of 21.7 ± 0.3 kcal/mol and a $\Delta S^{\ddagger}$ of –7.4 ± 0.9 e.u.. The favorable fitting to a first order kinetic model suggests that the isomerization proceeds in a one to one fashion, but the lack of observed intermediates precludes a full mechanistic analysis from this data alone.

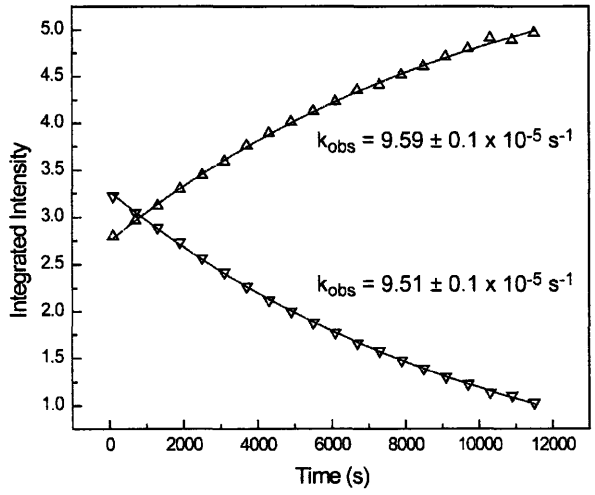

T (°C)	k_{obs} (s^{-1})
22.2	2.94×10^{-5}
31.8	9.57×10^{-5}
41.5	3.09×10^{-4}
Activation Parameters	
$\Delta H^{\ddagger}$ = 21.7 ± 0.3 kcal/mol $\Delta S^{\ddagger}$ = –7.4 ± 0.9 e.u.	

Figure 4.6. Isomerization kinetics for **2** to **3** carried out over the temperature range 20–40°C in C_6D_6. Tabulated observed rate constants and activation parameters, right, and integrated intensity vs. time for the isomerization at 31.8°C, left.

Additional insight into the rate determining step for the isomerization of **2** to **3** can be gained by isotopic labeling experiments, wherein isotopic substitution should only affect the observed isomerization rate if C–H bond formation or cleavage processes are implicated in the rate determining step. To examine this possibility the deuterated products, **2**-d_{10} and **3**-d_{10}, were synthesized using C_6D_5MgBr in place of C_6H_5MgBr by an analogous procedure to that which

afforded **2** and **3**. Structural congruency in solution is evidenced by equivalent N–Me resonances for both **2**-d_{10} and **3**-d_{10} with their protio counterparts from NMR analyses. For **2**-d_{10}, the deuteride resonance exhibits a slight downfield shift to –13.61 ppm (from –13.73 ppm), and is observed as a doublet of multiplets in the ^{2}H NMR with a greatly reduced $^2J_{P-D}$ coupling constant of 37 Hz. The upfield portion in the ^{2}H NMR spectrum of **3**-d_{10} is analogous, with a slight downfield shift to –9.70 ppm (from –9.79 ppm) and reduced $^2J_{P-D}$ coupling to the trans phosphorus of 34 Hz. In both cases the deuterium resonances for the benzyne and terminal phenyl moieties in the ^{2}H NMR are observed as broadened overlapping multiplets and are uninformative. X-ray structural analysis on single crystals of **2**-d_{10} affords a solid state structure completely analogous to **2**, providing definitive evidence for the intuitive assumption that isotopic substitution does not significantly perturb the overall bimetallic construct (data not shown).

Infrared spectroscopic analysis provides further evidence of structural homogeneity between the protio and deutero derivatives as the isotopic shift in the Ir–D stretching frequency is readily predicted from a harmonic oscillator model. The Ir–H stretching frequencies of **2** and **3** are observed at 2069 and 2023 cm^{-1} respectively in CD_3CN solutions. A simple Hooke's law calculation would predict a bathochromic shift to 1463 and 1426 cm^{-1} for these vibrations upon isotopic substitution of deuterium for hydrogen. This simplistic calculation fares remarkably well as the Ir–D stretches for **2**-d_{10} and **3**-d_{10} are observed at 1453 and 1415 cm^{-1} respectively, deviating from the theoretical values by ~10 cm^{-1}.

Kinetic measurements for the isomerization from **2**-d_{10} to **3**-d_{10} exhibit significant rate enhancement relative to those observed for complex **2** at the same temperature. The observed rate constant of $2.17 \pm 0.1 \times 10^{-4}$ s^{-1} for the isomerization of **2**-d_{10} to **3**-d_{10} at 31.8°C in C_6D_6 solution leads to a k_{obs}^{H}/k_{obs}^{D} of 0.44 ± 0.1, indicating an inverse isotope effect for the overall isomerization reaction. As for **2**, the activation parameters were calculated from kinetic data measured over the range of 20–40°C and yielded a $\Delta H^{\ddagger}$ of 24.9 ± 0.7 kcal/mol and a $\Delta S^{\ddagger}$ of –6.4 ± 2.4 e.u., Figure 4.7. Although the overall isomerization reaction is not likely elementary, the inverse isotope effect is striking as it indicates significant involvement of Ir–H(D)/C–H(D) bond making/breaking along the reaction coordinate. These data taken along with the lack of observable intermediates over the course of the isomerization strongly indicates that the rate determining step takes the form of an Ir–H(D)/C–H(D) bond making/breaking event, with any

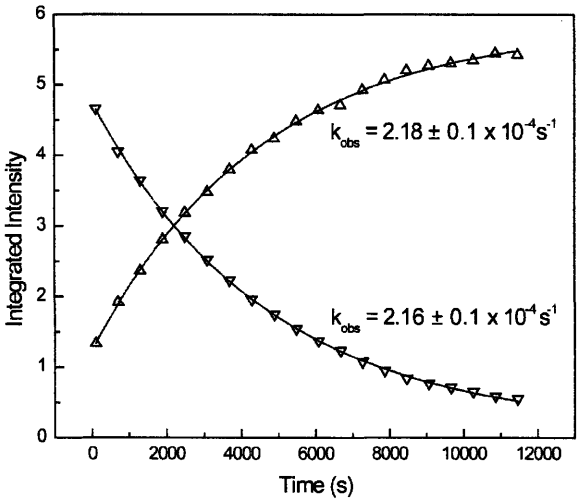

T (°C)	k_{obs} (s^{-1})
22.2	5.14×10^{-5}
31.8	2.17×10^{-4}
41.5	7.52×10^{-4}
Activation Parameters	
$\Delta H^{\ddagger} = 24.9 \pm 0.7$ kcal/mol	
$\Delta S^{\ddagger} = -6.4 \pm 2.4$ e.u.	

Figure 4.7. Isomerization kinetics for **2**-d_{10} to **3**-d_{10} carried out over the temperature range 20–40°C in C_6D_6. Tabulated observed rate constants and activation parameters, right, and integrated intensity vs. time for the isomerization at 31.8°C, left.

subsequent rearrangement steps leading to the formation of **3** occurring fast on the NMR timescale.

Taking into account the inverse isotope effect for the isomerization of **2** and **2**-d_{10} it seems reasonable to postulate the involvement of a C–H(D) bond in the transition state for the isomerization. Specifically a reductive coupling of the benzyne and hydride on a single iridium center in **2** should generate an intermediate with either an open coordination site or a labile σ-C_6H_5 or η^2-π-C_6H_6 complex on the low valent Ir^0 center, Scheme 4.3, which could be viewed as the microscopic reverse of the ortho C–H activation that leads to the formation of **2**. The intermediacy of σ-C_6H_6 or η^2-π-C_6H_6 in either the reductive elimination, or in the microscopic reverse reaction, oxidative addition, of benzene has been debated in the literature.[24,25] The propensity to adopt either a σ-C_6H_6 or η^2-π-C_6H_6 binding mode appears to be entirely system dependent, and no unifying scheme has been elucidated. For example in Cp*M(PMe_3)(C_6H_5)(H)

Scheme 4.3.

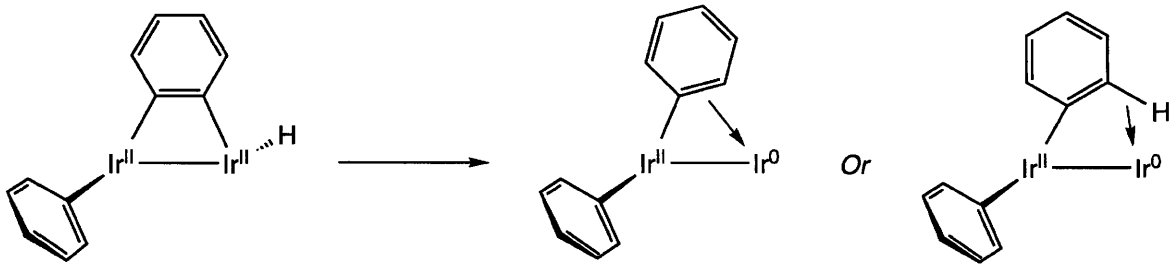

(Cp* = pentamethylcyclopentadienyl anion) systems for M = Rh, Jones has invoked the existence of an η^2-π-C_6H_6 intermediate in the reductive elimination of C_6H_6,[26,27] while for M = Ir, Bergman has postulated precoordination of a σ-C_6H_6 intermediate in the oxidative addition of C_6H_6 to Cp*Ir(PMe_3) and not an η^2-π-C_6H_6 interaction.[28] The kinetic data obtained here cannot distinguish between these two possibilities as no intermediates are observed in the overall transformation, and thus both interactions will be referred to as σ-arene complexes for simplicity.

The rate enhancement for the isomerization of **2**-d_{10} to **3**-d_{10} relative to their protio congeners implicates the involvement of C–H(D) bond forming/breaking in the rate determining step. Inverse isotope effects of this nature have seen precedence for the reductive coupling of alkyl hydrides[29–41] and less commonly aryl hydrides[40,42] in the literature,[43] typically in constructs where the scrambling of hydrides (deuterides) into cis ligated alkyl or aryl groups is observed. Explanations for inverse isotope effects in the literature generally attribute the observed rate enhancements to an inverse equilibrium isotope effect and only rarely to an inverse kinetic isotope effect (i.e. $K_{H/D} < 1$[44] and not $k_H/k_D < 1$). The arguments begin by observing that the σ-alkane product of reductive coupling of alkyl hydride (deuteride) possesses a strong C–H(D) bond rather than a much weaker M–H(D) bond, and consequently the force constants for C–H bonds are much greater than those of M–H bonds. Accordingly the force constant for a C–D bond is less than a C–H bond, manifesting itself in a smaller zero point energy (ZPE) for the C–D bond relative to the C–H bond. The same argument applies for M–D vs. M–H bonds, only the magnitude of the difference is much less, meaning that the $\Delta ZPE_{MH/MD} < \Delta ZPE_{CH/CD}$. Consideration of the energetic requirements for the reductive coupling of an alkyl hydride (deuteride) to form the σ-alkane product in the context of the above discussion gives rise to two distinct cases where an inverse isotope effect would be observed, Figure 4.8.[45]

In the first case (Figure 4.8a) partial formation or breakage of the C–H(D) bond reduces the force constant relative to free C–H(D) and thus the ZPE for this intermediate species is presumed to fall between that of free C–H(D) and M–H(D). If this species is implicated in the transition state of the rate determining step, then the differences in ZPE should engender a slight energetic preference (a ΔΔZPE in the form of $\Delta G^{\ddagger}$) for reductive coupling in the deuterated complex. This thermodynamic preference would result in rate enhancement for this step, i.e. $k_{RC}{}^{H}/k_{RC}{}^{D} < 1$. The microscopic reverse, oxidative cleavage, would be initiated from the σ-alkane product which possesses intact C–H(D) bonds. Applying the same ZPE arguments as for the

reductive coupling step would indicate a slight energetic preference for the protio case, and thus a normal isotope effect, i.e. $k_{OC}{}^{H}/k_{OC}{}^{D} > 1$. Taking a combination of these rate constants gives an overall inverse equilibrium isotope effect.

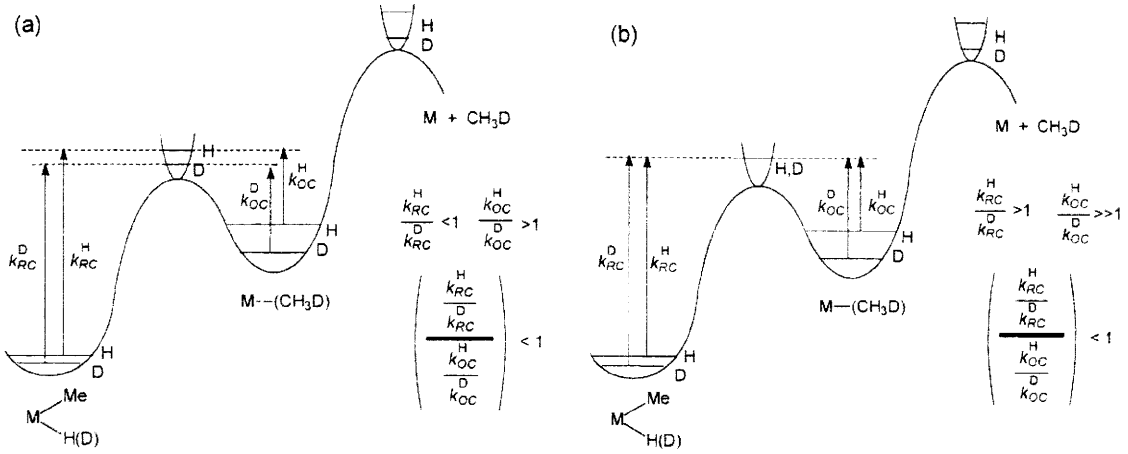

Figure 4.8. Two scenarios for the observation of an inverse isotope effect involving a σ-alkane complex separating C–H(D) oxidative cleavage/reductive coupling events at a transition metal center, see text for details. Figure taken from reference 41.

In the second case, Figure 4.8b, the C–H(D) stretching frequency is assumed to disappear as it becomes the reaction coordinate for the bond scission/formation. In this case normal kinetic isotope effects are expected for both the reductive coupling of the alkyl hydride and the oxidative cleavage of the resulting σ-alkane complex. The inverse isotope effect for the overall transformation arises due to the juxtaposition of the two normal kinetic isotope effects for the individual steps. In particular when the magnitude of the normal kinetic isotope effect for oxidative cleavage of the σ-alkane complex is greater than that for the reductive coupling an overall inverse isotope effect results.

In general it is difficult to determine whether the observed inverse isotope effect arises as a result of a true inverse kinetic isotope effect (as in case of Figure 4.8a for the reductive coupling event) or an inverse equilibrium isotope effect arising from two normal kinetic isotope effects (as in case of Figure 4.8b), and only in special circumstances and with careful study has this been determined.[37,41] Nevertheless, in the case of alkyl hydride complexes the observation of an inverse isotope effect has become a standard measure for the intermediacy of σ-alkane complexes. These studies have been carried over to arene complexes in a few examples,[40,42] and the same analyses applied. The only exception is that the precise nature of the reductive coupling

product is more ambiguous as both arene σ-C–H interactions (agostic type) and η^2-π-arene interactions are possible as opposed to alkyl hydrides where only agostic C–H σ-alkane complexes are tenable intermediates. Carrying through with the same logic as above, the observation of an inverse isotope effect on the isomerization from **2** to **3** vs. **2**-d_{10} to **3**-d_{10} is informative as it implicates an intermediate with σ-C_6H_5 or η^2-π-C_6H_6 character resulting from a C–H(D) reductive coupling event along the reaction coordinate as depicted in Scheme 4.3.

4.2.3 Divergent Hydrogen Reactivity

With a postulated low valent coordinatively unsaturated Ir^0 intermediate along the reaction coordinate from **2** to **3**, conditions targeted at trapping this intermediate were sought. Trapping experiments where solutions of **2** were treated with excess donor ligands such as PMe_3 or CN^tBu showed the formation of multiple intractable products by ^1H and $^{31}P\{^1H\}$ NMR, precluding unambiguous chemical assignments. However, under identical conditions solutions of **3** treated with PMe_3 and CN^tBu were completely unperturbed, indicating that the PMe_3 and CN^tBu reaction products are derived solely from **2**. If an open coordination site is indeed generated during the course of the redox isomerization from **2** to **3**, as implicated by the results of the kinetic analysis, then in principle this could be ascertained by treatment of **2** with hydrogen owing to the extensive reactivity of related rhodium and iridium systems ligated by tfepma for hydrogen activation at vacant coordination sites.[9–12] To examine this hypothesis, complexes **2** and **3** were exposed to a hydrogen atmosphere in a resealable NMR tube and the progress of the reaction monitored by ^1H NMR spectroscopy. The mixed valence complex **3** did not react with hydrogen and decomposed after days at elevated temperatures (80 – 100°C). In contrast, **2** reacts smoothly with hydrogen to form the tetrahydride $Ir_2^{II,II}(tfepma)_3(H)_4$ (**4**) with concomitant formation of two equivalents of benzene. The ^1H NMR in THF-d_8 (20°C) reveals two sets of hydride resonances at ~ –11.51 and –14.25 ppm, Figure 4.9 right. The region typical for N–Me groups displays four broadened resonances at 2.59, 2.70, 2.86, and 2.90 ppm, Figure 4.9 left. Further examination reveals two sets integrating in a 2:1 ratio at 2.70, 2.90 ppm and 2.86, 2.59 ppm. The two pairs integrate in a ~ 3:2 ratio. Integration over all the N–Me resonances and all the hydrides gives a ratio of 9:4, as expected for the $Ir_2^{II,II}(tfepma)_3(H)_4$ formulation. The hydrides are broadened and do not show the fine coupling observed for **2** and **3**. The resonance centered at ~ –11.58 ppm is composed of two broad singlets at –11.51 and –11.64 ppm that integrate in a 3:2 ratio in keeping with that observed for the two pairs of N–Me resonances. The

broad overlapping multiplet at −14.25 ppm resembles the hydrides of *syn*-$Rh_2^{II,II}(tfepma)_3(H)_2Cl_2$, allowing for the tentative assignment of this resonance as originating from the equatorial hydrides trans to P(2) and P(5); leaving the resonances at −11.51 and −11.64 ppm assigned as axially bound hydrides.

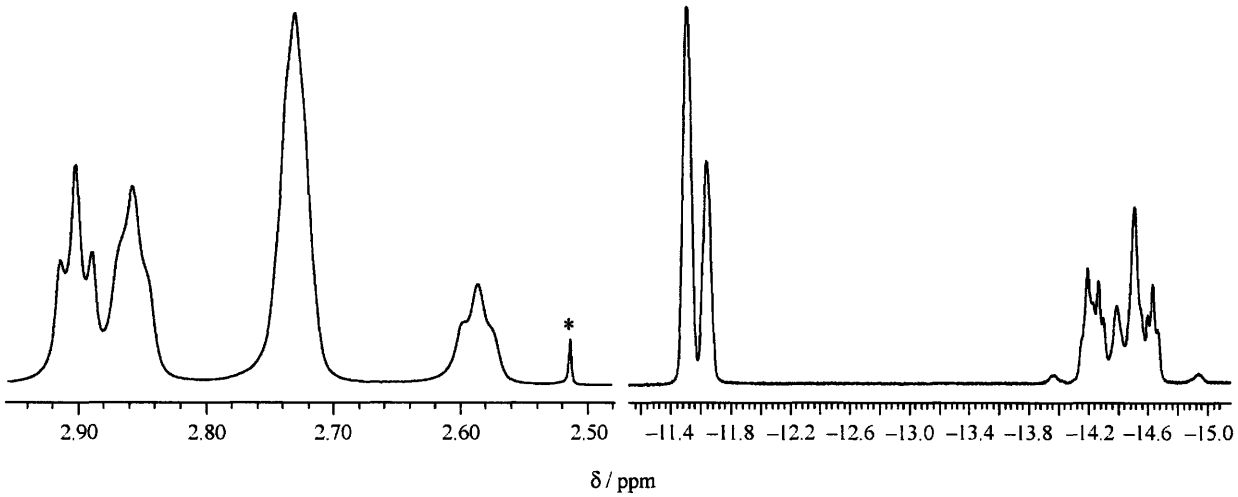

Figure 4.9. Solution ^1H NMR spectrum of single crystals of **4** dissolved in THF-d_8 (20°C) highlighting the N–Me (left) and hydride regions (right). Multiple components with broadened resonances are diagnostic of dynamic solution behavior, however the spectrum does not exhibit appreciable sharpening down to −80°C, see text for details.

For iridium the *syn*-isomer could be separated and independently characterized by X-ray crystallography. Ether solutions of the hydrogenated products left to stand deposited single crystals as large colorless blocks suitable for X-ray diffraction, Figure 4.10 left, and reveals a symmetric, triply bridging diiridium diphosphazane core. Selected bond lengths and angles are listed in Table 4.3. The core of complex **4**-*syn* is comprised of two octahedral iridium centers separated by 2.8389(3) Å and with overall pseudo-C_{2v} symmetry. The elongated Ir–Ir bond (relative to **2** and **3**) may result in part due to the absence of the bridging benzyne and to the presence of two terminal hydrides trans to the internuclear axis.[46] In addition, without the strained benzyne bridging unit the geometry is closer to that expected for an octahedron with cis phosphite angles in the range of 95–99° (Table 4.3). Only a slight decrease in the *trans*-spanning phosphite angles is observed (∠P(1)–Ir(1)–P(3) = 165.13(3)° and ∠P(4)–Ir(2)–P(6) = 164.09(4)°) due to the small size of the hydride ligands in the equatorial positions. A twist of ~24° along the Ir–Ir bond axis created by the bridging tfepma ligands can be seen in Figure 4.10 (as measured by the average bridging tfepma dihedral angle).

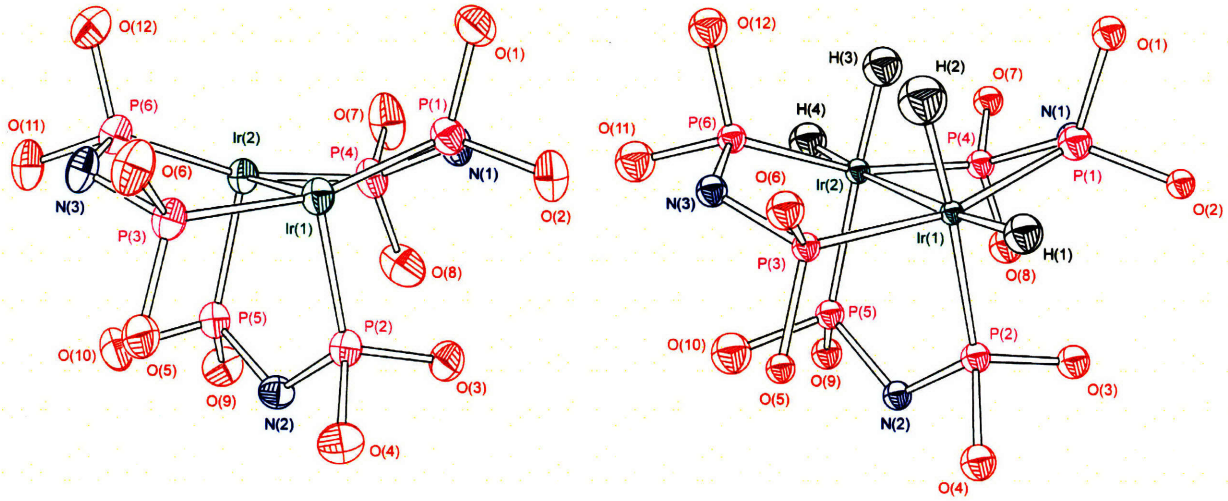

Figure 4.10. Single crystal structure determinations for $Ir_2^{II,II}(tfepma)_3(H)_4$ (**4**) by X-ray (left) and neutron (right) diffraction methods. The neutron data unambiguously reveals the presence of four terminal hydrides ligated in a syn disposition over the bimetallic core of **4**.–Me, $–CH_2CF_3$ groups are omitted for clarity with thermal ellipsoids drawn at the 50% probability level. Atomic displacement parameters were isotropically refined in the neutron structure.

Table 4.3. Bond Lengths (Å) and Angles (°) for $Ir_2^{II,II}(tfepma)_3(H)_4$ (**4**) from X-ray and preliminary refinement of neutron diffraction data.

Bond Lengths (Å)					
	X-ray	*Neutron*		*X-ray*	*Neutron*
Ir(1)–Ir(2)	2.8389(2)	2.816(11)	Ir(2)–P(6)	2.2323(9)	2.242(19)
Ir(1)–P(1)	2.2420(9)	2.278(21)	Ir(1)–H(1)	–	1.636(30)
Ir(1)–P(2)	2.2514(9)	2.242(22)	Ir(1)–H(2)	–	1.647(33)
Ir(1)–P(3)	2.2263(8)	2.213(20)	Ir(2)–H(3)	–	1.599(30)
Ir(2)–P(4)	2.2223(9)	2.255(25)	Ir(2)–H(4)	–	1.612(32)
Ir(2)–P(5)	2.2467(9)	2.193(23)			
Bond Angles (°)					
P(1)–Ir(1)–P(3)	165.13(3)	165.4(9)	P(5)–Ir(2)–P(6)	95.66(3)	96.6(8)
P(1)–Ir(1)–P(2)	97.02(3)	97.1(8)	H(1)–Ir(1)–H(2)	–	87.0(16)
P(2)–Ir(1)–P(3)	97.50(3)	97.1(8)	H(2)–Ir(1)–P(2)	–	174.4(12)
P(4)–Ir(2)–P(6)	165.09(4)	163.0(9)	H(3)–Ir(1)–H(4)	–	81.0(16)
P(4)–Ir(2)–P(5)	99.84(3)	99.9(9)	H(4)–Ir(1)–P(5)	–	175.5(13)
Dihedral Angles (°)					
P(1)–Ir(1)–Ir(2)–P(4)	23.01(4)	22.5(7)	P(3)–Ir(1)–Ir(2)–P(6)	23.95(4)	24.0(7)
P(2)–Ir(1)–Ir(2)–P(5)	25.74(4)	26.1(7)	H(2)–Ir(1)–Ir(2)–H(4)	–	32.2(12)

The hydrides could not be located reliably in the difference Fourier map obtained from X-ray diffraction, but single crystal neutron diffraction methods could provide an unambiguous determination of the hydrogen coordinates. The neutron data reveals a structure consistent with that found by X-ray crystallographic techniques, Figure 4.10 right and Table 4.3, excepting that the two pseudooctahedral iridium centers are completed by the presence of four

crsytallographically located terminal hydride ligands. The hydrides exhibit slightly compressed cis angles of 87.1(16)° and 81.0(16)° for the H(1)–Ir(1)–H(2) and H(3)–Ir(2)–H(4) respectively, and form nearly linear H–Ir–P angles with the trans phosphite on each iridium center. The hydrides refine at full occupancy and suggest against the participation of site disordered hydrides bridging the diiridium core in the solid state.

Although the X-ray and neutron data established the coordination geometry of **4**-*syn* in the solid state, variable temperature NMR studies were conducted in attempts to characterize the dynamic behavior and broadened resonances observed in solution. A J. Young NMR tube was charged with single crystals of *syn*-$Ir_2^{II,II}(tfepma)_3(H)_4$ (**4**-*syn*) left over from the crystallographic structure determination, attached to a high vacuum line, and THF-d_8 vac transferred into the tube while maintained at 77K. The solution was then allowed to warm just until the solvent thawed and then immediately placed into the magnetic field of an NMR spectrometer at –80°C. As in the room temperature spectra, multiple products were observed and the hydride resonances did not display any significant sharpening even at this low temperature. The $^{31}P\{^1H\}$ NMR at –80°C is uninformative and is observed as a series of overlapping broadened multiplets. This dynamic behavior, even at very low temperatures, suggests that the two isomeric forms of $Ir_2^{II,II}(tfepma)_3(H)_4$ observed in room temperature solution are separated by extremely low energetic barriers.

The solution behavior could be assigned as a syn to anti isomerization by analogy with the $Rh_2^{II,II}(tfepma)_3(H)_2Cl_2$ system, Figure 4.11 right.[9] Alternatively the observation of multiple products could be attributed to a dihydride-dihydrogen isomerization, Figure 4.11 left, in keeping with that observed for many mono- and polynuclear metal polyhydrides.[47,48] Metal dihydrogen complexes typically are quite sensitive, and often dissociate or exchange hydrogen readily, thus to assess the intermediacy of a dihydrogen complex solutions of **4** in THF-d_8 were exposed to 1 atm of deuterium. In the case of **4** however, the solution remains completely unperturbed with a stagnant ratio of N–Me to hydride protons of 9:4 observed over the course of the exchange experiment. H/D exchange is not an exclusive prerequisite of dihydride-dihydrogen isomerizations and the broadened resonances observed for **4** in THF-d_8 could also arise from either dynamic solution behavior or from enhanced nuclear relaxation of hydrides. Another standard characterization method for metal dihydrogen complexes involves the measurement of the T_1 relaxation time for the ^1H nuclei of the η^2-H_2 ligand.[49] In brief, the enhanced relaxation

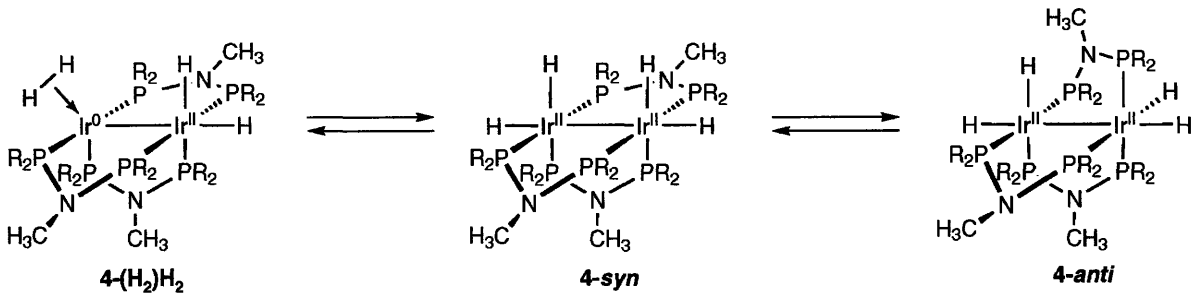

Figure 4.11. Potential isomerization pathways for $Ir_2^{II,II}(tfepma)_3(H)_4$, the intermediacy of **4**-*syn* separating the **4**-$(H_2)H_2$ and **4**-*anti* isomers is not required or implicated experimentally, but is drawn in this manner for simplicity.

arises from the close proximity two spin active ^1H nuclei to one another, which introduces dipole-dipole nuclear spin relaxation mechanisms, and thus abnormally low T_1 relaxation times are observed for the interacting ^1H nuclei. Although this method is typically not sufficient to accurately determine H–H distances in dihydrogen complexes,[50] short T_1 values of < 50 ms are consistent with an η^2-H_2 formalism, while classical terminal hydrides have T_1 values >> 100 ms with typical relaxation times of ~ 500 ms. T_1 analysis conducted on THF-d_8 solutions of **4** at room temperature give relaxation times spanning a range from 540 ms to 586 ms, strongly indicating that the isomeric forms of **4** observed in solution maintain terminal hydride character.

Taken together these results suggest that the observation of multiple products in solution can be attributed to rapid isomerization between **4**-*syn* and **4**-*anti* isomeric forms, by analogy with that observed for tfepma bridged $Rh_2^{II,II}(H)_2Cl_2$ cores. In the rhodium case, isomerization from the isolable syn isomer to the anti and cis forms proceeds slowly at room temperature, but the dynamic behavior of $Ir_2^{II,II}(H)_4$ cores observed at low temperatures suggests that the interconversions are significantly more facile. Although speculative at best, the apparent decreased energy barrier could be attributed to the shuffling of small hydrogen atoms about the bimetallic core in place more sterically demanding halogens. The participation of a bridging hydride, although most likely an intermediate along the isomerization pathway from **4**-*syn* to **4**-*anti*, cannot be ruled out as one of the components observed in solution. If this were the case however the bridging hydride would be expected to have a significantly altered chemical shift and not appear as overlapping multiplets as observed in the ^1H NMR spectrum of **4** in solution.

4.2.4 Summary

With the data from the previous sections in hand a rationalization for the inverse isotope effect and a mechanism for the isomerization from **2** to **3** can be postulated. According to Scheme 4.4 (tfepma ligands omitted for clarity) two plausible scenarios can be envisioned that lead to the observed products. The first involves migration of a phenyl group, and the second implicates a bridging hydride intermediate. In the bottom portion of Scheme 4.4 the reaction initiates with the bending of the hydride to bridge the bimetallic core, which then reductively couples with the benzyne at the adjacent iridium center. This generates a valence symmetric $d^8 \cdots d^8$ diiridium core each ligated by a terminal phenyl group. This species could then undergo oxidative cleavage of an ortho C–H(D) bond to generate the two-electron mixed valence $Ir_2^{I,III}$ core of **3**. The other pathway, outlined on the top of Scheme 4.4 begins with reductive coupling of the hydride and cis ligated benzyne generating a two-electron mixed valence $Ir_2^{0,II}$ core. This reaction can be viewed as the microscopic reverse of the C–H bond activation that generates complex **2** from the reaction of **1** and PhMgBr. This intermediate could either reactivate the ortho C–H bond or generate a μ-η^1-C_6H_5 intermediate by migration of the terminal phenyl group to a position bridging the bimetallic core.[51] Subsequent relaxation from a μ-η^1-C_6H_5 to an η^1-C_6H_5 converges the two distinct pathways at a common intermediate. Finally C–H(D) oxidative cleavage at the Ir^I center would generate the observed product **3**. The two pathways diverge in their initial step, and both involve a C–H(D) reductive coupling event followed by a C–H(D)

Scheme 4.4.

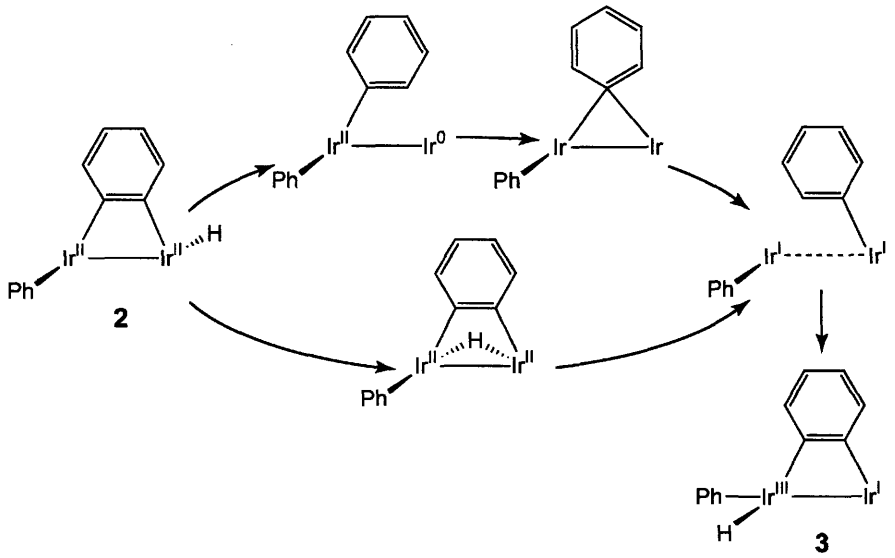

oxidative cleavage event. These two possibilities however, are kinetically indistinguishable in this study as presently formulated.

This work is similar to classic investigations involving H/D scrambling, the oxidative additions of R–H vs. R–D, or the reductive eliminations of R–H vs. R–D where inverse isotope effects are observed, excepting that all previously reported systems are monometallic. In this case the scope is expanded to include C–H activation chemistry at multiple metal centers. In particular, if the upper pathway in Scheme 4.4 is operative then the metals where the oxidative cleavage and reductive coupling events take place are distinct. Otherwise, if the lower pathway in Scheme 4.4 is followed, the bimetallic cooperation stems from the ability of the hydride to bridge the diiridium core, with both the C–H(D) reductive coupling and oxidative cleavage events occurring at the same metal center. Regardless of which pathway is followed the redox isomerization of **2** to **3** represents a true cooperative event of two metal centers.

The present study cannot distinguish between the two possibilities of Scheme 4.4, but some arguments can be presented for each pathway. In favor of the bridging hydride, our previous studies have shown the ability of tfepma bridged bimetallic iridium systems to reversibly shuttle hydrogen atoms between the two metal centers,[9,11] and thus it seems reasonable to postulate a similar intermediate in the present study. The upper pathway cannot be ruled out however, and the rationale for this stems from the observation that the ortho C–H activation to generate complex **2** is under kinetic control. This means that although downhill from the putative primary arylation product of **1**, complex **2** is not a thermodynamic sink. With the isotope effect necessitating C–H reductive coupling along the reaction coordinate, it seems reasonable to postulate a reversal of the initial C–H activation step that led to the formation of **2**. Arguments in favor of the reductive coupling of the hydride and cis ligated benzyne of **2** can be made by examining the structural and electronic differences between **2** and **3**. While both have the same cis ligation of a hydride and benzyne, the reasons for the reactivity difference between **2** and **3** can be rationalized to stem from two different causes: i) that the product **3** attains a stable octahedral Ir^{III} d^6 electronic configuration as opposed to the octahedral Ir^{II} d^7 configuration of **2**, and ii) that the chelating tfepma ligand coordination motif on the Ir^{II} center ligated with the benzyne and hydride on **2** engenders a more facile dissociation of the phosphite arm trans to the hydride, allowing for the generation of a five coordinate intermediate from which C–H bond coupling ensues. The stability of octahedral 18 electron d^6 M^{III} complexes is a fundamental

principle of organotransition metal chemistry. Octahedral rhodium complexes are typically capable of reductive elimination reactions to generate 16 electron Rh^{I} species for reentry into catalytic cycles, the stronger metal ligand bonds for iridium vs. rhodium often render the corresponding iridium complexes catalytically inert. A classic example is the iridium congener of Wilkinson's catalyst, which does not hydrogenate olefins due to the inability of the $Ir^{III}(PPh_3)_3(H)_2Cl$ complex to dissociate phosphine to open a site for coordination of the unsaturated substrate.[46] For complex **2** the Ir–P bond trans to the hydride (Ir(2)–P(6)) is noticeably longer than the corresponding interaction in **3** by ~0.072 Å. This bond length increase cannot reasonably be justified by the difference in oxidation states alone, and is taken to indicate weaker binding to the metal center. The chelating coordination motif would also rationally be expected to increase the lability of the tfepma ligand in order to relieve ring strain in the four atom Ir–P–N–P metallacycle. These two effects are thought to conspire for the increased lability of the Ir^{II} centers of complex **2**. This could lead to the enhanced formation of five coordinate intermediates from which the C–H(D) reductive coupling could be greatly facilitated,[52–55] giving rise to isomerization by the upper pathway of Scheme 4.4. Dissimilar labilization of P(6) in **2** and **2**-d_{10} prior to ligand loss is not thought to factor into the observed inverse isotope effect as the Ir(2)–P(6) bond lengths trans to the hydride (deuteride) in **2** and **2**-d_{10} are nearly equivalent (2.3197(11) Å and 2.3222(9) Å respectively).

4.3 *Concluding Remarks*

This work demonstrates that two-electron mixed valence cores of diiridium are active for the multielectron redox chemistry of interest to the organometallic community. As opposed to many monometallic complexes wherein the oxidative addition of aryl C–H bonds is irreversible, the bimetallic iridium cores examined here give rise to additional organometallic chemistry for the initial sp^2 C–H activation product. The divergent hydride reactivity and inverse isotope effects for the isomerization from **2** to **3** implicate either hydride transfer or phenyl group transfer over the bimetallic core along a reaction coordinate that involves both C–H reductive coupling and oxidative cleavage. Hydrogenation of **2** generates the tetrahydride **4** that isomerizes in solution between syn and anti conformations at the lowest attainable temperatures and only maintains a single conformation in the solid state. The geometric malleability of the organometallic and hydride complexes examined in this chapter stand as a testament to the

unique abilities of bimetallic cores bridged by flexible tfepma ligands to engender bimetallic cooperation.

4.4 *Experimental Section*

4.4.1 General Considerations

All manipulations were carried out in an N_2-filled glovebox or under an inert atmosphere provided by a Schlenk line unless otherwise noted. All solvents were reagent grade (Aldrich) or better and were dried and degassed by standard methods.[56] $[Ir^{I}(COD)Cl]_2$ (Strem), C_6H_5MgBr (1.0 M in THF, Aldrich), C_6D_5Br (Cambridge Isotope Labs) were purchased from the suppliers indicated and used without further purification. H_2 (BOC gases, grade 5.0) and D_2 (Cambridge Isotope Labs) were passed through a U-tube immersed in liquid nitrogen prior to admission into the reaction vessels. C_6D_5MgBr,[57] tfepma,[58,59] and $Ir_2^{0,II}(tfepma)_3Cl_2$[10,15] were synthesized according to published procedures.

4.4.2 Physical Methods

NMR data were collected at the MIT Department of Chemistry Instrument Facility (DCIF) on a Varian Inova Unity 500 spectrometer. NMR solvents (CD_3CN) were purchased from Cambridge Isotope labs and purified by standard procedures prior to use.[60] ^1H NMR spectra (500 MHz) were referenced to the residual protio impurities of the given solvent. $^{31}P\{^1H\}$ NMR (202.5 MHz) spectra were referenced to an external 85% H_3PO_4 standard. ^2H NMR spectra (76.8 MHz) were collected in protio solvent and reference to the natural abundance deuterium signal of the given solvent. All chemical shifts are reported in the standard δ notation in parts per million; positive chemical shifts are to higher frequency from the given reference. Elemental analyses were performed by Robertson Microlit Laboratories, Madison NJ. IR spectra were recorded on a Bio–Rad XPS 150 FT–IR spectrometer in a Perkin–Elmer liquid cell equipped with KBr windows.

4.4.3 Crystallographic Procedures

Single crystals were immersed in a drop of Paratone N oil on a clean microscope slide, affixed to either a glass fiber or a human hair coated in epoxy resin and then cooled to either –75 or –173 °C. The crystals were then mounted on a Bruker K8 three circle goniometer platform equipped with an APEX CCD detector. A graphite monochromator was employed for

wavelength selection of the Mo K_α radiation (λ = 0.71073 Å). The data were processed and refined using the program SAINT supplied by Siemens Industrial Automation Inc. Structures were solved by a Patterson heavy atom map and refined by standard difference Fourier techniques in the SHELXTL program suite (6.10 v., Sheldrick G. M., and Siemens Industrial Automation Inc., 2000). Disordered atoms in the $-CH_2CF_3$ groups were fixed at idealized bond lengths where necessary, site occupancies refined, and refined anisotropically for those groups that were split evenly. Otherwise the minor components of unevenly split $-CH_2CF_3$ groups were refined isotropically. Hydrogen atoms were placed in calculated positions using the standard riding model and refined isotropically; all other atoms were refined anisotropically. Unit cell parameters, morphology, and solution statistics for complexes **2**, **2**-d_{10}, **3**, and **4** are summarized in Tables 4.4 and 4.5. All thermal ellipsoid plots are drawn at the 50% probability level, with $-CH_2CF_3$ groups, –N–Me groups, and solvents of crystallization omitted for clarity.

4.4.4 Neutron Diffraction Methods

Neutron diffraction data were obtained at the Intense Pulsed Neutron Source (IPNS) at Argonne National Laboratory using the time-of-flight Laue single-crystal diffractometer (SCD). At the IPNS, pulses of protons are accelerated into a heavy-element target 30 times a second to produce pulses of neutrons by the spallation process. With two position-sensitive area detectors and a range of neutron wavelengths, a solid volume of reciprocal space is sampled with each stationary orientation of the sample and the detectors. The SCD has two ^{6}Li-glass scintillation position-sensitive area detectors, each with active areas of 15 × 15 cm^2 and a spatial resolution of < 1.5 mm. One of the detectors is centered at a scattering angle of 75° and a crystal-to-detector distance of 23 cm, and the second detector is at 120° and 18 cm. A crystal of *syn*-$Ir_2^{II,II}(tfepma)_3(H)_4$ (**4**-*syn*), with approximate dimensions of 2 × 2 × 1 mm^3 and a weight of 6.8 mg, was coated with fluorocarbon grease, wrapped in aluminum foil, and glued to an aluminum pin that was mounted on the cold stage of a closed-cycle helium refrigerator cooled to –80(1) °C under flowing N_2. Details of the data collection and analysis procedures have been published previously.[60–63] The GSAS software package was used for structural analysis.[64] Initial atomic positions were taken from the X-ray structure of **4**, structural refinement then proceeded directly from the neutron diffraction data. Hydride ligands bound to iridium were clearly located by difference Fourier maps. However the elevated temperatures required to maintain crystallinity,

structural complexity from disordered $-CH_2CF_3$ groups, and limited data restricted the solution to isotropic refinement of the anisotropic displacement parameters.

4.4.5 NMR Kinetic Measurements

Variable temperature NMR kinetics studies were performed in C_6D_6, wherein a saturated solution of complex **2** (or **2**-d_{10}) in C_6D_6 was prepared; the solution was then filtered and sealed in a J. Young NMR tube. Kinetic runs were carried out over the range of 20–40°C (calibrated temperatures 22.2, 31.8, and 41.5°C) in 10 degree increments. Temperature calibration was carried out using 100% ethylene glycol. Spectra were recorded every 10 minutes for 200 minutes for each run. Relative concentrations of **2** and **3** (**2**-d_{10} and **3**-d_{10}) were assessed by integration over one of the –N–Me resonances characteristic for each complex in C_6D_6 (2.60 and 2.48 ppm respectively). The integral over both peaks was then set to 6H and then each peak was integrated separately. This analysis effectively gives a ratio of **2** to **3** (**2**-d_{10} to **3**-d_{10}) in solution and thus no internal standard was employed for this study. In all cases both the rise of **3** and the decay of **2** (**3**-d_{10} and **2**-d_{10}) were independently fit to a single exponential with rate constants that agree within error.

4.4.6 Preparation of $Ir_2^{II,II}(tfepma)_3(\mu\text{-}C_6H_4)(C_6H_5)H$ (2)

500 mg of $Ir_2^{0,II}(tfepma)_3Cl_2$ (0.261 mmol, 1 equiv) was dissolved in 5 ml of THF and the solution frozen in a coldwell. In a separate vial 2.1 equivalents of C_6H_5MgBr (548 μL, 1.0 M THF solution) was diluted with 1 mL THF and frozen. Immediately upon thawing the Grignard was added to the iridium complex dropwise, affecting a color change to light yellow. The solvent was then immediately removed, and the residue triturated with pentane (3 × 2 mL), then taken up in Et_2O (5 mL) and filtered through a plug of Celite. The light yellow solution was then concentrated to about 3 mL and placed in a freezer (–35°C) overnight. The supernatant was decanted and the resulting colorless solid was washed with a 2 mL of pentane to give 359 mg (69%) of $Ir_2^{II,II}(tfepma)_3(\mu\text{-}C_6H_4)(C_6H_5)H$ (**2**) as a colorless powder. ^1H NMR (THF-d_8) δ/ppm: –13.72 (ddt, 244.8 Hz, 20.4 Hz, 10.2 Hz, 1 H), 2.13 (m, 1H), 2.74 (t, 8.9 Hz, 3H), 2.82 (t, 10.2 Hz, 3H), 2.83 (t, 6.4 Hz, 3H), 3.24 (m, 1H), 3.85 – 5.21 (m, 22H), 6.62 (t, 6.8 Hz, 1H), 6.67 (t, 6.4 Hz, 2H), 6.78 (t, 10.2 Hz, 1H), 6.83 (t, 10.2 Hz, 1H), 7.01 (t, 5.9 Hz, 1H), 7.64 (t, 6.8 Hz, 1H), 8.00 (t, 8.1 Hz, 2H). $^{31}P\{^1H\}$ NMR (THF-d_8) δ/ppm: 24.09 (ddd, 370.4 Hz, 74.1, 26.7 Hz), 34.90 (m), 39.56 (dddd, 68.1 Hz, 35.6 Hz, 20.7 Hz, 8.9 Hz, 1P), 62.24 (dddd, 367.4 Hz, 91.8 Hz, 20.7

Hz, 8.9 Hz, 1P), 104.14 (dddd, 269.6 Hz, 30.0 Hz, 17.8 Hz, 8.9 Hz), 120.48 (ddd, 269.6 Hz, 26.7 Hz, 20.7 Hz). IR(CD_3CN) ν_{Ir-H} /cm^{-1}: 2069. Anal. Calc. for $C_{39}H_{43}N_3O_{12}F_{36}P_6Ir_2$: C, 23.42; H, 2.17; N, 2.10. Found: C, 23.21; H, 2.07; N, 1.99. Crystals suitable for X-ray diffraction were grown from concentrated Et_2O solutions layered with pentane at –35°C as colorless blocks.

4.4.7 Preparation of $Ir_2^{II,II}(tfepma)_3(\mu\text{-}C_6D_4)(C_6D_5)D$ (2-d_{10})

Preparation of **2**-d_{10} proceeded in a similar manner to that of complex **2**. 220 mg of $Ir_2^{0,II}(tfepma)_3Cl_2$ (0.115 mmol, 1 equiv) was dissolved in 5 ml of THF and the solution frozen in a coldwell. In a separate vial 2.1 equivalents of freshly prepared C_6D_5MgBr (482 µL, 0.5 M THF solution) was diluted with 1 mL THF and frozen. Immediately upon thawing the Grignard was added to the iridium complex dropwise, affecting a color change to light yellow. Workup proceeded as outlined for **2**, giving 209 mg (90%) of $Ir_2^{II,II}(tfepma)_3(\mu\text{-}C_6D_4)(C_6D_5)D$ (**2**-d_{10}) as a colorless solid. ^1H NMR (CD_3CN) δ/ppm: 2.56 (t, 6.4 Hz, 3H), 2.58 (t, 9.8 Hz, 3H), 2.78 (t, 9.8 Hz, 3H), 3.28 (m, 1H), 3.38 (m, 1H), 4.3–4.9 (m, 20H), 4.13 (m, 1H), 5.306 (m, 1H). $^{31}P\{^1H\}$ NMR (CD_3CN) δ/ppm: 26.29 (dddd, 318.0 Hz, 32.4 Hz, 21.5 Hz, 9.9 Hz), 31.84 (dddd, 924.5 Hz, 32.4 Hz, 26.1 Hz, 18.7 Hz), 56.50 (ddm, 318.0 Hz, 113.2 Hz), 65.10, (ddd, 113.2 Hz, 23.6 Hz, 9.9 Hz), 83.3 (dm, ~200 Hz), 93.33 (dddd, 924.5 Hz, 195.4 Hz, 26.1 Hz, 21.1 Hz). ^2H NMR (CH_3CN) δ/ppm: –13.61 (dm, 37 Hz), 6.5–7.2 (bm), 7.4–8.1 (bm). IR(CD_3CN) ν_{Ir-D} /cm^{-1}: 1453. Anal. Calc. for $C_{39}H_{33}D_{10}N_3O_{12}F_{36}P_6Ir_2$: C, 23.30; H, 2.66; N, 2.09. Found: C, 23.58; H, 2.29; N, 1.93.

4.4.8 Preparation of $Ir_2^{I,III}(tfepma)_3(\mu\text{-}C_6H_4)(C_6H_5)H$ (3)

235 mg of $Ir_2^{II,II}(tfepma)_3(\mu\text{-}C_6H_4)(C_6H_5)H$ (0.118 mmol) was suspended in 3 ml of C_6H_6 in a thick walled glass bomb giving a light yellow solution. The flask was then placed in an oil bath at 50°C for six hours. The oil bath was then allowed to cool slowly and the solvent decanted to give 150 mg (64%) of $Ir_2^{I,III}(tfepma)_3(\mu\text{-}C_6H_4)(C_6H_5)H$ (**3**) as a colorless single crystals. ^1H NMR (CD_3CN) δ/ppm: –9.79 (ddt, 233.3 Hz, 23.8 Hz, 6.4 Hz, 1H), 2.47 (t, 7.0 Hz, 3H), 2.79 (t, 6.4 Hz, 3H), 2.87 (t, 9.8 Hz, 3H), 3.2–3.4 (m, 4H), 3.75–4.01 (m, 2H), 4.1–4.9 (ovm, 18H), 6.75 (t, 6.4 Hz, 1H), 6.83–6.92 (m, 4H), 6.99 (t, 6.4 Hz, 1H), 7.20 (t, 6.4 Hz, 1H), 7.74 (bs, 2H). $^{31}P\{^1H\}$ NMR (CD_3CN) δ/ppm: 17.47 (m), 28.45 (dt, 833.3 Hz, 42.4 Hz), 87.0 (m), 90.64 (dt, 174.90 Hz, 32.39 Hz), 92.45 (dd, 213 Hz, 14.977 Hz), 97.19 (dm, 213 Hz). IR(CD_3CN) ν_{Ir-H} /cm^{-1}: 2023. Anal. Calc. for $C_{39}H_{43}N_3O_{12}F_{36}P_6Ir_2$: C, 23.42; H, 2.17; N, 2.10. Found: C, 23.33;

H, 2.08; N, 2.00. Crystals suitable for X-ray diffraction were picked from the recrystallized product as colorless blocks.

4.4.9 Preparation of $Ir_2^{I,III}(tfepma)_3(\mu\text{-}C_6D_4)(C_6D_5)D$ (3-d_{10})

Arylation with C_6D_5MgBr proceeded as in the preparation of **2**-d_{10}, using 328 mg of $Ir_2^{0,II}(tfepma)_3Cl_2$ (0.171 mmol) and 180 μL of C_6D_5MgBr (0.5 M THF solution, 2.1 equiv). The material was then worked up as in **2**-d_{10} except that after filtration through Celite the Et_2O solution was allowed to stir at ambient temperature for 16 hours and then concentrated to 3 mL and placed in a freezer at –35°C overnight to give 241 mg (70 %) $Ir_2^{I,III}(tfepma)_3(\mu\text{-}C_6D_4)(C_6D_5)D$ (3-d_{10}) as a colorless solid. Complex **3**-d_{10} can also be prepared by gently heating solutions of **2**-d_{10} in an analogous manner to that which gave complex **3** from **2**. ^1H NMR (CD_3CN) δ/ppm: 2.38 (m, 1H), 2.47 (t, 6.7 Hz, 3H), 2.79 (t, 7.3 Hz, 3H), 2.87 (t, 9.8 Hz, 3H), 3.15–3.35 (ovm, 3H), 3.75–4.02 (m, 2H), 4.1–4.9 (ovm, 18H). ^2H NMR (CH_3CN) δ/ppm: –9.70 (dm, 34 Hz), 6.5–7.5 (bm), 7.79 (bm). $^{31}P\{^1H\}$ NMR (CH_3CN) δ/ppm: 22.48 (m), 33.56 (ddd, 874.0 Hz, 173.7 Hz, 31.7 Hz), 91.5 (m), 95.57 (ddd, 874.0 Hz 173.7 Hz, 31.7 Hz), 97.57 (dd, 212.3 Hz, 16.5 Hz), 102.14 (ddd, 212.3 Hz, 31.7 Hz, 26.6 Hz). IR(CD_3CN) ν_{Ir-D} /cm^{-1}: 1415. Anal. Calc. for $C_{39}H_{33}D_{10}N_3O_{12}F_{36}P_6Ir_2$: C, 23.30; H, 2.66; N, 2.09. Found: C, 23.79; H, 2.09; N, 1.95.

4.4.10 Preparation of $Ir_2^{II,II}(tfepma)_3(H)_4$ (4)

374 mg of $Ir_2^{0,II}(tfepma)_3Cl_2$ was dissolved in 4 mL THF with stirring solution frozen in a coldwell. In a separate vial, C_6H_5MgBr (410 μL, 1.0 M THF solution, 2.1 equiv) was diluted with 1 mL THF and frozen. Reaction and workup proceeded as for complex **2**. The resulting Et_2O solution (5 mL) was loaded into a thick walled glass bomb with a Teflon valve and the vessel attached to a high vacuum line. The solution was freeze pump thawed (1×10^{-5} Torr) for three cycles and then 1 atm of hydrogen was introduced to the reaction vessel after passing through a U–tube immersed in liquid nitrogen. The reaction vessel was sealed, shaken vigorously for 10 minutes, and then allowed to stand overnight at which point some colorless material precipitated from solution. The vessel was then pumped into a glovebox and 2 mL of Et_2O was added to dissolve the precipitate. The solution was then filtered and placed in a freezer (–35°C) overnight to afford 170 mg (47%) of $Ir_2^{II,II}(tfepma)_3(H)_4$ (**4**) material as a colorless solid. Dynamic behavior is evident in the NMR of **4**, while complexes **2** and **3** exhibit sharp, well

defined, hydride and N–Me resonances, those of **4** in THF-d_8 are considerably broadened. Four N–Me resonances are observed at 2.59, 2.73, 2.86 and 2.90 ppm. Integration reveals a 2:1 ratio for the peaks at 2.73 and 2.90 ppm, a 2:1 ratio is also identified for the resonances at 2.86 ppm and 2.59 ppm. The two sets of peaks integrate in a 3:2 ratio, favoring the peaks at 2.73 ppm and 2.90 ppm, indicative of two products in solution. The hydride region also indicates multiple components with resonances at –11.51 ppm and –11.64 ppm observed as broad singlets, and a resonance centered at –14.40 ppm as overlapping broad multiplets. Integration over all N–Me resonances and all hydrides gave a 9:4 ratio, as expected for the $Ir_2^{II,II}(tfepma)_3(H)_4$ formulation. Crystals suitable for X-ray diffraction were grown from a subsequent reaction following the same procedure as above except that the reaction mixture in Et_2O was allowed to stand for several days, resulting in the deposition of large colorless blocks of *syn*-$Ir_2^{II,II}(tfepma)_3(H)_4$. The crystals obtained in this manner cracked and lost crystallinity at temperatures below –80°C, necessitating data collection at elevated temperatures relative to **2** and **3**, resulting in significant disorder of the $-CH_2CF_3$ groups of the tfepma ligands. After X-ray analysis the remaining crystals were loaded into a J. Young resealable NMR tube, attached to a high vacuum line, and THF-d_8 vacuum transferred into the tube while immersed in liquid nitrogen. The tube was warmed until the THF thawed and then was immediately placed into the magnetic field of an NMR spectrometer maintained at –80°C. Analysis by ^{1}H NMR evidenced multiple components and neither the hydride nor the N–Me resonances exhibited noticeable sharpening. ^{1}H NMR (THF-d_8, 20°C) δ/ppm: –14.65– –14.20 (ovm, 3.5H), –11.51 (bs, 2H), –11.64 (bs, 1.5H), 2.59 (b, 1.5H), 2.70 (bs, 6H), 2.86 (b, 3.9H), 2.90 (t, 6.7 Hz, 3H), 4.05–4.86 (ovm, 40H). ^{1}H NMR (THF-d_8, –80°C) δ/ppm: –14.35 (ovm, 3.5 H), –11.58 (bs, 1.4 H), –11.405 (bs, 2H), 2.55 (b, 1.5H), 2.64 (bs, 6H), 2.88 (b, 4H), 3.02 (t, 6.7 Hz, 3H), 4.05–4.90 (ovm, 40H). ^{31}P{^{1}H} NMR (THF-d_8, –80°C): 102.5 (m), 110.2 (m), 113.0 (m), 115.4 (m), 118.1 (m), 121.5 (m). IR(CD_3CN) ν_{Ir-H} /cm^{-1}: 2036 (sharp), 1966 (broad shoulder). Anal. Calc. For $C_{27}H_{37}N_3O_{12}F_{36}P_6Ir_2$: C, 17.53; H, 2.02; N, 2.27. Found: C, 17.64; H, 2.04; N, 2.18. The synthesis of **4** can also be initiated from isolated samples of **2**, but the hydrogenation competes with isomerization from **2** to **3**, and so in the interests of maximizing yields the hydrogenation was initiated from freshly prepared solutions of **2**. Neutron diffraction experiments were performed at the IPNS at Argonne National Laboratories (*vide supra*) on large single crystals of **4** (2 × 2 × 1 mm^3; 6.8 mg). Hydride ligand

fractional occupancies refine to a value of unity for each ligand; suggesting that the hydrides are not disordered over the bimetallic core in the solid state.

4.5 Crystallographic Tables

Table 4.4. Crystallographic data and structural refinement parameters for $Ir_2^{II,II}(tfepma)_3(\mu\text{-}C_6H_4)(C_6H_5)H$ (**2**), $Ir_2^{II,II}(tfepma)_3(\mu\text{-}C_6D_4)(C_6D_5)D$ (**2-d_{10}**), $Ir_2^{I,III}(tfepma)_3(\mu\text{-}C_6H_4)(C_6H_5)H$ (**3**).

	2 · (CH_2Cl_2)	**2-d_{10} · (CH_2Cl_2)**	**3**
Empirical formula	$C_{40}H_{45}F_{36}Ir_2N_3O_{12}P_6Cl_2$	$C_{40}H_{35}D_{10}F_{36}Ir_2N_3O_{12}P_6Cl_2$	$C_{39}H_{43}F_{36}Ir_2N_3O_{12}P_6$
Formula weight	2084.91	2094.91	1999.98
Temperature	−173(2)°C	−173(2)°C	−173(2)°C
Wavelength	0.71073 Å	0.71073 Å	0.71073 Å
Crystal system	Triclinic	Triclinic	Monoclinic
Space group	$P\bar{1}$	$P\bar{1}$	$P2_1/c$
Unit cell dimensions	a = 12.975(2) Å	a = 12.957(2) Å	a = 21.1423(13) Å
	b = 13.951(2) Å	b = 13.860(2) Å	b = 16.6501(10) Å
	c = 20.478(3) Å	c = 20.390(4) Å	c = 18.5674(12) Å
	α = 95.609(3)°	α = 95.552(3)°	α = 90°
	β = 104.539(3)°	β = 103.892(3)°	β = 98.7750(10)°
	γ = 108.063(3)°	γ = 107.641(3)°	γ = 90°
Volume	3348.6(10) Å^3	3317.6(10) Å^3	6459.6(7) Å^3
Z	2	2	4
Density (calc)	2.068 Mg/m^3	2.086 Mg/m^3	2.057 Mg/m^3
Absorption coefficient	4.349 mm^{-1}	4.389 mm^{-1}	4.424 mm^{-1}
F(000)	2008	2006	3848
Crystal size (mm)	0.20 × 0.12 × 0.10	0.25 × 0.20 × 0.10	0.12 × 0.10 × 0.06
Θ range for data collection	1.05 to 28.29°	1.71 to 28.29°	0.97 to 28.27°
Index Ranges	$-17 \le h \le 17$	$-17 \le h \le 17$	$-23 \le h \le 28$
	$-18 \le k \le 12$	$-9 \le k \le 18$	$-22 \le k \le 22$
	$-26 \le \ell \le 27$	$-27 \le \ell \le 27$	$-24 \le \ell \le 20$
Reflections collected	24320	23734	46411
Ind. reflections	16261	15974	15975
Absorption correction	Empirical SADABS	Empirical SADABS	Empirical SADABS
Refinement method	Full–matrix ls on F^2	Full–matrix ls on F^2	Full–matrix ls on F^2
Data	16261	15974	15975
Restraints	4	0	7
Parameters	939	913	907
Goodness-of-fit on F^2 [a]	1.028	1.051	1.013
Final R indices [I>2σ(I)][b]	R_1 = 0.0341	R_1 = 0.0334	R_1 = 0.0297
	wR_2 = 0.0873	wR_2 = 0.0871	wR_2 = 0.0604
R indices (all data)[b]	R_1 = 0.0383	R_1 = 0.0362	R_1 = 0.0412
	wR_2 = 0.0907	wR_2 = 0.0890	wR_2 =0.0658
largest diff. peak	1.692 e/Å^3	2.228 e/Å^3	1.513 e/Å^3
largest diff. hole	−2.174 e/Å^3	−1.753 e/Å^3	−1.528 e/Å^3

[a] GOF = $[\Sigma w(F_o^2 - F_c^2)^2/(n-p)]^{1/2}$ (n = number of data, p = number of parameters varied.
[b] $R_1 = \Sigma||F_o| - |F_c||/\Sigma|F_o|$; $wR_2 = [\Sigma w(F_o^2 - F_c^2)^2/\Sigma wF_o^4]^{1/2}$.

Table 4.5. Crystal data and structural refinement parameters for $Ir_2^{II,II}(tfepma)_3(H)_4$ (**4**) from both X-ray and neutron diffraction methods. The neutron data represented here is the result of a preliminary refinement.

	4 (*X-ray*)	**4** (*Neutron*)
Empirical formula	$C_{27}H_{37}F_{36}Ir_2N_3O_{12}P_6$	$C_{27}H_{37}F_{36}Ir_2N_3O_{12}P_6$
Formula weight	1849.82	1849.82
Temperature	–75(2)°C	–80(1)°C
Wavelength	0.71073 Å	*NA*
Crystal system	Triclinic	Triclinic
Space group	$P\bar{1}$	$P\bar{1}$
Unit cell dimensions	a = 12.0419(6) Å	a = 11.982(4) Å
	b = 12.2511(6) Å	b = 12.206(5) Å
	c = 21.5922(11) Å	c = 21.559(8) Å
	α = 80.6240(10)°	α = 80.42(3)°
	β = 80.1890(10)°	β = 79.95(3)°
	γ = 61.5970(10)°	γ = 61.61(2)°
Volume	2748.7(2) Å^3	2718(2) Å^3
Z	2	2
Density (calc)	2.230 Mg/m^3	2.247 Mg/m^3
Absorption coefficient	5.188 mm^{-1}	5.188 mm^{-1}
F(000)	1760	1760
Crystal size (mm)	0.20 × 0.12 × 0.10	2 × 2 × 1
Θ range for data collection	0.96 to 28.29°	
Index Ranges	$-14 \le h \le 16$	
	$-16 \le k \le 16$	
	$-28 \le \ell \le 28$	
Reflections collected	47965	3781
Ind. reflections	13584	2258
Absorption correction	Empirical SADABS	
Refinement method	Full–matrix ls on F^2	Full–matrix ls on F^2
Data	13584	3781
Restraints	6	
Parameters	999	581
Goodness-of-fit on F^2 [a]	1.016	1.53
Final R indices [I>2σ(I)][b]	R_1 = 0.0269	
	wR_2 = 0.0664	
R indices (all data)[b]	R_1 = 0.0327	R_1 = 0.184
	wR_2 = 0.0699	wR_2 = 0.184
largest diff. peak	1.378 e/Å^3	
largest diff. hole	–0.874 e/Å^3	

[a] GOF = $[\Sigma w(F_o^2 - F_c^2)^2/(n-p)]^{1/2}$ (n = number of data, p = number of parameters varied.
[b] $R_1 = \Sigma||F_o| - |F_c||/\Sigma|F_o|$; $wR_2 = [\Sigma w(F_o^2 - F_c^2)^2/\Sigma wF_o^4]^{1/2}$.

4.6 References

(1) Dulebohn, J. I.; Ward, D. L.; Nocera, D. G. *J. Am. Chem. Soc.* **1990**, *112*, 2969-2977.

(2) Kadis, J.; Shin, Y. K.; Dulebohn, J. I.; Ward, D. L.; Nocera, D. G. *Inorg. Chem.* **1996**, *35*, 811-817.

(3) Heyduk, A. F.; Macintosh, A. M.; Nocera, D. G. *J. Am. Chem. Soc.* **1999**, *121*, 5023-5032.

(4) Gray, T. G.; Nocera, D. G. *Chem. Commun.* **2005**, 1540-1542.

(5) McCollum, D. G.; Bosnich, B. *Inorg. Chim. Acta* **1998**, *270*, 13-19.

(6) Bosnich, B. *Inorg. Chem.* **1999**, *38*, 2554-2562.

(7) Muetterties, E. L.; Rhodin, T.N.; Band, E,; Brucker, C,; Pretzer, W. R. *Chem. Rev.* **1979**, *79*, 91-137.

(8) For some examples see and the references cited within: a) Wheatley, N.; Klack, P. *Chem. Rev.* **1999**, *99*, 3379-3419. b) van den Beuken, E. K.; Feringa, B. L. *Tetrahedron* **1998**, *54*, 12985-13011.

(9) Esswein, A. J.; Veige, A. S. Nocera, D. G. *J. Am. Chem. Soc.* **2005**, *127*, 16641-16651.

(10) Heyduk, A. F.; Nocera, D. G. *J. Am. Chem. Soc.* **2000**, *122*, 9415-9426.

(11) Gray, T. G.; Veige, A. S.; Nocera, D. G. *J. Am. Chem. Soc.* **2004**, *126*, 9760-9768.

(12) Veige, A. S.; Gray, T. G.; Nocera, D. G. *Inorg. Chem.* **2005**, *44*, 17-26.

(13) Heyduk, A. F.; Nocera, D. G. *Science* **2001**, *293*, 1639-1641.

(14) Veige, A. S.; Nocera, D. G. *Chem. Commun.* **2004**, 1958-1959.

(15) Heyduk, A. F.; Nocera, D. G. *Chem. Commun.* **1999**, 1519-1520.

(16) Bennet, M. A.; Wenger, E. *Chem. Ber./Recl.* **1997**, *130*, 102-1042.

(17) Jones, W. M.; Klosin, *J. Adv. Organomet. Chem.* **1998**, *42*, 147-221.

(18) Brait, S.; Deabate, S. Knox, S. A. R.; Sappa, E. *J. Clust. Sci.* **2001**, *12*, 139-173.

(19) Rausch, M. D.; Gastinger, R. G.; Gardner, S. A.; Brown, R. K.; wood, J. S. *J. Am. Chem. Soc.* **1977**, *99*, 7870-7876.

(20) Grushin, V. V.; Vymenits, A. B.; Yanovskii, A. I.; Struchkov, Y. T.; Vol'pin, M. E. *Organometallics*, **1991**, *10*, 48-49.

(21) McGhee, W. D.; Foo, T.; Hollander, F. G.; Bergman, R. G. J. Am. Chem. Soc. **1988**, *110*, 8543-8545.

(22) Bennet, M. J.; Graham, W. A. G.; Stewart, R. P., Jr.; Tuggle, R. M. *Inorg. Chem.* **1973**, *12*, 2944-2949.

(23) Retbøll, M.; Edwards, A. J.; Rae, A. D.; Willis, A. C.; Bennet, M. A.; Wenger, E. *J. Am. Chem. Soc.* **2002**, *124*, 8348-8360.

(24) Johansson, L.; Tilset. M.; Labinger, J. A.; Bercaw, J. E. *J. Am. Chem. Soc.* **2000**, *122*, 10846-10855.

(25) Albéniz, A. C.; Schulte, G.; Crabtree, R. H. *Organometallics* **1992**, *11*, 242-249.

(26) Belt, S. T.; Duckett, S. B.; Helliwell, M.; Perutz, R.N. *J. Chem. Soc. Chem. Commun.* **1989**, 929-930.

(27) Belt, S. T.; Dong. L.; Duckett, S. B.; Jones. W. D.; Partridge, M. G.; Perutz, R. N. *J. Chem. Soc. Chem. Commun.* **1991**, 266-269.

(28) For example see: Peterson, T. H.; Golden, J. T.; Bergman, R. G. *J. Am. Chem. Soc.* **2001**, *123*, 455-462.

(29) Buchanan, J. M.; Stryker, J. M.; Bergman, R. G. *J. Am. Chem. Soc.* **1986**, *108*, 1537-1550.

(30) Periana, R. A.; Bergman, R. G. *J. Am. Chem. Soc.* **1986**, *108*, 7332-7346.

(31) Bullock, M. R.; Headford, C. E. L.; Hennessy, K. M.; Kegley, S. E.; Norton, J. R. *J. Am. Chem. Soc.* **1989**, *111*, 3897-3908.

(32) Parkin, G.; Bercaw, J. E. *Organometallics* **1989**, *8*, 1172-1179.

(33) Gould, G. L.; Heinekey, D. M. *J. Am. Chem. Soc.* **1989**, *111*, 5502-5504.

(34) Wang, C.; Ziller, J. W.; Flood, T. C. *J. Am. Chem. Soc.* **1995**, *117*, 1647-1648.

(35) Stahl, S. S.; Labinger, J. A.; Bercaw, J. E. *J. Am. Chem. Soc.* **1996**, , *118*, 5961-5976.

(36) Wick, D. G.; Reynolds, K. A.; Jones, W. D. *J. Am. Chem Soc.* **1999**, *121*, 3964-3983.

(37) Northcutt, T. O.; Wick, D. G.; Vetter, A. J.; Jones, W. D. *J. Am. Chem. Soc.* **2001**, *123*, 7257-7270.

(38) Lo, C. H.; Haskel, A.; Kapon, M.; Keinan, E. *J. Am. Chem. Soc.* **2002**, *124*, 3226-3228. Although the explanations for the observed isotope effects have been recently disputed in the literature, see references 40 and 41.

(39) Iron, M. A.; Lo, C. H.; Martin, J. M. L.; Keinan, E. *J. Am. Chem. Soc.* **2002**, *124*, 704-705. Although the explanations for the observed isotope effects have been recently disputed in the literature, see references 40and 41.

(40) Churchill, D. G.; Janak, K. E.; Wittenburg, J. S.; Parkin, G. *J. Am. Chem. Soc.* **2003**, *125*, 1403-1420.

(41) Jones, W. D. *Acc. Chem. Res.* **2003**, *36*, 140-146.

(42) Jones, W. D.; Feher, F. J. *J. Am. Chem. Soc.* **1986**, *108*, 4814-4819.

(43) A note on nomenclature at this point, a true reductive elimination is not required (and sometimes not observed) for the observation of an inverse isotope effect, a reductive coupling event of the alkyl hydride (deuteride) to give a σ–alkane complex is sufficient.

(44) The equilibrium isotope effect $K_{eq}^{H/D}$ can be expressed as: $K_{eq}^{H/D} = \frac{k_{RC}{}^{H} / k_{OC}{}^{H}}{k_{RC}{}^{D} / k_{OC}{}^{D}} = \frac{k_{RC}{}^{H} / k_{RC}{}^{D}}{k_{OC}{}^{H} / k_{OC}{}^{D}}$

(45) For more detailed discussions see references 40 and 41.

(46) Crabtree, R. H. *The Organometallic Chemistry of the Transition Metals*; Wiley: New York, **1994**.

(47) For an authoritative treatise see: Kubas, G. J. *Metal Dihydrogen and σ–Bond Complexes*; Kluwer Academic/Plenum Publishers: New York, 2001; and references within.

(48) For other recent reviews see: a) Heinekey, D. M.; Lledós, A.; Lluch, J. M. *Chem. Soc. Rev.* **2004**, *33*, 175-182; b) Yousufuddin, M.; Bin Wen, T.; Mason, S. A.; McIntyre, G. J.; Jia, G.; Bau, R. *Angew. Chem. Intl. Ed.* **2005**, *44*, 7227-7230.

(49) Crabtree, R. H. *Acc. Chem. Res.* **1990**, *23*, 95-101.

(50) Desrosiers, P. J.; Cai, L.; Lin, Z.; Richards, R.; Halpern, J. *J. Am. Chem. Soc.* **1991**, *113*, 4173-4184.

(51) Species such as this have seen precedent in the literature, some crystallographically characterized examples on late metals include: a) Evans, D. G.; Hughes, G. R.; Mingos, D. M. P.; Bassett, J. M.; Welch, A. J. *J. Chem. Soc. Chem. Commun.* **1980**, 1255-1257. b) Nobel, D.; van Koten, G.; Spek, A. L. *Angew. Chem. Intl. Ed. Engl.* **1989**, *28*, 208-210. c) Meyer, E. M.; Gamborotta, S.; Floriani, C.; Chiesi-Villa, A.; Guastini, C. *Organometallics* **1989**, *8*, 1067-1079. d) Bradford, C. W.; Nyholm, R. S.; Gainsford, G. J.; Guss, J. M.; Ireland, P. R.; Mason, R. *J. Chem. Soc. Chem. Commum.* **1972**, 87-89. e) Hlavinka, M. L.; Hagadorn, J. R. *Organometallics* **2005**, *24*, 5335-5341.

(52) Crumpton, D. M.; Goldberg, K. I. *J. Am. Chem. Soc.* **2000**, *122*, 962-963.

(53) Fekl, U.; Goldberg K. I. *J. Am. Chem. Soc.* **2002**, 124, 6804-6805.

(54) Jensen, M. P; Wick, D. D.; Reinartz, S.; White, P. S.; Templeton, J. L.; Goldberg, K. I. *J. Am. Chem. Soc.* **2003**, *125*, 8614-8624.

(55) Crumpton-Bregel, D. M; Goldberg, K. I. *J. Am. Chem. Soc.* **2003**, *125*, 9442-9456.

(56) Armarego, W. L. F.; Perrin, D. D. *Purification of Laboratory Chemicals*, 4th ed.; Butterworth-Heinmann: Oxford, 1996.

(57) Bianco, V. D.; Doronzo, S. *Inorg. Synth.* **1976**, *12*, 164-166.

(58) Ganesan, M; Krishnamurthy, S. S.; Nethaji, M. *J. Organomet. Chem.* **1998**, *570*, 247-254.

(59) Balakrishna, M. S.; Prakasha, T. K.; Krishnamurthy, S. S.; Siriwardane, U; Hosmane, N. S. *J. Organomet. Chem.* **1990**, *390*, 203-216.

(60) Schultz, A. J. S., K.; Teller, R. G.; Williams, J. M.; Lukehart, C. M., *J. Am. Chem. Soc.* **1984,** 106, 999-1003.

(61) Jacobson, R. A. *J. Appl. Phys.* **1986**, *19*, 283-286.

(62) Schultz, A. J. *Trans. Am. Crystallogr. Assoc.* **1987**, *23*, 61-69.

(63) Schultz, A. J.; Van Derveer, D. G.; Parker, D. W.; Baldwin, J. E. *Acta Crystallogr. C* **1990**, *46*, 276-279.

(64) Larson, A. C.; Von Dreele, R. B. *General Structure Analysis System--GSAS*, Los Alamos National Laboratory, 2000.

Arthur was born on July 10th 1980 in Rochester NY to Dr. Vivian E. and Dr. Arthur J. Esswein. Arthur was the middle child and has four sisters Karen, Christine, Carolyn and Katherine. When Arthur was 5 his family moved to the small Cape Cod town of Falmouth MA. It was here that Arthur's interests in solar energy began to take shape thanks to many sunny afternoons on the beach. After graduating from Falmouth High School in 1998, he continued his education at the Johns Hopkins University in Baltimore MD where he originally intended to study Chemical Engineering. In his sophomore year he decided to focus on chemistry and joined the laboratories of Professor Gerald J. Meyer as an undergraduate researcher. In these labs he was first introduced to dye-sensitized solar cells and solar energy research in general. After earning a B.A. in both Chemistry and Mathematics in the spring of 2002, Arthur decided to pursue a doctoral degree at the Massachusetts Institute of Technology under the tutelage of Professor Daniel G. Nocera. Arthur's PhD research has focused on the study of multielectron chemistry and photochemistry of two-electron mixed valence bimetallic complexes. After completing his PhD, Arthur plans to conduct postdoctoral research in the laboratories of Professor T. Don Tilley at the University of California, Berkeley. His research will focus on the electrocatalytic oxidation of water to oxygen using small molecule mimics of the photosynthetic oxygen evolving complex.

Arthur J. Esswein

Department of Chemistry, 2-301
77 Massachusetts Avenue
Cambridge MA, 02139-4307

Massachusetts Institute of Technology

Phone: 617-258-7268 *Fax:* 617-253-7670 *Email:* aesswein@mit.edu

Education

2002-2007 **Massachusetts Institute of Technology**, PhD in Inorganic Chemistry, (September 2007). Research Advisor: Professor Daniel G. Nocera. Thesis: "Late Transition Metal Bimetallics for Photocatalytic Hydrogen Production, M–X and C–H Bond Activation."

1998-2002 **Johns Hopkins University**, B.A. in Chemistry with honors.
Research Advisor: Professor Gerald J. Meyer.

1998-2002 **Johns Hopkins University**, B.A. in Mathematics

Research Experience

2002-2007 **Massachusetts Institute of Technology** with Professor Daniel G. Nocera.

1999-2002 **Johns Hopkins University** with Professor Gerald J. Meyer.

Talks, Seminars, Poster Presentations

"Photocatalytic Hydrogen Production" Arthur J. Esswein, Adam S. Veige, and Daniel G. Nocera. Gordon Research Conference: Solar Fuels. January 2007. Poster Presentation.

"Heterobimetallic Rh^{II}–Au^{II} Complexes for Photoinduced M–X Bond Activation" Arthur J. Esswein, Jillian L. Dempsey and Daniel G. Nocera. 232nd ACS National Meeting, San Francisco, CA; September 2006. Poster Presentation.

"A Photocycle for Hydrogen Production" Arthur J. Esswein, Adam S. Veige and Daniel G. Nocera. 231st ACS National Meeting, Atlanta, GA; March 2006. Oral Presentation.

"The Molecular Challenges of Consequence to Renewable Energy" Arthur J. Esswein and Daniel G. Nocera. ACS PRF summer school on Sustainable Energy and the Environment, summer 2005. Guest Lecturer.

Publications

"Intramolecular C–H Bond Activation and Redox Isomerization Across Two-electron Mixed Valence Diiridium Cores" Arthur J. Esswein, Adam S. Veige and Daniel G. Nocera. *Submitted to Organometallics.*

"Metal-Halide Bond Photoactivation from a Pt^{III}–Au^{II} Complex" Timothy R. Cook, Arthur J. Esswein and Daniel G. Nocera. *Accepted for publication in the Journal of the American Chemical Society.*

"Molecular Photocatalytic Hydrogen Production" Arthur J. Esswein and Daniel G. Nocera. *Accepted for publication in Chemical Reviews.*

"Luminescent, Three-Coordinate Azadipyrromethene Complexes of d^{10} Copper, Silver, and Gold" Thomas S. Teets, David V. Partyka, Arthur J. Esswein, James B. Updegraff and Thomas G. Gray. *Inorganic Chemistry, in press.*

"Gold(I) Pyrenyls: Excited State Consequences of Carbon-Gold Bond Formation" David V. Partyka, Arthur J. Esswein, James B. Updegraff, Mattias Zeller, Allen D. Hunter and Thomas G. Gray. *Organometallics* **2007**, *26*, 3279-3282.

"A Rh^{II}–Au^{II} Bimetallic Core with a Direct Metal–Metal Bond" Arthur J. Esswein, Jillian L. Dempsey and Daniel G. Nocera. *Inorganic Chemistry* **2007**, *46*, 2362-2364.

"A Photocycle for Hydrogen Production from Two-electron Mixed Valence Complexes" Arthur J. Esswein, Adam S. Veige and Daniel G. Nocera. *Journal of the American Chemical Society* **2005**, *127*, 16641-16651.

"Molecular Chemistry of Consequence to Renewable Energy" Jillian L. Dempsey, Arthur J. Esswein, David R. Manke, Joel Rosenthal, Jake D. Soper and Daniel G. Nocera. *Inorganic Chemistry* **2005**, *44*, 6879-6892.

"Oxygen and Hydrogen Photocatalysis by Two-electron Mixed-Valence Coordination Compounds" Joel Rosenthal, Julien Bachman, Jillian L. Dempsey, Arthur J. Esswein, Thomas G. Gray, Justin M. Hodgkiss, David R. Manke, Thomas D. Luckett, Bradford J. Pistorio, Adam S. Veige and Daniel G. Nocera. *Coordination Chemistry Reviews* **2005**, *249*, 1316-1326.

Teaching/Mentorship Experience

Summer 2007	Catalyst program for the education of gifted high school students
Fall 2004	Teaching Assistant (TA) mentor for the Dept. of Chemistry at MIT
Fall 2003	TA mentor for the Dept. of Chemistry at MIT
Spring 2003	TA for 5.111 "Introduction to Chemical Principles"
Fall 2002	TA for 5.112 "Advanced Introduction to Chemical Principles"

There are a lot of people that need to be thanked for helping me during my time at MIT. I won't have time to give them all the attention they deserve, but, so it goes (RIP Kurt). First of all I'd like to thank a few postdocs that really helped me get going in my first few years. Matt Shores taught me nearly everything I know about X-ray crystallography. It was slow going for a while, and I had a lot of questions, but somehow you had the patience to deal with me. I just had to buy you beer. I still can't believe you didn't take that job at MIT. N i e l s "wait, what am I looking at here?" Damrauer taught me a lot about critical thinking, questioning fearlessly, the evils of sugar packets, and perhaps most importantly, N i e l s introduced me to the B-Side Lounge. I hope you're having fun driving your Prius around Boulder you smug motherf@cker. I had never made a compound before arriving at MIT. Adam Veige changed that by introducing me to the unique joys of synthetic chemistry. Adam your ability to crystallize compounds is unparalleled; it's not hyperbole to say that you could probably drop a deuce in a J. Young tube and somehow get single crystals of what you ate for dinner last night. Thank you also for introducing me to the Canadian ballet and for being at the heart of nearly all of the best and worst Nocera group moments. I've been getting a lot of mileage out of those stories. Thomas Gray, thanks for teaching me how to run calculations. It was and still is great working with you. You have a unique charm that always brings a smile to my face. Your group meeting on second order Jahn-Teller effects was riveting. May your soda always be flat.

Towards the end of my time Matt Kanan, Dino Villagran, and Ted Betley joined the lab as postdocs. You guys have all been great and gave me a much needed boost when things were looking bleak. Matt, thanks for the spirited debates at the Muddy and for introducing me to Grafton Street and the Kong. Matt, you also shouldered the responsibility of being the token conservative in the lab remarkably well after the departure of David Manke (more on this later). Dino, I learned a lot about computational chemistry from you, thank you for being so patient. You also taught me a lot about Mexican culture, who knew that Mexicans have a mouse instead of the tooth fairy? Ted, despite having only one knee you were a home-run hitting machine, and I've never been hit on by a married woman like that time we went out together. If one of your food allergies or the tenure process at Harvard doesn't kill you first, I look forward to being friends for a long time. Professionally you were a fantastic sounding board for ideas, and the lab just isn't the same without you nancying around. All of you are destined to do great things, unlike those clowns in the previous paragraph.

Despite having a reputation for being large and aggressive, the graduate students in the Nocera lab took me in and made me feel very comfortable. The big faces at the time: Aetna Wun, Bart Bartlett, and David Manke were especially welcoming. Aetna, we'll get some fish tacos together when I move out to California; I know you can't get enough of them. Bart Martell Bartlett, I don't even know where to begin. A night out with you was always an experience. I look forward to seeing you again in Berkeley, but can you please never put those binder clips on your nipples in front of me again? David, I'll probably never get along with someone as conservative as you ever again. You were always a major player in group fun and even though Dan liked to say that you were boring, the lab got a lot less exciting when you left. You also hold the distinction of being the only person I know who has slept on a bench in central square.

Jenny Yang, Joel Rosenthal, Julien Bachman, and Justin Hodgkiss: the J-crew. Jenny, thanks for being an absolute sweetheart, and for baking the group nice things to eat all the time. I loved going out to eat in Chinatown with you; hopefully that will continue in San Francisco. Joel "Let's Go Mets" Rosenthal, not much of a third baseman, but a good friend. I don't know how you do it, but you're the only one sometimes that can make Dan shut his face. Julien, thanks for

putting up with all the messes I would make in the glovebox and vacline. Your relentless optimism was legendary and always made me smile. I hope you'll always be all "Swiss" about everything that life throws at you. Justin, it was great to have another clown around the lab, and you threw a mean party. The way you corrupted Z-Loh would have made even Charles Manson proud. Becky, you somehow always managed to remain cheerful and upbeat; I always appreciated your positive attitude. Emily, I wish you all the luck in finishing up at MIT and in life. Liz thanks for being such a good sport. Joel and I used to have so much fun picking on you, at least on my end it was all good natured. I'm really sorry I called you a bulldyke that one time, and for that other practical joke. Glen, grow your hair out again, that was way hotter than what you've got going on now. Tiiiiiimmmmmeeeeeeaaaa! You made the job of being your mentor really easy, keep up the great work Frodo. To be honest though, I really was sad when I realized that you didn't need me anymore. Little Emily, thanks for buying *The Chronic* and *Ready to Die* on vinyl so I could feel cool at your parties. I'll have Manhattan fixings ready for whenever you come out to California. You can ever wear pointy shoes and I promise I won't make fun of them. Yogesh, thanks for being such a great deskmate, the smell certainly improved upon your arrival. Mike, it's been great having you in the lab, Manke was right. You need to bring back the Nocera group edge. Don't worry though, the freedom fest is closer than you think. Jay Yang, I really can't believe that you sincerely asked me for a right handed screwdriver; that totally made my day.

My classmates deserve a special section. Yelena, I hope you've found happiness in whatever you're doing now. Streece, where to begin...Having Steven Reece as a classmate at MIT has been fantastic and also very humbling. Streece you are an absolute machine and are by far the most productive person I've ever had the pleasure of working with. Beyond that, you put up with my ridiculous antics, like the time I called you at 11 PM to come back to MIT to play *Amazing Grace* on your bagpipes while I buried Dan's dead guinea pig in the atomic courtyard.

Even though the Nocera group was pretty xenophobic, there were some students outside the group that deserve some words of thanks: Josh Figueroa, Chris Clough, and Alex Fox. Josh "the Dark Specialist" Figueroa, you're the only person I know who can give can themselves a nickname. You have a unique point of view and talking to you was always a lot of fun. You have Big Face. Chris Clough, sometimes I don't know how you're still alive, but I'm glad you are. The circus that is C-manis must go on. Alex Fox, I'd like to think that I pretty much single handedly talked you down from the ledge before your 3rd year orals, but in reality it took half the inorganic division. Arfox, don't worry, they already know. I'm sorry I called you out at the end of my 4th year talk, but I just couldn't resist. Keep in touch; you're welcome in my house anytime Lobsterboy.

There are a lot of people outside MIT that kept me sane. Claudia and Giselle, the ladies from the B-Side Lounge, thank you for everything. Dilek, you're the best friend I've ever had. Thank you for putting up with me during my PhD, I know I got a little crazy at times. I hope you're always an integral part of my life. I'll miss throwing a Halloween party with you this year. Liam, how long has it been? 7th grade? Your friendship means more to me than I let on. Thanks also for reminding me that graduate school isn't at all representative of the "real" world, I don't think you know how refreshing that was to hear. Linus, thanks for being such a fantastic roommate. For the record, the dent that I put in your car magically healed itself so it doesn't count.

My family has also been incredibly supportive, especially my mom, Vivian, and all my sisters (deep breath) Karen, Christine, Carolyn, and Katherine. Mom, thanks for understanding

when it goes more than a month between calls. I know I'll be farther away, but I'll try to be closer. Karen, I can only aspire to be as strong and brave as you are; you amaze me. Christine, I only hope I can find someone that makes me as happy as Baron makes you. Carolyn, I can't wait to go snowboarding with you in Tahoe. Katherine, you've somehow become the sympathetic ear for the entire family. I think you've done more to hold us together than you realize. Bob you've been so great to Mom for all these years; pop the question already! Dad, I'm sorry we don't get along at times. All I can do is try.

I guess that brings me to Dan. Dan, thank you for teaching me how to think about science. I'm sure all the lessons (read: diatribes that usually begin with the word "dumbf@ck") will come in handy in the future. Despite what some might consider abuse, you've been a great advisor and motivator. My favorite motivational tidbit was the note I found on my desk one Monday morning: "Glad, That your career is going so well you don't work weekends." Working for you has been intense, but also a lot of fun. I think it's safe to say that I'll never work for anyone like you again… ever. I've grown a lot over my time at MIT, and I have you to thank for a lot of that. Thank you for believing in me and for giving me the occasional kick in the ass that I desperately needed.